Silver Nanoparticle Controlled Synthesis and Implications in Spectroscopy, Biomedical and Optoelectronics Applications

by

Kevin Stamplecoskie

Thesis submitted to the
Faculty of Graduate and Postdoctoral Studies
In partial fulfillment of the requirements
For the Ph.D. degree in
Chemistry

Chemistry
Science
University of Ottawa

Abstract

The surge in nanomaterials research in the past decade has occurred largely because of many interesting properties of materials that emerge on this size scale. Of these materials, colloidal solutions of metal nanoparticles have been found to display many interesting optical and physical properties that differ from those of the bulk metal form. Using silver nanoparticles (AgNP) as an example, the increased surface area to volume ratio has made it possible to use these nanomaterials as catalysts where bulk silver is otherwise inactive. AgNP have also recently been incorporated into materials and biological systems as antibacterial agents, with much higher and prolonged activity than silver salt solutions ($AgNO_3$). One of the most obvious and interesting properties of colloidal AgNP is the optical absorption in the visible region of the electromagnetic spectrum, which gives rise to intensely coloured solutions. The colour of these colloids arises from a plasmon excitation, which is an excitation of metal electrons resulting in an oscillating electromagnetic field. The absorption maxima, and therefore the colour of the colloids, is easily controlled by manipulating their size and shape.

This thesis focusses on fabrication of silver nanoparticles, often colloidal solutions, and in some occasions embedded in thin films. New photochemical methods for controlling the particles morphology and optical properties are discovered and described herein, always with end-use of these specific particles in mind. Application of these materials in antibacterial studies, in order to use them in artificial cornea and artificial skin matrices is described. Evaluation of the effect of size and shape of AgNP colloids on the enhanced Raman spectrum of Rhodamine 6G (R6G) is performed, along with the determination of the optimal particle size for highest sensitivity in surface enhanced Raman spectroscopy (SERS) measurements is discovered. Through control of the particles morphology, and optical properties, novel photochemical methods for generating lithographic features below the diffraction limit, and not fundamentally diffraction limited, have been discovered and described herein. Lastly, excitation of the plasmon absorption of AgNP has been used to self-assemble polymer@AgNP, core-shell particles, that act as nanometer sized lasers. This new material has great potential for the optoelectronics industry, which is searching for active optical gain materials of this type.

Overall, the content of this thesis describes the synthesis of AgNP with a high degree of morphological control, which is paramount since the performance of these materials in the described applications is so intimately related with the size, shape and optical properties of the material.

Acknowledgements

I can not express how lucky I am to have been a graduate student in the Scaiano lab. This group calls people from around the world and my experiences here have helped shape an important part of me. I now have colleagues and dear friends around the world, including Spain, Italy, and Argentina. Aside from the relationships within the lab, Tito has been an incredible mentor. I thank Tito and Elda for welcoming me into this group and into their home and cottage. This lab has an exceptional amount of instrumentation and expertise that I was able to take full advantage of over the past few years. Tito is also a fountain of photochemistry knowledge that I think I have only seen the surface of, but it has certainly made me a more complete chemist. He is not only a perfect supervisor, but also a friend, that I will cherish for ever.

I would also like to specifically thank some of my friends in the lab that have helped me grow personally and professionally. I'd first like to thank Andrea Vance, who I will forever be indebted to for being there with empathy like I have never seen in anyone else, and the kindest heart. Andrea, you care for people so much, and taught me so well how to survive this crazy world. Paul and Jessie Billone, who began as great sources of knowledge in the lab, and then great friends. Our camping trips and great times over beer will hopefully continue forever, whenever our paths cross. The Decans, including Stella, for fun times and great friendship. Chiara Fasciani for her brutal honesty, when no one else will tell you the truth that you need to hear; ti voglio bene.

Avelino Corma and Hermenegildo Garcia, thank you both for welcoming me into your labs and mentoring me for 3 months that really was a growing experience, personally and professionally. The experience in Spain was one that I value deeply. Maria Luisa Marin, who I met in Valencia, but did not really get to know well until her visit here to Ottawa. Welcoming me into your home here, you really are a dear friend, wonderful colleague, and a source of inspiration for young students. I would say that you are like a second mother, but I think you are more of a friend, and somehow like family.

For those that I did not mention specifically, this past few years have been an irreplaceable growing experience. Thank you all for that.

Contents

List of Tables

List of Figures

0.1 Contribution Statement

None of the work herein would have been possible without the mentorship of Professor Scaiano. Additionally, several people mentioned here have made important contributions to specific projects. More importantly, it is necessary that I outline the work predominantly done by myself, so that readers may know the direct contributions herein.

The excited state character and lifetime and the photoinitiator (I-2959) was investigated by other groups originally, and was first used for making AuNP by a previous member of the group, Kathy McGilvray. Similarly, the first fluorescent silver nanoparticle solutions were reported by Luca Maretti and Paul Billone. Since then, some of the review articles written by myself and professor Scaiano have led us to a better understanding of the reactions involved in making nanoparticles. Specifically, through determining the mechanism of formation of Ag dimers, a better understanding of the role of the proton coupled electron transfer for ketyl radical reduction of cationic metals is one of my more important contributions. Also, the mechanism of formation of silver dimers and the particular stability of these neutral species in the pathway towards forming AgNP in non-protic solvents is of interest in the field. For these reason this work was later highlighted in the Journal of the American Chemical Society.

The formation of different shapes of silver nanoparticles, from AgNP seeds, with LED irradiation was an independent venture. Chemistry literature had seen the formation of different AgNP with different shapes, made with many different stabilizing agents, and with many different claimed mechanisms that seemed overly complex and incomplete. For this reason, when I wanted to make AgNP with different shapes and optical densities, I decided to try to simplify the many processes into one, and gain first-hand understanding of this phenomenon, which proved successful.

The surface enhanced Raman spectroscopy studies were a collaboration between our group and that of Professor Hanan Anis. The particle preparation as well as sample prep and characterization were done by myself, while Raman spectra were collected by Vidhu S. Tiwari in Professor Anis's labs.

The first lithography experiments that used pre-synthesized AgNP to generate cross-linked methacrylate polymers below the diffraction limit, was a thought inspired mostly by a collaboration with Intel. The work was largely done by myself and an undergraduate student, Dayle Larson, while under the additional guidance of a post-doctoral fellow, Natalia Pacioni.

The work making a hierarchy of lithographic features by a two step irradiation process,

making AgNP and then polymerizing via heat with caprolactam, was again largely a personal venture, but it would not have been possible without the use of a thermally induced polymerization process. For this Chiara Fasciani provided the integral piece of the puzzle, caprolactam, a molecule that she was studying at the time for use in exactly this type of plasmon induced heating that could result in a chemical reaction, in this case polymerization.

The anti-bacterial studies with AgNP have been a collaboration involving many people, for which I must confess I played a very minor role. These projects involve several members of the Scaiano lab, lead mostly by Emilio Alarcon, as well as collaborators in May Griffith's labs in Sweden. I was the "nanoparticle guy", showing the initial synthesis of silver nanoparticles and helping with some of the work to produce nanoparticles stable in biological media, as well as consulting on the conditions for which these particles can and cannot be handled. All of the cell viability studies and bacteria time-kill and colony formation studies were performed by others with more skilled hands in this type of work.

As for the final chapter on dipole nanolasers, we had seen the paper by Noginov et al, and Tito had asked the question to me; "Can we do something like this?" This work looked overly synthetically involved, and our understanding of selective polymerization on the surface of AgNP was the enabling tool for making the spasers that we report here. I took on this project as a person challenge.

The peer reviewed contributions coming from this thesis work are listed here, and I believe the order of authorship is a good indication of my actual contributions in these studies.

Contributions

1. Scaiano, J.C., **Stamplecoskie, K.G.**; From designer particles to custom application, can their surface plasmon fields provide a new way to photosensitize organic reactions?, Journal of Physical Chemistry Letters, 2013, 4(7), 1177-1187.

2. Alarcon, E.I., Bueno-Alejo, C.J., Noel, C.W., **Stamplecoskie, K.G.**, Pacioni, N.L., Poblete, H., Scaiano, J.C.; Human serum albumin as protecting agent of silver nanoparticles: role of the protein conformation and amine groups in the nanoparticle stabilization, Journal of Nanoparticle Research, 2013,15, 1374-7.

3. Gobbo, P., Ghiassian, S., Hesari, M., **Stamplecoskie, K.G.**, Kazemi-Kanjani, N., Lagugne-Labarthet, F. and Workintin, M.S.; Electrochemistry of Robust Gold Nanoparticles-Glassy Carbon Hybrids Generated Using a Patternable Photochemical Approach, Journal of Materials Chemistry, 2012, 22, 23971-23980.

4. **Stamplecoskie, K.G.**, J.C., Self-Assembled Dipole Nanolasers, In preparation.

5. **Stamplecoskie, K.G.**, Fasciani, C., Scaiano, J.C., Dual-stage Sub-wavelength Lithographic Features from a Light Driven, Plasmon Assisted Process, Langmuir, 2012, 28 (30), 10957-10961.

6. **Stamplecoskie, K.G.**, Hallet-Tapley, G.L., J.C. Scaiano, Photochemical Norrish Type I Reaction as a Tool for Metal Nanoparticle Synthesis: Importance of Proton Coupled Electron Transfer. Chem. Comm., 2012, 48, 4798-4808.

7. **Stamplecoskie, K.G.**, Scaiano, J.C., Silver as an Example of the Applications of Photochemistry to the Synthesis and Uses of Nanomaterials. Photochem. Photobiol., 2012, 88(4), 762-768.

8. Scaiano, J.C., **Stamplecoskie, K.G.**, McGilvray, K.M., Pacioni, N.L., A Paradigm for the Radical-Mediated photochemical synthesis of metal nanostructures. Pub. Date: March 27, 2012, Encyclopedia of Radicals in Chemistry, Biology and Materials, Chapter 73, vol.12.

9. Alarcon, E., Udekwu, K., Skog, M., Pacioni, N.L., **Stamplecoskie, K.G.**, Gonzalez-Bejar, M., Polisetti, N., Wickham, A., Richter-Dahlfors, A., Griffith, M., Scaiano, J.C., Silver Nanoparticles Revisited: Collagen-stabilized, Photochemically Prepared Silver Nanoparticles for Biomedical Applications, Biomaterials, 2012, 33(19), 4947-56.

10. **Stamplecoskie, K.G.**, Pacioni, N.L., Larson, D., Scaiano, J.C., Plasmon-mediated Photopolymerization Maps Plasmon Fields for Silver Nanoparticles, J. Am. Chem. Soc, 2011, 133(24), 9160-9163.

11. (alphabetical after professors) J.C. Scaiano, Jos C. Netto-Ferreira, Emilio Alarcon, Paul Billone, Carlos J. Bueno Alejo, Charles-Oneil L. Crites, Matthew Decan, Chiara Fasciani, Mara Gonzalez-Bejar, Geniece Hallett-Tapley, Michel Grenier, Katherine L. McGilvray, Natalia L. Pacioni, Andrea Pardoe, Laetitia Ren-Boisneuf, Rachel Schwartz-Narbonne, M. Jazmin Silvero, **Stamplecoskie, K.G.** and Tse-Luen Wee; Tuning plasmon transitions and their applications in organic photochemistry, Pure Appl. Chem., 2011, 83(4), 913-930.

12. **Stamplecoskie, K.G.**, Scaiano, J.C., Kinetics of the Formation of Silver Dimers (Ag_2): Early Stages in the Formation of Silver Nanoparticles, J. Am. Chem. Soc., 2011, 133(11), 3913-3920.

13. **Stamplecoskie, K.G.**, Scaiano, J.C., Tiwari, V.S., Anis, H., Optimal Size of Silver Nanoparticles for Surface-Enhanced Raman Spectroscopy, J. Phys. Chem. C, 2011, 115(5), 1403-1409.

14. **Stamplecoskie, K.G.**, Scaiano, J.C., Light Emitting Diode Irradiation Can Control the Morphology and Optical Properties of Silver Nanoparticles, J. Am. Chem. Soc, 2010, 132(6), 1825-7.

List of Acronyms

AFM atomic force microscopy

AgNP silver nanoparticles

AgNP seeds AgNP seeds

AIBN azobisisobutyronitrile

AuNP gold nanoparticles

CHA cyclohexylamine

DNQ diazonaphtoquinones

EM electromagnetic field

EMF electromagnetic field

fcc face-centred cubic

HAT Hydrogen atom transfer

HOMO highest occupied molecular orbital

HSA human serum albumin

ISC intersystem crossing

LED light emitting diodes

LFP laser flash photolysis

LUMO lowest unoccupied molecular orbital

MIC minimum inhibitory concentration

MNP metal nanoparticles

PAG photoacid generator

PCeT proton coupled electron transfer

PVP poly (vinyl pyrrolidone

R6G Rhodamine 6G

SEM scanning electron microscopy

SERS surface enhanced Raman spectroscopy

TEM trasmission electron microscopy

thf tetrahydrofuran

TMPTA trimethylpropanetriacrylate

TOF turn over frequency

Some important molecules used in this thesis as well as the corresponding acronyms used in the text.

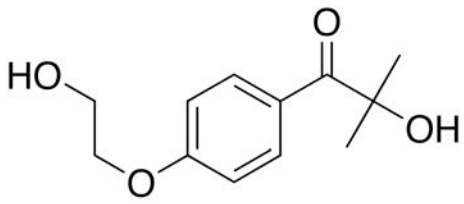

I-2959

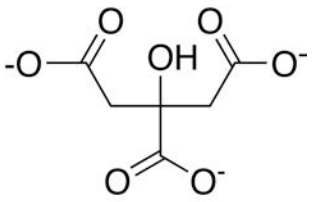

citrate

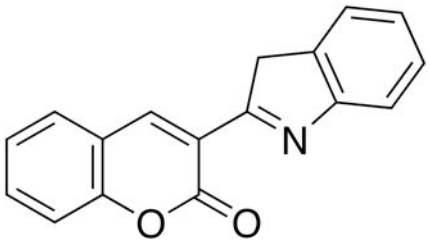

C6

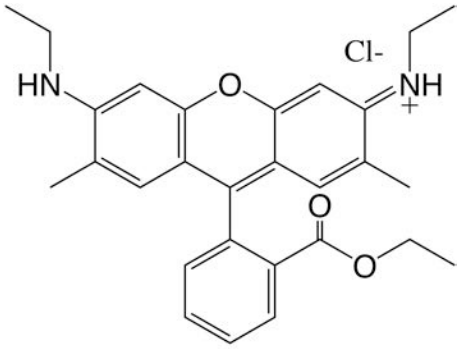

R6G

Chapter 1

Introduction

1.1 Nanomaterials and Nano Size Effects

Nanomaterials in general have gained interest in chemical research in the past couple of decades. This is largely due to the discovery of properties of materials that change dramatically at the nanoscale. A common example is quantum dots, like CdS, that display intense emission below a certain critical particle size, that happens to be on the nanometer scale. This effect arises from a quantum confinement phenomenon, where the exciton (e-/hole+) separation in the semiconductor material exceeds the particle size. When the particles have no direction in which they are larger than the exciton, the exciton is quantum confined to the particle, and they are said to be zero dimensional.

For noble metal nanoparticles (the topic of this thesis) like Cu, Ag and Au, when the particle size is smaller than the wavelength of light, they can absorb particular frequencies giving rise to different colours of colloidal solutions. The colour is not only dependant on the material, but the exact size, shape, whether or not the particles are single particle colloids or aggregates, and on the dielectric constant of the medium surrounding the particles. To understand this better it is sometimes convenient to discuss bulk metal plasmons first. Bulk metal is known to support both bulk plasmons and surface plasmon polaritons on flat surfaces, which has been exploited in making surface plasmon sensors. Conceptually one can visualize a flat piece of metal as a periodic array of positive charges (the nuclei of the crystalline metal) with a cloud of electrons loosely bound to the metal by an electrostatic interaction between the negatively charged electrons and positively charged nuclei. When light, polarized with its oscillating electric field component perpendicular to the surface of the metal, interacts with the surface of

the metal, it is possible for the metal to transiently displace the electrons according to the frequency of light as shown by the surface plasmon polariton in Figure 1.1. The overall result is that the metal is able to absorb light of a given frequency, confine the light to the surface, and transmit that light with high efficiency along the surface over short distances. The nuclei, serve as a restoring force on the displaced electrons, and so the identity of the metal determines, in part, the particular frequency of light that can be absorbed (how easily the electrons/nuclei are displaced into the polaritons).

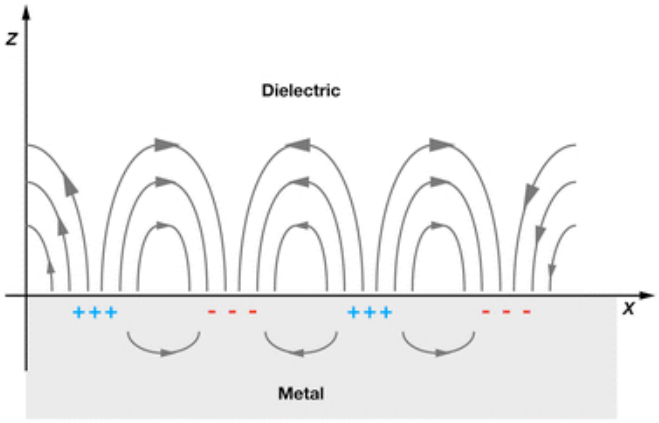

Figure 1.1: Surface plasmon polariton, or simply surface plasmon, for a bulk metal slab. Arrows indicate direction of instantaneous polarization of the metal surface.

As illustrated in Figure 1.1, the surface plasmon wave penetrates into both the metal and the dielectric layer. Therefore, the dielectric constant of both metal and dielectric play an important role in the properties of the surface plasmon. A schematic illustrating a typical design for a surface plasmon sensor is shown in Figure 1.2 below. The key features here are a prism that directs the light to a metal surface at an optimal angle, and a smooth metal surface that guides light using the surface plasmon polariton effect. Gold is often the metal of choice for these sensors due to its superior inertness towards oxidation. Overall, at a specific angle, metal slabs will guide/absorb light along the surface of the metal, and only for a frequency range that is particular to the metal chosen. Surface plasmon polaritons are alternating positive/negative charges that move rapidly along a surface of the metal coupling strongly with the light that has been absorbed. The frequency of light is therefore determined partly by the metal due to the dielectric constant of the metal, or in other words, the energy required to displace electrons in the

metal. The particular frequency of light guided is also strongly affected by the dielectric constant of the surface, which is why these materials can be used as sensors. A typical sensor has been functionalized with a receptor molecule that specifically binds an analyte, and upon binding, the dielectric constant changes (since the molecule is different from the solvent that was there before), and this binding can cause a spectral shift in the frequency of guided light as shown in Figure 1.2.

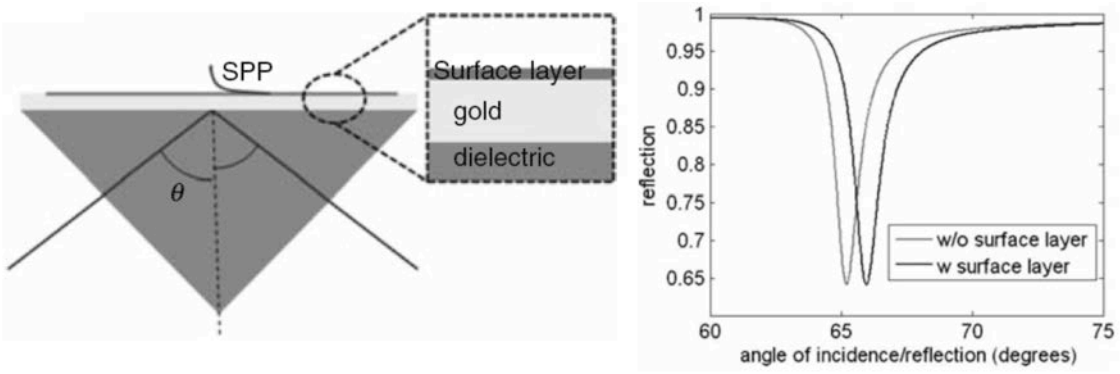

Figure 1.2: Schematic of a typical surface plasmon sensor (left) and a typical spectral shift observed due to change in surface plasmon absorption upon binding of a 'surface layer' (right), adapted from ref [1].

So how is this relevant to nanoparticles? Metal nanoparticles can be viewed simply as very small metal slabs, that also absorb light similar to surface plasmon polaritons. However, for small nanoparticles the curvature of the surface becomes very important, in that it is no longer planar on the length scales of the wavelength of light used to excite it. Also, nanoparticles are small enough that the surface plasmon penetrates through the entire particle, so that nanoparticles have surface plasmons, but not bulk plasmons. The result is that the polaritons are actually just an oscillating EM field that is trapped on the particle. All of the electrons in the particle oscillate together but, as one can see from Figure 1.3, only the surface experiences an oscillating charge. That is why, for nanoparticles, they are called surface plasmons. The particular size effects described here for small particles are the reason that nanoparticles absorb light of different wavelengths than the bulk material, and it also becomes intuitive that particle shape strongly affects the spectral position of this plasmon absorption. What is common to both nanoparticles and the bulk metals though, is that both can absorb light, and in doing so concentrate that light on the surface of the material. The resultant EM field decays with typical

evanescent behaviour from the surface of the material.

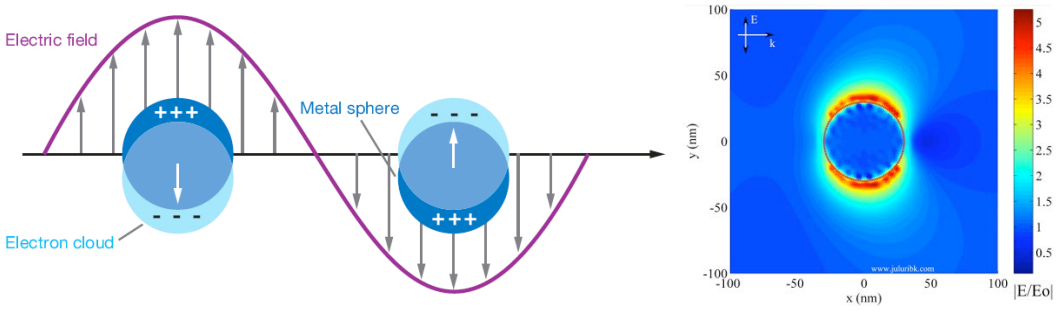

Figure 1.3: Interaction of light with a spherical metal nanoparticle such as silver, and the resultant EM field, adapted from ref [2].

The phenomenon of plasmon absorption of small spherical particles was first described by Gustav Mie in 1908, by solving Maxwell's equations for spherical particles assuming they are homogeneous dielectric materials.[3] Nanoparticles can support many plasmon modes, but for simplicity, when one considers spherical particles that are much smaller than the wavelength of light (radius $\ll \lambda$), only a dipolar mode contributes significantly to absorptions. The polarizability (ability to absorb light) for a particle can be described by equation 1.1 [4];

$$\alpha = 3\epsilon_0 V \frac{\epsilon - \epsilon_m}{\epsilon + 2\epsilon_m} \tag{1.1}$$

where, α is the polarizability, ϵ_0 is the permittivity of a vacuum, V is the volume of the particle, ϵ is the permittivity of the material, and ϵ_m is the permittivity of the medium surrounding the particle. The equation is shown here simply to illustrate that a maximum occurs for the case when;

$$\epsilon = -2\epsilon_m \tag{1.2}$$

What this shows is that the real part of the dielectric constant (which is a complex number) has to be negative to support a plasmon absorption. This requirement is satisfied for metal nanoparticles such as gold, silver and copper. The total extinction of a particle is comprised of scattering and absorption components such that:

$$\text{Total Extinction} = \text{Absorption} + \text{Scattering} \tag{1.3}$$

such that;

$$\text{Absorption} = k\text{Im}(\alpha) \tag{1.4}$$

and,

$$\text{Scattering} = \frac{k^4}{6\pi}|\alpha|^2 \tag{1.5}$$

where, Im represents the imaginary part of the permittivity and k is the wave vector of light, and can be described with the following relation according to the permittivity of the medium;

$$k = \frac{2\pi\epsilon_m^{1/2}}{\lambda} \tag{1.6}$$

The absorption component of the excitation of surface plasmons occurs due to collisions of oscillating electrons and the scattering component can be viewed as a lossless interaction, where overall the plasmon is a very short-lived phenomenon. Figure 1.4, provides an illustrated summary of the light interacting with a particle, describing the events of plasmon absorption.

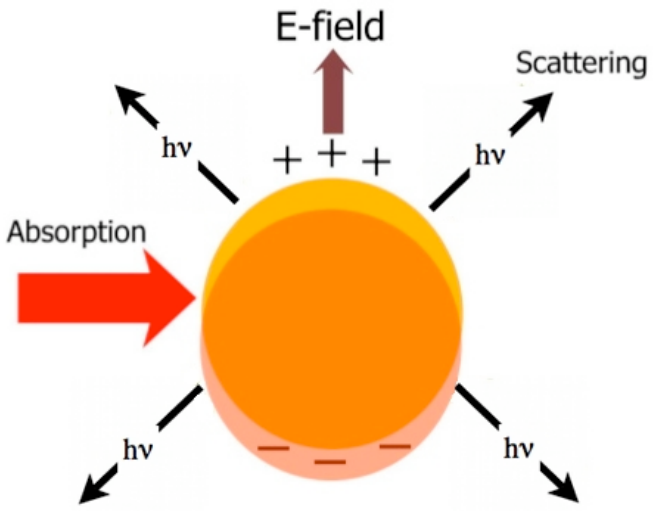

Figure 1.4: Illustration of the events contributing to the extinction or surface plasmon absorption of a metal nanoparticle.

The decay of the plasmon occurs through dephasing of the collective coherent oscillation of electrons in the particle. For 75 nm AgNP the surface plasmon excited state lifetime (dephasing time) has been measured to be 10 fs.[5] In that short time, light is concentrated at the particle surface, where the frequency of light is determined by the material, medium, and the particle shape and size. The concentrated light can be used in what has been referred to as an antenna mechanism, to enhance vibrational and electronic transitions in molecules nearby; an effect that has been used to dramatically

increase sensitivity in surface enhanced Raman spectroscopy (SERS). The surface plasmon generally produces negligible emission, and decays almost exclusively thermally, by releasing heat. For AgNP, the extinction coefficient for absorption is approximately 19,000 $M^{-1}cm^{-1}$ per reduced atom, or in other words, 4.75 x10^9 $M^{-1}cm^{-1}$ for a 10 nm particle containing 250 000 atoms [6]. This is a very large number, which means that the nanoparticles absorb a lot of light. In an intelligent experiment Novotny *et al* were able to observe this EM field enhancement effect around a single nanoparticle. In the experiment, a single gold nanoparticle was placed on the end of an AFM tip, and the tip was brought close to a single dye molecule in a film, and as the particle approached the molecule, the fluorescence from the molecule was monitored. The setup and experimental results are shown in Figure 1.5. When the nanoparticle is sufficiently far from the dye molecule, the molecule emits at a normal count rate. As the AuNP is brought closer to the dye molecule the dye emission increases to an optimal position of approximately 5 nm separation. At this point the dye molecule is "feeling" the enhanced electromagnetic field, which makes the molecule more polarizable as well as increasing the quantum yield of emission once excited. At closer distances, the EM field becomes exponentially stronger, but the nanoparticle is close enough now to facilitate quenching of the dye molecule excited state. For this reason the dye emits very little when it is less than a few nanometers from the particle surface.[7]

The surface plasmon generally produces negligible emission, and decays almost exclusively thermally, by releasing heat. Both the EM field and localized heating have been used in novel applications, specifically pertaining to lithography, as part of this thesis as well.

1.1.1 About This Thesis

A common theme for the work presented in this thesis is control over the size and shape of AgNP to implement them in new technologies. In order to realize this, one requires an in depth understanding of the nucleation and growth processes involved in nanoparticle formation, in order to be able to chemically manipulate the synthesis of these particles to direct the growth. Long before 'nano' became popular, Henglein had began the study of small cluster formation (Ag_x) in aqueous conditions by pulsed radiolysis techniques. He was able to identify several major transient species ($Ag_x{}^{n+}$) with absorption maxima in the UV (250-300 nm) that form first, but aggregate quickly into larger nanoparticles that can then support a plasmon absorption at 400 nm, characteristic of spherical

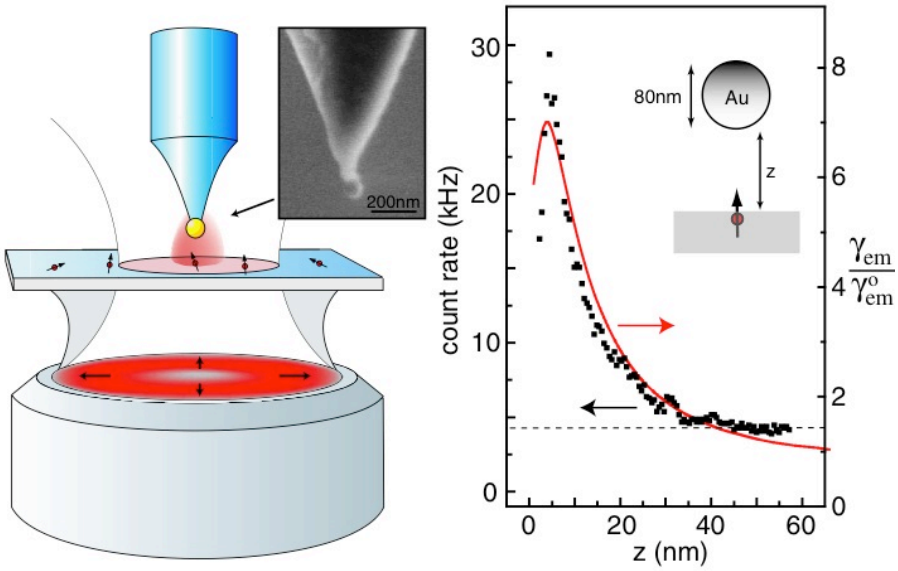

Figure 1.5: Experiment performed by Novotny *et al* illustrating the EM field enhancement effect of metal nanoparticles (AuNP) on the fluorescence intensity of a dye molecule as a function of proximity. The red curve on the right is a theoretical curve and the black dots are experimental data for emission counts. Adapted from reference [7], with permission from L. Novotny.

AgNP.[8, 6] Earlier research in the Scaiano group lead to the discovery of fluorescent silver nanoparticles.[9] It was postulated that the anomalous fluorescence was due to the concurrent formation of small silver cluster (Ag_2) and AgNP, that was only possible in organic solvents like toluene and tetrahydrofuran. This lead to the kinetic study, described herein, of the formation of these Ag dimers. Reduction of metals with radicals, as commonly done here, and in the work by Henglein, usually produces a proton. The major differences from the work done by Henglein is that our work is performed in solvents that do not easily accept a proton. Under these conditions, using solvents that do not easily accept a proton, we have found that introducing a base to accept a proton, and so, PCeT becomes crucial to the overall process. This work has added to the understanding of the formation and dynamics of metal nanoparticles, particularly in organic solvents, which is crucial to controlling the synthesis of these materials.

Many of the properties of nanoparticles that differ from their bulk arise from the different electronic band structure of these small materials, as compared to the band structure of their bulk counterparts. In fact, nanoparticles can be described well by thinking of them as a species somewhere between that of molecules and bulk materials. For example, the band structure (density of states) for materials starts to build up from the centre of the band, and the edges of the electronic bands correspond to surface states. Nanoparticles, have less developed band structure (lower density of states) compared with bulk materials, and a higher contribution from surface states, so that the band structure of nanomaterials lies somewhere between the bands of bulk material and discrete electronic states of molecules. The relationship between size and band structure is depicted for metals in Figure 1.6.[10, 11] The free energy for materials is strongly affected by the surface atoms as well, and due to the high number of surface atoms to bulk ratio in nanomaterials, the thermodynamic properties of nanoparticles can be drastically affected by size. A good example is the melting point, which can be depressed dramatically with reduced particle size, as shown for AgNP in Figure 1.6 below for both the melting of the surface, and the entire nanoparticle. Despite these differences, it has been observed that nanocrystalline morphologies and morphologies of larger extended crystals, are the same, exposing the same facets, because growth of particles is a fundamental property originating from the unit cell. This allows one to manipulate the surface energies using all of the same techniques used for large extended crystals, and therefore, having another level of control of the properties of nanomaterials.

The emission from quantum dots and the colour of colloidal metal nanoparticles (MNP) solutions are nice examples of macroscopically observable effects that arises when

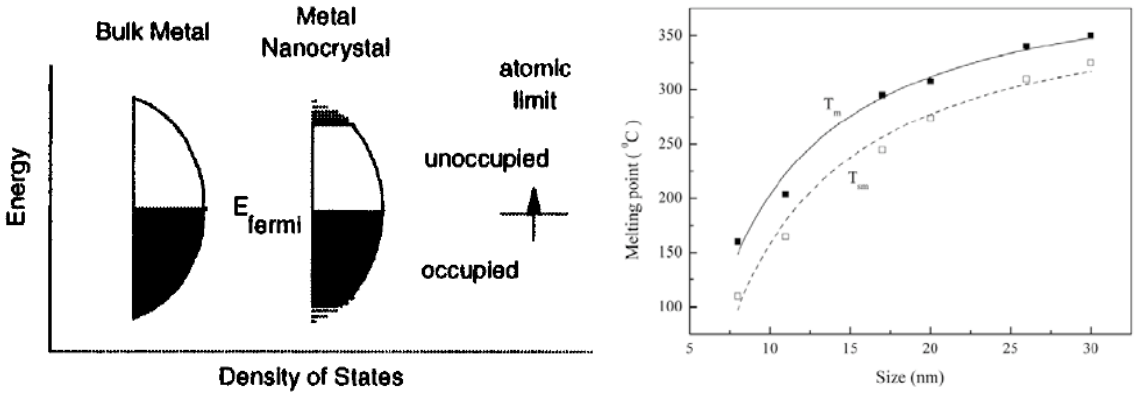

Figure 1.6: Density of states diagram for a bulk, nanoparticle and atomic metal (left), as well as the melting point of AgNP surfaces (T_{sm}) and AgNP (T_m) as a function of particle size (right), adapted with permission from references [10] and [11], respectively.

particles are on the nanoscale size regime. However, there are many other effects of nano that are less obvious to the macroscopic observer. For example, metallic gold was long thought to be too inert as a catalyst in many applications like oxidations. However, there has been a recent explosion of research using gold nanoparticles (AuNP) for various oxidation reactions, and even to do difficult synthesis like catalyzing Sonogashira coupling reactions. While bulk gold has a very low surface area to volume ratio, this value is much higher for AuNP, especially small AuNP. Gold was thought to be inert for so long because only the surface atoms are catalytically active, and in bulk gold there are proportionally very few of these atoms. In small AuNP, the surface area is so much larger with respect to the volume, and so there are many surface atoms that can contribute as catalytically active sites. Corma *et al.* illustrate well this correlation between AuNP surface atoms and catalytic activity.[12] The fractional number of surface atoms as a function of particle size for AgNP is shown in Figure 1.7 (a similar curve can be generated for AuNP), as well as the turn over frequency (TOF) of the oxidation of cumyl peroxide as a function of particle size (fractional surface atoms), as determined by Corma *et al.* From Figure 1.7 one can see a drastic increase in surface atoms below approximately 10 nm diameter particles. This is the major reason for the increased reactivity of nanoparticles, and it is also the reason that very small and homogeneous nanoparticles are required for catalysis.[12]

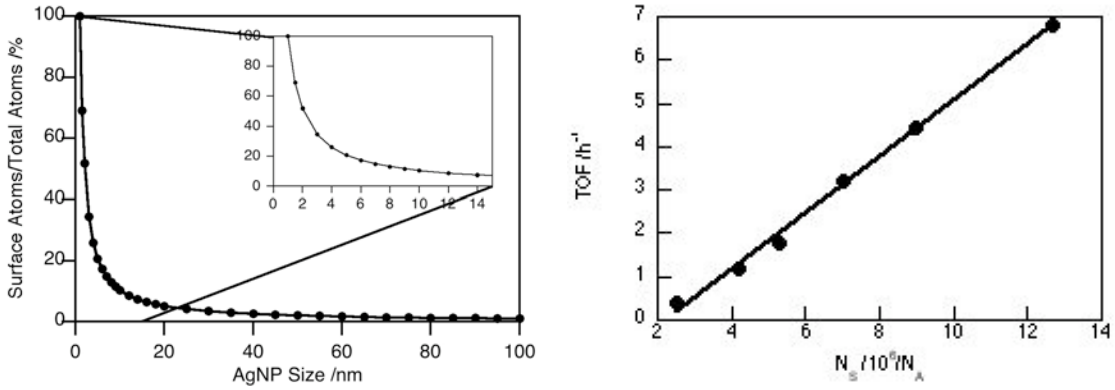

Figure 1.7: Surface atoms to total atom ratio for AgNP (left) and reactivity towards the oxidation of cumyl peroxide vs fractional surface gold atoms, as determined by Corma *et al* (right), adapted from ref [12].

1.2 Making Nanoparticles

Over the past decade the Scaiano group has made significant progress in discovering and understanding photochemical routes to the formation of noble metal nanoparticles.[13, 14, 15, 16, 17] The chemical approach to making noble metal nanoparticles is usually a bottom up method, which involves reducing a metal salt to its atomic form. The concentration of reduced metal atoms increases in solution until supersaturation is reached, where nucleation of small clusters occurs, and these clusters subsequently grow into nanoparticles. The overall process is described by equation 1.7, and Figure 1.8. For most chemical methods the metal salt is reduced with a harsh chemical reducing agent, most commonly $NaBH_4$.[18] Material surfaces are often highly reactive, and nanoparticles have a high surface area to volume ratio, so they are inherently reactive species. Therefore, the metal nanoparticles tend to aggregate unless they are capped by organic molecules. When making AgNP or AuNP, commonly the capping agents contain S, N or P that bind strongly to the particle surface and arrest the growth.[19, 20] One of the main advantages from the original work in the Scaiano group with making AuNP is that the particles solutions do not generally contain any S, N or P, so that the surface can be easily modified post-synthesis (ie. ligand exchange).[14, 21] This provides some versatility in that the solubility and reactivity of the nanoparticles can be easily controlled post-synthesis by controlling the surface functionality.

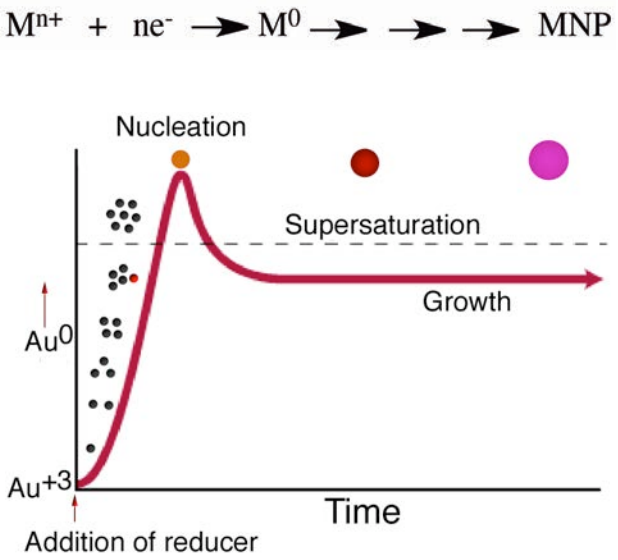

$$M^{n+} + ne^- \rightarrow M^0 \rightarrow \rightarrow \rightarrow MNP \tag{1.7}$$

Figure 1.8: Curve, illustrating the progress of nanoparticle nucleation and growth in time. The concentration of metal atoms increases in solution until supersaturation where nucleation of particles occurs followed by growth, which is a combination of Ostwald ripening type processes and consuming reduced atoms in solution, until a stable solution of colloids is obtained.

In the photochemical method, the idea is to exploit excited states that are capable of making free radicals that are sufficiently strong reducing agents. The α-hydroxy or α-amino carbon centered radicals are the two common choices to generate as a reducing species. The radicals can be formed by either intermolecular reactions of the transient excited molecule (usually abstract a hydrogen from a suitable donor), or by intramolecular reactions (usually Norrish chemistry) that generates the reducing species. Acetone is a convenient example as a possible photoinitiator that uses intermolecular reactions and will be used here to guide the discussion. A Jablonski diagram for acetone is shown in Figure 1.9 as well, illustrating the excited states involved and the reducing radical made from the transient excited state of acetone.

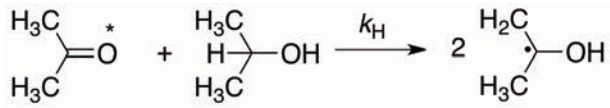

(1.8)

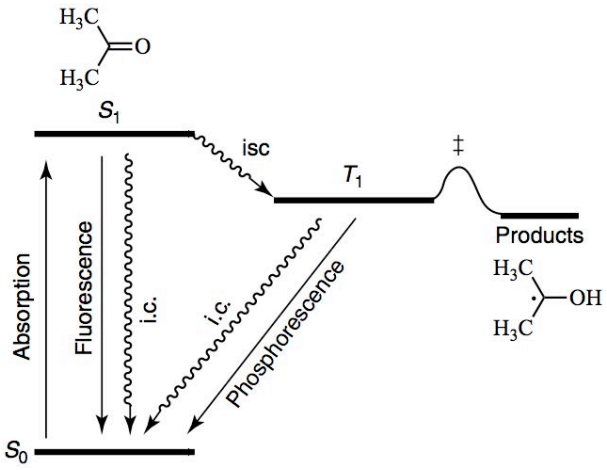

Figure 1.9: Jablonski diagram illustrating the excited states involved in radical formation for acetone as a possible photoinitiator for metal nanoparticle formation.

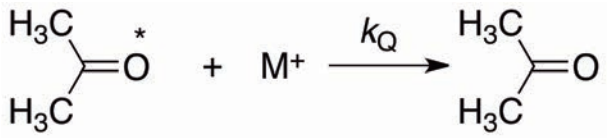

(1.9)

In order to have intermolecular reactivity from an excited state, the excited state must have an appreciable lifetime, which usually means triplet excited states. Singlet excited states live for ns, while triplets generally live for μs. When referring to intermolecular reactions, if the excited state only lives for a couple of ns, even if the hydrogen donor in this case is reacting at a diffusion controlled rate, the excited state does not live long enough or react enough to generate a significant steady state concentration of reducing radicals. In short, generating radicals efficiently from excited transients requires triplet excited states. That being said, there are two very obvious requirements for a photoinitiator; (1) a high quantum yield of intersystem crossing (ISC) to the triplet, and (2) generation of reducing radicals, such as α-hydroxy radicals, from the excited state. Acetone has a quantum yield of ISC of nearly unity and upon hydrogen extraction by the triplet generates two α-hydroxy radicals that are great reducing agents. So why then is acetone NOT a good photoinitiator for making noble metal nanoparticles?

In order to have a high steady state concentration of radicals, the photoinitiator must generate the excited state efficiently. Acetone, has a very low extinction coefficient ($\epsilon_{280nm} = 12.4\ \mathrm{M^{-1}cm^{-1}}$), so it does not get excited efficiently. Also, the reaction to form radicals is an intermolecular reaction, for which it is possible to generate MNP, however,

the excited triplet lives for microseconds and is most often competitively quenched by metal salts, reducing the efficiency of hydrogen abstraction and therefore the yield of nanoparticle formation. Equation 1.8 shows the reaction to form reducing radicals from excited acetone and equation 1.9 shows the competing quenching of the excited state. Values for k_H are known to be only approximately 10^6 $M^{-1}s^{-1}$, while k_Q is diffusion controlled (10^{10} $M^{-1}s^{-1}$). Therefore, even though quenching of the excited state of acetone results in the ground state molecule again, if acetone would require very long irradiation times to form nanoparticles. For this reason, intramolecular reactions, which occur much faster than diffusion controlled reactions, are often preferred for photoinitiators in making MNP.

A list of special requirements that must be met by the photoinitiator is provided here as a guideline for evaluating photoinitiators for their use in making nanoparticles:[13]

1. Photoinitiator must absorb respectably at a convenient wavelength, usually UV.

2. Photoinitiator must have a high extinction coefficient to generate excited states, and therefore, reducing species with a good quantum efficiency ($\epsilon_{UVA} \gtrsim 1000$ $M^{-1}cm^{-1}$).

3. High quantum yield of radical formation from the excited state ($\phi \gtrsim 0.1$).

4. Radical production via fast unimolecular cleavage, ie. Norrish type I photocleavage, can compete with diffusion controlled quenching of excited states by metal precursor ions. A high steady state concentration of reducing radicals also results in higher concentration of nucleation sites and smaller resultant nanoparticles, which is often desirable.

5. If intermolecular reactions are required, a good photoinitiator should be chosen by points 1-3 and a good hydrogen donor ($k_H \gtrsim 10^7$ $M^{-1}s^{-1}$) so as to minimize the effect of excited state quenching by the metal salts.

6. Photoinitiators must be soluble in the reaction medium up to millimolar concentrations, the concentrations of metal salts commonly used for nanoparticle synthesis.

7. It is best if the products of the photoreactions are volatile, or easily removed from the reaction medium post-synthesis, in order to minimize the chemical debris that may be problematic when utilizing the nanoparticle colloids in further applications such as catalysis.

8. For biological applications, precursors and products of the photoreaction must have minimal toxicity.

Several Irgacure photoinitiators have been found to meet all or most of the above requirements, namely I-2959 and I-907, shown in equations 1.10 and 1.13. Using I-2959 as an example for our criteria for a good photoinitiator, I-2959 has an $\epsilon_{280nm} = 1000 M^{-1} cm^{-1}$, so that it strongly absorbs UV light, it has a high quantum yield of Norrish type I photocleavage to form the hydroxy radical ($\phi_{Norrish} = 0.29$) and the excited state has a 10 ns lifetime so that it is not easily quenched by metal salts.[22] The products of photocleavage, acetone and 4-hydroxyethoxybenzoic acid have been shown to be non-toxic[23] and while acetone is volatile and easily removed, 4-hydroxyethoxybenzoic acid is a mild stabilizing agent that is easily replaced during or after the synthesis. Therefore, the general scheme for producing metal nanoparticles in the Scaiano group is shown here, using silver as the simplest example because it is a M^{1+} salt.

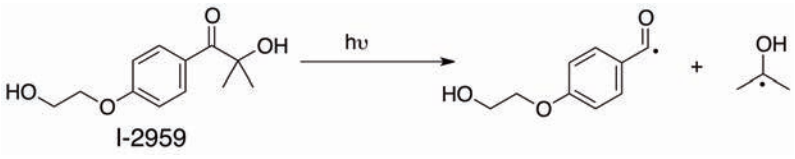

(1.10)

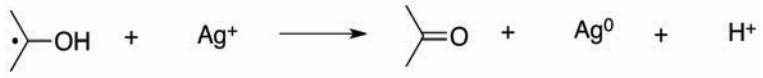

(1.11)

(1.12)

I-2959 is the most commonly used photoinitiator used to make nanoparticles in the Scaiano group, however, largely due to its high solubility in water, which most of our research is performed in. However, sometimes a stronger reducing agent than the α-hydroxy radical is required, in which case I-907 is used, as shown in equation 1.13. The I-907 photocleavage gives the α-aminoalkyl radical, which is a stronger reducing agent.

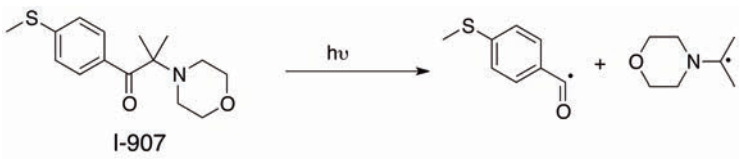

(1.13)

The photochemical approach to making nanoparticles has several advantages, most notably the spatial and temporal control of the formation of the materials. Because light can be directed where needed, and since the photochemical reactions are initiated

by light without any thermal reactivity in most cases, the generation of nanoparticles by photochemical methods can be used to deliver nanoparticles in particular area with high degree of spatial control, whenever they are required. In this thesis, the synthesis of AgNP in various different environments is discussed, in some cases with spacial confinement provided by generating the particles in exposed regions through a lithographic mask, a good example where the spatial and temporal control of photochemical synthesis is required. AgNP have been synthesized in these various environments for their use in a multitude of applications described herein as well, including; fluorescent AgNP for imaging, biological applications including antibacterial studies and photothermal therapy, surface enhanced Raman spectroscopy (SERS), photolithography applications where the plasmon absorption has been used generate polymer features that are not diffraction limited, and for surface plasmon lasers that can serve as a much needed optical gain medium for optoelectronics.

1.2.1 Conclusions

Overall, nanomaterials have fundamentally different properties from their bulk counterparts, which can be well understood and manipulated in novel materials. There are two important underlying themes of this work; (1) that light can be used to generate a multitude of different AgNP with drastically different chemical and optical properties, and (2) that the interaction of light with these materials, if well understood, can be exploited in a variety of novel applications with potentially significant impact in a broad range of fields. While the synthesis has been discussed here, the particular applications are discussed throughout the remainder of this work in corresponding areas. This chapter provides the background knowledge that pertains to the following chapters of synthesis and application of these interesting materials. It also allows a more complete understanding of the fundamentals involved in much of this thesis.

REFERENCES

[1] M Zourob, A Lakhtakia, AG Brolo, R Gordon, and D Sinton. *Springer Series on Chemical Sensors and Biosensors*, volume 7. Springer, 2009.

[2] KA Willets and RP Van Duyne. Localized surface plasmon resonance spectroscopy and sensing. *Annual Reviews of Physical Chemistry*, 58:267–297, 2007.

[3] G Mie. Beitrage zur optik truber medien, speziell kolloidaler metallosungen. *Annallen der Physik*, 25:377, 1908.

[4] U Kreibig and M Vollmer. *Optical Properties of Metal Clusters*. Springer, 1995.

[5] YH Liau, AN Unterreiner, Q Chang, and NF Scherer. Ultrafast dephasing of single nanoparticles studied by two-pulse second-order interferometry. *Journal of Physical Chemistry B*, 105(11):2135–2142, 2001.

[6] S Link, ZL Wang, and MA El-Sayed. Alloy formation of gold-silver nanoparticles and the dependence of the plasmon absorption on their composition. *Journal of Physical Chemistry B*, 103(18):3529–3533, 1999.

[7] P Anger, P Bharadwaj, and L Novotny. Enhancement and quenching of single-molecule fluorescence. *Physics Review Letters*, 96(11):113002, 2006.

[8] A Henglein. Small-particle research: physicochemical properties of extremely small colloidal metal and semiconductor particles. *Chemical Reviews*, 89(8):1861–1873, 1989.

[9] L Maretti, PS Billone, Y Liu, and JC Scaiano. Facile photochemical synthesis and characterization of highly fluorescent silver nanoparticles. *Journal of the American Chemical Society*, 131(39):13972, 2009.

[10] AP Alivisatos. Perspectives on the physical chemistry of semiconductor nanocrystals. *Journal of Physical Chemistry*, 100(31):13226–13239, 1996.

[11] OA Yeshchenko, IM Dmitruk, AA Alexeeko, and AV Kotko. Surface plasmon as a probe for melting of silver nanoparticles. *Nanotechnology*, 21(4):045203, 2010.

[12] A Corma and H Garcia. Supported gold nanoparticles as catalysts for organic reactions. *Chemical Society Reviews*, 37(9):2096, 2008.

[13] JC Scaiano, KG Stamplecoskie, KL McGilvray, and NL Pacioni. *A Paradigm for the Radical-Mediated Photochemical Synthesis of Metal Nanostructures*. John Wiley and Sons Ltd, 2012.

[14] KL McGilvray, MR Decan, D Wang, and JC Scaiano. Facile photochemical synthesis of unprotected aqueous gold nanoparticles. *Journal of the American Chemical Society*, 128(50):15980–15981, 2006.

[15] M Luisa Marin, KL McGilvray, and JC Scaiano. Photochemical strategies for the synthesis of gold nanoparticles from au(iii) and au(i) using photoinduced free radical generation. *Journal of the American Chemical Society*, 130(49):16572–16584, 2008.

[16] KG Stamplecoskie and JC Scaiano. Light emitting diode irradiation can control the morphology and optical properties of silver nanoparticles. *Journal of the American Chemical Society*, 132(6):1825–7, 2010.

[17] KG Stamplecoskie and JC Scaiano. Kinetics of the formation of silver dimers: Early stages in the formation of silver nanoparticles. *Journal of the American Chemical Society*, 133(11):3913–3920, 2011.

[18] S Eustis and MA El-Sayed. Why gold nanoparticles are more precious than pretty gold: Noble metal surface plasmon resonance and its enhancement of the radiative and nonradiative properties of nanocrystals of different shapes. *Chemical Society Reviews*, 35(3):209, 2006.

[19] F Mirkhalaf, J Paprotny, and DJ Schiffrin. Synthesis of metal nanoparticles stabilized by metal?carbon bonds. *Journal of the American Chemical Society*, 128(23):7400–7401, 2006.

[20] VJ Gandubert and RB Lennox. Assessment of 4-(dimethylamino)pyridine as a capping agent for gold nanoparticles. *Langmuir*, 21:6532–6539, 2005.

[21] KG Thomas and PV Kamat. Chromophore-functionalized gold nanoparticles. *Accounts of Chemical Research*, 36(12):888–98, 2003.

[22] S Jockusch, MS Landis, B Freiermuth, and NJ Turro. Photochemistry and photophysics of r-hydroxy ketones. *Macromolecules*, 34:1619–1626, 2001.

[23] EI Alarcon, K Udewku, M Skog, N Polisetti, NL Pacioni, KG Stamplecoskie, M Gonzalez-Bejar, A Richter-Dahlfors, M Griffith, and JC Scaiano. The biocompatibility and antibacterial properties of collagen-stabilized photochemically prepared silver nanoparticles. *Biomaterials*, 33(19):4947–56, 2012.

Chapter 2

Photochemical Synthesis of Silver Nanoparticles

2.1 Some Photochemistry Basics

The Scaiano Group has a solid history in mechanistic organic photochemistry, and only more recently has become well versed in photochemical routes to the synthesis of noble metal nanoparticles, for which an understanding of molecular photochemistry is an essential component. As described briefly in the Introduction, the molecule of choice for generating noble metal nanoparticle colloids is I-2959, see equation 1.10. The choice is not random.

I-2959 photochemistry from the excited state occurs through a Norrish type I cleavage, one of the first reactions any photochemist becomes familiar with, and certainly one of the most well understood photochemical reactions. The Norrish type I and II reactions are shown in equations 2.1 and 2.2 respectively, where the * represents excited states. The Norrish type I cleavage can occur for aliphatic or aromatic ketones, from either the singlet or triplet excited state, however, the triplet reaction is more common for a trivial reason. Excited singlet states generally have ns lifetimes, which is a short time for reactions to occur, but excited triplets usually have μs lifetimes, which is certainly long enough for the Norrish type I or II intramolecular reactions. It is common to represent the non-bonding or π-bonding states molecular orbitals involved in photochemical reactions as n,π^* or π,π^* states, (n = non-bonding molecular orbital, and $\pi = \pi$ bonding molecular orbital). The first symbol in this notation represents the type of highest occupied molecular orbital (HOMO) in the ground state and the second represents the type of HOMO of the excited

state, which is a singly occupied molecular orbital for the excited state. Therefore, an n,π^* excited state occurs for a molecule that has a non-bonding HOMO, which is common for ketones, where the non-bonding electrons on oxygen are the highest energy electrons in the molecule (in the HOMO, and one of these non-bonding electrons is promoted to a π antibonding excited state. Solvent effects on excited state reactivity are usually negligible for π,π^* excited states. However, n,π^* excited states, on the other hand, can be conceptually thought of as an oxygen centred transient radical, since one of the electrons of the non-bonding orbital of oxygen has been effectively promoted to the π^* system. The transient oxygen centred radical reactivity is strongly affected by the polarity, and the hydrogen bond donating ability of the solvent.

(2.1)

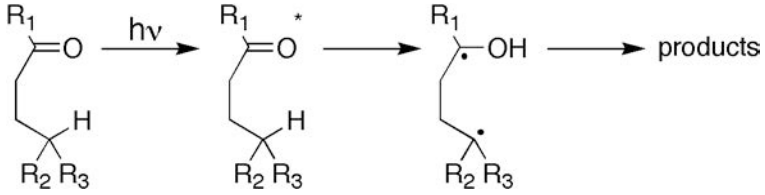

(2.2)

For the common triplet state reaction, Norrish type I photocleavage can involve n,π^* or π,π^* excited states. I-2959 belongs to a family of phenyl substituted α-hydroxy ketone molecules that were studied by Turro *et al.*[1] In that study, the nature of the para substitution was varied in order to determine the effect on the nature of the excited state and the photochemical reactivity for the phenyl substituted α-hydroxy ketones **1-5** shown here:

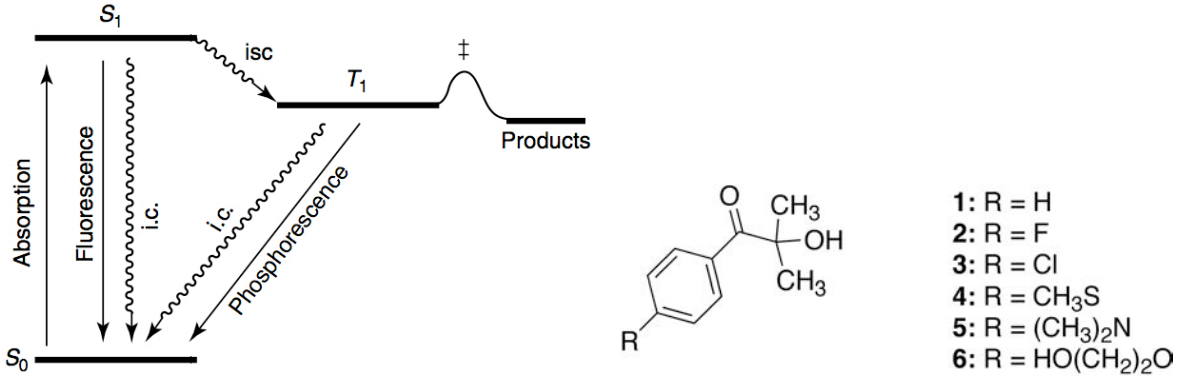

For the simplest molecule, 2-hydroxy-2-methyl-1-phenyl propanone (**1**), with H as the substitution, the triplet is an n,π^* state and the quantum yield of α-C-C bond cleavage is

0.38. For electron withdrawing groups, F and Cl (**2,3**), the triplet remains an n,π^* state, but the quantum yield of α-C-C bond cleavage increases to 0.67 and 0.60 respectively. However, when the substitution is electron donating, the triplet has more π,π^* character, and the quantum yield for **4** and **5** are 0.01 and 0.03 respectively. For molecule **6**, however, which is the I-2959 used for our nanoparticle work, the quantum yield of α-C-C cleavage is an intermediate value (0.29), which has been attributed to a mixing of the excited state characteristics.[1] Wagner *et al* have described a mechanism for Norrish type II reactions where the n,π^* and π,π^* excited states are thermally equilibrated, but reactivity comes from the n,π^* state. From the work by Turro *et al* where substitution of the para position of the phenyl ring can give either excited state, the n,π^* and π,π^* states for I-2959 must be close in energy, and so Norrish type I cleavage of I-2959 is believed to occur from a thermal equilibrated n,π^* state.[2]

It was briefly stated that triplets are required for having significant reactivity from the excited state, for the simple reason that the triplet lives long enough to react. When reducing a metal ion is required, the reducing ability of photochemically generated radicals is usually considered, to ensure that the radicals produced are capable of performing the reduction. However, the excited state dynamics, which play a crucial role in reaction yield are often overlooked. Metal ions, such as gold, copper and silver, are well known quenchers of excited states, with rate constants approximately diffusion controlled ($k_q > 10^9$ $M^{-1}s^{-1}$).[3, 4] Since the excited state is the one responsible for generating the reducing radicals, quenching of this excited state can play an important role in reducing the efficiency of nanoparticle formation. The overall efficiency of radical formation is determined then by several factors including; (1) the quantum yield of triplet formation, (2) the yield of intersystem crossing (ISC), (3) the rate of triplet quenching (k_q), and (4) the lifetime of the excited state. In regards to I-2959, we have already discussed the first point, but we examine now how the efficiency of the triplet for forming radicals is not only determined by the quenching by metal ions, but also the excited state lifetime of the triplet. Equation 2.3 shows the dependance of the efficiency of quenching on both the quenching rate constant, (k_q), and the triplet lifetime (τ_T), and when rearranged, equation 2.4 shows how these factors relate to the efficiency of triplet formation.[3, 5, 6]

$$\%\ \text{triplets quenched} = E_q = 100\frac{k_q\left[M^{n+}\right]}{k_q\left[M^{n+}\right] + \tau_T^{-1}} \tag{2.3}$$

$$\%\ \text{triplets surviving} = E_s = 100 - E_q = 100\frac{\tau_T^{-1}}{k_q\left[M^{n+}\right] + \tau_T^{-1}} \tag{2.4}$$

From equation 2.4, it can be deduced that a short excited state lifetime is best for most efficient unimolecular radical formation from the triplet. Therefore, one of the most important properties of I-2959, not yet discussed, is the short triplet lifetime (10 ns).[1] Triplets often live for hundreds of nanoseconds, which makes them easy to observe by laser flash photolysis. However, since the Norrish I reaction is an intramolecular reaction, the fragmentation occurs quickly. It is common in nanoparticle synthesis to use approximately 1 mM concentrations for metal ions, for which the product of the diffusion controlled rate constant for quenching (10^{10}) and the concentration of metal ions (10^{-3}), gives $k_q[M^{n+}] = 10^7$. Figure 2.1 shows curves representing 10, 50 and 90% quenching of the triplet excited state of different lifetimes, with respect to the quenching rate of the metals (x-axis). The dotted lines in Figure 2.1 represent I-2959 under typical (1 mM metal salt) conditions, which illustrates one of the most important properties of I-2959 that has enabled its use for efficient nanoparticle formation. With a triplet lifetime of I-2959 of only 10 ns, the maximum quenching of the excited state is 10 %, but there is at least 90 % efficiency of radical generation from the triplet state.

In contrast, benzophenone along with a suitable hydrogen donor, has also been used to make nanoparticles, in the cases of AgNP and AuNP, from Ag^+ and Au^{3+} salts respectively. Benzophenone has a high quantum yield of the triplet ($\phi_T \simeq 1.0$), which is needed to have reactivity, but the triplet has a very long lifetime, 300 ns.[7, 8] With reference to Figure 2.1, this lifetime corresponds to greater than 50 % quenching of the excited state by millimolar metal ions. For this reason, micelles are used to physically separate benzophenone from metal ions, as well as incorporating good hydrogen donors like cyclohexadiene into the micelles to ensure radical formation. Once the radicals are generated, they then leave the micelles and react with metal salts in the aqueous phase.[4, 3] Not only are these methods more synthetically involved, since micelles are required to separate reagents, there are many instances when micelles are simply not feasible (ie. lithographic films, concentrated MNP samples, biological systems etc.), limiting the applicability of these methods.

Following along the path to making nanoparticles from photochemical reactions, we have discussed the photophysical and photochemical properties of the initiators required to produce reducing radicals with reasonably high yields. One last consideration is worth noting. Some molecules can generate α-hydroxy radicals with good redox properties in high yield, and yet are unsuitable in most cases for preparing nanoparticles. For example, equation 2.5 shows the typical reaction pathways that occur upon photoexcitation of valerophenone. One can see that upon excitation, valerophenone quickly undergoes

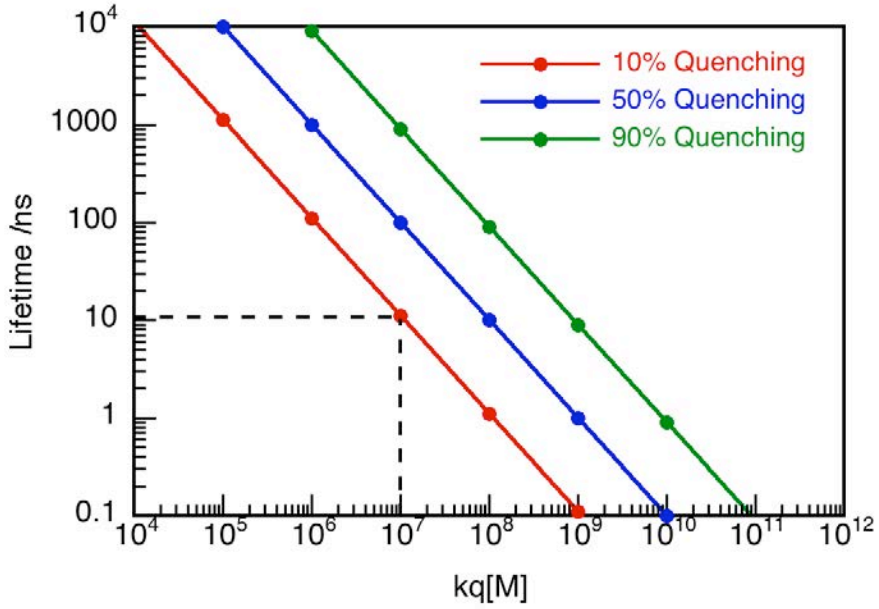

Figure 2.1: Plot illustrating curves for 10, 50 and 90 % quenching efficiency of excited states with variable lifetimes assuming diffusion controlled quenching, with the dotted lines indicating the excited state lifetime of I-2959 and typical conditions for the rate of quenching in nanoparticle synthesis reactions.

intramolecular hydrogen abstraction and forms a biradical, one end of which is an α-hydroxy radical with good reducing properties similar to monoradicals.[9, 10, 11] The lifetime of this biradical, however, is 30-100 ns, which is too short for sub-millimolar metal ions to efficiently compete and become reduced.

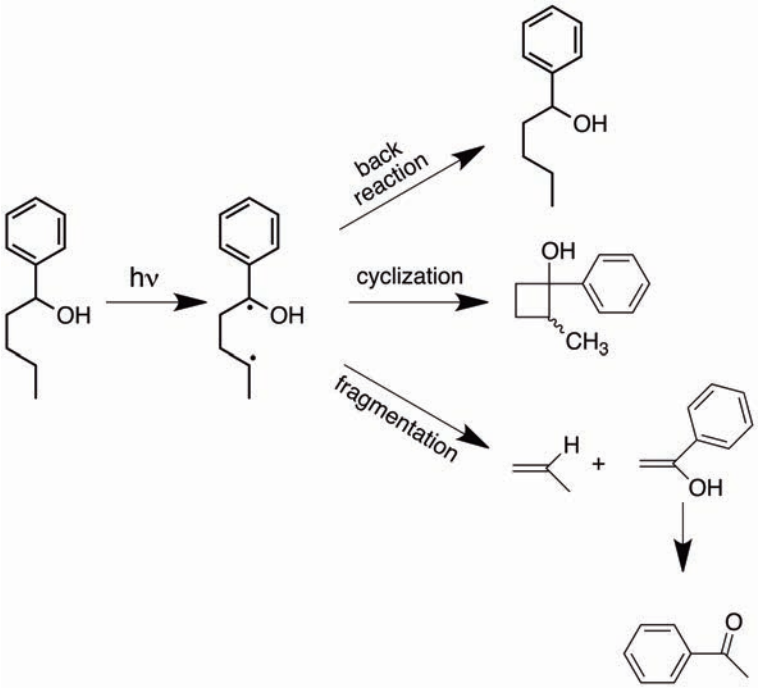

(2.5)

The α-hydroxy radical from I-2959, when generated from the triplet, has a much longer lifetime in solution to react with metal ions. The only side reactions are radical-radical reactions, and since the radicals are born from the triplet, there is no solvent cage effect for recombination to the starting material. The radicals are usually generated with micromolar or lower steady state concentrations, and react at a diffusion controlled rate, therefore making reaction with approximately millimolar metal ions more likely.

2.2 I-2959 in AgNP Synthesis

Now that we have familiarized ourselves with why I-2959 is a good molecule to use when reducing metal ions to form nanoparticles, and why it is the molecule of choice most often in the Scaiano group, we can move on to the multitude of AgNP colloids described herein.

2.2.1 AgNP "seeds" - Experimental

Equations 1.10, 1.11 and 1.12, describe the overall scheme for formation of reduced metal ions, and subsequently AgNP from Ag^+ salts, only omitting the capping agents required for nanoparticle stability. Unless otherwise stated, a typical solution for the synthesis of aqueous AgNP contained, 1 mM trisodium citrate, 0.2 mM I-2959 and 0.2 mM silver nitrate ($AgNO_3$). Solutions were purged for 20-30 min with N_2 or Ar to remove dissolved oxygen, which competes for reactivity with radicals. The purged solutions were then irradiated in a Luzchem photoreactor equipped with UVA bulbs. Samples made in this way undergo a colour change from clear to yellow, due to the plasmon absorption as shown in Figure 2.2. While it is expected that reducing the number of UVA bulbs can result in larger particles, since the rate of nucleation would be decreased with less light intensity, small AgNP were most often required, and so the maximum number of bulbs was always used. The particle size, as measured by TEM (see Figure 2.2, left) for these particles is typically 3.3 $\pm$0.4 nm.[12] Colloids prepared in this way will henceforth be called AgNP seeds.

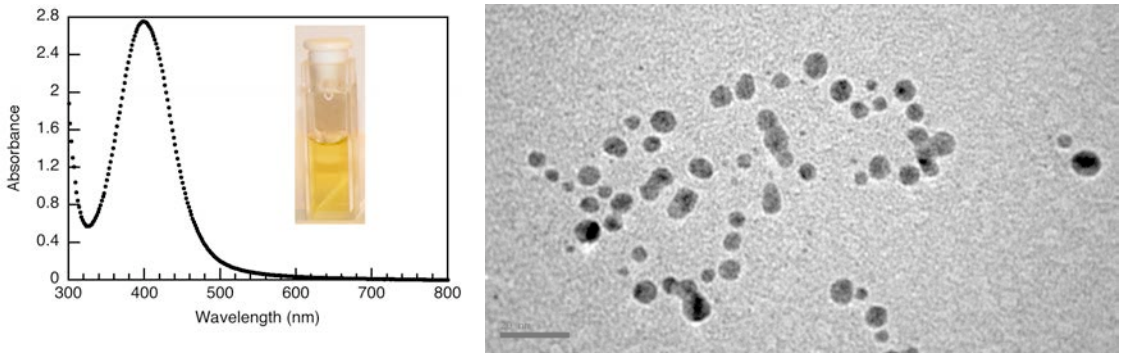

Figure 2.2: Plot of a typical absorption spectrum of AgNP seeds and an image of a cuvette containing the colloidal solution (left), as well as a typical TEM image with a scale bar of 20 nm, of the particles as synthesized(right).

Solutions of AgNP seeds, as shown in Figure 2.2, stored in the dark are stable indefinitely. AgNP seeds are stable in solution without addition of acids or bases, as well as without introducing salt or phosphate buffers. Addition of particles to buffers or salt results in rapid aggregation and oxidation. With the intent of incorporating AgNP into cells and with biological systems, AgNP seeds have been made by the same method, but capped with human serum albumin (HSA), and collagen instead of citrate. Collagen

stabilized particles are stable enough with both buffer and NaCl to be introduced into cell culture media, and incorporated into biological samples.[13]

2.3 Shaping Particles and the Plasmon with Light

It was mentioned above that AgNP seeds are stable if stored in the dark. This is because AgNP can undergo size and shape change when the plasmon is excited with visible light. In fact many groups have reported on thermal methods, as well as light induced morphological control of AgNP colloids.[14, 15, 16, 17, 18, 19, 20, 21, 22, 23, 24, 25, 26, 27, 28, 29, 30, 31, 12]

For thermal methods of making nanoparticles, the presence of twinning defects in crystals as well as the choice of capping agents are two crucial factors to consider. Twinning defects occur when a single particle has at least two portions that are lattice mismatched with respect to each other. That is to say that these particles have crystalline regions but a plane between them since the crystalline portions do not align. Figure 2.3 depicts these types of particles, as well as a particle without twinning defects that can be formed from the migration of twinning defects upon annealing. It has been suggested that twinning defects are necessary in the formation of silver decahedra that are multi-twinned and silver nanoplates that have only one defect plane parallel to the plane of the largest exposed facets.[29, 32]

The other major factor to consider in growing different shapes by thermal methods is the capping agent. AgNP crystalize in the face-centred cubic (fcc) crystal structure, and so, while spherical and spheroid nanoparticles expose both {111} and {100} facets, it is thermodynamically more stable for particles to form that expose the lowest energy {111} facets.[22, 34] However, the different possible facets in a crystal have different surface energies, and different molecules bind preferentially to different facets. Therefore, by selecting the appropriate capping agent that preferentially binds to certain facets, one can slow down the addition of silver on these facets and in doing so control the final particle size and shape. This is the main idea in the well known polyol synthesis for making nanoparticles of specific shapes. The polyol synthesis is possibly the most common synthesis technique for making various shapes of AgNP and AuNP. In this method, usually ethylene glycol serves as both the solvent and reducing agent, and poly (vinyl pyrrolidone (PVP) serves as a capping agent. The ratio between metal salt and PVP concentrations are crucial to the final morphology of the particles. The final shape of the particles is determined by the ratio of the growth rates on the {100} and {111} facets,

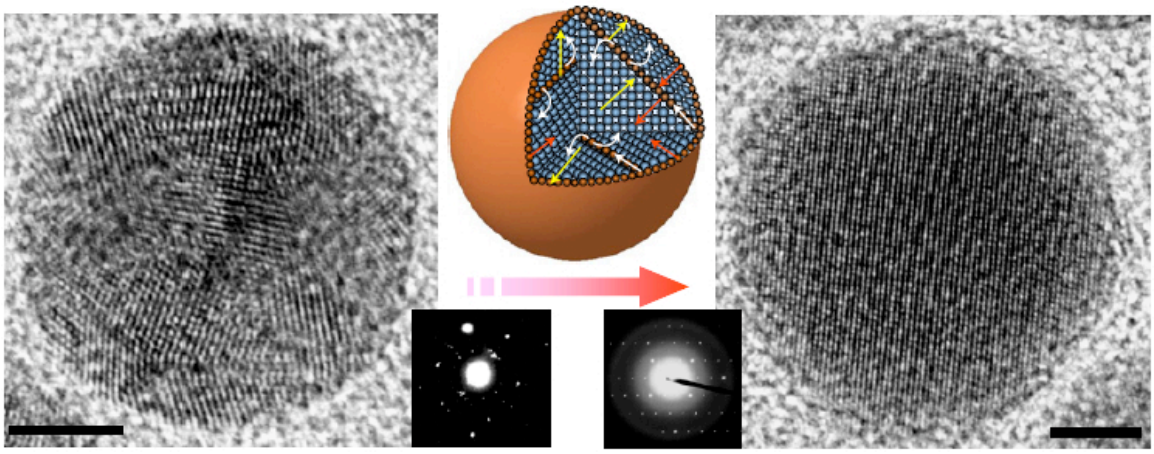

Figure 2.3: High resolution TEM image of particles with twinning defects (left), and a particle after the process of thermally migrating these phase boundaries to make a single crystalline particle (right), scale bars are 5 nm. Adapted from ref [33]

where a ratio of 1.73 provides octahedra and tetrahedra shaped particles that expose {111} facets, whereas a ratio of 0.58 provides cubic particles with less stable {100} facets exposed. It is believed that PVP either retards the growth rate on the {100} facets or increases the growth rate on the {111} facets, in which case the ratio of the growth rates is appropriate for forming cubes.[35, 36]

Different particle morphologies expose surface atoms that can behave chemically different depending on which facet they are in, or if they are at vertices in a crystal. That is why various shapes of nanoparticles are often desirable in catalysis, for much the same reason that capping agents can affect the morphology during growth, which is due to preferential binding to particular facets. For example, the oxidation of styrene has been shown to occur preferentially on different shapes of nanoparticles.[22, 34] Nanoplates, truncated nanocubes and other shapes have also been made by modified polyol processes. [34, 37]

Photochemical synthesis of AgNP with various shapes has also been realized by a number of different groups.[38, 39, 40, 31] In many of these reports, the realization of particular shapes has been attributed to twinning defects directing the growth of the particles, and in others the choice of capping agents has been attributed with the resultant shapes. From the large variety of shapes that were attainable from reaction solutions, and from the fact that precursor solutions with significant variations could be

used to make the same morphologies of particles, the question of what the true growth mechanism is in most photochemical routes was brought into question.

2.3.1 AgNP shapes - Experimental

Starting solutions for shape control were the same solutions described above as AgNP seeds, made from 1 mM trisodium citrate, 0.2 mM I-2959 and 0.2 mM silver nitrate ($AgNO_3$). A single solution of these AgNP seeds was used for a series of experiments, subdivided into 3 mL samples for each shape. An image of the experimental setup is shown in Figure 2.4, which depicts the power supply used to control the current and voltage applied to the LED, and a "quad" of four LED that have been attached to aluminum blocks and heat sinks to cool the sample. Fans for cooling are always used as well to ensure that the LED do not overheat. A cuvette containing 3 mL of AgNP seeds is then placed in the centre of the quad to provide maximum light intensity to the solution and achieve a sufficiently fast conversion. The key features of the LED are that they provide intense light, that is relatively monochromatic, and at a much lower cost than continuous wave lasers.

Figure 2.4: Experimental setup for controlling the shape of AgNP formed from AgNP seeds, setup on the left and zoomed in LED/heat sinks on the right.

To obtain different shapes, the same AgNP seed solution was used, but the wavelength of LED irradiation was changed by changing LED in the apparatus shown. Figure 2.6 summarizes the excitation wavelength, spectral changes observed, and times of irradiations for the various shapes that can be made by this method as well as including SEM

(or TEM images where possible) of the respective particles. The reaction was followed by UV-Vis absorption spectroscopy and an endpoint was assigned as a time when the decrease in 400 nm absorption for AgNP seeds and the increase in major absorption of the corresponding shape plateaued. The AgNP seeds as well as the different shapes were imaged by SEM and TEM microscopy.

To prove that citrate can act as a reducing agent, a solution of AgNP seeds and 2.7 mL of H_2O was placed in two cells of an oxygen uptake apparatus. The apparatus for pressure measurements (described as an "oxygen uptake apparatus" even if many other gases can be measured) was described elsewhere previously.[41] Various amounts of a solution containing 5 mM $AgNO_3$ and sodium citrate (as indicated in Figure 2.8) were injected to both cells prior to irradiation. One cell (the reference) was covered with aluminum foil, while the other sample was irradiated with 400 nm light from an LED. The change in pressure with respect to the reference sample is recorded with the oxygen uptake apparatus and can be correlated (after calibration) with a volume and/or molarity of gas produced. The pressure increase is monitored in time until a plateau is reached, as shown in Figure 2.8. Upon addition of various quantities of trisodium citrate and $AgNO_3$, the increase in pressure upon irradiation is shown in Figure 2.8.

2.3.2 AgNP shapes - Results and Discussion

We believed that the most important factor in photochemically making different shapes of AgNP was in fact the wavelength of light used to generate the particles. To test this hypothesis, a single AgNP seeds solution was separated into 3 mL portions and irradiated with different wavelengths of light. Since the absorption bands for different shapes vary, due to the particular plasmon modes supported by different shapes of particles, the change in optical density of the solutions was monitored by UV-Vis spectroscopy as a measure of conversion of the seeds to various shapes.[42]

We postulated, that the photochemical growth mechanism for various shapes of metal nanoparticles is a "pulling" mechanism, where shapes that form have maximal optical density near the wavelength of excitation. In this way, exposing AgNP seeds to 405 nm light should excite the dipolar mode of spherical particles the most, and promote the growth to larger spheres. This is in fact the case. Figure 2.5 shows the change in optical density, and the change in size of the particles (inset) measured at various times of irradiation, as well as a representative image of the particles after 26 hours of 405 nm LED irradiation. The reaction solution was aliquoted at various times and the particle sizes

were averages taken from scanning electron microscopy (SEM) images of the aliquoted particles. In Figure 2.5 below, there are a couple of things to note; (1) the small red-shift in the absorbance spectrum, as well as (2) the large polydispersity in the particles obtained as the particle size increases. The red-shift in absorbance is due to the fact that larger nanoparticles can support more than just the dipolar absorbance associated with spheres, and the increasing contributions of higher order modes, that absorb longer wavelengths, serves to red-shift the particle absorbance. The increasing polydispersity of the particles comes from the fact that this growth process relies on plasmon excitation, and so larger particles, that absorb stronger, tend to grow faster, causing a snow ball effect and an unavoidable polydispersity. While this is not the method to choose if one desires low polydispersity, some applications require the opposite, where a range of sizes may help different aspects of an application. For example, in photocatalysis larger particles have stronger field effects, and smaller particles have better catalytic properties, so a combination of particle sizes may be most effective to maximize light absorption and surface reactivity. It is also fully consistent with the proposed mechanism (see below).

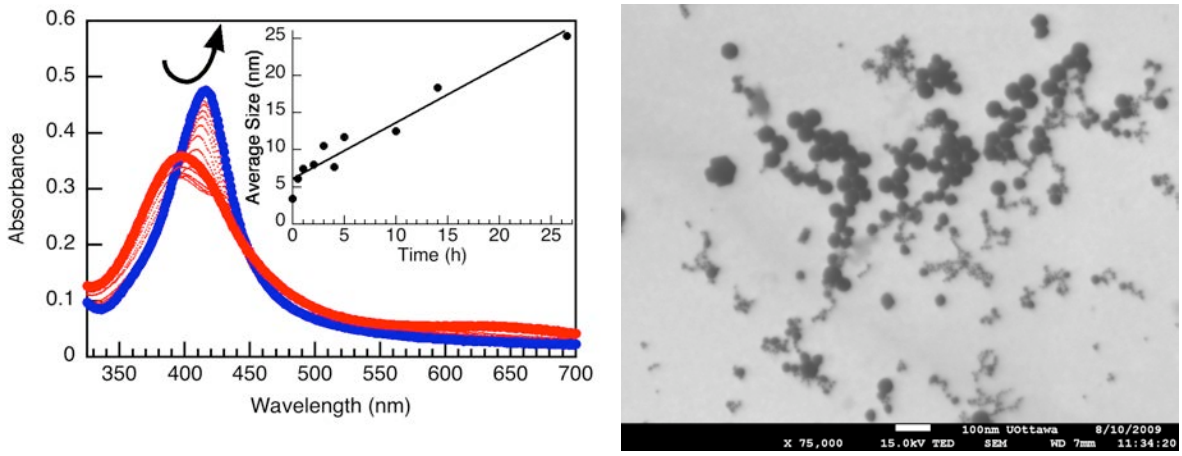

Figure 2.5: Change in UV-Vis absorbance (left) and size of AgNP seeds (left inset) upon 405 nm LED excitation, as well as a SEM image of the particles obtained after 26 h or irradiation (right), scale bar is 100 nm.

By simply changing to different LED in the quad, the shape of the particles can then be changed. Decahedra are the most thermodynamically stable particles formed, as they have only {111} facets exposed, followed by plates that have predominantly {111} facets, but also the edges that are {100}. Hexagonal plates are the same as truncated triangular

plates with respect to facets that they have large {111} facets and all edges are {100}. Rods, however, like cubes have the least stable {100} facets exposed.

This process cannot be only driven by the capping agents, since citrate is the only capping agent used, and it can not be only twinning defects, since the same precursor solution is used to make all of the various shapes. The time profile for the spectral change from AgNP seeds to decahedra is shown in Figure 2.7. From the time profile one can see that there is an induction period, followed by rapid conversion and slowing down when the conversion is complete.

This pattern is observed for the other shapes as well. Maillard *et al.* have shown that citrate is necessary for the formation of Ag nanodisks.[43] Citrate is used to reduce Ag^+ in solution anisotropically onto AgNP. The same process is occurring here, where an equilibrated Ag^+ concentration in solution is photochemically reduced onto AgNP, but due to the longer wavelength of light used, it is higher order plasmon modes that are excited, and the formation of anisotropic seeds eventually occurs. It is this slow formation of anisotropic seeds that are the reason for the induction period.

To further prove that citrate can reduce AgNP under visible irradiation, the oxidation of citrate was monitored using an oxygen uptake apparatus.[24] The idea is to excite the surface plasmon band of AgNP seeds and cause reduction of the nanoparticle seeds instead of metal salt. The metal seeds then grow by the addition of positively charged metal salt to the reduced seeds as shown in equation 2.6 and elaboration of 3.1. As mentioned, Maillard *et al.* [43] had claimed that the excitation of metal nanoparticles with citrate results in citrate reduction of the particles, but this speculation was not previously confirmed.

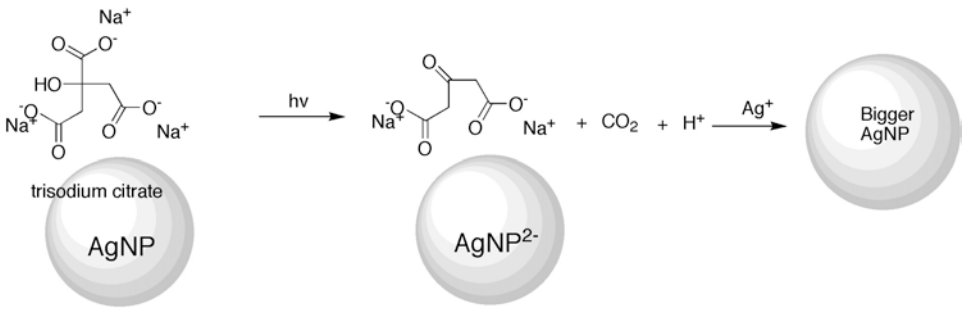

(2.6)

Important to note from scheme 2.6 is that one of the products of the reaction is CO_2, which can be measured as an increase in gas pressure in a sealed system. The initial rapid pressure increase is due to a temperature increase when the LED turns on presumably

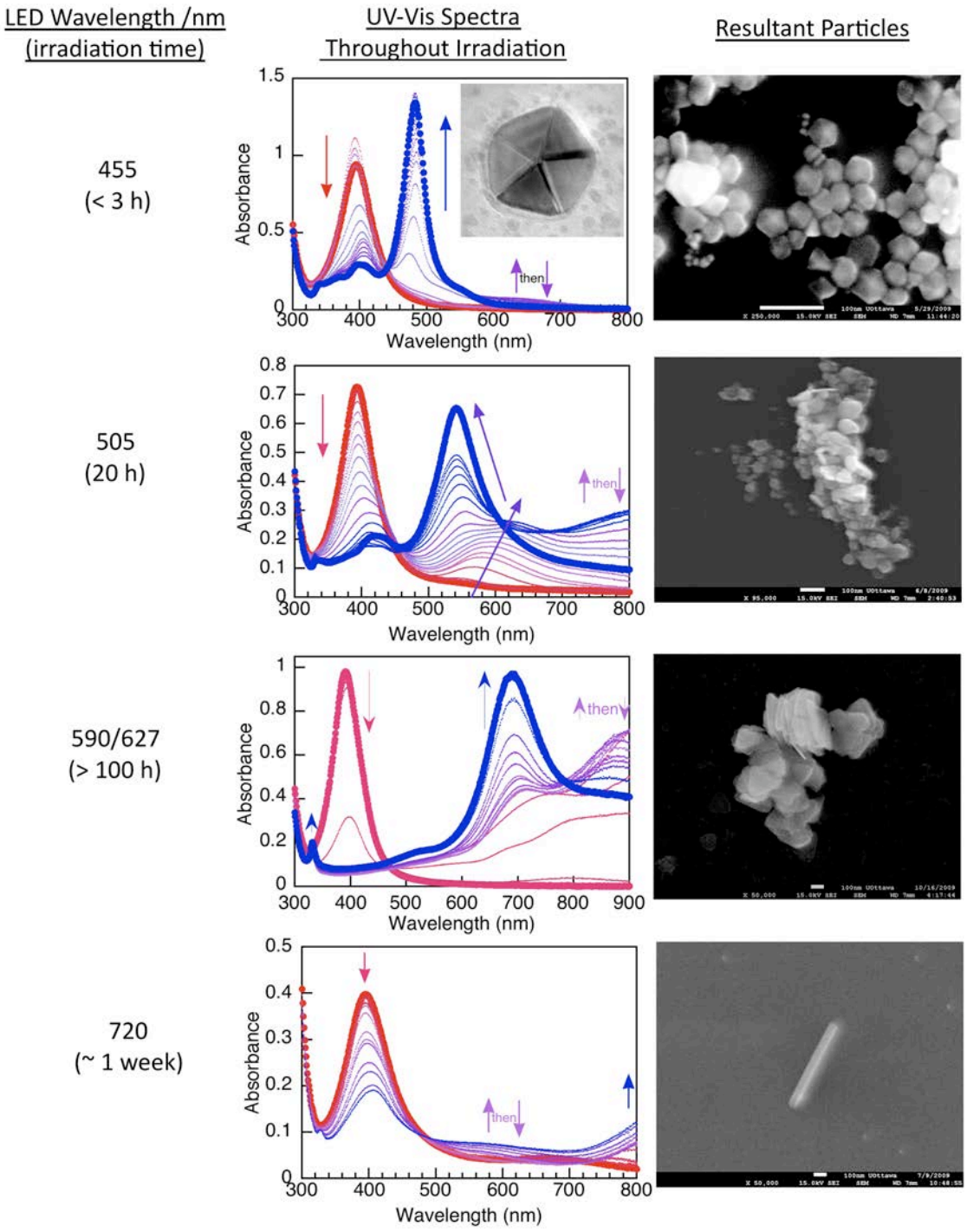

Figure 2.6: LED wavelength used, duration of exposure, corresponding spectral shift, and microscopy images of corresponding resultant nanoparticles as obtained through LED irradiation of AgNP seeds, scale bars are all 100 nm.

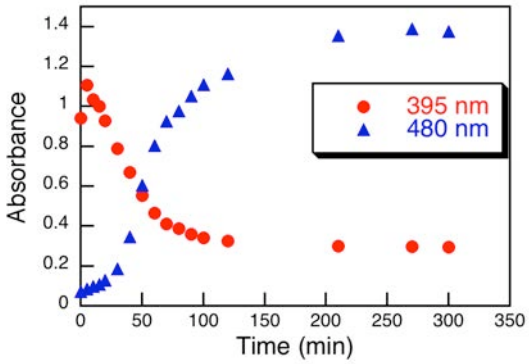

Figure 2.7: Change in absorbance of AgNP seeds solution at 395 nm (spheres) and 455 nm (formation of decahedra) during 455 nm LED irradiation.

due to heating of the AgNPs, while the following linear increase in pressure is due to gas produced. From equation 2.6, the CO_2 produced can be correlated with the oxidation of citrate. It is important to note that there is no increase in pressure when the LED is off, and also that the 400 nm LED is chosen to selectively excite the AgNP SPB and not the reducing agent (citrate) that absorbs only in the UV region. We note that quantitative analysis shows that the amount of gas produced correlates with either citrate or $AgNO_3$ added, whichever is the limiting reagent. Therefore, both reagents are needed for citrate to reduce the AgNPs and Ag^+ to add in the growth mechanism in Scheme 2.6.

The plasmon absorption after successive additions of $AgNO_3$ and citrate was also recorded using a CARY 100 UVvis spectrophotometer. One can see from Figure 2.8 that the plasmon absorption increases systematically after each irradiation. This increase in absorption and red-shift of the SPB is consistent with the addition of Ag and the formation of larger AgNP.[12, 44, 45] This process can be repeated by re-diluting the particle solutions and reusing them as seeds for new citrate/$AgNO_3$ growth solutions. With reference to the shape control experiments, the oxygen uptake results are taken as a proof of part of the mechanism where citrate can act as a reducing agent and cause reversible growth with visible light excitation.

Another common feature that one can see from the UV-Vis spectra in Figure 2.6 is that there is a transient absorbance at longer wavelengths during the synthesis of decahedra, hexagonal plates and triangular plates. This transient absorbance has been attributed to the formation of aggregates of AgNP that collectively absorb at longer

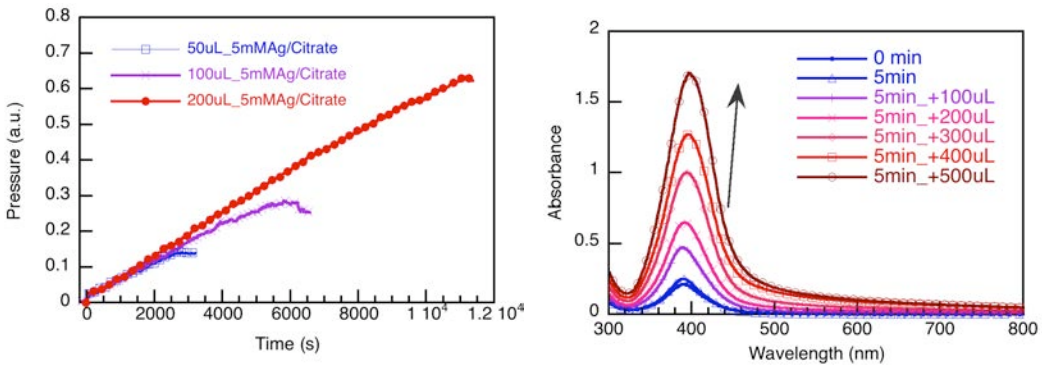

Figure 2.8: (left) Pressure change over irradiation time of samples of AgNP after adding 50, 100, and 200 μL of 5mM $AgNO_3$/citrate to an initial 5 mL sample of seeds; (right) UVvis absorption spectra of solutions of AgNP seeds after 100 μL additions of 5 mM $AgNO_3$/citrate and 400 nm LED exposure.

wavelengths due to coupling of particle plasmons. Light has been used to optically trap molecules and to bring particles together in solution to give remarkably strong Raman signals of trapped molecules.[46] We believe that the same effect occurs here, causing light-induced aggregation of the anisotropic AgNP. The aggregated particles experience extreme heating from the plasmon excitation, so that they coalesce into the observed final particle shapes. The addition of small particles to large particles that have coalesced becomes increasingly fast since it is plasmon excitation that induces the aggregation and causes the heating. This is why there is an increased rate of transformation after the formation of anisotropic seeds, and the process does not slow down until there is a limiting concentration of seeds available to add to the larger particle shapes. The overall process is depicted in Figure 2.9, as well as an image of each of the particle colloids and the wavelength of light used to form them.

While twinning defects cannot be ruled out as an effect, since the AgNP seeds may contain particles with various twinning defects, capping agents such as citrate are necessary but they are certainly not the only, or most important factors in making various shapes of silver nanoparticles. Since the growth mechanism provided here depends so much on the particular plasmon modes excited, it is believed that the wavelength of light chosen to grow larger AgNP shapes is the most important factor.

The light emitting diodes used here to make the various shapes are extremely inexpensive, costing only approximately $5 each. Overall, an affordable and facile method

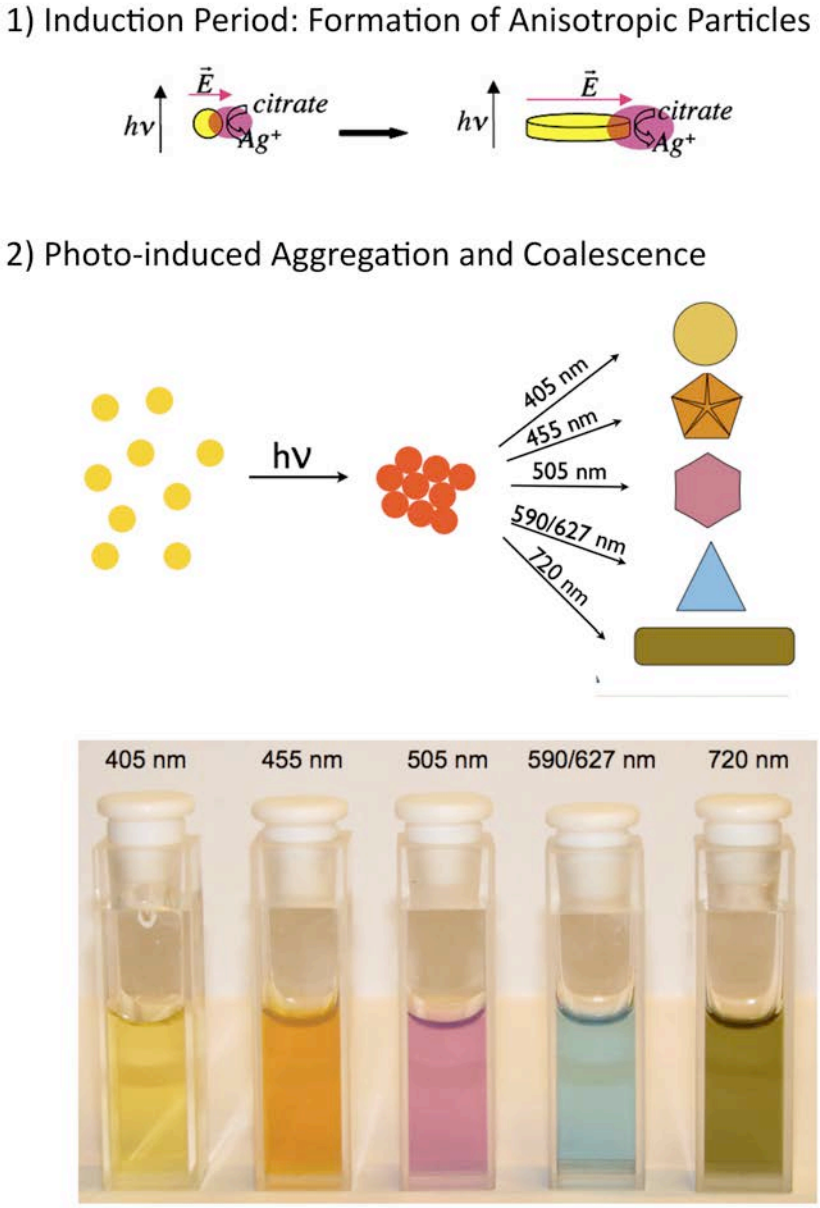

Figure 2.9: Mechanism of the formation of different shapes of AgNP with LED irradiation, 1) is adapted from ref [43].

for achieving various shapes is provided. The particles made by this method have the added advantage that they all contain only citrate as a surface capping agent so that, if

they are to be used in applications such as catalysis, any variations in reactivity can be truly attributed to either differences in absorption (photocatalysis) or differences in the nature of exposed surface atoms, without any variation in organic surface functionality.

2.4 Kinetics of the formation of Ag_2 Clusters: Insight into the Early Stages of AgNP Formation

The quantum yield of emission from plasmon excitation of metal nanoparticles is essentially zero. However, under particular reactions conditions (in toluene and THF) we have found it possible to generate solutions of AgNP with absorption at 450 nm that have anomalously high emission upon excitation at that wavelength.[47, 48] The emission has been attributed to the formation of Ag_2 clusters in solution.

To understand the formation and stability of Ag_2 in colloidal solutions leading to AgNP, the kinetics of the formation of Ag_2 were monitored using laser flash photolysis (LFP). To generate nanoparticles in these organic solutions, the precursors need to be re-evaluated based on solubility. For aqueous AgNP, we always begin with the idea that we need a metal salt, usually $AgNO_3$, and a capping agent that keeps the nanoparticles stable, usually trisodium citrate. However, in toluene and thf, both $AgNO_3$ and citrate are insoluble. Therefore, for these experiments solutions containing 5 mM each of I-2959, CF_3COOAg as the metal precursor and cyclohexylamine (CHA) as the stabilizing agent were used.

Equation 2.7 shows the reactions involved in the synthesis of Ag_2 clusters.

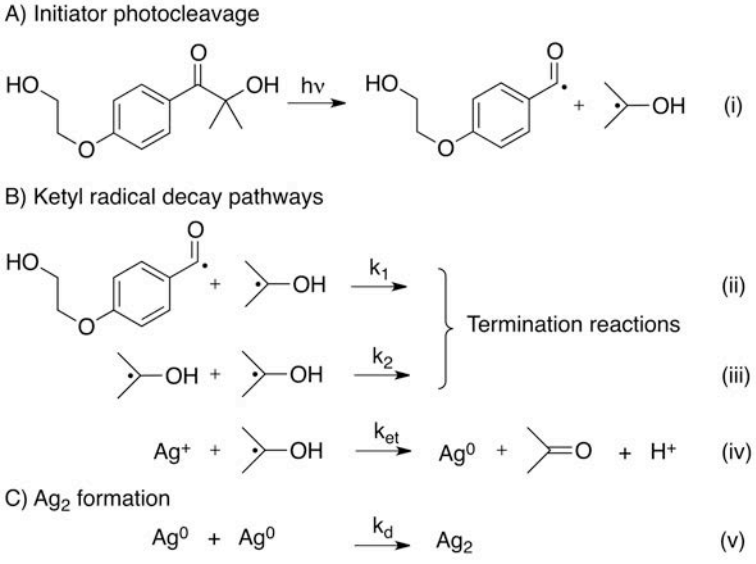

(2.7)

2.4.1 Experimental

Unless otherwise stated typically toluene solutions for LFP experiments contained 10 mM CF_3COOAg as Ag precursor, 5 mM Irgacure-2959 (I-2959) as a photochemical reducing agent and 5 mM cyclohexylamine as a NP stabilizing agent.

The LFP solutions were irradiated with a 355 nm, ∼6 ns pulse width Nd-Yag laser to initiate the photocleavage of I-2959. The change in absorbance after each laser pulse is monitored with a customized Luzchem LFP system, and the transient data are recorded and averaged using Luzchem LFP software. The reactions that occur upon excitation of these solutions are shown in Equation 2.7. It is important to note that the LFP solutions were normally flowed rapidly through a quartz cuvette to avoid bleaching of Ag_2 (evident when solutions are not flowed or flowed slowly, see Figure 2.15) by subsequent laser pulses irradiating already reduced silver.

A scheme describing the experimental setup for LFP is shown in Figure 2.10 where the laser used for excitation is a Surelite Nd:Yag and the third harmonic is used to obtain the 355 nm wavelength. In a typical LFP experiment, the AgFNP solutions (described in the main text) are purged with N_2 in a reservoir designed to deliver solutions through a quartz cuvettes with an inlet and outlet for flowing solutions. A Masterflex pump positioned in line after the cuvette is used to control the flow rate and draw the LFP solution through the cuvette.

For LFP there is a monitoring light source (in this case a Xe lamp) for which changes in the absorbance of the solution are measured as changes in the transmitted light through the sample directly after a perpendicular laser pulse excites the sample. In all LFP experiments, the laser is allowed to irradiate the sample usually with a 1 pulse/sec rate and the change in absorbance is measured after each laser pulse and typically an average of 10 pulses is taken to ensure an accurate signal with improved signal to noise.

To examine the stability of Ag dimers, two laser experiments were performed as well where the first laser pulse is used to generate Ag_2 and the second is delayed and generates more Ag_2. The laser pulses are delayed such that the second pulse arrives within the window of time of data recording after the first pulse, so that the effect of both are recorded in a single trace.

In order to rule out the possibility that the signal at 450 nm in AgFNP solutions is from a plasmon absorption, silver nanoparticles were formed in a typical LFP setup using a 266 nm laser. Non-fluorescent silver nanoparticles (AgNP) were also prepared using LFP, and the formation of particles that support a surface plasmon absorption was

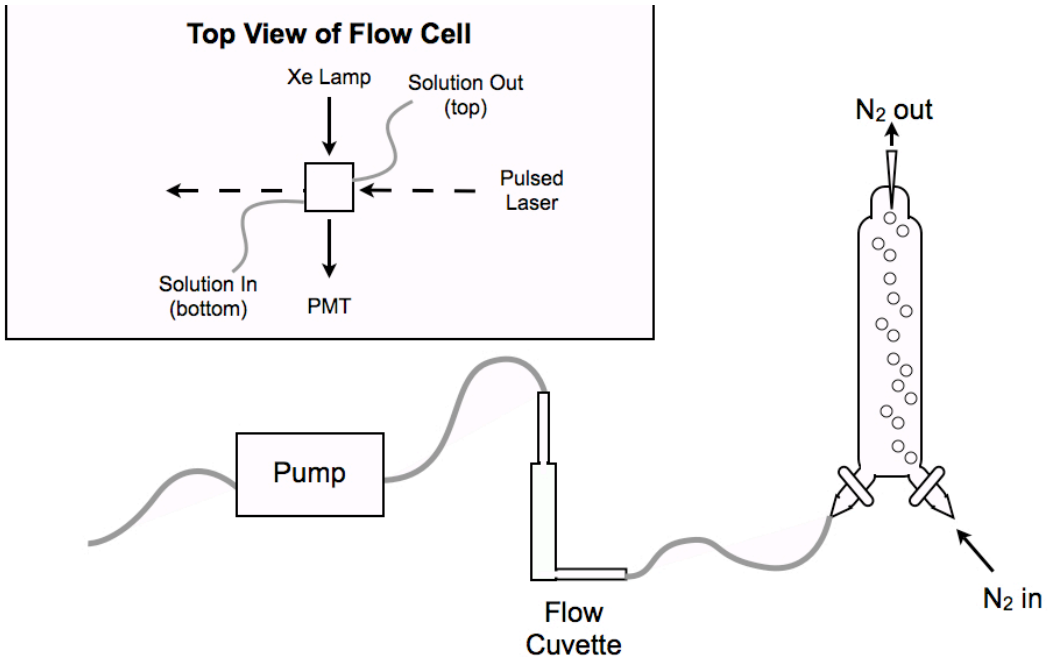

Figure 2.10: Experimental setup for the flow system used in LFP experiments, and a schematic of the optical arrangement used in LFP (inset).

followed spectroscopically in order to rule out the possibility that the signal at 450 nm was a plasmon absorption of AgNP. For non-fluorescent AgNP it has become common practice in our group to use varying concentrations of $AgNO_3$, I-2959 and trisodium citrate ([trisodium citrate] $\geqslant$ $AgNO_3$) as was the case here.[12] These aqueous solutions were purged with nitrogen and photolyzed in 7x7 mm^2 cuvettes with the same LFP setup described above, but with a 266 nm laser in order to generate high concentrations of ketyl radicals that subsequently reduce Ag^+ to Ag^0.

2.4.2 Results and Discussion

In order to prove that the emissive species here was in fact small metal clusters, laser flash photolysis (LFP) experiments were performed to follow the transient species involved, and the increase in absorbance at 450 nm at short time scales after a laser pulse. This proved to be a difficult task, partly since the reactions were performed in toluene, which has a cut-off in transmission at 300 nm. This is a problem since none of the species in Equation 2.7 in i, ii, iii or iv give an observable transient signal, and so we are left only

with the formation of the 450 nm absorbance signal to study the mechanism, which we have assigned to Ag_2.

Transient spectra for the change in absorbance of LFP solutions after a 355 nm laser pulse are shown in Figure 2.11 (a). Also shown in Figure 2.11 (a), is an absorption spectrum for the AgFNP solution taken after it was completely photolyzed with UVA irradiation in a Luzchem photoreactor, and it shows a similar absorption maximum at 450 nm to that obtained in the LFP experiments at short time scales. Larger Ag clusters show longer wavelength absorption maxima as the cluster size increases.[49] Therefore, the fact that the 450 nm absorption maximum never shifts suggests that the immediately formed Ag_2 clusters are not only stable, but are also the major absorbing chromophore in solution. The change in absorbance at 450 nm in an LFP experiment is plotted in Figure 2.11 (b); kinetic analysis gives a good fit to a second order rate law (correlation factor = 0.995) with a value of $2k_d/\epsilon_{Ag2} = 1.9 \times 10^6$ cm s^{-1}. The second order behavior for the formation of the optical signal at 450 nm is consistent with two reduced silver atoms associating as shown in Scheme 2.7. However, in order to obtain an absolute rate constant it is necessary to determine the extinction coefficient for Ag_2. Also interesting to note is that, if one turns off the monitoring beam in LFP, and records the emission intensity after exciting the species that forms and absorbs at 450 nm, it can be seen that the intensity of the fluorescent emission from the Ag_2 clusters also increases at the same rate and overlaps with the increase in absorption at 450 nm.

To better understand the kinetics of Ag_2 formation the intensity of the excitation laser was varied, which is equivalent to changing the initial ketyl radical concentration (Reaction (i) in Equation 2.7). The maximum absorbance at long times after a laser pulse, and thus the final concentration of Ag_2, followed a square root law with the laser dose as shown in 2.12. The square root dependence was initially intriguing as one could expect the total formation of Ag_2 to depend linearly on the laser power (i.e., the initial ketyl radical concentration). However, the square root dependence is a common result for photochemically generated radicals with competing terminating and product formation reactions where the terminating reactions are fast (reactions (ii) and (iii) in Equation 2.7 are known to be diffusion controlled).[50]

The above result suggests that the rate constant for the electron transfer from the ketyl radical to Ag^+ (reaction (iv) in scheme 2.7) is slower than diffusion controlled reactions (reactions (ii) and (iii) in Scheme 2.7), but does not give an estimate of the actual value of the rate constant. The ketyl radical generated from photolysis of α-phenylbenzoin (Scheme 2.8) is a weaker reducing agent than the isopropyl radical used

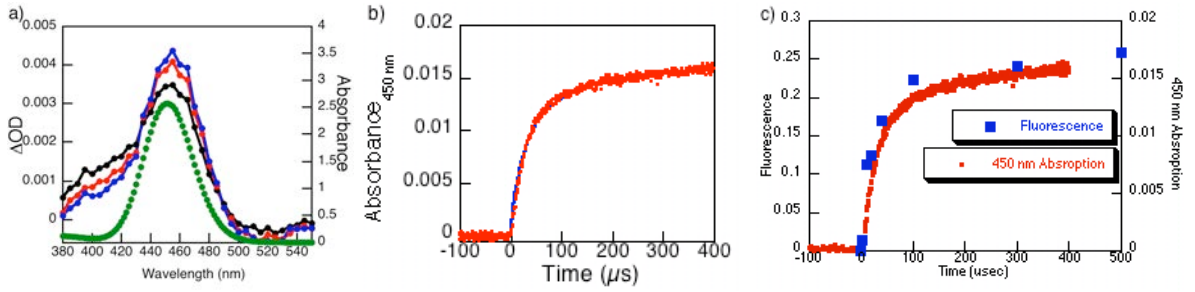

Figure 2.11: a)LFP experimental data: transient spectra (left axis) recorded 200 μs (black), 500 μs (red) and 750 μs (blue) after the 355 nm laser pulse, overlaid with the spectrum (right axis) from a stable AgFNP solution in toluene long after irradiation (green). Also shown in b) is the change in absorbance at 450 nm of an LFP solution after a 355 nm laser pulse (red) fit to a second order rate law (blue), and c) the same growth in 450 nm absorbance (red) overlaid with the increase in fluorescence (blue) when this species is excited.

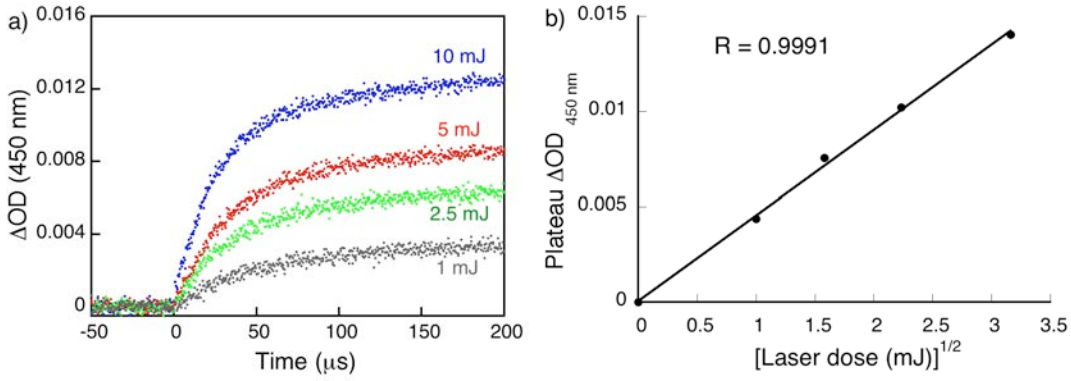

Figure 2.12: Growth in 450 nm absorbance with different 355 nm laser doses (left) and plot of the plateau ΔOD (determined from the kinetic fit) versus the square root of the laser dose, for a typical LFP solution in toluene (right).

here. This is known from the fact that radiolysis of isopropanol solutions of benzophenone give benzopinacol as the only product, as shown in Scheme 2.8.[51] However, the advantage here is that the ketyl radical generated from photolysis of α-phenylbenzoin is easily observable in LFP with an absorption maximum at 545 nm. Scheme 2.8(i) depicts how α-phenylbenzoin is used to generate a reducing radical and shows the proposed subsequently quenching by CF_3COOAg. A nitrogen purged, 5 mM solution of α-phenylbenzoin in toluene was excited by a 355 nm laser and the transient spectrum in Figure 2.13 and the change in ΔOD at 545 nm due to the benzophenone ketyl radical transient decay, as shown in Figure 2.13, were recorded. The transient absorption spectrum has an absorption maximum at ~540 nm that corresponds well with that of the benzophenone ketyl radical.[52, 53] Also shown in Figure 2.13 is the transient decay in the presence of 0-500 mM CF_3COOAg, which shows no significant quenching of the ketyl radicals. This implies that the transfer of an electron from an α-hydroxyl radical to Ag^+ in toluene is much slower than diffusion control.

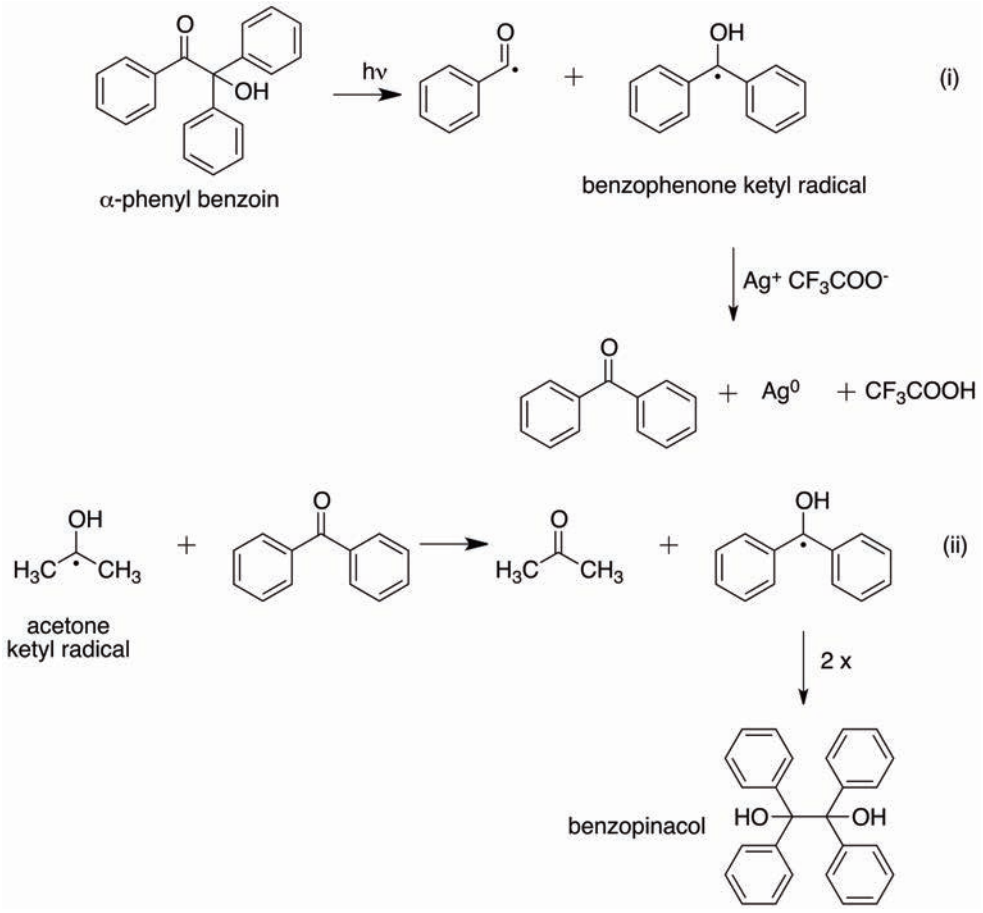

(2.8)

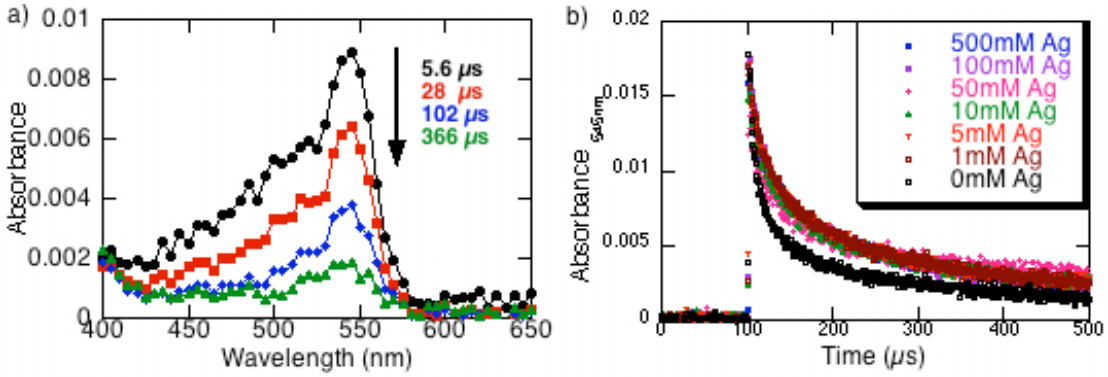

Figure 2.13: (a) Transient absorption spectrum for the benzophenone α-hydroxyl radical at 5.6 μs (black), 28 μs (red), 102 μs (blue) and 366 μs (green) after the laser pulse, and (b) corresponding decay traces of the 545 nm absorption upon quenching with various concentrations of CF_3COOAg.

Until this point what has been shown is; reaction (i) in scheme 2.7 is considered instantaneous (during the laser pulse) and reactions (ii) and (iii) are known to be diffusion controlled while reaction (iv) is comparatively very slow ($k_{et} \ll k_{ii}+k_{iii}$). Also, we observe clean second order kinetics for the formation of Ag_2, but without an extinction coefficient for Ag_2 the rate constant for Ag^0 dimerization (k_d) cannot be determined. In order to obtain ϵ_{Ag2}, bromothymol blue (BTB-H) was used as an indicator to measure the amount of the base form of CHA remaining in AgFNP solutions. Scheme 2.9 shows how CHA acts as a proton sink when Ag^+ is reduced by the ketyl radical. Also shown in Scheme 2.9 (reaction iii) is how BTB-H can be used as an indicator of the amount of CHA in the base form, and thus be used to quantify the amount of reduced Ag in solution.

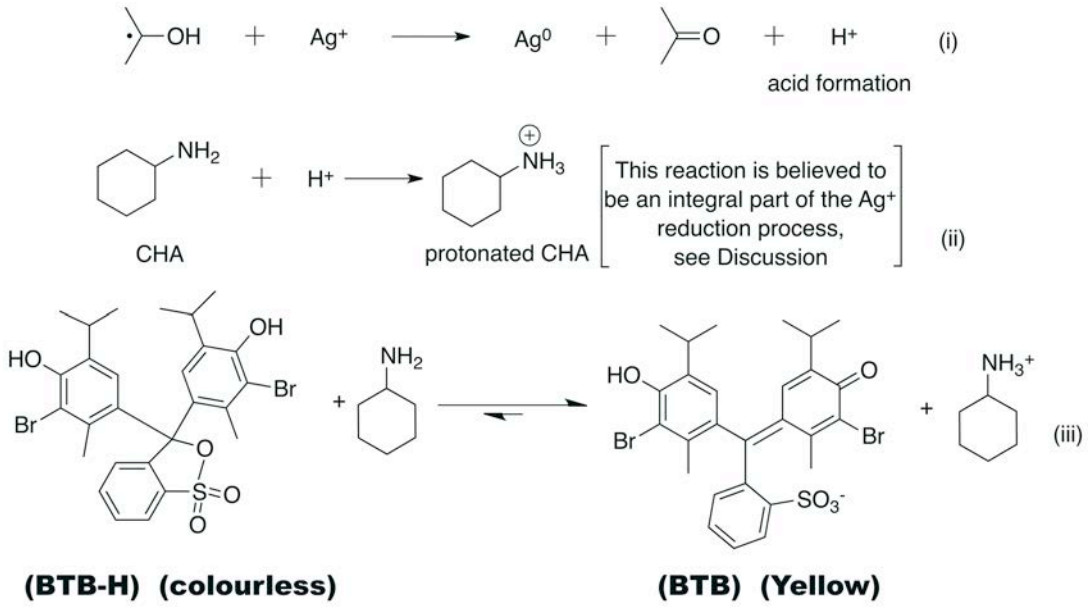

(2.9)

Using BTB-H as an indicator of CHA, the change in absorption spectrum recorded after the addition of aliquots an AgFNP solution (that was never photolyzed and so had no reduced CF_3COOAg)) is shown in Figure 2.14. The change in absorption indicates the amount of CHA in the basic form in solution (since CHA has a pKa of 10.6 and bromothymol blue has a pKa of 7.0)[54, 55] by deprotonating the BTB-H (to BTB) indicator and causing the observed color change. More specifically, in this experiment, a typical LFP precursor solution (described above) is photolyzed with UVA irradiation in a Luzchem photoreactor and the absorption spectrum of the resultant AgFNP recorded using a Cary 100 UV-Vis spectrometer. The photolyzed LFP solution is then added in small aliquots to a solution of BTB-H and the absorption spectrum of the BTB-H solutions is recorded. The basic form of BTB has a strong absorption at 400 nm that was also monitored using a Cary 100 UV-Vis spectrometer. The increase in absorbance at 400 nm in a BTB-H/BTB solution is monitored in two separate experiments where; (1) a non-photolyzed LFP solution and (2) a photolyzed AgFNP solution were added. A comparison of the change in absorbance at 400 nm for BTB-H/BTB for the two parallel experiments was compared and used as a measure of the difference in CHA concentration and therefore a measure of the H^+, or in other words as a measure of Ag^0 that was reduced and eventually forms the Ag_2 clusters as described by reaction (iv) in Scheme 2.7. It is important to note that small aliquots of the toluene solutions were added to much larger volumes of aqueous indicator solutions in which case the CHA/CHA-H^+

were soluble and detected in the aqueous phase containing the indicator. However after reaction (iii) in Scheme 2.9, CHA is protonated and is no longer available to deprotonate BTB-H. Overall, by comparing an LFP solution that has been photolyzed with one that has not, the change in CHA can be correlated with a concentration of H^+ produced as in Scheme 2.9. The key assumption is that H^+ and Ag^0 are produced in equimolar quantities, and so the measure of H^+ is also a measure of Ag^0 produced. Repeating this experiment several times and plotting the absorbance at 450 nm of the AgFNP solutions (Figure 2.14(b)) versus the determined concentration of Ag_2 (from Figure 2.14(a)), the extinction coefficient for Ag_2 is then taken as the slope of the linear best fit as shown in Figure 2.14(b) (inset), which is $\epsilon Ag_2 = 25{,}400 \pm 2600\ M^{-1}cm^{-1}$.

With the extinction coefficient, it was determined that the rate constant for the formation of Ag_2 is then $k_d \sim 2.4 \pm 0.24\ x10^{10}\ M^{-1}s^{-1}$. Using the Debye equation, diffusion controlled reactions in toluene have a rate constant of $1.1\ x10^{10}\ M^{-1}s^{-1}$ and so the rate constant determined here can be approximated as a diffusion controlled association of Ag^0 into dimers.[8]

In further exploratory experiments to assess the stability/reactivity of the Ag_2 clusters at short time scales two types of experiments were performed including (1) no-flow experiments and (2) two-laser experiments. In the no-flow experiments, a typical LFP experiment was performed with the only modification being that the solution was static rather than flowing through the cuvette, thus forcing the accumulation of Ag_2; the sample was exposed to ten laser shots and the data averaged. The data recorded are shown in Figure 2.15, leading to observable bleaching of the sample, followed by recovery; the bleaching signals are largely acquired in the later shots, as Ag_2 accumulates. Bleaching refers to the reduction in sample absorbance upon laser excitation and is common in LFP. In this case, the transient ΔOD at 450 nm was monitored (Figure 2.15) revealing a bleaching of the 450 nm signal followed by a recovery and growth of the signal that again followed a second order growth with the same rate as the flow solutions.

In the two laser experiments, two separate 355 nm laser pulses separated in time by 200 μs were used to photolyze a flowing LFP solution, with the resultant change in ΔOD at 450 nm shown in Figure 2.16; note that no significant flow takes place in 200 μs, so that for practical purposes the solution is static in this time scale. In this experiment the Ag_2 generated from the first laser pulse will be present during the second laser pulse that generates additional ketyl radicals and thus Ag^0. We observed that the growth in ΔOD after each laser pulse (fresh solution or after one laser pulse) occurs at the same rate, with both growth curves fitting a second order rate law. The differences observed

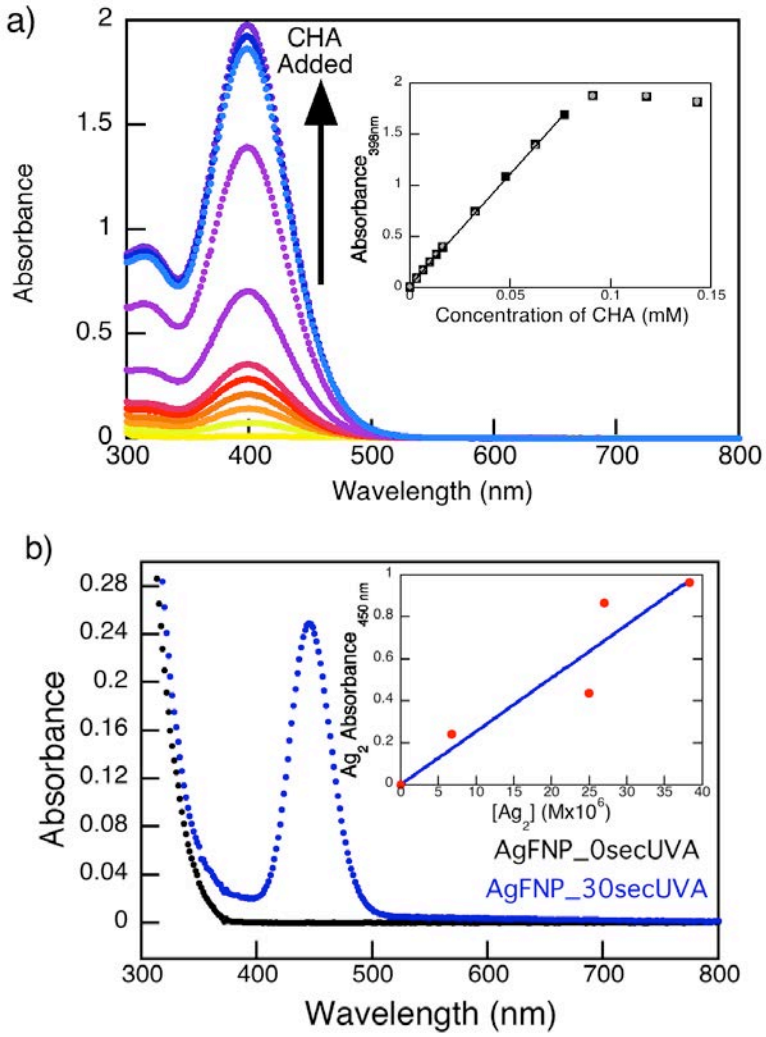

Figure 2.14: (a) Absorbance spectra of BTB-H/BTB upon addition of AgFNP solution starting with no AgFNP added (yellow) and ending when the BTB-H/BTB is completely deprotonated by CHA (blue), as well as (inset) a plot of the change in absorbance at 400 nm due to BTB plotted versus the concentration of CHA added from an AgFNP solution that was never irradiated (grey) and one that was irradiated for 30 s with UVA (black). (b) The absorbance of the AgFNP solution before (black) and after irradiation (blue) with UVA. Inset: absorbance for AgFNP solutions plotted against calculated Ag_2 concentrations.

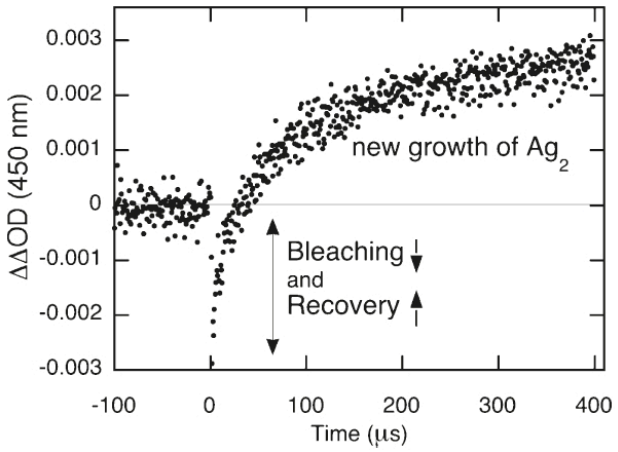

Figure 2.15: Transient absorption at 450 nm for an AgFNP solution without flow showing the bleach and recovery of the 450 nm signal and formation of more Ag_2. The solution used contained 5 mM I-2959 and CHA, and 10 mM CF_3COOAg in toluene. The laser was pulsed at 1 Hz and the signal is obtained as an average of ten consecutive pulses without flowing fresh solution between pulses; bleaching signals may be slightly enhanced by emission from accumulated photoproducts.

in total ΔOD are a result of a lower intensity second laser pulse, which generates less ketyl radicals, and thus less Ag_2. The normalized absorbance spectrum at the times indicated by the 1 (172 μs), 2 (222 μs) and 3 (374 μs) in Figure 2.16(a) are plotted in Figure 2.16(b), showing that there is also no difference in absorbance spectra between laser pulses as well.

In order to rule out the possibility that the signal at 450 nm in AgFNP solutions is from a plasmon absorption, silver nanoparticles were formed in a typical LFP setup but using a 266 nm laser. 266 nm was used because there was not enough absorption at 355 nm to cause enough radical production, and therefore an observable signal for the plasmon of particles, unless 266 nm excitation was used. This is initially taken as an indication that the signal seen in toluene could not be due to plasmon absorption of particles. In this case the growth of the plasmon absorption, and therefore the nanoparticles, is followed by an increase in absorption at 420 nm. It should be noted that flow solutions containing $AgNO_3$ and I-2959 showed no change in absorbance on the time scales monitored by LFP (up to 5 ms after the laser pulse). This result indicates that AgNP cannot form large enough particles to support a plasmon absorption within the

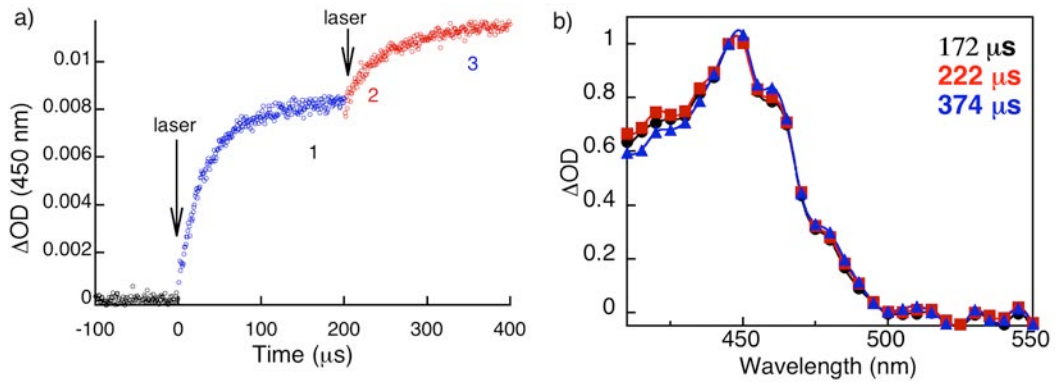

Figure 2.16: (a) Transient absorption for a flowing AgFNP solution in toluene irradiated with two 355 nm laser pulses separated in time by 200 μs, and (b) transient absorption spectrum of the same two laser LFP experiment and for times labeled in (a). A slight bleaching occurs with the second laser (beginning of red trace).

time scale of these experiments. However, when the solution was not flowed the black trace shown in Figure 2.17(c) was obtained. This is likely the case because nanoparticles form over microseconds after the first pulse, but the nucleation steps for the formation of an AgNP, large enough to support a plasmon absorption, are too long to be monitored on these time scales. However, when the solution is not flowed what is monitored is actually the addition of Ag^0 to AgNP seeds already formed in earlier laser pulses. A typical transient absorption spectrum for both fluorescent and non-fluorescent AgNP solutions is shown in Figure 2.17(a), as well as a steady state UV-Vis absorption spectrum of each is given in Figure 2.17(b) for comparison. It is clear in Figures 2.17(a) and (b) that the absorption spectrum for the silver plasmon not only appears at shorter wavelengths, but it has to be monitored at much longer times than the AgFNP signal due to the slower growth. The red shift in the absorption maximum when AgNP are formed is indicative of the formation of larger AgNP as Ag^0 adds, which is again not observed for the signal attributed to Ag_2 in the AgFNP solutions.[12] It is also interesting to note that the spectrum in Figure 2.17(b) for both AgFNP and non-fluorescent AgNP, after UV irradiation, show in both cases that the transient signal corresponds well with the long-term spectra of each. Lastly, shown in Figure 2.17(c) is a comparison between the transient signals for an AgFNP solution (monitored at 450 nm) with that of a non-fluorescent AgNP solution (monitored at 420 nm). It is clear from the comparison of the two traces that the appearance of the plasmon occurs on a drastically different time scale and with a much

lower final intensity than the formation of the 450 nm signal for Ag_2. In fact, in the case of AgFNP in toluene or THF our earlier work shows that in long time scales small nanoparticles are formed (∼3.4 nm) surrounded by highly fluorescent clusters.[47]

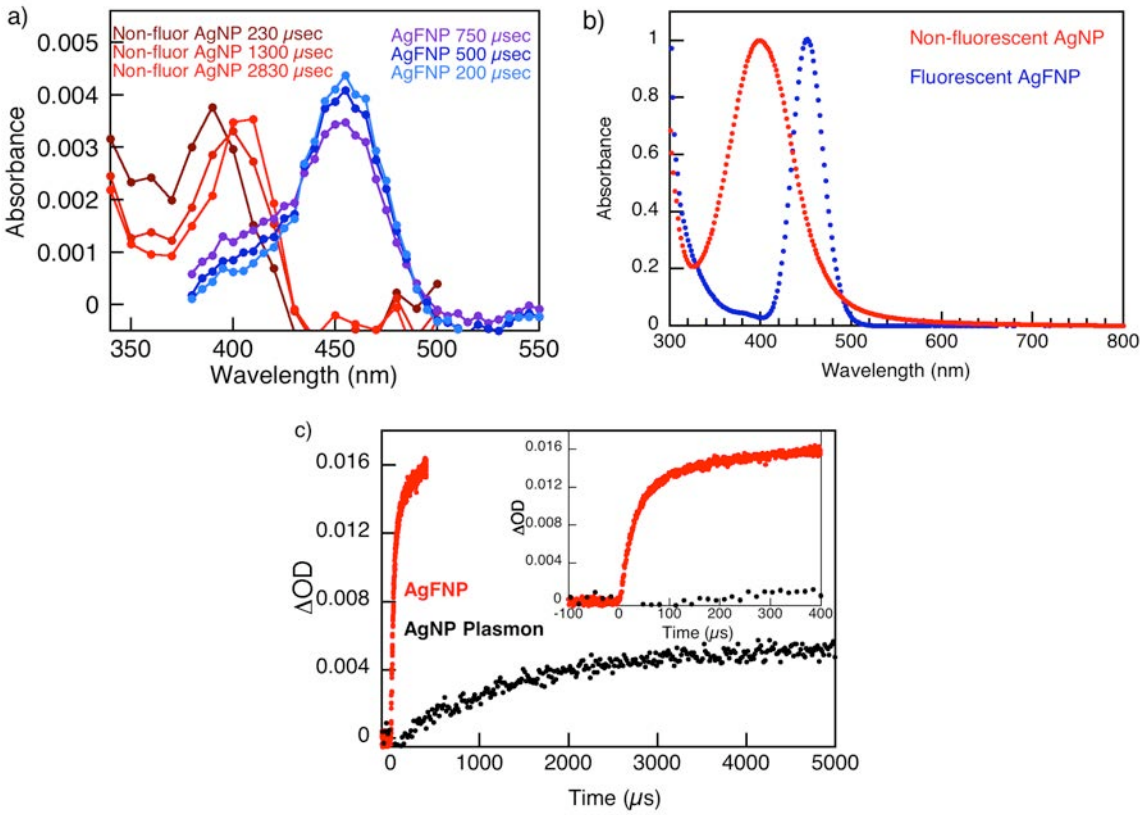

Figure 2.17: (a) Comparison of the transient absorption spectra recorded by LFP in the formation of non-fluorescent AgNP in water compared with that of AgFNP in toluene, (b) a comparison of the absorption spectra after long irradiation times of an AgFNP solution in toluene with 3.3 nm non-fluorescent citrate stabilized AgNP in water (normalized respect each maximum), and (c) a comparison of the transient absorption obtained in photolysis forming AgNP in water monitored at 410 nm contrasted with that of the AgFNP solutions in toluene monitored at 450 nm.

Small silver clusters provide a valuable link between atomic metals and nanoparticles. Thus, studying the mechanism of formation of these clusters can be a convenient way of determining the initial stages of nanoparticle formation in such systems as the one here (organic solvent with amine stabilizing agent). The first step in determining the

mechanism of the formation of Ag_2 is, therefore, to determine the kinetic parameters given in Scheme 2.7. The termination reactions (ii and iii) of Scheme 2.7 are known to be limited by diffusion and spin statistics.[56] However, none of the compounds in reaction (iv) are expected to give an absorption that can be easily monitored in toluene by LFP. Further, the extinction coefficient for Ag_2 was previously unknown, yet Ag_2 is the only species readily detectable in Scheme 2.7. While we were able to measure $2k_d/\epsilon_{Ag_2}$, the determination of an absolute rate constant required a procedure to evaluate ϵ_{Ag_2}. Figure 2.11 (b) shows that the increase in absorption at 450 nm attributed to Ag_2 formation fits extremely well to a second order rate law. Small silver clusters have been previously reported to have lower energy absorption maxima than the plasmon of AgNP, and similar values for the extinction coefficient as determined here. Specifically, Vosch et al. have observed larger Ag clusters with an extinction coefficient of 32,000 $M^{-1}cm^{-1}$, that absorb in the visible region at energies lower than spherical AgNP plasmon absorptions.[49, 57] Using the extinction coefficient for Ag_2, estimated from titration of a solution of BTB-H, gives a rate constant for the formation of Ag-Ag dimers of 2.4 x$10^{10} M^{-1}s^{-1}$, which is on the order of diffusion controlled reactions in toluene. These experiments to determine the extinction coefficient involve four approximations:

1. That at low conversion and at 450 nm, the absorbance at 450 nm is directly proportional to the concentration of Ag_2 formed and the amount of Ag^+ reduced.

2. That the absorbance of Ag_2 follows Beers law.

3. That no protons are lost to chemistry other than the protonation of CHA.

4. That any plasmonic enhancements to the extinction coefficient for Ag_2 can be neglected under our experimental conditions.

5. That protons formed are a direct measure of Ag^+ reduced.

Errors introduced by (1) and (4) would cause the value of ϵ_{Ag_2} to be too high, while errors in (3) would cause it to be too low. The extinction coefficient obtained here would be a lower limit if H^+ is lost to other reactions (unlikely), but any increase in extinction coefficient would give a rate constant for the formation of Ag_2 that is higher than diffusion controlled (and thus not possible), which supports assumption 3. Assumption (2) is impossible to test, given that we do not have a standard solution of Ag_2. We believe that the errors are small and not enough to change the key conclusion that the reaction Ag^0 + Ag^0 to give Ag_2 is diffusion controlled. The long times for the formation of Ag_2

in the LFP traces are due to the low initial concentration of Ag_0 (1 μM) generated in the reduction of Ag^+ after the laser pulse.

Equations 2.10 and 2.11 depict the two possible mechanisms by which Ag_2 clusters can form from reduced Ag^0. Equation 2.11 would require that ketyl radicals persist in solution long enough for Ag^+ to react with Ag^0 hypothetically leading to Ag_2^+, and still be present at significantly high concentrations to react with Ag_2^+ to form Ag_2. This is very unlikely since the termination reactions are diffusion controlled and since the formation of Ag_2 fits to a second order growth equation with a correlation of R = 0.9945, which is not necessarily expected for Equation 2.11. Therefore, reaction 2.10 better represents the mechanism.

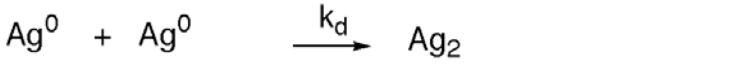

(2.10)

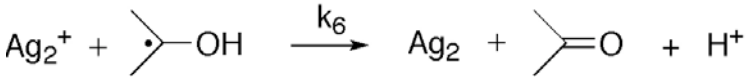

(2.11)

In an attempt to determine k_{et} in reaction (iv) (Scheme 2.7) α-phenylbenzoin in toluene was used to determine the rate at which CF_3COOAg quenches ketyl radicals. It was found that the quenching of the ketyl radical by Ag^+ was barely competitive with other radical decay processes. In radical polymerization processes where the termination reactions are much faster than the polymerization, the rate of polymerization is known to follow a square root dependence on the light intensity.[50] This is reflected here as well as in that reactions (ii and iii) approach diffusion control, and the competing reaction is not the formation of Ag_2 (v) which is fast, but rather the quenching of ketyl radicals by Ag^+ (iv) which is relatively slow in toluene. Therefore, the square root dependence on the laser power shown in Figure 2.12 can be explained if $k_{et} \ll k_1 + k_2$.

The low quenching rate of α-phenylbenzoin with CF_3COOAg, and the square root of the laser power dependence on the plateau of the ΔOD implies that reaction (iv) (Scheme 2.7) is slower than reactions (ii) and (iii) in toluene, and much slower than the quenching of ketyl radicals in aqueous solutions. Ketyl radicals are expected to react with Ag^+ in aqueous systems at a diffusion-controlled rate, just as Au^{3+} does.[3, 58] The results here, on the other hand, suggest that ketyl radicals react with Ag^+ more slowly in non-polar solvents. This may be related to the production of H^+ in reaction (iv) that is easily stabilized in water, but not in non-polar solvents like toluene. One of the roles of the amine in this work is to serve as a proton sink, by acting as a base as shown in Scheme 2.9. This does not require reaction (iv) in Scheme 2.7 to be reversible, but rather the presence of a kinetic barrier to H^+ release in non-polar solvents.

Amines are also known to be NP stabilizing agents, as well as affecting the reduction potential of Ag^+/Ag^0, however, their role can be quite complex.[59, 60] Equimolar amine is necessary for the long term stability of fluorescent AgNP solutions,[47] but it is not essential to form an unstable Ag_2 signal at 450 nm in the LFP experiments (see Figure 2.18).[48]. While the overall yield of Ag_2 in an LFP experiment is strongly dependant on the concentration of CHA used, the rate of formation of Ag_2 is unaffected by the amine, as expected, since the observed kinetics are dominated by the major process (reactions (ii) and (iii)). Thus, it would appear that proton capture by a base plays a key role as an enabling factor for reaction (iv) to occur efficiently and irreversibly.

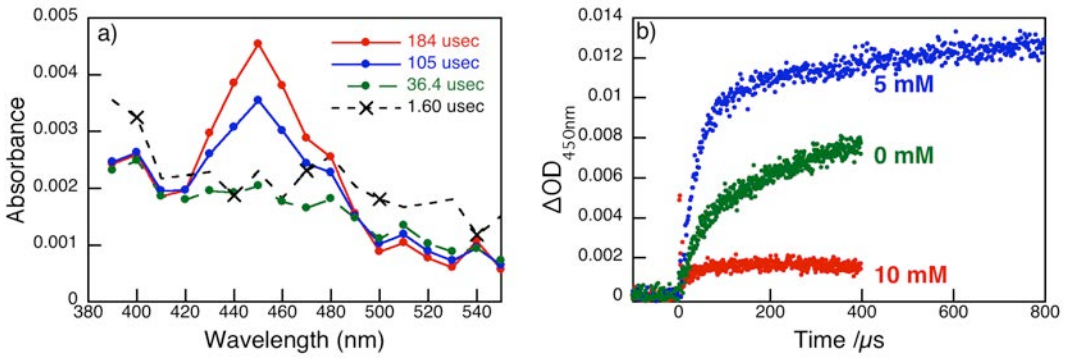

Figure 2.18: Transient Absorption Spectrum of a Typical LFP Solution with 0 mM CHA (no amine) (a) and the Effect of the Concentration of CHA on the Transient Absorption at 450 nm Attributed to the Formation of Ag_2.

In the 1970s and 80s several studies by Henglein examined the mechanism of formation of small Ag clusters by LFP of aqueous solutions of Ag^+.[61, 62] These studies account for the short-term stability of small silver clusters by charge stabilization of Ag_n^+ clusters with n $\geqslant$ 2. These small clusters had absorption maxima around 260 nm (dependant upon the size and charge of the clusters) that could be followed by transient spectroscopic techniques. The transient absorption of these charged clusters also decays on the time scale of milliseconds and the decay corresponds well with the increase in absorption near 400 nm due to the formation of large clusters that support a surface plasmon.[62] On the other hand, the absorption of Ag_2 clusters that we observe has an absorption maximum at 450 nm, approximately 200 nm red shifted from the charged clusters observed by Henglein; their spectrum does not resemble that of positively charged silver clusters. Since most of our work is carried out in toluene, we expect that charged clusters would not

be stabilized by the solvent, but the absorption at 450 nm also shows a long term stability not seen by the charged clusters even in aqueous environments. Clearly the absorption at 450 nm cannot be due to charged metal clusters, but the increase in absorption shows no induction and plateaus in approximately 100 μs, which is 200 times faster than that observed for AgNP formation by Henglein as well. Figure 2.17 also exemplifies the differences in the absorbance observed by LFP for solutions that generate AgNP, showing that the intensity, rates and absorption maxima for Ag_2 are all significantly different from that of AgNP by LFP; the latter is due to plasmon transitions. In flowing a solution to make non-fluorescent AgNP, the growth is presumably so slow (greater than milliseconds, reported by Henglein) that a change in absorbance at wavelengths from 400 to 500 nm could not be detected, but rather when the solution is not flowed the change in ΔOD can be attributed to growth of existing AgNP. This growth happens by addition of Ag^0 to AgNP that were formed on previous laser pulses. Even in this case, the rate of growth is significantly slower than the formation of Ag_2.

Overall, the major conclusion to be taken from analysis of Figures 2.16 and 2.17 is that the absorption at 450 nm observed in AgFNP solutions cannot be attributed to the plasmon absorption for AgNP, which occurs at a different wavelength maximum and on a much slower time scale. This is consistent with the fact that the 450 nm signal could not be due to AgNP since the emission upon 450 nm excitation is quite intense with a 2.6 ns lifetime, while the plasmon is extremely weak and has a femtosecond lifetime.

For the overall scheme, the second order growth as $2Ag^0$ dimerize to form Ag_2, the intense emission of the silver clusters and position of the absorption maximum support the conclusion that the absorption at 450 nm is in fact due to Ag_2 clusters, and that their rate of formation is diffusion controlled. The difference in reactivity in non-polar solvents also suggest that the eventual formation of nanoparticles does not go through charged Ag_n^+ species, as was the result found by Henglein in aqueous systems, but rather via neutral Ag_n cluster intermediates.[61, 62]

The particular selectivity for forming Ag_2, that is seen in the bleach and recovery experiment (Figure 2.15) and the two laser experiments (Figure 2.16), have some interesting possible implications. Due to the particular stability of Ag_2 it is difficult to imagine a route to the formation of AgNP (generated in AgFNP solutions as well) that involves Ag_3, because that would imply the addition of Ag^0 to and Ag_2 cluster, but Ag_0 seems to have a preference for dimerization. In fact, this implies that the early stages in the formation of AgNP in non-polar solvents may in fact go through even number atomic clusters as these Ag-Ag dimers aggregate. In a flow system (as used here) where

no AgNP seeds are present, this must be the first step in the conception of the nascent AgNP. To the best of our knowledge this is the first reported value for the rate constant for the Ag^0-Ag^0 bond formation. This result is based on our estimation of ϵAg_2 ~25,400 $M^{-1}cm^{-1}$ for Ag_2. A mechanism for the formation of Ag_2 is also proposed, including a low rate constant for ketyl radical quenching by Ag^+ in toluene, something that most likely applies to other non-polar media.

2.5 The Role of PCeT in Metal Nanoparticle Synthesis

The role of CHA in the formation of fluorescent Ag_2 clusters was highlighted in the previous section, but the role as a proton acceptor in that reaction has lead us to a better understanding of the chemistry involved in nanoparticle formation by the photochemical routes used in the Scaiano group. We know that the α-hydroxy radical produced by photolysis of I-2959 reduces a metal and releases a proton, and in water this reaction goes easily at a diffusion controlled rate. The fact that water is acting as a proton acceptor was for a long time overlooked. However, this is not trivial for non-protic solvents like toluene and THF that do not easily accept a proton. The implication above is that the reaction of the α-hydroxy radical to reduce a metal in non-protic solvents must be less favourable. This is in fact the reason that this reaction is so much slower than in water, and alludes to the necessity of including a proton acceptor.

Hydrogen atom transfer (HAT) is the simplest form of PCeT, where the proton and the electron go together to the same place. However, PCeT also refers to instances where a proton and electron are transfered to different positions of a molecule simultaneously, or when the proton and electron are transfered to two different molecules (described as multisite PCeT). Furthermore, PCeT should not be confused with the more common and simple cases where proton and electron transfer happen in two separate steps, where distinct intermediates are formed from either proton transfer or electron transfer. These reactions can be understood by simple and well understood theories on proton and electron transfer.[63, 64] The intermediates, however, in these sequential process are necessarily reactive species that must have a free energy somewhere between the reagents and the products (or else they would be the reagents or the products). Simultaneous proton and electron transfer or PCeT, on the other hand, has no spectroscopically detectable intermediates. Therefore, the $\triangle$G for a PCeT process is necessarily more negative than

that of the rate determining step in sequential proton and electron transfer processes. This is illustrate in Figure 2.19.

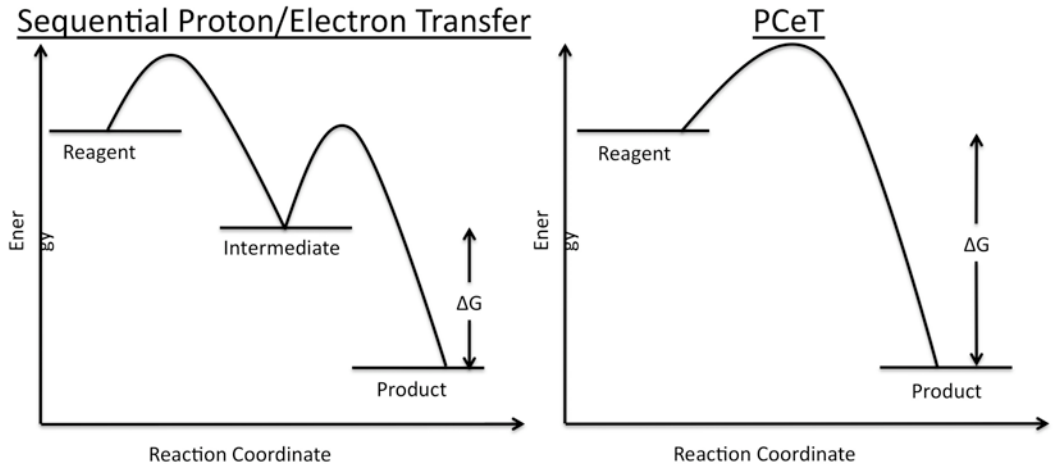

Figure 2.19: The free energy diagram for sequential proton/electron transfer as well as PCeT, illustrating the difference in free energy of the reaction for the two processes.

Why then, if it is thermodynamically favourable, is PCeT more rare than the related sequential proton and electron transfer process? The reason is that PCeT requires the formation of a particular transition state, that is often kinetically unfavourable when compared with the more simple initiating proton or electron transfer. Nevertheless, when these intermediates are highly unstable or when the transition state for PCeT is easily achieved, concerted PCeT often occurs. The reactions of the α-hydroxy radical photochemically derived from I-2959 to reduce metal ions discussed herein, represents both of these situations depending on the solvent system. For reactions in non-protic solvents, like the formation of fluorescent Ag_2 clusters, the intermediate formed in sequential proton/electron transfer steps would be highly reactive charged species that are too unstable in these solvents. On the other hand, for the same reaction in water the solvent molecules act as proton acceptors, making the transition state for PCeT easily attained so that the process happens without spectroscopically detectable intermediates. Both of these reactions fall in the category of multisite PCeT, where the proton and electron are delivered to two different receiving molecules. The general process is shown

in Equation 2.12 here, illustrating the proton and electron acceptors explicitly.

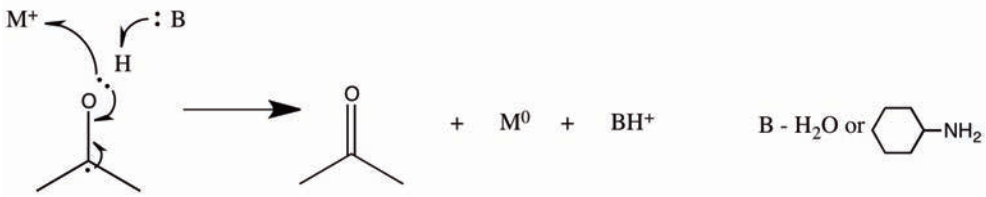

(2.12)

It is more clear now the overall role of CHA in the formation of fluorescent AgNP, which provides a better overall understanding of the reactions governing AgNP formation from photochemically derived α-hydroxy radicals. In aqueous conditions, the proton acceptor is water, and so easily overlooked, whereas the proton acceptor in non-protic solvents has to be added, in the example used herein it is CHA. Recent work has lead to a more thorough understanding of the PCeT process, especially pertaining to the rate constants and energetics of these reactions. Much of this work has been done by Mayer, in his work that has elaborated on Marcus theory, where he has established a cross correlation relationship based on self exchange reactions and free energy (G) of reaction species.[65, 66] As mentioned briefly above, the electron and proton do not have to go to the same site. Tyrosine oxidation and imino-oxime reactions have been described well with these theories of multisite PCeT, and provide a good analogy to electron transfer reactions leading to nanoparticle formation described herein.[67, 68]

Shukla *et al*, have studied the PCeT process in a system remarkably similar to our own.[69] In this study, α-hydroxy radicals (diphenylketyl radicals, the same radicals used to evaluate the rate constant of Ag^+ quenching shown in Figure 2.13) are photochemically generated and used to reduce 1,2,4,5-tetracyanobenzene, which can be observed by LFP in the reduced form. The choice of reagents in that work was based on the redox potentials for the diphenylketyl radical (E^{ox} = -0.25 V vs. SCE) and 1,2,4,5-tetracyanobenzene (E^{red} = -0.65 V vs. SCE) are such that the electron transfer is endothermic by 0.4 eV. This is due to the fact that one of the products of electron transfer is the protonated ketone (R_2COH^+), and ketones are extremely weak bases (therefore unstable when protonated). However, with a suitable proton acceptor that can complex either one of the reagents and make proton transfer more favourable in a PCeT process this unfavourable reaction can be made thermodynamically favourable. This is described by Scheme 2.13, where

the base is represented by (B).

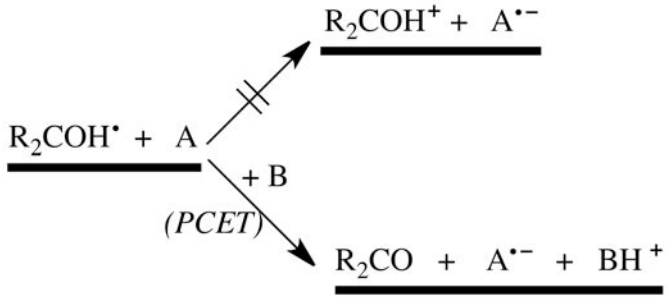

(2.13)

Through varying the concentration of reagents, including several pyridine derivatives used as proton acceptors, and following the reduction process by LFP, it was determined that PCeT does in fact take place. In fact, with the appropriate base, almost diffusion controlled reactions (1.5 x10^{10} $M^{-1}s^{-1}$) can be reached simply by adding pyridine derivatives. It is discovered from this work as well, that the complex that forms is between the proton acceptor and ketyl radical and not the electron acceptor, making this result most applicable to our work, since the major difference with our study is the electron acceptor (Ag^+), which should not affect PCeT. From this work, it becomes intuitive that PCeT must play a role in the chemistry for the formation of Ag_2 as well, which provides possibly the best explanation for the role of amine in our work.

2.5.1 Conclusions

The mechanism of formation of AgNP in protic solvents has been studied by Henglein, *et al.* as early as the 1980's, and much of this work and others has been generally accepted as the mechanism for metal nanoparticle formation. The mechanism for formation of these metal nanoparticles is the platform on which synthetic strategies for these particles are based. Also, due to the explosion of research in methal nanoparticles over the past couple of decades, and from a physical organic chemist point of view, the mechanism of formation of these materials is very important. Therefore, discovering the role of PCeT in the primary reactions in the reduction of metal salts like $AgNO_3$, constitutes a major contribution to this field. This is especially important in non-protic solvents, where the rate of reduction of metal salts can be greatly affected by the presence of a proton acceptor, a role that the solvent can play in protic solvents like water. The discussion in this chapter on the LFP results also indicates a different nucleation and growth mechanism than the one provided by Henglein, presumably due to instability of charged metal clusters in solvents such as toluene. For these reasons, the article published

in the Journal of the American Chemical Society that describes the work discussed in this chapter on the formation of Ag dimers, was highlighted in that journal for its contribution to the field.

Several reviews have also been written containing some of the work discussed in this chapter, that have contributed to the body of knowledge surrounding photochemical methods for nanoparticles synthesis, and in particular, the choice of photoinitiators used. This chapter discusses some of the important characteristics of the photoinitiators used throughout this thesis that make them a good choice for this type of work. Also, this chapter provides a clear description of how an understanding of the fundamentals of the photochemistry of these photo-initiator molecules is important to the complete understand of nanoparticle synthesis by photochemical methods.

REFERENCES

[1] S Jockusch, MS Landis, B Freiermuth, and NJ Turro. Photochemistry and photophysics of r-hydroxy ketones. *Macromolecules*, 34:1619–1626, 2001.

[2] PJ Wagner, AE Kemppainen, and HN Schott. Effects of ring substituents on the type ii photoreactions of phenyl ketones. how interactions between nearby excited triplets affect chemical reactivity. *Journal of the American Chemical Society*, 95:5604–5614, 1973.

[3] M Luisa Marin, KL McGilvray, and JC Scaiano. Photochemical strategies for the synthesis of gold nanoparticles from au(iii) and au(i) using photoinduced free radical generation. *Journal of the American Chemical Society*, 130(49):16572–16584, 2008.

[4] JC Scaiano, C Aliaga, S Maguire, and D Wang. Magnetic field control of photoinduced silver nanoparticle formation. *Journal of Physical Chemistry B*, 110(26):12856–9, 2006.

[5] KL McGilvray, MR Decan, D Wang, and JC Scaiano. Facile photochemical synthesis of unprotected aqueous gold nanoparticles. *Journal of the American Chemical Society*, 128(50):15980–15981, 2006.

[6] JC Scaiano and GL Hallett-Tapley KG Stamplecoskie. Photochemical norrish type 1 reaction as a tool for metal nanoparticle synthesis: Importance of proton coupled electron transfer. *Chemical Communications*, 48:4798–4808, 2012.

[7] JC Scaiano, EB Abuin, and LC Stewart. Photochemistry of benzophenone in micelles. formation and decay of radical pairs. *Journal of the American Chemical Society*, 104(21):5673–5679, 1982.

[8] V Ramamurthy, NJ Turro, and JC Scaiano. *Modern Molecular Photochemistry of Organic Molecules*. John Wiley and Sons Ltd, 2009.

[9] JC Scaiano. Laser flash-photolysis studies of the reaction of some 1,4-biradicals. *Accounts of Chemical Research*, 15(8):252–258, 1982.

[10] RD Small and JC Scaiano. Photochemistry of phenyl alkyl ketones - lifetime of intermediate biradicals. *Journal of Physical Chemistry-Us*, 81(22):2126–2131, 1977.

[11] RD Small and JC Scaiano. Reaction of type 2 biradicals with paraquat ions - measurement of biradical lifetimes. *Journal of Physical Chemistry-Us*, 81(9):828–832, 1977.

[12] KG Stamplecoskie and JC Scaiano. Light emitting diode irradiation can control the morphology and optical properties of silver nanoparticles. *Journal of the American Chemical Society*, 132(6):1825–7, 2010.

[13] EI Alarcon, K Udewku, M Skog, N Polisetti, NL Pacioni, KG Stamplecoskie, M Gonzalez-Bejar, A Richter-Dahlfors, M Griffith, and JC Scaiano. The biocompatibility and antibacterial properties of collagen-stabilized photochemically prepared silver nanoparticles. *Biomaterials*, 33(19):4947–56, 2012.

[14] BJ Wiley, YJ Xiong, ZY Li, YD Yin, and YA Xia. Right bipyramids of silver: A new shape derived from single twinned seeds. *Nano Letters*, 6:765–768, 2006.

[15] X Tian, K Chen, and G Cao. Seedless, surfactantless photoreduction synthesis of silver nanoplates. *Materials Letters*, 60(6):828–830, 2006.

[16] XC Jiang, CY Chen, WM Chen, and AB Yu. Role of citric acid in the formation of silver nanoplates through a synergistic reduction approach. *Langmuir*, page 091203125427072, 2009.

[17] D Yu and VW Yam. Controlled synthesis of monodispersed silver nanocubes in water. *Journal of the American Chemical Society*, 126(41):13200–1, 2004.

[18] ZQ Tian, ZL Yang, B Ren, JF Li, Y Zhang, XF Lin, JW Hu, and DY Wu. Surface-enhanced raman scattering from transition metals with special surface morphology and nanoparticle shape. *Faraday Discussions*, 132:159, 2006.

[19] YG Sun, B Mayers, T Herricks, and YN Xia. Polyol synthesis of uniform silver nanowires: A plausible growth mechanism and the supporting evidence. *Nano Letters*, 3(7):955–960, 2003.

[20] T Deckert-Gaudig, F Erver, and V Deckert. Transparent silver microcrystals: Synthesis and application for nanoscale analysis. *Langmuir*, 25(11):6032–6034, 2009.

[21] BJ Wiley, Z Wang, J Wei, Y Yin, DH Cobden, and Y Xia. Synthesis and electrical characterization of silver nanobeams. *Nano Letters*, 6(10):2273–2278, 2006.

[22] R Xu, D Wang, J Zhang, and Y Lia. Shape-dependent catalytic activity of silver nanoparticles for the oxidation of styrene. *Chemistry Asian Journal*, 1:888–893, 2006.

[23] XS Shen, GZ Wang, X Hong, X Xie, W Zhu, and DP Li. Anisotropic growth of one-dimensional silver rod-needle and plate-belt heteronanostructures induced by twins and hcp phase. *Journal of the American Chemical Society*, 131:10812–3, 2009.

[24] JC Scaiano, JC Netto-Ferreira, E Alarcon, P Billone, CJ Bueno Alejo, COL Crites, M Decan, C Fasciani, M González-Béjar, G Hallett-Tapley, M Grenier, KL Mcgilvray, NL Pacioni, A Pardoe, L René-Boisneuf, R Schwartz-Narbonne, J Silvero, KG Stamplecoskie, and T Wee. Tuning plasmon transitions and their applications in organic photochemistry. *Pure and Applied Chemistry*, 83(4):913–930, 2011.

[25] DE Charles, D Aherne, M Gara, DM Ledwith, YK Gun'ko, JM Kelly, WJ Blau, and ME Brennan-Fournet. Versatile solution phase triangular silver nanoplates for highly sensitive plasmon resonance sensing. *ACS Nano*, 4(1):55–64, 2010.

[26] Q Zhang, J Ge, T Pham, J Goebl, Y Hu, Z Lu, and Y Yin. Reconstruction of silver nanoplates by uv irradiation: Tailored optical properties and enhanced stability. *Angewandte Chemistry International Edition*, 48(19):3516–3519, 2009.

[27] Q Zhang, N Li, J Goebl, Z Lu, and Y Yin. A systematic study of the synthesis of silver nanoplates: Is citrate a "magic" reagent? *Journal of the American Chemical Society*, 133(46):18931–18939, 2011.

[28] J Zeng, Y Zheng, M Rycenga, J Tao, ZY Li, Q Zhang, Y Zhu, and Y Xia. Controlling the shapes of silver nanocrystals with different capping agents. *Journal of the American Chemical Society*, 132(25):8552–3, 2010.

[29] B Wiley, Y Sun, and Y Xia. Synthesis of silver nanostructures with controlled shapes and properties. *Accounts of Chemical Research*, 40:1067–1076, 2007.

[30] Andrea R Tao, Susan Habas, and Peidong Yang. Shape control of colloidal metal nanocrystals. *Small*, 4(3):310–325, 2008.

[31] B Pietrobon and V Kitaev. Photochemical synthesis of monodisperse size-controlled silver decahedral nanoparticles and their remarkable optical properties. *Chemistry of Materials*, 20:5186–5190, 2008.

[32] T Rocha and D Zanchet. Structural defects and their role in the growth of Ag triangular nanoplates. *Journal Physical Chemistry C*, 111:6989–6993, 2007.

[33] Y Tang and M Ouyang. Tailoring properties and functionalities of metal nanoparticles through crystallinity engineering. *Nature Materials*, 6(10):754–9, 2007.

[34] RJ Chimentao, I Kirm, F Medina, X Rodriguez, Y Cesteros, P Salagre, and JE Sueiras. Different morphologies of silver nanoparticles as catalysts for the selective oxidation of styrene in the gas phase. *Chemical Communications*, 2004(7):846–847, 2004.

[35] YG Sun and Y Xia. Shape-controlled synthesis of gold and silver nanoparticles. *Science*, 298(5601):2176–2180, 2002.

[36] ZL Sun. Transmission electron microscopy of shape-controlled nanocrystals and their assemblies. *Journal of Physical Chemistry B*, 104(6):1153–1175, 2000.

[37] C Wang, C Kan, J Zhu, X Zeng, X Wang, H Li, and D Shi. Synthesis of high-yield gold nanoplates: Fast growth assistant with binary surfactants. *Journal of Nanomaterials*, 2010:969030, 2010.

[38] RC Jin, YC Cao, EC Hao, GS Metraux, GC Schatz, and CA Mirkin. Controlling anisotropic nanoparticle growth through plasmon excitation. *Nature*, 425(6957):487–490, 2003.

[39] A Callegari, D Tonti, and M Chergui. Photochemically grown silver nanoparticles with wavelength-controlled size and shape. *Nano Letters*, 3(11):1565–1568, 2003.

[40] X Zheng, X Zhao, D Guo, B Tang, S Xu, B Zhao, W Xu, and J Lombardi. Photochemical formation of silver nanodecahedra: Structural selection by the excitation wavelength. *Langmuir*, 2009.

[41] V Filippenko, M Frenette, and JC Scaiano. Solvent-independent antioxidant activity from thermally generated carbon-centered radical antioxidants. *Organic Letters*, 11(16):36343637, 2009.

[42] KL Kelly, E Coronado, LL Zhao, and GC Schatz. The optical properties of metal nanoparticles: The influence of size, shape, and dielectric environment. *Journal of Physical Chemistry B*, 107:668–677, 2003.

[43] M Maillard, PR Huang, and L Brus. Silver nanodisk growth by surface plasmon enhanced photoreduction of adsorbed [Ag^+]. *Nano Letters*, 3(11):1611–1615, 2003.

[44] U Kreibig and M Vollmer. *Optical Properties of Metal Clusters*. Springer, 1995.

[45] SA Maier. *Plasmonics: Fundamentals and Applications; 1st Edition*. Springer, New York, 2006.

[46] Yoshito Tanaka, Hiroyuki Yoshikawa, Tamitake Itoh, and Mitsuru Ishikawa. Surface enhanced raman scattering from pseudoisocyanine on ag nanoaggregates produced by optical trapping with a linearly polarized laser beam. *Journal of Physical Chemistry C*, 113:11856–11860, 2009.

[47] L Maretti, PS Billone, Y Liu, and JC Scaiano. Facile photochemical synthesis and characterization of highly fluorescent silver nanoparticles. *Journal of the American Chemical Society*, 131(39):13972, 2009.

[48] KG Stamplecoskie and JC Scaiano. Kinetics of the formation of silver dimers: Early stages in the formation of silver nanoparticles. *Journal of the American Chemical Society*, 133(11):3913–3920, 2011.

[49] H Xu and KS Suslick. Sonochemical synthesis of highly fluorescent Ag nanoclusters. *ACS Nano*, 4(6):3209–3214, 2010.

[50] JK Kochi. *Free Radicals*. John Wiley and Sons Ltd: New York, 1973.

[51] N Filipescu and FL Minn. Photoreduction of benzophenone in isopropyl alcohol. *Journal of the American Chemical Society*, 90(6):1544–1547, 1968.

[52] JC Scaiano and EB Abuin. Absolute measurement of the rates of radical exit and of radical-pair intersystem crossing in anionic micelles. *Chemical Physics Letters*, 81(2):209–213, 1981.

[53] JC Scaiano and EB Abuin. Photochemistry of benzophenone in micelles. formation and decay of radical pairs. *Journal of the American Chemical Society*, 104(21):5673–5679, 1982.

[54] FJ Green. *Sigma-Aldrich Handbook of Stains, Dyes and Indicators, 2nd ed.* Aldrich Chemical Co. Inc., 1990.

[55] JV Sinisterra, FG Blanco, M Iglesias, and JM Marinas. The nature of active-sites in $Ba(OH)_2$ catalyst. *Reaction Kinetics and Catalysis Letters*, 25(3-4):277–282, 1984.

[56] J Lipscher and H Fischer. Absolute rate constants for the self-termination of the isopropyl radical and for the decarbonylation of the 2-methylpropanoyl radical. *Journal of Physical Chemistry*, 88:2555–2559, 1984.

[57] T Vosch, Y Antoku, JC Hsiang, CI Richards, JI Gonzalez, and RM Dickson. Strongly emissive individual DNA-encapsulated Ag nanoclusters as single-molecule fluorophores. *Proceedings of the National Academy of Science*, 104(31):12616–12621, 2007.

[58] JC Scaiano, P Billone, CM Gonzalez, L Maretti, M Luisa Marin, KL McGilvray, and N Yuan. Photochemical routes to silver and gold nanoparticles. *Pure and Applied Chemistry*, 81(4):635–647, 2009.

[59] A Frattini, N Pellegri, D Nicastro, and O Sanctis. Effect of amine groups in the synthesis of Ag nanoparticles using aminosilanes. *Materials Chemistry and Physics*, 94(1):148–152, 2005.

[60] I Texier, S Rmita, P Archirel, and M Mostafavi. Reduction of $Ag_1^1(NH_3)_2^+$ to $Ag_1^0(NH_3)_2$ in solution. redox potential and spectral study. *Journal of Physical Chemistry*, 100(30):12472–12476, 1996.

[61] A Henglein. Small-particle research: physicochemical properties of extremely small colloidal metal and semiconductor particles. *Chemical Reviews*, 89(8):1861–1873, 1989.

[62] A Henglein and R Tausch-Treml. Optical absorption and catalytic activity of subcolloidal and colloidal silver in aqueous solution: A pulse radiolysis study. *Journal of Colloid and Interface Science*, 80(1):84–93, 1980.

[63] JM Mayer. Proton-coupled electron transfer: A reaction chemist's view. *Annual Reviews in Physical Chemistry*, 55:363–390, 2004.

[64] JM Mayer. Understanding hydrogen atom transfer: From bond strengths to Marcus theory. *Accounts of Chemical Research*, 44(1):36–46, 2011.

[65] RA Marcus. On the theory of oxidation-reduction reactions involving electron transfer. *Journal of Chemical Physics*, 24:966–978, 1956.

[66] RA Marcus. On the theory of electronchemical and chemical electron transfer processes. *Canadian Journal of Chemistry*, 37(1):155–163, 1959.

[67] CJ Fecenko, TJ Meyer, and HH Thorp. Electrocatalytic oxidation of tyrosine by parallel rate-limiting proton transfer and multisite electron/proton transfer. *Journal of the American Chemical Society*, 128(34):11020–11021, 2006.

[68] GA DiLabio and KU Ingold. A theoretical study of the iminoxyl/oxime self-exchange reaction. a five-center, cyclic proton-coupled electron transfer. *Journal of the American Chemical Society*, 127(18):6693–6699, 2005.

[69] D Shukla, W G Ahearn, and S Farid. Reducing power of photogenerated α-hydroxy radicals. proton-coupled electron transfer. *Journal of Physical Chemistry A*, 108:10386–10394, 2004.

Chapter 3

Application of Silver Nanoparticles in Raman Sensing: Effects of Size and Shape

It was earlier stated that one main theme in this thesis is the controlled synthesis of nanomaterials always with the intent of obtaining the desired properties. The synthesis of different sizes and shapes of nanoparticles directly affects the optical properties and reactivity of these materials. The original intent of controlling the shape and size of AgNP presented in this chapter, was to study the effect of these nanoparticles on the Raman spectrum of adsorbed molecules.

3.1 Colloidal AgNP as a SERS Active Substrate

3.1.1 Optimal Size of Spherical AgNP for SERS

With the advent of lasers in 1960, Raman spectroscopy emerged as a powerful molecular finger printing technique, since Raman active modes for a given molecule can be collectively very characteristic. However, Raman spectroscopy (especially off resonance Raman spectroscopy) continues to suffer from low signal-to-noise due to the fact that only one out of every 10^8 photons undergoes Raman scattering.[1] Therefore, the widespread use of Raman spectroscopy was limited until the 1970s when authors like Albrecht and Creighton reported enhanced Raman signals of adsorbed pyridine on metals such as silver.[2] Surface Enhanced Raman Scattering (SERS) has now become recognized as a

sensitive optical diagnostic tool for detecting species adsorbed on the surface of primarily metals, and most often metal nanoparticles.[3, 4, 5, 6, 7, 8, 9, 10, 11, 12, 13, 14, 15]Silver nanoparticles (AgNP) exhibit a surface plasmon resonance absorption that is dependent on many factors including; the dielectric constant of both metal and surface, the inter-particle distance and the shape and size of the particles.[16, 17] For spherical AgNP the plasmon absorption is centered at ∼400 nm with the exact peak position dependent on the size of the particles. The excitation of this plasmon absorption results in a strong local electromagnetic field enhancement in the vicinity of the nanoparticles. It is this local field enhancement that is responsible for the major enhancement in the Raman spectra of molecules near the surface of metal particles.[16] In fact, there are four major factors that can contribute to the total SERS enhancement effect (depending on the experimental conditions) including; (1) Electromagnetic (EM) enhancement resulting from excitation of the metal, (2) charge transfer from metal to adsorbate resulting from excitation of the metal, (3) a resonance mechanism (resonant Raman spectroscopy) where the excitation corresponds to an electronic transition in the molecule and (4) an off resonance enhancement (usually described as excitation to virtual states) due to metal-adsorbate interaction.[18]

It is known that the local EM increases with increasing particle size,[16, 19] but as particle size increases the particles absorb less light and scatter more through inelastic scattering,[20] which should decrease the overall SERS intensity. Moreover, with an increase in the AgNP size while maintaining a fixed amount of Ag, the total surface area for adsorption decreases and is expected to somewhat offset the increased EM field of larger particles. Hence, it is important to ascertain the optimal size of colloidal spherical AgNP to provide a balance between EM field increase and scattering/limited surface area so as to realize maximum SERS intensity. Here we report a method for controlling the size of AgNP through a seeded growth process where small photochemically generated AgNP are used as catalysts and substrates for growth into larger spherical AgNP. The SERS spectrum of R6G in colloidal solutions of the prepared AgNP is evaluated as a function of the particle size in order to determine the optimal size of colloidal AgNP for SERS. Overall, the goal of this chapter is two fold, to examine the effect of particle size on the Raman spectrum of an analyte as well as the effect of particle shape for several shapes that were made as described in the previous chapter.

3.1.2 Experimental

Synthesis of AgNP for SERS

The synthesis of various sizes of AgNP with a broad size range, but low polydispersity within a given sample, was a two-step process including: 1) The synthesis of AgNP seeds as described in chapter two and 2) the seeded growth of AgNP seeds into larger AgNP using L-ascorbic acid. These seed AgNP have a lower reduction potential than $AgNO_3$, and as such act as both a catalyst for the reduction by L-ascorbic acid, and as a substrate to which additional Ag^+ add in subsequent growth experiments as shown in Equation 3.1.

For the seeded growth of AgNP, solutions containing 0.2 mM $AgNO_3$, 1 mM trisodium citrate and various amounts of seed AgNP were prepared. To these solutions 1 mL of 10 mM L-ascorbic acid was added over a period of 10 min with a syringe pump. The concentration of initial seed AgNP was varied to control the final size of the AgNP. For higher initial concentrations of seed AgNP the final size after seeded growth was smaller compared with the cases when fewer AgNP seeds are used.

The particles were imaged using a JSM-7500F FESEM from Japan Electron Optics Laboratory Co (JOEL) and the average particle size was determined. To measure a given particle using the JEOL software involves the user physically selecting the diameter of each particle and a value of the distance is shown (in nm) for the selected area that are then tabulated and averaged to obtain the average particle sizes.

Preparation of Samples for SERS

Due to the tendency for R6G to form dimers and aggregate in water at high concentrations, 5 mL nanoparticle samples of various sizes were centrifuged to isolate them from the original aqueous solutions and re-suspended in 5 mL of ethanol. To ensure that the resultant particles had not agglomerated in the ethanol solutions UV-Vis spectra of the resultant particles in ethanol were obtained. In all cases there was no significant broad red shifted absorption from the major dipole absorption of the colloidal spheres, which can be taken as an indication that the nanoparticles did not aggregate.[17, 21, 22] Typical samples for SERS contained 1.8 mL of AgNP (different sizes) dispersed in ethanol and 0.2 mL of 10^{-2} M R6G in ethanol so that the final concentration of R6G was 10^{-3} M. Using five identical samples containing 30.5 nm AgNP and 10^{-3} M R6G made in the same way as described above it was determined that the error in the measurements in Figure 3.6(c) is approximately 4.5 %, which was consistently obtained for these types

of measurements. In fact, deviations in SERS intensity as well as deviations in particle size were approximately 5 % and therefore, using two standard deviations the error bars in Figure 3.6(c) were obtained. The G-value is mathematically derived from the SERS intensity, and so the 5 % standard deviation is expected in the G-value as well.

SERS Spectra Measurements

The experimental configuration involved a 785 nm continuous wavelength (cw) multimode laser (BandW Tek Inc., BRM-785-0.45-100-0.22-SMA) with maximum output power of 450 mW. The laser beam was coupled to a sample solution of R6G and AgNP in a cuvette by means of X40 microscope objective lens. The output beam was allowed to pass through a long-pass filter (IRIDIAN PN-ZX000445), which was centered at 785 nm for rejecting the scattered laser light. The SERS signal was collected in transmission mode by a multimode fiber bundle and fed to a Kaiser f/1.8 spectrograph with a TE-cooled Andor camera and monitored on a computer. The excitation wavelength of 785 nm was chosen for Raman measurements since it is conveniently separated from the AgNP absorption band for truly realizing the non-resonant SERS enhancement. In this way colloidal solutions of AgNP containing R6G were excited in a wavelength region of the spectrum where R6G does not absorb. Hence, it minimizes any photochemical reactions resulting from electronic excitation of R6G, and therefore eliminates any effects that may arise from photodegradation of the adsorbate.

3.1.3 Results and Discussion

AgNP Size and UV-Vis Absorption Spectra

Ascorbic acid is a weak reducing agent that is unable to reduce Ag^+ to Ag^0 under the conditions of seeded growth used here, unless AgNP seeds are already present (see below). The seeds act as both a catalyst for the oxidation of ascorbic acid (and reduction of solvated Ag^+) and as a seed onto which reduced silver adds in order to grow into larger AgNP.[23] This process is illustrated below in scheme 3.1. Rapid addition of the reducing agent, as would be the case if the L-ascorbic acid were quickly added to the growth solution, can result in new nucleation of AgNP and thus a larger polydispersity in the final colloids.[23] Therefore, slow addition of ascorbic acid over 10 minutes using a syringe pump was performed to minimize the polydispersity of the size of the resultant AgNP.

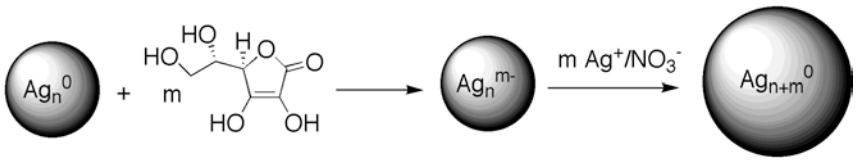

(3.1)

The seeded growth of AgNP using small AgNP seeds (∼3 nm) as catalysts for the further reduction of $AgNO_3$ and addition to seeds was used as a superior method for the formation of AgNP with controllable size and relatively low polydispersity. As mentioned the slow addition of ascorbic acid to the solution of AgNP seeds and $AgNO_3$ was performed in order to avoid secondary nucleation and formation of new nanoparticles. Also, the choice of reducing agent (ascorbic acid) was important in combination with AgNP seeds. The reduction potential of ascorbic acid is ∼ -0.1V (at pH =∼5-6 as is the case here),[24] which is not strong enough to reduce $AgNO_3$ (E_{red}= 0.8)[25] efficiently at 0.2 mM concentrations of both, unless the reduction is catalysed by AgNP seeds. The validity of this statement was tested in seeded growth experiments with and without the addition of AgNP seeds added to ∼3 mL of seeded growth solution. The results are shown in Figure 3.1, clearly showing that without any seed AgNP there is no surface plasmon band at approximately 400 nm and therefore there is no reduction of $AgNO_3$ to AgNP. We attribute the catalytic action of AgNP seeds to the fact that AgNP are easier to reduce than $AgNO_3$ and so ascorbic acid first reduces the AgNP seeds (to $Ag_n{}^{m-}$) and Ag^+ adds to the reduced seeds as in scheme 3.1. The seeded growth of AuNP with ascorbic acid has been previously reported by Jana *et al*,[23] however in all cases with Au it was difficult to avoid secondary nucleation because Au^{3+} (E_{red}= 1.002 , as $AuCl_4^-$)[25] is more easily reduced than Ag^+. Therefore, ascorbic acid works very well here as no AgNP formation is observed without the presence of AgNP seeds.

The average particle size was determined as a statistical average of AgNP deposited on carbon coated copper grids and imaged by SEM. Representative SEM images of the different particle solutions are illustrated in Figure 3.2 a)-f), and they show that a reasonably low polydispersity of the particles is obtained by this method. Histograms of the particle sizes determined in this way are also given in Figure 3.3 for the respective particles. These data are taken as further confirmation that the slow addition of reducing agent did not give rise to any significant degree of secondary nucleation, which would result in two very different populations of sizes.

As mentioned, the final size of the particles was controlled by adjusting the amount of seeds (catalyst and substrate for growth) that were added. Table 3.1 summarizes the

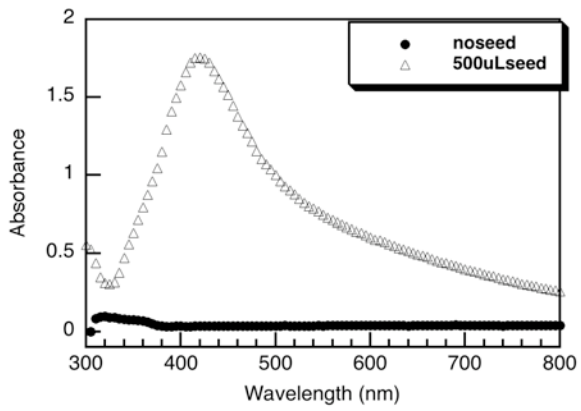

Figure 3.1: Representative UV-Vis absorption spectra with and without the addition of AgNP seeds.

volume of seeds added to 50 mL of growth solution, as well as the absorbance maximum and final particle size.

Table 3.1: Size and Absorption Maximum for AgNP

seed AgNP volume (μL)	peak position of plasmon (nm)	final AgNP diameter (nm)
25	432	69.5
50	430	59.3
125	414	40.3
250	414	33.0
500	409	29.4
1250	402	20.6

Note, these particle sizes are different from those found in Figure 3.3 because the sets of data are on two different full sets of experiments that had consistent results as indicated in Figure 3.6 b) and c) as blue or red dots for respective batches.

UV-Vis spectra for each of the various nanoparticle sizes are shown in Figure 3.4. It is not surprising that the absorption maximum due to the dipole absorption of the various solutions of different sized particles changes. Figure 3.4b) shows that the peak height decreases, as well as becoming broadened and red shifted as one goes from colloids of small ($\sim$20 nm) to larger ($\sim$69 nm) particles. The broadening and red shift for larger particles is due to an increasing contribution of higher order plasmon modes for larger

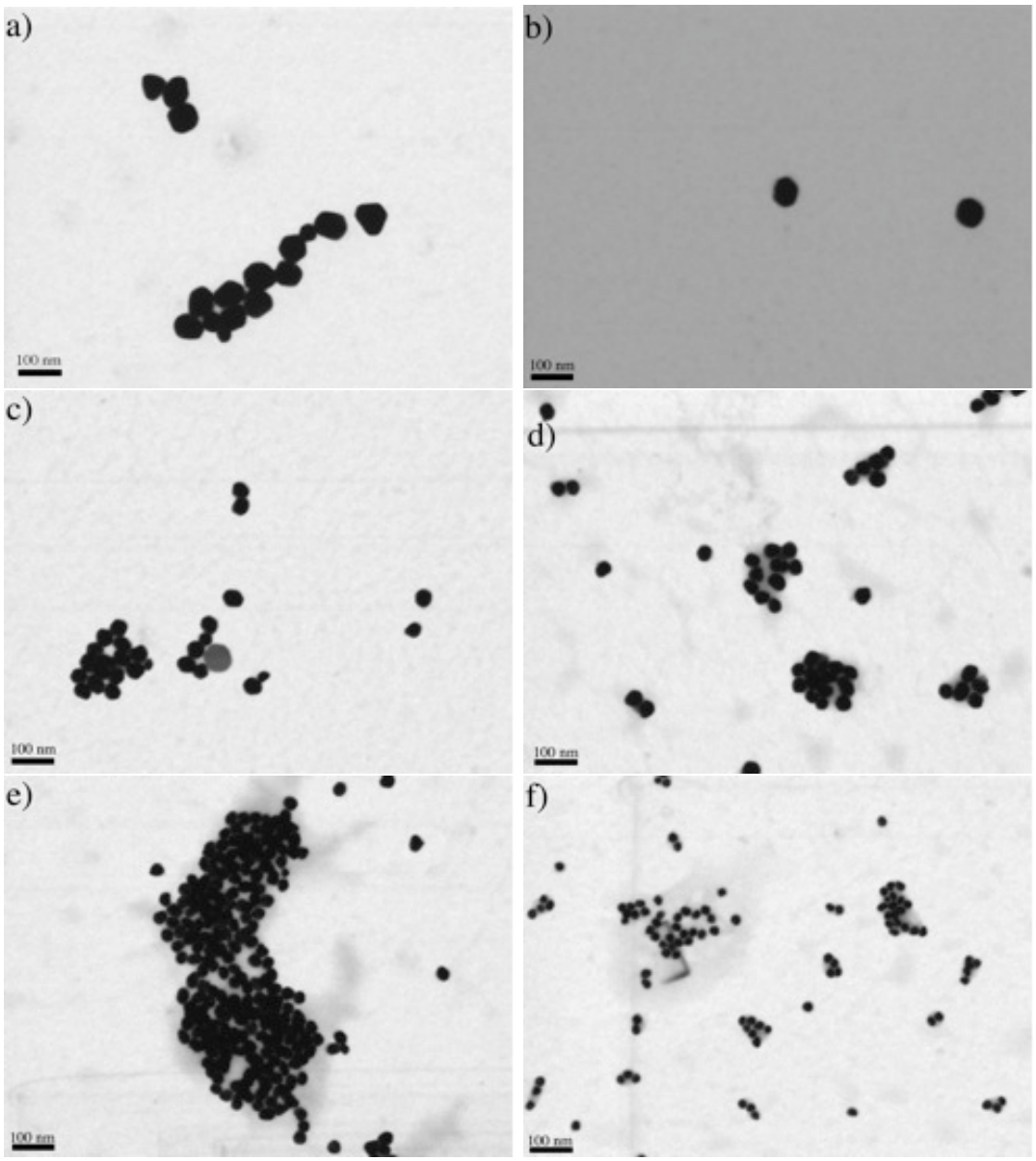

Figure 3.2: Representative images of sizes of AgNP made by the seeded growth mechanism and used in the measurement to determine the optimal size of AgNP for SERS, (a) the smallest seed volume (25 μL) leading to the largest particles (69.5 nm), and (f) the largest volumes of seeds (1.25 mL) leading to the smallest particles (20.6 nm).

particles.[16, 26, 22, 27, 28]

In Figure 3.4 c), UV-Vis absorption spectra of 18.2 nm particles are shown with

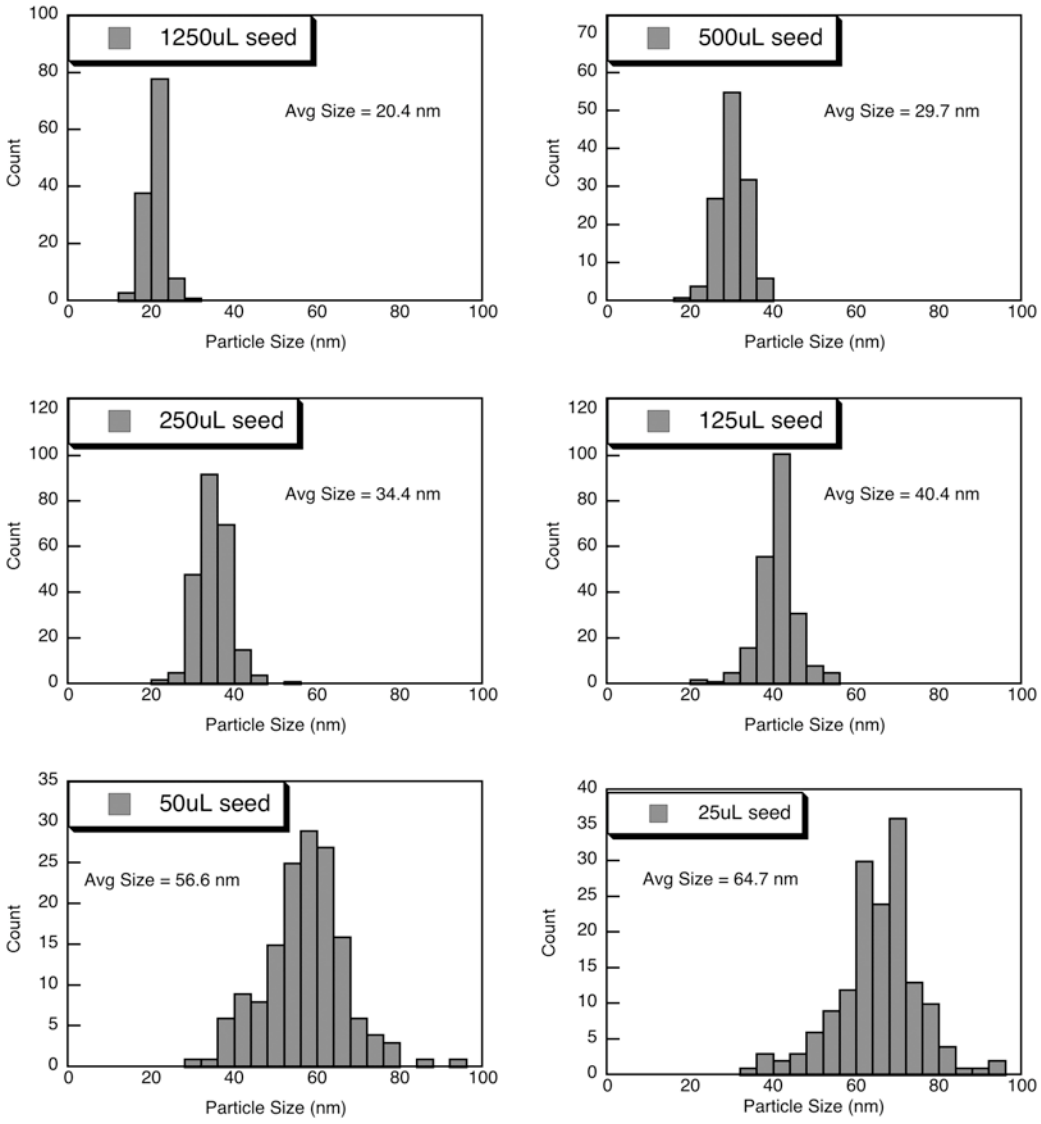

Figure 3.3: Histograms of particle sizes measured from corresponding images in Figure 3.2 of sizes of AgNP made by the seeded growth mechanism. Each histogram is made from measuring particles in a number of images of the same sample to improve the average size determined, that are later used in the Raman experiments to determine the optimal size of AgNP for SERS.

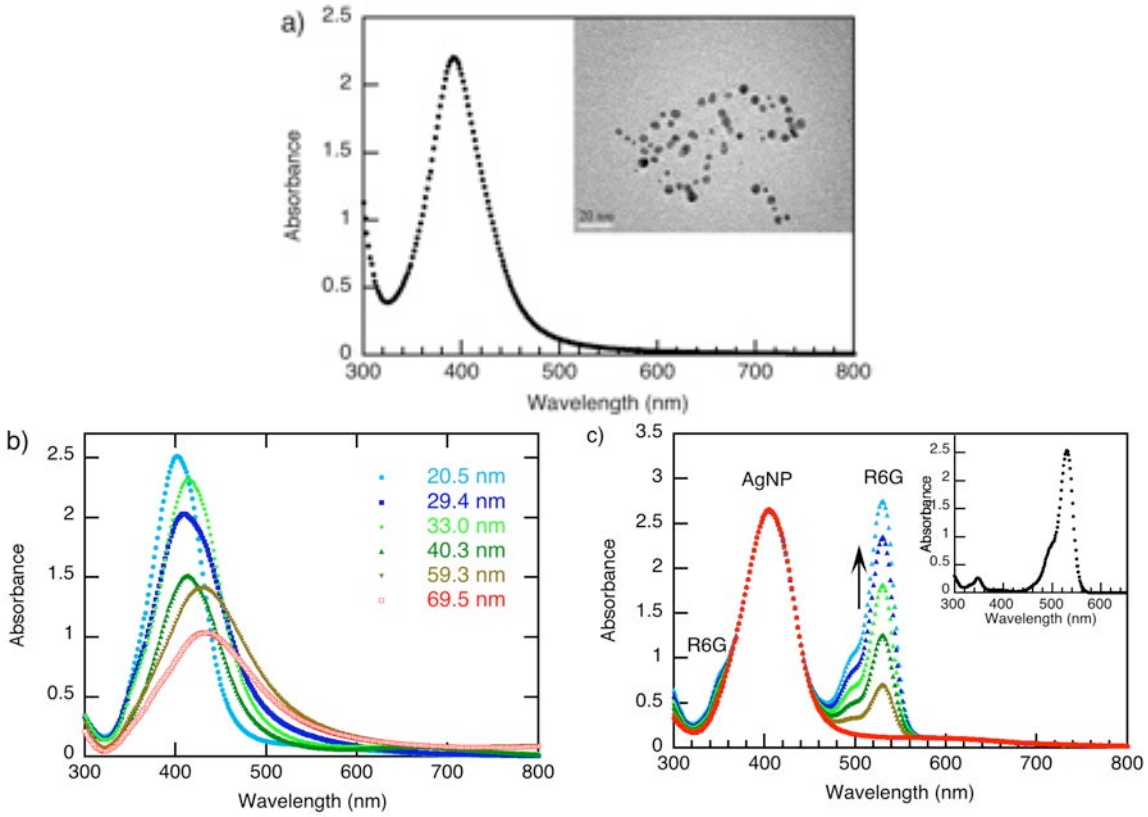

Figure 3.4: a) Absorption spectrum and representative image of seeds used for seeded growth, b) Absorption spectra of various sized samples of AgNP used in SERS measurement, and c) Absorption spectra of R6G alone (inset) and 18.2 nm AgNP with R6G added to a final concentration of 2.5 x10^{-5} M

increasing concentrations of R6G added from 0 - 2.5 x10^{-5} M (higher concentrations would saturate the instrument response). The addition of R6G to the AgNP solution does not change the absorption spectrum of the AgNP, and most importantly does not cause an increased absorption at longer wavelengths that would indicate aggregation of the particles. Any new bands at longer wavelengths would be expected to result in higher absorption of the laser light, which is not the case here. Similarly, the addition of R6G to 52 nm AgNP has no effect on the absorption properties of these colloids either (data not shown), indicating that there is no differing effect for larger particles that could affect the SERS measurements. It is also important to note that all of the AgNP solutions have similar, and very low absorption/scattering around 785 nm, which corresponds to the

laser excitation wavelength. This is truly an off-resonance experiment where the AgNP and the R6G are both off resonance with the excitation line.

3.1.4 SERS Intensity as a Function of AgNP Size

The intent of this study was to determine experimentally the effect of spherical AgNP size on SERS intensity of molecules adsorbed onto the surface of citrate stabilized colloidal AgNP, thereby determining an optimal size of AgNP to maximize the SERS signal. A common way to express the Raman enhancement effect in SERS is to use a G-value that gives a measure of the enhancement of the Raman signal per molecule adsorbed on the surface of a SERS active species.[29] The G-value is calculated as shown in equation 3.2:

$$G = \frac{[I_{SERS}]}{[I_{Raman}]} \mathrm{x} \frac{[M_{Bulk}]}{[M_{Monolayer}]} \tag{3.2}$$

where I_{SERS} and I_{Raman} are the Raman intensity that has been enhanced by AgNP and the unenhanced (no AgNP) intensity, respectively, and M_{Bulk} and $M_{Monolayer}$ are the molar concentrations of the analyte in a non-AgNP enhanced experiment solution and the molar concentration of the analyte bound to the surface of AgNP in a SERS experiment, respectively.

As particle size increases and if the total Ag concentration is fixed the available surface area for R6G absorption onto Ag is decreased due to the fact that the surface area to volume ratio decreases with increasing particle size such that;

$$\text{Particle Density (particles/L} = \frac{([Ag])(N_A)}{\text{Atoms/Particle}} \tag{3.3}$$

and:

$$\text{Surface Atoms (mol/L)} = \frac{4(\text{Atoms/Particle})^{2/3}(\text{Particle Density})}{N_A} \tag{3.4}$$

where N_A is Avogadro's number. Therefore, if the nanoparticles used in SERS measurements were entirely coated with R6G and concentrations above a monolayer coverage were used then one would expect the SERS versus particle size to decrease with increasing particle size regardless of any other effects but simply due to limited absorption onto AgNP of larger sizes. R6G covers on average 0.4 nm^2 per R6G molecule,[30] which corresponds to a surface atomic coverage of ~ 5.96 surface Ag atoms per R6G molecule. Therefore, a monolayer coverage would be:

$$\text{[R6G] for a monolayer (mol/L)} = \frac{\text{Surface Ag Atoms (mol/L)}}{\text{Surface Atomic Coverage per R6G}} \tag{3.5}$$

Using equation 3.5 for monolayer coverage, Figure 3.5 is constructed that shows the R6G concentration required for total surface coverage. It is clear then that using a [R6G] of 1.32 x10^{-3} M, as was done in all the SERS measurements shown, the R6G is always well in excess of monolayer coverage. Therefore, in all cases limited [R6G] to undergo absorption to the Ag surface should be considered in the overall SERS intensity. In other words, to evaluate the effect of limited R6G adsorption onto AgNP it is common to use a G-value, which corrects for lower concentrations of adsorbed R6G on larger particles.

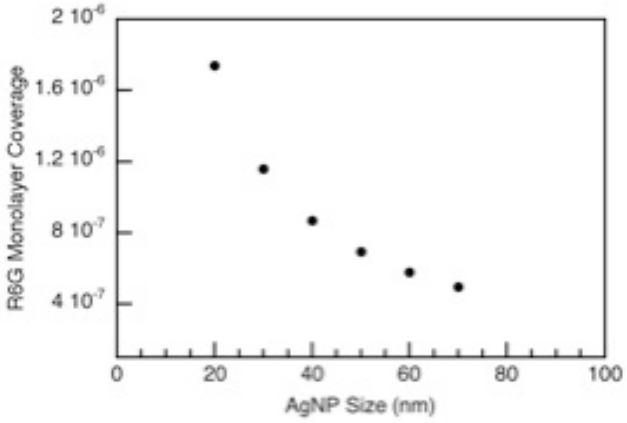

Figure 3.5: The concentration of Rhodamine 6G (in mol/L) needed for a monolayer coverage calculated as a function of AgNP size. With silver content held constant, the total surface area is smaller for larger particle samples, resulting in lower concentrations of Rhodamine 6G required for total surface coverage.

It is important to note that R6G has good photostability (does not change significantly with prolonged laser excitation) and has been extensively studied using SERS,[31, 32, 33, 34] which is why it was chosen here as a standard to study the particle size effect on SERS. Figure 3.6 a) shows typical SERS spectra obtained for a solution containing 59.3 nm particles and 10^{-3} M R6G, for which the peaks in the Raman spectra correspond well to those of R6G.[35, 36] The SERS intensity for various AgNP/R6G samples was monitored at 1365 cm^{-1} (strong characteristic off-resonance frequency described by Watanabe et al[36]), and the calculated G-value versus AgNP size is plotted in Figure 3.6 b). The baseline in all cases was taken as the minimum intensity between 1400-1430 cm^{-1} with the peak intensities in Figure 3.6 c) plotted with respect to these baseline values. It is important to note that the blue and red data points correspond to two

completely different sets of AgNP with R6G. The data for these two sets of samples was recorded approximately 12 months apart, which shows that the data is truly reproducible as well.

Looking at Figure 3.4 c) in the area of laser excitation (785 nm) there is not a significant absorption in our samples at that wavelength. Therefore, the question arises as to why a SERS signal is observed and more importantly why an enhancement in this signal is observed if there is not a significant absorption of the excitation source. First of all, the actual samples used in SERS measurements are significantly more concentrated than the solution for Figure 3.4 c), and should therefore have a slightly higher absorption. Most importantly though, it has been shown that metal nanoparticles do not need to be excited directly on resonance (400 nm) to see an electromagnetic field enhancement. In fact, there is significant enhancement simply due to the fact that the excitation source is passing through two media of very different refractive indices.[37] Beyond this fact, with increasing particle size there is an increasing contribution from multipole absorption in the extinction spectra of AgNP that broaden and red shift the plasmon band.[16] This increasing contribution of higher order plasmon modes as well as the increasing size of the enhanced EM field around larger AgNP is attributed with the increasing SERS intensity with larger AgNP size seen here.

In Figure 3.6 c) the particles with the maximum SERS enhancement are approximately 50-60 nm in diameter (maximum of the green line). It is also important to note that this optimal size for SERS is only applicable when the concentration of analyte exceeds what is required for monolayer coverage of silver nanoparticles. Therefore, the G-value is a better representation of the enhancement by AgNP because it takes into account the lower surface area (and therefore lower surface coverage) for R6G binding. When the calculated G factor for Raman enhancement is plotted against particles size as in Figure 3.6 b) an almost linear relationship is obtained but without the clear maximum found in Figure 3.6 (c). This suggests that saturated surface adsorption plays an important role in limiting the overall SERS intensity, and also confirms the theoretical prediction that increasing particle size results in increased EM enhancement. Nevertheless, Figure 3.6 c) provides a measure of the optimal size of AgNP colloids for SERS when keeping total silver concentration constant and increasing particle size. It is also important to note that in all cases we are using R6G concentrations that are above the amount required for monolayer coverage of particles. Therefore, while the Raman intensity increases with increasing particle size in agreement with the theoretical prediction of increasing EM field for larger particles[19]; the apparent plateau in Raman intensity

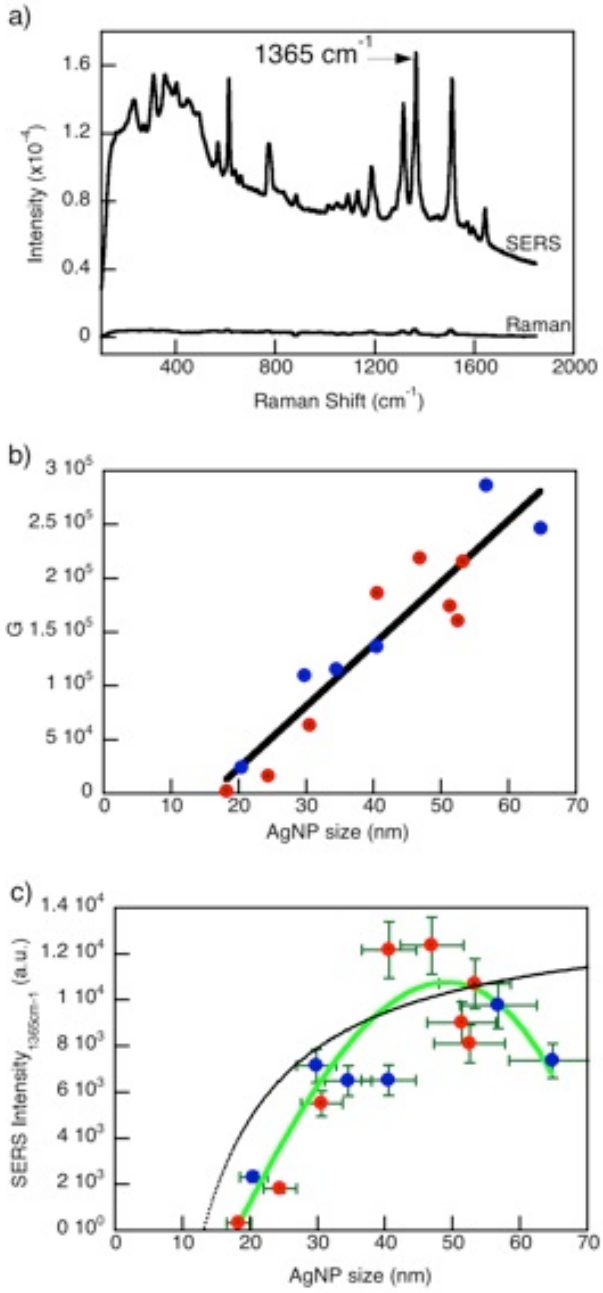

Figure 3.6: a) Raman and SERS (59.3 nm particle size example) of 10^{-3} M R6G, b) calculated G-value for given particle size samples, and c) direct correlation between AgNP size and SERS intensity measured at 1365 cm^{-1} with a curve fit for the theoretical calculated from the best fit line in b), as well as a polynomial fit to the data (green line) to guide the eye to see the observed trend in SERS vs AgNP size.

that was seen in going from ∼50-60 to 70 nm AgNP may also be due to lower total adsorbed R6G for larger particles. When the metal particle size increases, especially to very large particles, there is not only an increase in electromagnetic field, but also an increase in scattering efficiency, which would result in lower Raman signals (less light is being absorbed because it is scattered more efficiently). Therefore, while the curve fitting in Figure 3.6 c) shows a plateau due to limited adsorption of R6G, it is expected that additional effects like scattering and radiation damping for larger particles would in fact cause the curve to decrease. Fang *et al.* described that the SERS intensity is a result of a competition between radiation damping with respect to surface scattering and dynamic depolarization so that there is always an optimal size for SERS.[38] Therefore, while the optimal size for SERS found here was not established previously, the plot in Figure 3.6 c) appears to have a maximum and a subsequent decrease in SERS at very large sizes. Meier *et al.* predict an optimal size of silver nanoparticles for SERS to be ∼25 nm (12.5 nm radius) based on this balance between radiation damping with respect to surface scattering and dynamic depolarization.[39] However, in that work the severe broadening and red shift of the particle absorption is expected to decrease the resultant EM field assuming equal excitation. Here, the longer wavelength absorption of larger particles causes an increase in the excitation of larger particles. Larger particles are then excited more by the off resonance 785 nm excitation source and have a larger resultant EM field.[40] With a further increase of the particle size the increased excitation is offset by increased scattering and decreasing total R6G adsorbed until at a particle diameter of ∼70 nm we see a decrease in SERS intensity. Overall, the plot in Figure 3.6 c) is still expected with such long wavelength excitation, but it is not surprising that the optimal size is larger than expected for equal excitation (when the excitation is biased to larger particles). Similar studies have been performed to determine the optimal size of AuNP, which was 120-135 nm, though this result neglects variations due to changes in inter-particle distance on a support.[41] Others have attempted to measure the SERS intensity of trans-1,2-bis(4-pyridyl)ethylene versus AgNP size with the result that small particles give the highest EM enhancement, but the polydispersity in this work was very high and the characterization of size was of low resolution.[27]

Morton *et al.* have found that the charge transfer mechanism is not affected by the amount of charge transferred but that it is only dependant on the $HOMO_{metal}$-$LUMO_{molecule}$ energy gap.[18] Also, the $HOMO_{metal}$-$LUMO_{molecule}$ gap is not likely to change significantly for a given adsorbate as a function of particle size because of the similar band structure of particles greater than ∼15 nm. It is more intuitive to under-

stand that the resonant enhancement mechanisms should not be significantly changed by changing the size of the metal because the resonant mechanism is an inherent molecular property. Also, since there are no quantum size effects on SERS for particles >15 nm, the non-resonant mechanism is not expected to be affected by changing particle size at least above ∼15 nm.[19] Overall, the local electromagnetic field is the only factor affecting SERS expected to change with particle size, and this is independent of the particle-metal interaction. Thus, we anticipate that, while the total enhancement will differ depending on adsorbate, the trend in SERS vs. particle size for the AgNP/R6G system measured here could be extended to other adsorbates on the surface of spherical AgNP.

Overall, a seeded growth mechanism for the formation of AgNP with the same silver concentration but varying particle size is described. The high degree of control over particle size makes it feasible to determine the best size of AgNP for obtaining a maximum SERS intensity of R6G. With an off-resonance excitation source of 785 nm that is greater than both the electronic excitation of R6G and the maximum surface plasmon absorption of spherical silver nanoparticles, it was found that 50-60 nm AgNP particles are of optimal size for maximizing SERS intensity when total Ag content is held constant. Based on the competing radiation damping for surface scattering and dynamic depolarization, as well as limited surface area for adsorption on larger AgNP, the plot with an optimal size for SERS of 50-60 nm is rationalized. Moreover, when a G-value is used to correct for limited adsorption of R6G on larger particles a linear relationship is obtained between SERS intensity and AgNP size that confirms theoretical predictions of increasing SERS intensity with increasing AgNP size.

3.1.5 Effect of Particle Shape on SERS

From the above discussion it is clear that particle size plays an important role in the intensity of Raman scattering, and the major factor to consider is the larger electromagnetic field (EMF) induced by larger particles. The shape of nanoparticles can have also have a dramatic effect on the intensity of the EMF as well. Not only does the shape of the particle affect the shape and magnitude of the EMF, but shape also affects the optical properties of the solution such that laser excitation might be absorbed more strongly by the particles resulting in a larger EMF.[16, 42, 43, 44]

In order to evaluate the effect of shape on the intensity of the Raman spectrum, various particle shapes made by the LED irradiation method described in Chapter 2 were used in combination with R6G in similar experiments to those for determining

the optimal size for SERS. Any attempts to calculate surface area of these samples, or to determine a G-value, would certainly be erroneous, especially in the case of Ag nanoplates, where there is a large polydispersity in particle size (only aspect ratio remains relatively constant). Solely based on surface area one would expect the Raman intensity of the seeds to be the highest, followed by decahedra and then plates. However, the story is further complicated due to the fact that Ag nanoplates have an appreciable absorbance for the laser wavelength (785 nm) and should, therefore, have a very high field enhancement effect. The raw data for the Raman scattering spectrum of R6G with AgNP seeds, decahedra and nanoplates are all shown in Figure 3.7.

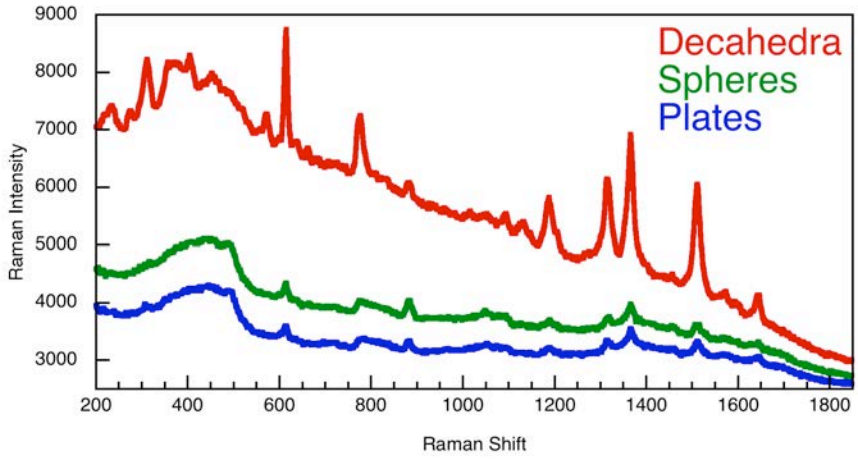

Figure 3.7: SERS spectrum of R6G recorded with AgNP seeds, triangular nanoplates and decahedra as indicated.

Based solely on the surface area, AgNP seeds should have the most intense Raman spectrum, or based solely on plasmon excitation, the nanoplates should have the most intense Raman spectrum, but neither of these are the case. It has been postulated that the decahedral AgNP have such high Raman enhancements due to the fact that they are multi-twinned particles. The vertices and twinning planes should have very high electromagnetic field enhancements, similar to what is observed for the points between aggregated particles.[45, 46] Therefore, the extreme electromagnetic field enhancement of decahedral AgNP makes them a very good substrate for SERS. SERS is often studied for particles deposited on a surface, since there are many advantages to making a sensor with the sensing unit immobilized (not colloidal). However, Pietrobon *et al.* briefly mention

that decahedra do not pack well as a film, which may lead to difficulty in maximizing these particles on surfaces.[45] However, they do provide a means to study the packing of pentagonal shapes on surfaces, which may be of interest in itself.

3.1.6 Conclusions

The SERS studies presented in this chapter provide an optimal size of AgNP spheres for enhancing the Raman signal of molecules. Raman is becoming a more important characterization technique due to the discovery of metal enhancement of Raman spectra, and Ag is the metal of choice, when stable, due to its superior optical and photophysical properties for enhancing Raman signals. Therefore, discovering the optimal size of AgNP for SERS constitutes a major contribution in the field. Also discussed in this chapter is a synthetic strategy that allows for the controlled synthesis of AgNP of different sizes, with a low polydispersity. High polydispersities are a common problem in nanoparticle synthesis, and this methodology makes many studies with narrow polydispersities in particle size possible.

Furthermore, several shapes of NP were tested for their enhancement of the Raman intensity for Rhodamine 6G and it was found that decahedra are a very strong SERS active substrate, even more so than spheres. It is expected that the combination of facile synthesis of decahedra presented in the previous chapter, and the strong enhancement provided by these particles, will make them an important substrate for studying SERS.

REFERENCES

[1] JR Ferraro, K Nakamoto, and CW Brown. *Introductory Raman Spectroscopy, 2nd Edition*. Accademic Press, 2003.

[2] M Albrecht and J Creighton. Anomalously intense raman spectra of pyridine at a silver electrode. *Journal of the American Chemical Society*, 99(15):5215–5217, 1977.

[3] P Johansson and M Käll. Surface-enhanced raman scattering and fluorescence near metal nanoparticles. *Physical Review B*, 72(3):035427, 2005.

[4] W Hill, B Wehling, CG Gibbs, CD Gutsche, and D Klockow. Detection of aromatics in aqueous-solution by surface-enhanced raman-scattering by substrates chemically-modified with p-tertbutylcalix-4-arenetetrathiol. *Analytical Chemistry*, 67(18):3187–3192, 1995.

[5] T Dadosh, J Sperling, G Bryant, R Breslow, T Shegai, M Dyshel, G Haran, and I Bar-Joseph. Plasmonic control of the shape of the Raman spectrum of a single molecule in a silver nanoparticle dimer. *ACS Nano*, 3(7):1988–1994, 2009.

[6] M Culha, M Kahraman, N Tokman, and G Tuerkoglu. Surface-enhanced Raman scattering on aggregates of silver nanoparticles with definite size. *Journal of Physical Chemistry C*, 112(28):10338–10343, 2008.

[7] R Aroca. *Surface-Enhanced Vibrational Spectroscopy*. Wiley, 2006.

[8] S Abalde-Cela, S Ho, B Rodríguez-González, M Correa-Duarte, R Alvarez-Puebla, L Liz-Marzán, and N Kotov. Loading of exponentially grown LBL films with Ag nanoparticles and their application to generalized SERS detection. *Angewandte Chemistry International Edition*, 121(29):5426–29, 2009.

[9] JR Lombardi, RL Birke, T Lu, and J Xu. Charge-transfer theory of surface enhanced raman spectroscopy: Herzberg-Teller contributions. *Journal of Chemical Physics*, 84(8):4174–4180, 1986.

[10] MA Mahmoud, CE Tabor, and MA El-Sayed. Surface-enhanced Raman scattering enhancement by aggregated silver nanocube monolayers assembled by the Langmuir-Blodgett technique at different surface pressures. *Journal of Physical Chemistry C*, 113(14):5493–5501, 2009.

[11] MM Maitani, DAA Ohlberg, Z Li, DL Allara, DR Stewart, and RS Williams. Study of sers chemical enhancement factors using buffer layer assisted growth of metal nanoparticles on self-assembled monolayers. *Journal of the American Chemical Society*, 131(18):6310–6311, 2009.

[12] AM Michaels, J Jiang, and L Brus. Ag nanocrystal junctions as the site for surface-enhanced Raman scattering of single rhodamine 6G molecules. *Journal of Physical Chemistry B*, 104(50):11965–11971, 2000.

[13] AC Sant'Ana, TCR Rocha, PS Santos, D Zanchet, and MLA Temperini. Size-dependent SERS enhancement of colloidal silver nanoplates: the case of 2-amino-5-nitropyridine. *Journal of Raman Spectroscopy*, 40(2):183–190, 2009.

[14] X Tian, K Chen, and G Cao. Seedless, surfactantless photoreduction synthesis of silver nanoplates. *Materials Letters*, 60(6):828–830, 2006.

[15] X Zou and S Dong. Surface-enhanced Raman scattering studies on aggregated silver nanoplates in aqueous solution. *Journal of Physical Chemistry B*, 110(43), 2006.

[16] KL Kelly, E Coronado, LL Zhao, and GC Schatz. The optical properties of metal nanoparticles: The influence of size, shape, and dielectric environment. *Journal of Physical Chemistry B*, 107:668–677, 2003.

[17] M Quinten. The color of finely dispersed nanoparticles. *Applied Physics B: Lasers and Optics*, 73(4):317–326, 2001.

[18] SM Morton and L Jensen. Understanding the molecule-surface chemical coupling in SERS. *Journal of the American Chemical Society*, 131(11):4090–4098, 2009.

[19] V Pustovit and T Shahbazyan. SERS from molecules adsorbed on small Ag nanoparticles: A microscopic model. *Chemical Physics Letters*, 420(4-6):469–473, 2005.

[20] SA Maier. *Plasmonics: Fundamentals and Applications; 1st Edition*. Springer, New York, 2006.

[21] XL Li, WQ Xu, JH Zhang, HY Jia, B Yang, B Zhao, BF Li, and Y Ozaki. Self-assembled metal colloid films: Two approaches for preparing new SERS active substrates. *Langmuir*, 20(4):1298–1304, 2004.

[22] O Siiman, LA Bumm, R Callaghan, CG Blatchford, and M Kerker. Surface-enhanced raman-scattering by citrate on colloidal silver. *Journal of Physical Chemistry*, 87(6):1014–1023, 1983.

[23] NR Jana, L Gearheart, and CJ Murphy. Evidence for seed-mediated nucleation in the chemical reduction of gold salts to gold nanoparticles. *Chemistry of Materials*, 13(7):2313–2322, 2001.

[24] H Borsook and G Keighley. The energy of urea synthesis. ii. the effect of varying hydrogen ion concentration with different metabolites. *Proceedings of the National Accademy of Science: Physiology*, 19(7):720–725, 1933.

[25] DR Lide. *CRC Handbook of Chemistry and Physics; 90th Edition*. National Institute for Standards and Technology, 2010.

[26] KG Stamplecoskie and JC Scaiano. Light emitting diode irradiation can control the morphology and optical properties of silver nanoparticles. *Journal of the American Chemical Society*, 132(6):1825–7, 2010.

[27] CS Seney, BM Gutzman, and RH Goddard. Correlation of size and surface-enhanced Raman scattering activity of optical and spectroscopic properties for silver nanoparticles. *Journal of Physical Chemistry C*, 113(1):74–80, 2009.

[28] I Pastoriza-Santos and LM Liz-Marzan. Colloidal silver nanoplates. state of the art and future challenges. *Journal of Materials Chemistry*, 18(15):1724–1737, 2008.

[29] VS Tiwari, T Oleg, GK Darbha, W Hardy, JP Singh, and PC Ray. Non-resonance SERS effects of silver colloids with different shapes. *Chemical Physics Letters*, 446(1-3):77–82, 2007.

[30] R Sasai, T Fujita, N Iyi, H Itoh, and K Takagi. Aggregated structures of rhodamine 6G intercalated in a fluor-taeniolite thin film. *Langmuir*, 18(17), 2002.

[31] Y Maruyama and M Futamata. Anion induced SERS activation and quenching for R6G adsorbed on Ag nanoparticles. *Chemical Physics Letters*, 448(1-3):93–98, 2007.

[32] Y Maruyama, Mitsuru Ishikawa, and M Futamata. Single molecule detection with SERS. *Analytical Sciences*, 17, 2001.

[33] A Kudelski. Raman studies of rhodamine 6G and crystal violet sub-monolayers on electrochemically roughened silver substrates: Do dye molecules adsorb preferentially on highly SERS-active sites? *Chemical Physics Letters*, 414(4-6):271–275, 2005.

[34] C Caro, C López-Cartes, P Zaderenko, and JA Mejías. Thiol-immobilized silver nanoparticle aggregate films for surface enhanced raman scattering. *Journal Raman Spectroscopy*, 39(9):1162–1169, 2008.

[35] J Guthmuller and B Champagne. Resonance raman scattering of rhodamine 6G as calculated by time-dependent density functional theory: Vibronic and solvent effects. *Journal of Physical Chemistry A*, 112(14):3215–3223, 2008.

[36] H Watanabe, N Hayazawa, Y Inouye, and S Kawata. Dft vibrational calculations of rhodamine 6G adsorbed on silver: Analysis of tip-enhanced Raman spectroscopy. *Journal of Physical Chemistry B*, 109(11), 2005.

[37] K Tanabe. Field enhancement around metal nanoparticles and nanoshells: A systematic investigation. *Journal of Physical Chemistry C*, 112(40):15721–15728, 2008.

[38] P Fang, J Li, Z Yang, L Li, and B Ren. Optimization of SERS activities of gold nanoparticles and gold-corepalladium-shell nanoparticles by controlling size and shell thickness. *Journal of Raman Spectroscopy*, 39(11):1679–1687, 2008.

[39] M Meier and A Wokaun. Enhanced fields on large metal particles - dynamic depolarization. *Optics Letters*, 8(11):581–583, 1983.

[40] AD McFarland, MA Young, JA Dieringer, and RP Van Duyne. Wavelength-scanned surface-enhanced Raman excitation spectroscopy. *Journal of Physical Chemistry B*, 109(22):11279–11285, 2005.

[41] T Deckert-Gaudig, F Erver, and V Deckert. Transparent silver microcrystals: Synthesis and application for nanoscale analysis. *Langmuir*, 25(11):6032–6034, 2009.

[42] NI Cade, T Ritman-Meer, KA Kwakwa, and D Richards. The plasmonic engineering of metal nanoparticles for enhanced fluorescence and Raman scattering. *Nanotechnology*, 20(28):285201, 2009.

[43] R Alvarez-Puebla and R Aroca. Synthesis of silver nanoparticles with controllable surface charge and their application to surface-enhanced Raman scattering. *Analytical Chemistry*, 81(6):2280–2285, 2009.

[44] ZQ Tian, ZL Yang, B Ren, JF Li, Y Zhang, XF Lin, JW Hu, and DY Wu. Surface-enhanced Raman scattering from transition metals with special surface morphology and nanoparticle shape. *Faraday Discussions*, 132:159–170, 2006.

[45] B Pietrobon and V Kitaev. Photochemical synthesis of monodisperse size-controlled silver decahedral nanoparticles and their remarkable optical properties. *Chemistry of Materials*, 20:5186–5190, 2008.

[46] W Li, PHC Camargo, L Au, Q Zhang, M Rycenga, and Y Xia. Etching and dimerization: A simple and versatile route to dimers of silver nanospheres with a range of sizes. *Angewandte Chemistry International Edition*, 49(1):164–168, 2009.

Chapter 4

Biocompatible Silver Nanoparticles and Antibacterial Study

4.1 Biological Applications of AgNP

Over the last two decades, metal nanoparticles have attracted a great deal of interest for biomedical applications as well as a wide variety of applications in the areas of catalysis, imaging, DNA-detection, and material engineering.[1, 2, 3, 4, 5] The uses of silver as an antibacterial agent date back to times when the ancient Romans and Phoenicians stored drinking water in silver containers for years.[6] Silver for many years was the primary antibacterial agent used in used medicine in the form of aqueous $AgNO_3$, and is still used today, administered as eye drops for newborn babies to prevent bacterial infections in babies eyes or as a cream on drops to lesions.[7, 6] Silver nanoparticles have been incorporated into a wide range of commercial products like bedding, underwear, bandages, toothpaste, shampoo, deodorants, paints, toys, a pair of socks Professor Scaiano received for Christmas, etc... and all for the antibacterial properties.[8] What may be most interesting about the medical applications of silver is that, for so many years it has been used without a clear understanding of the mechanism of antibacterial activity. What is known is that it is a broad spectrum antibacterial agent, that is effective against greater than 650 strains of viruses and bacteria. The activity has been attributed to the ability of silver ions to chelate proteins and affect their biological functions, but it has been postulated as well that the nanoparticles themselves can interact with proteins that normally assist in antioxidant activity, and when rendered inactive result in high levels of reactive oxygen species.[9, 10, 8] There are also claims that AgNP can be taken

up through endocytosis by bacteria, which then contributes in a different way (either by silver nanoparticle reactivity or the "trojan horse" effect of up-taking other detrimental material during endocytosis) than simply uptake of Ag^+ ions, to kill bacteria.[11] While it is clear that studying the mechanism and maximizing the efficacy of AgNP is important, a note of caution arises as well. If the antibacterial activity of silver comes from depressing the ability of bacteria to eliminate reactive oxygen species, the same effects may be possible in healthy cells. Therefore, it is important to not only evaluate the antibacterial activity of silver nanoparticles but concurrently investigate the possible cytotoxicity as well.

When evaluating the potential applications of metal nanomaterials in-vivo, it is essential to determine their stability under physiological conditions. Thus, several articles have focused on the development and/or post-synthesis stabilization of biocompatible metallic nanoparticles.[12, 13, 14, 15] The synthesis protocol for many of these materials frequently requires harsh conditions that not only decrease the overall particle yield, but more importantly, fail to ensure metal surface protection.[16, 17]

Some examples regarding the design of metallic nanoparticles stabilized with proteins have been documented in the literature.[18, 17, 19] Eby *et al.*[19], for instance, have recently prepared silver nanoparticles (AgNP) functionalized with lysozyme that exhibit potent antimicrobial activity. Further, Murawala et al.[17] have synthesized AgNP protected with bovine serum albumin (BSA) where the BSA itself functions as the reducing agent leading to an undesired protein oxidation. Additional reports have also documented that BSA is able to interact with AgNP electrostatically[20, 21, 22] affecting the binding capacity of the protein with small molecules.[22] However, there have been no reports on human serum albumin (HSA) and whether it behaves similarly to BSA. HSA is the most abundant protein in the human plasma where it can reach concentrations up to 0.6 mM,[23] and binds a large variety of small molecules and ions.[24, 25, 26, 23, 27, 28, 29, 30, 31] It has also been shown that HSA can effectively interact with quantum dots and gold nanoparticles (AuNP).[32, 18]

Despite the progress made, it remains unclear to what extent the nanoparticle presence changes protein conformation and/or the enzymatic activity. Thus, Bretschneider et al.[33] have synthesized AuNP anchored to horseradish peroxidase and studied the effect of surface plasmon band (SPB) excitation on enzymatic activity. SPB excitation also provides an efficient conversion of light-to-heat that can transfer heat to the microenvironment directly around nanoparticles.[34, 35] This local heating can promote partial protein denaturation or changes in its conformation as reported for small peptides.[36]

In fact, there is a range of mechanisms by which SPB excitation can lead to physical or chemical consequences beyond the aim of the present work.[37, 38] For protein/metallic nanoparticles hybrids, Holland et al.[39] recently prepared and characterized a biometallic glucose oxidase/AuNP composite where a reduction of the apparent catalytic activity of the enzyme and its KM was observed. In particular, Silver nanoparticles (AgNP) have been explored in Surface Enhanced Raman Scattering (SERS), catalysis, antibacterial activity, and biomedical applications.[40, 41, 42, 43, 44, 45, 46, 47, 16]

More specifically, we have recently observed that AgNP are unstable under physiological conditions due, to some extent, to the large ionic strength, which modifies the particle formal charge.[31] This has not been a barrier for exploring the in-vitro toxicity and antibacterial activity of AgNP.[41, 16] In the present study, we have employed HSA as model for exploring how proteins interact with AgNP. By manipulating the biomacromolecule conformation, and/or selectively blocking NH_2 groups we have shown that there is a combination of several non-covalent electrostatic interactions involved in such phenomenon, where NH_2 residues play a key role in the observed post-stabilization and synthesis of AgNP. We also explore to what extent SPB excitation with 405 nm LED can affect the protein conformation in the HSA@AgNP hybrid.

4.1.1 Synthesis of Biocompatible AgNP

In order to assess the antibacterial activity of silver nanoparticles the stability of the particles was first evaluated in biological media. Unfortunately, AgNP seeds stabilized by citrate (as described in Chapter 2) were found to be unstable in buffer solutions or even with low salt concentrations. Therefore, in order to access the antibacterial activity of AgNP our aim was to develop AgNP with high biocompatibility while retaining potent antimicrobial properties using a robust biocompatible matrix as protecting agent. To stabilize AgNP using type I collagen, the most abundant protein found in the human body, would be a significant achievement, since it was previously demonstrated the capacity for collagen-based hydrogels to regenerate corneal tissues and nerves in animal models [48] and, most recently, in clinical trials.[49] In cases of bacterial or viral keratitis in the eye or ulcerated skin, an effective anti-microbial or anti-viral agent, such as AgNP, that shows biocompatibility and capacity to induce regeneration would be of great benefit [9, 50, 51, 52, 53]. Therefore, we studied the photochemical synthesis, characterization, in vitro biocompatibility and anti-bacterial performance of collagen-coated AgNP as a potential anti-microbial agent. For comparison, we also examined α-polylysine and cit-

rate stabilizers, as well as ionic silver. The motivation for trying both collagen and PLL stabilized AgNP was that, under these conditions, PLL forms random coils while collagen is a structured protein, which may have an affect on the stabilization of the particles.

Experimental

The silver nanoparticles stabilized by collagen and polylysine were made by the same method as citrate stabilized AgNP seeds, but only replacing the citrate with varying concentrations of collagen or α-polylysine, respectively. The UV-Vis spectrum for each of collagen and poly-L-lisine stabilized AgNP are shown in Figure 4.1 made by 15 min of UVA irradiation of I-2959 (0.2 mM), $AgNO_3$ (0.2 mM) and varying concentrations of stabilizing agents as indicated. Further experimental details on zeta potential measurements and biocompatibility and cell toxicity are omitted from this section because I was not directly involved in the measurements.

Results and Discussion

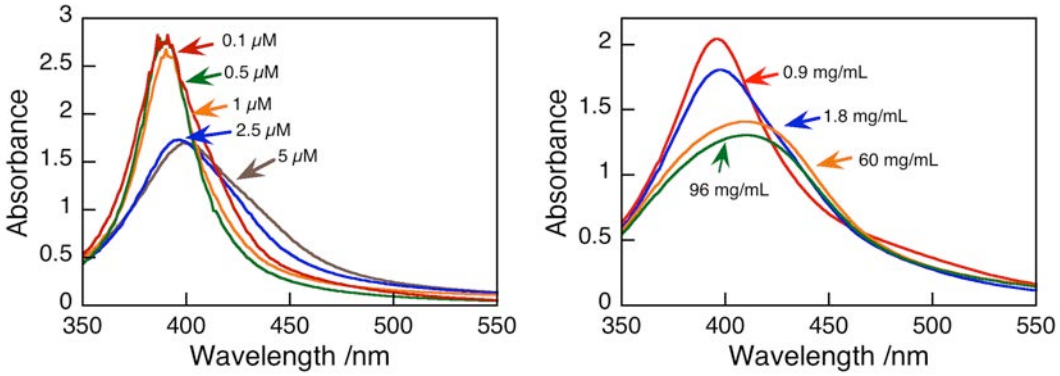

Figure 4.1: UV-Vis absorption spectrum of colloidal AgNP stabilized by collagen(left) and poly-L-lysine.

One interesting thing to note about the nanoparticles functionalized by both of these agents is that, higher concentrations of stabilizing agents result in lower yield of nanoparticles, or at least a broader longer wavelength absorbance. We believe that this is due to competitive reactions of the collagen and poly-L-lysine with ketyl radical photoproduct from I-2959, though these photoproducts do not oxidize the proteins. The competing

reactions slow down the rate of formation of reduced silver (Ag^0), which gives a slower rate of nanoparticle formation and larger particle sizes (confirmed by SEM).[31]

Aside from monitoring a loss in plasmon absorption, another common way to assess the stability of nanoparticles is to measure the zeta potential (ζ). Colloids can be stabilized in two ways; (1) by an electrostatic repulsion in the form of a double electric layer, or (2) by steric interactions whereby surface bound species provide a layer on particles such that floculation and aggregation can not occur. In aqueous systems it is most common to stabilize particles by electrostatic interactions, often provided by surface bound ionizable species such as -COOH, -SO_4Na etc... The particles themselves are often partially positively charged, which is balanced by the negative charged stabilizing agents bound to the particle surface. Very close to the surface particles are tightly bound, and farther from the surface they are more easily exchanged. An example of the distribution of ions is shown in Figure 4.2, which describes the layer of charges that surround a particle as it moves in solution. The boundary between solution and the region where ions "follow" a charged particle in solution is called the 'slip plane', and this is where the zeta potential is measured. The radius for the sphere bound by this slip plane is referred to as the hydrodynamic radius of the particles. For long term particle stability under these conditions (no aggregation) the electrostatic repulsion is such that the electrostatic repulsion energy (G_max) must be much greater than the thermal energy (kT) of the particles, or in other words, a ($G_max > 25kT$) which means a ζ of $> \pm$ 40 mV is required.[54] It has been shown experimentally however that greater than $\zeta\pm$ 30 mV can be sufficient for good short term (non infinite) nanoparticle stability.[55] Others still have reported that greater than only $\zeta\pm$ 20 mV is sufficient for nanoparticle stability, which is something that we have observed here and in other works as well.[56, 57]

Therefore, to assess the stability of the nanoparticles stabilized by both collagen and poly-L-lysine, the ζ was measured for various concentration of stabilizing agent and compared with that of citrate as a reference. Since both collagen and poly-L-lysine are positively charged stabilizing agents, the zeta potential for particles stabilized by these agents is positive. The zeta potentials for various concentrations of stabilizing agents are shown in Figure 4.3. As expected, citrate stabilized AgNP seeds show a very negative value (ζ = -40 mV), due to the negative charges of the carboxylate groups on citrate. However, collagen and poly-L-lysine are both positively charged stabilizing agents, and for this reason give the positive ζ-potentials in Figure 4.3. Nanoparticles stabilized with collagen are stable for all concentrations used, but for poly-L-lysine, concentrations less than 30 μM are unstable, which was corroborated by the low absolute value of the

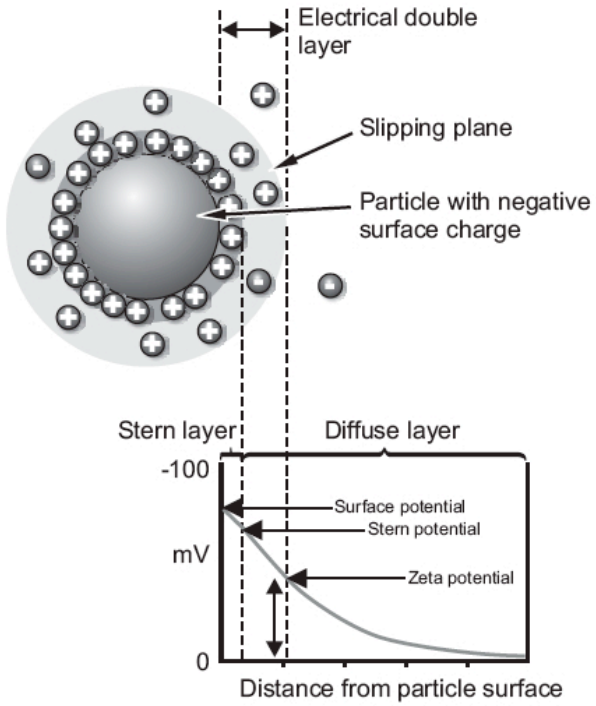

Figure 4.2: Schematic illustration of the double electric layer, and the position at which the zeta potential is measured.[55]

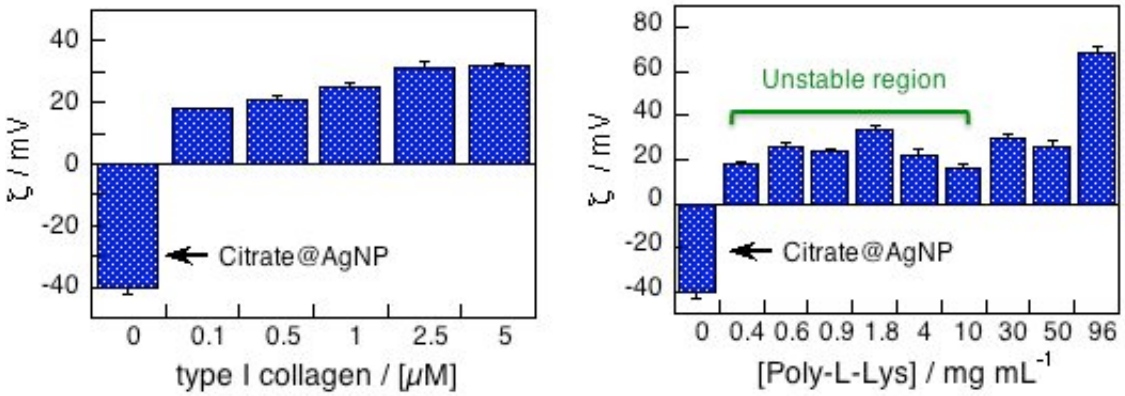

Figure 4.3: Zeta-potential measurements for nanoparticles stabilized by varied concentrations of collagen (left) and poly-L-lysine (right) as indicated.

measured ζ-potentials for these particles.

The particles described above have good long term stability as synthesized, but the stability under biological conditions is what needs to be evaluated. For this reason the stability of the different AgNP stabilized with citrate, poly-L-lysine and collagen were evaluated at different nanoparticle concentrations in Dulbecco's modified Eagle's medium (DMEM) buffer. DMEM buffer is simply a buffer solution contain high vitamin and glucose levels that can be used with a broad range of cells. Albumin helps to confer stability to the colloids, and was therefore also added to stabilize colloids that were otherwise unstable in DMEM buffer. The plasmon band maximum intensity is used to evaluate stability of the nanoparticles, and what is plotted in Figure 4.4 is the plasmon band intensity maximum where the error bars indicate six replicate experiments. Red asterisks indicate a color change from yellow to orange, which is also indicative of nanoparticle aggregation (instability).

Of note is that without serum albumin with citrate and poly-L-lysine these particles quickly aggregate, and are therefore not easily incorporated for antibacterial measurements. For poly-L-lysine, particle stability is not even achieved until relatively high concentrations of serum albumin are added $\geqslant$2.5 %. Only the collagen stabilized particles showed good stability in the DMEM buffer without the addition of albumin.

The application of nanoparticles in artificial skin matrices is of particular interest to the Scaiano group, an ongoing collaboration with the Griffith group in Sweden. For this reason, keratinocyte serum was also used in order to evaluate particle stability under these conditions. The results are shown in Figure 4.5, and again the only particles that displayed broad stability were the collagen stabilized colloids.

4.1.2 Antibacterial Activity of AgNP

With the above understanding of colloid stability, the particle antibacterial properties could be tested under conditions where the colloids are stable. Three bacterial species were chosen in order to assess the antibacterial activity of AgNP composites. They are representative of sporulating and non-sporulating gram positive bacteria (B.megaterium and S.epidermidis, respectively) as well as the pathogenic gram negative enteric bacterial strain of E.coli, CFT073. Testing for growth inhibition by the broth-microdilution minimum inhibitory concentration (MIC) assay, we observed that for each bacterium, mM concentrations of total silver were at least as growth inhibitory as $AgNO_3$ controls. This was the case for both poly-L-lysine and collagen stabilized nanoparticles although

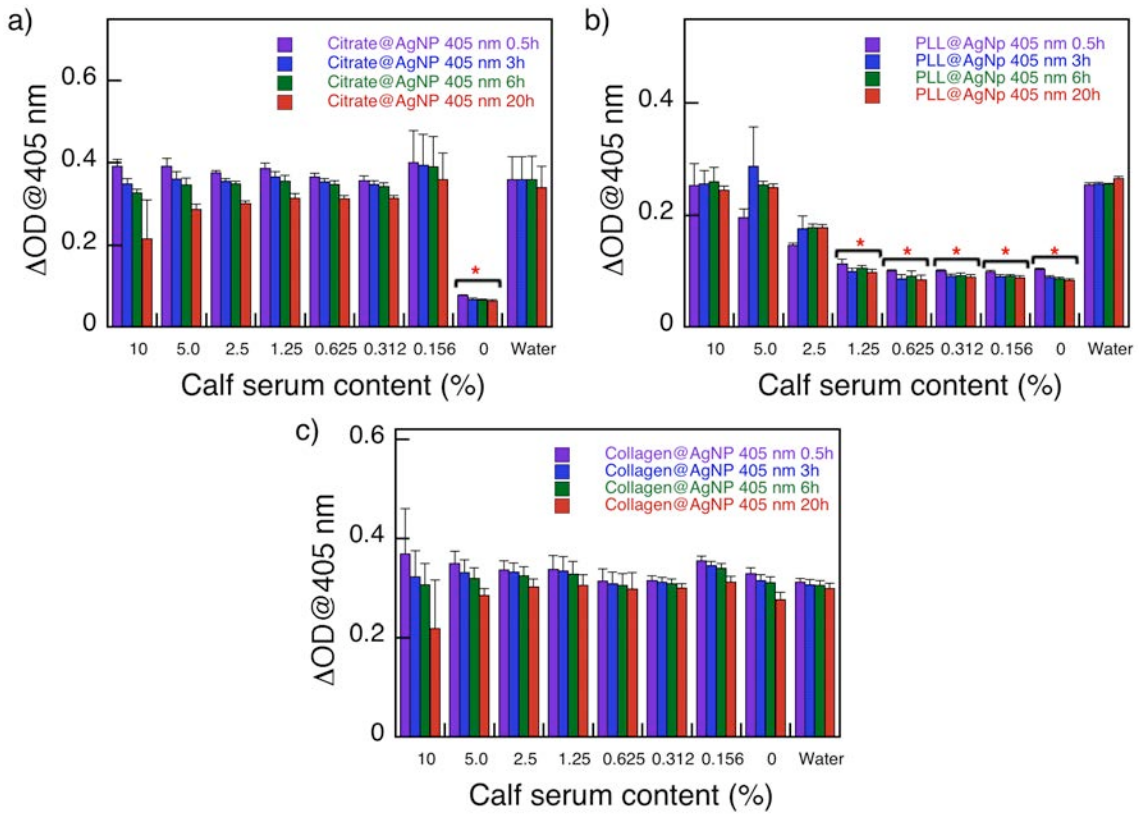

Figure 4.4: Plasmon band maximum as a measure of colloid stability in DMEM buffer with serum albumin as indicated, for AgNP stabilized by citrate, poly-L-Lysine and collagen.

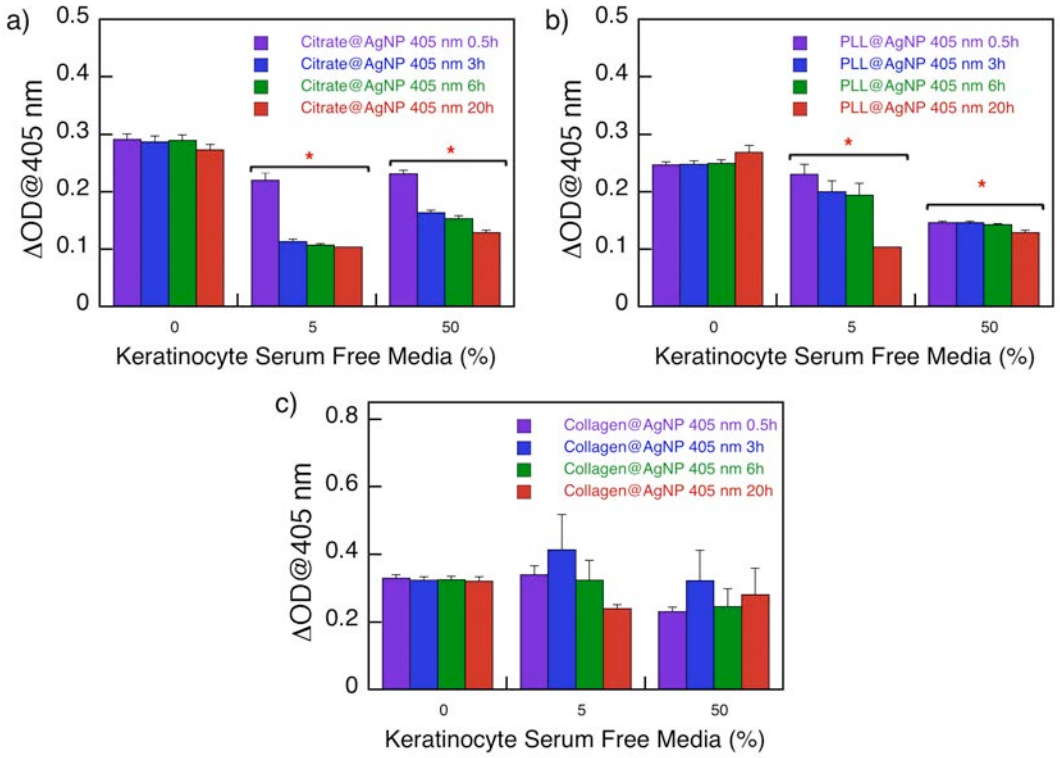

Figure 4.5: Plasmon band maximum as a measure of colloid stability with added keratinocyte serum, for AgNP stabilized by citrate, poly-L-Lysine and collagen.

in the former, the conjugate molecule alone was as anti-microbial as the conjugated one. Notably only collagen-based composites do not aggregate in this series as well, pointing again to the superior stability of these particles. MIC assay was carried out according to CLSI broth microdilution protocol.[58]

Notably, the AgNP in their conjugated form were at least as effective as $AgNO_3$ at inhibiting the growth of the bacteria tested. This data is supported in growth inhibition assays carried out in 96-well plates and summarized in Figure 4.6, which shows that the collagen-based silver nanocomposite (at 1.0 mM in collagen) has an improved activity with increasing lag time for bacterium growth at much lower concentrations than those employed for either citrate stabilized AgNP or ionic silver as $AgNO_3$; similar trends were observed for the other two AgNP stabilized by collagen formulations (data not shown) confirming that collagen is more than a simple stabilizing agent for these nanocomposites.

MICs and growth inhibition experiments alone cannot differentiate between bactericidal and bacteriostatic activity, otherwise discernible under time-kill conditions.[59, 60] Further, there is a profound bacterial cell density related effect on the efficacy of most antibiotics, at the very least for staphylococci.[61] Thus, short-term (3 h) time-killing studies were performed for both the collagen-conjugated nanoparticles and for poly-L-lysine stabilized AgNP. Each species was tested at low density ($\sim 10^5$ cfu ml^{-1}), with 1x and 2x MIC concentrations of each of the materials. These results are shown in Figure 4.7 for B. megaterium, E. coli and S. epidermidis respectively, and are an average of three repetitions. For B. megaterium and E. coli, there is a net decline in cell density as a result of exposure to 1x and 2x MIC concentrations for 1.0 μM collagen-conjugated NP. For $AgNO_3$ only for E.coli a net decline in the bacteria population was observed (see Figure 4.7 H). In the case of S.epidermidis however, no significant decline was observed in cell density during the course of the assay and the AgNP as well as $AgNO_3$ are effectively bacteriostatic (right column of Figure 4.7).

Based on the kinetics of killing, B.megaterium is more susceptible to the 1.0 μM (Figure 4.7 A) and 2.5 μM collagen-conjugated AgNP than to equivalent concentrations of the positive control. Importantly, this contrasts with the growth inhibition results where 0.5 and 1.0 μM concentrations inhibited more growth than 2.5 μM collagen stabilized AgNP at equivalent concentrations. The reason for this is unclear, although differential killing efficacy has been observed in several cases of quinolone and fluoroquinolone antibiotics.[61, 62] However, as reduced sensitivity is noted for the 0.5 μM collagen-conjugated NP in the time-killing assay, collagen is implicated in either stabilization of, or otherwise increasing the efficacy of the nanoparticles. This view is supported by the

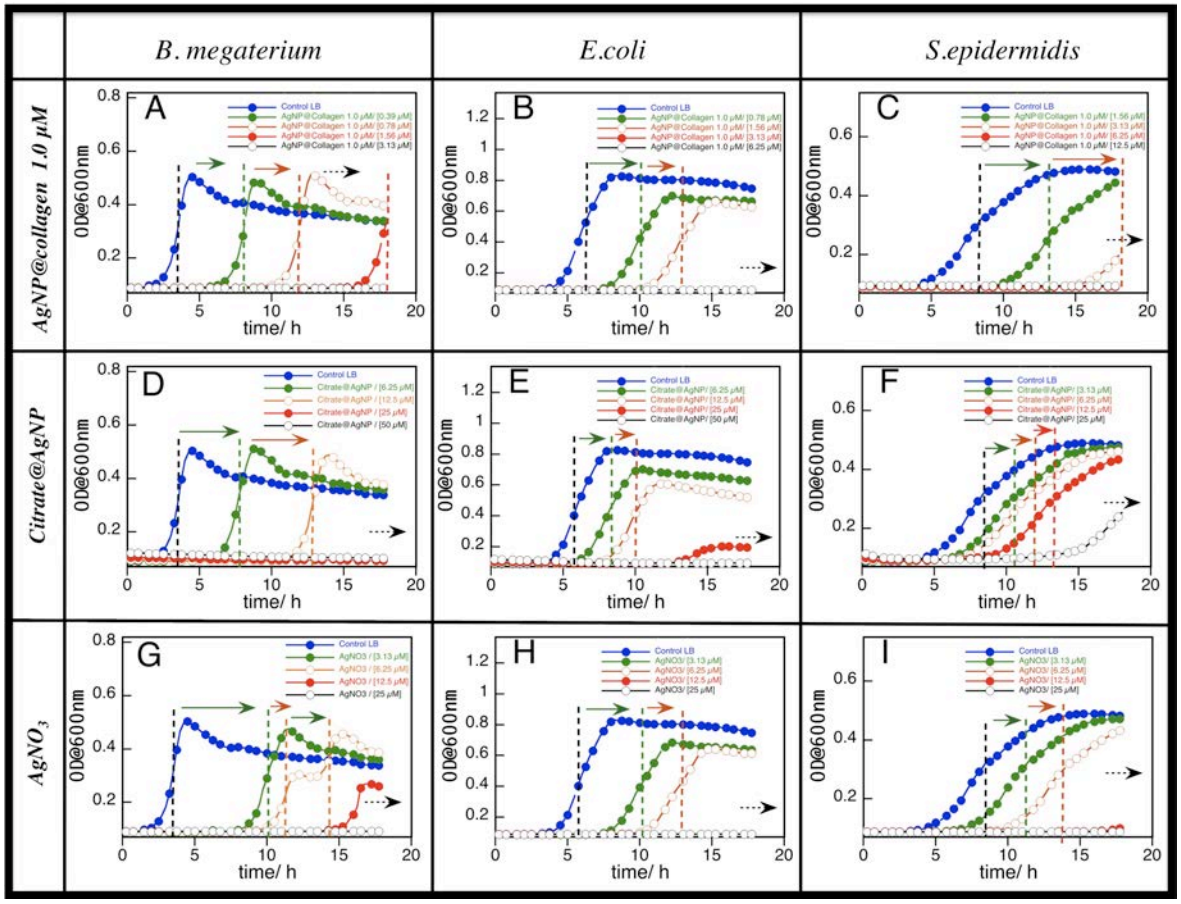

Figure 4.6: Bacteria colony growth inhibition study with different silver species as inhibitors as indicated.

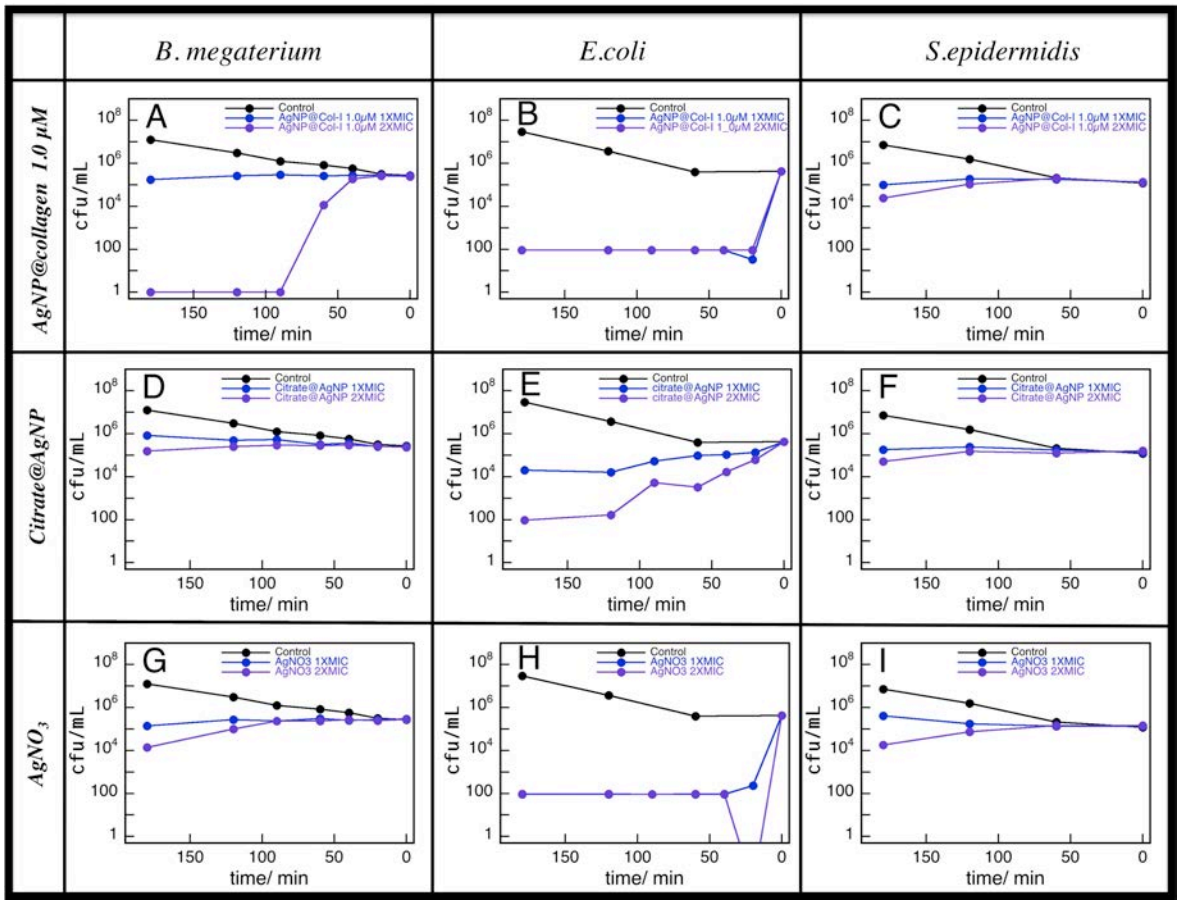

Figure 4.7: Bacteria time-kill profiles for B. megaterium (left column), E.coli (middle column), and S.epidermidis (right column) up to 180 min in the presence of collagen stabilized AgNP 1.0 mM (A-C), citrate stabilized AgNP (D-F), and $AgNO_3$ (GeI) at either 1xMIC or 2xMIC

.

observation that citrate stabilized AgNP (these particles aggregated spontaneously in the cell culture medium) are consistently more similar to the $AgNO_3$ (Figure 4.7 D-G) controls than the conjugated nanoparticles. Consistent with the noted differential efficacies of antibiotics, a different scenario is observed for E.coli: Firstly, collagen nanocomposites are all notably more bactericidal at this concentration (Figure 4.7 B) than citrate stabilized AgNP (which are aggregated); citrate stabilized particles are only slightly bactericidal at 1x MIC (Figure 4.7 E) while ionic silver as $AgNO_3$ is highly effective at these concentrations (see Figure 4.7 H). Differences between the two conjugated nanoparti-

cles are not discernible as the bacterial culture is rapidly cleared at 1x and 2x MIC. No significant difference is noted between the observed killing profiles for all collagen nanocomposites within the time frame of the assay, 3 h. Lastly, S.epidermidis susceptibility was primarily bacteriostatic at the concentrations tested (right column Figure 4.7).

Insignificant differences in time-kill bactericidal were observed between the activity of the AgNP, Ag^+ and even poly-L-lysine stabilized AgNP. Note that for all bacteria, the poly-L-lysine stabilized NP and poly-L-lysine alone controls were equivalently inhibitory to growth implying that the bactericidal efficacy of such conjugated NP was mostly dependent on the conjugant. Additionally, in order to explore AgNP activity in semisolid state, we assessed their efficacy on bacterial populations embedded in 1% agarose as previously described in the testing of anti-microbial peptides.[63] These studies were inconclusive as no apparent inhibition zones were observed in any of the test cases, whether Ag^+ or conjugated/unconjugated AgNP were used. Thus, our anti-microbial cumulative data point to the efficacy of AgNP being strongly affected by conjugation as showed for silver nanoparticles conjugated to type I collagen, where the macromolecule may be the source of improved efficacy compared to the seed AgNP.

4.1.3 Cytotoxicity Studies of AgNP

Incubation of various NP samples in cell-free media showed that 10% FCS in DMEM prevented the aggregation of poly-L-lysine and citrate stabilized AgNP, while collagen stabilized AgNP showed no serum-dependent response since they were stable regardless, consistent with incorporation of AgNP the collagen protein. Further, in KSFM, either citrate or poly-L-lysine protected AgNP spontaneously aggregate (see Figures 4.4 and 4.5). Only collagen stabilized AgNP nanocomposites were stable under the same conditions. Thus, in order to evaluate the biocompatibility and potential cytotoxicity of our materials, their toxicity in human serum fibroblasts (only data obtained using 10% FCS has been included here) and serum keratinocytes (grown in free FCS media) were evaluated using the MTS assay. Non-toxicity for I-2959 (photoinitiator) or 4-HEBA (photoproduct) was established in all cell-cultured lines employed here (see Figure 4.8 A-B). $AgNO_3$, however, was shown to be toxic at dilution factors lower than 4 and 2 for fibroblasts and keratinocytes, respectively. Additionally, poly-L-lysine appear to be equipotent cytotoxic than their respective poly-L-lysine stabilized AgNP at dilutions lower than 8, suggesting that these nanoparticle composites are not ideal for antibacterial studies.[31]

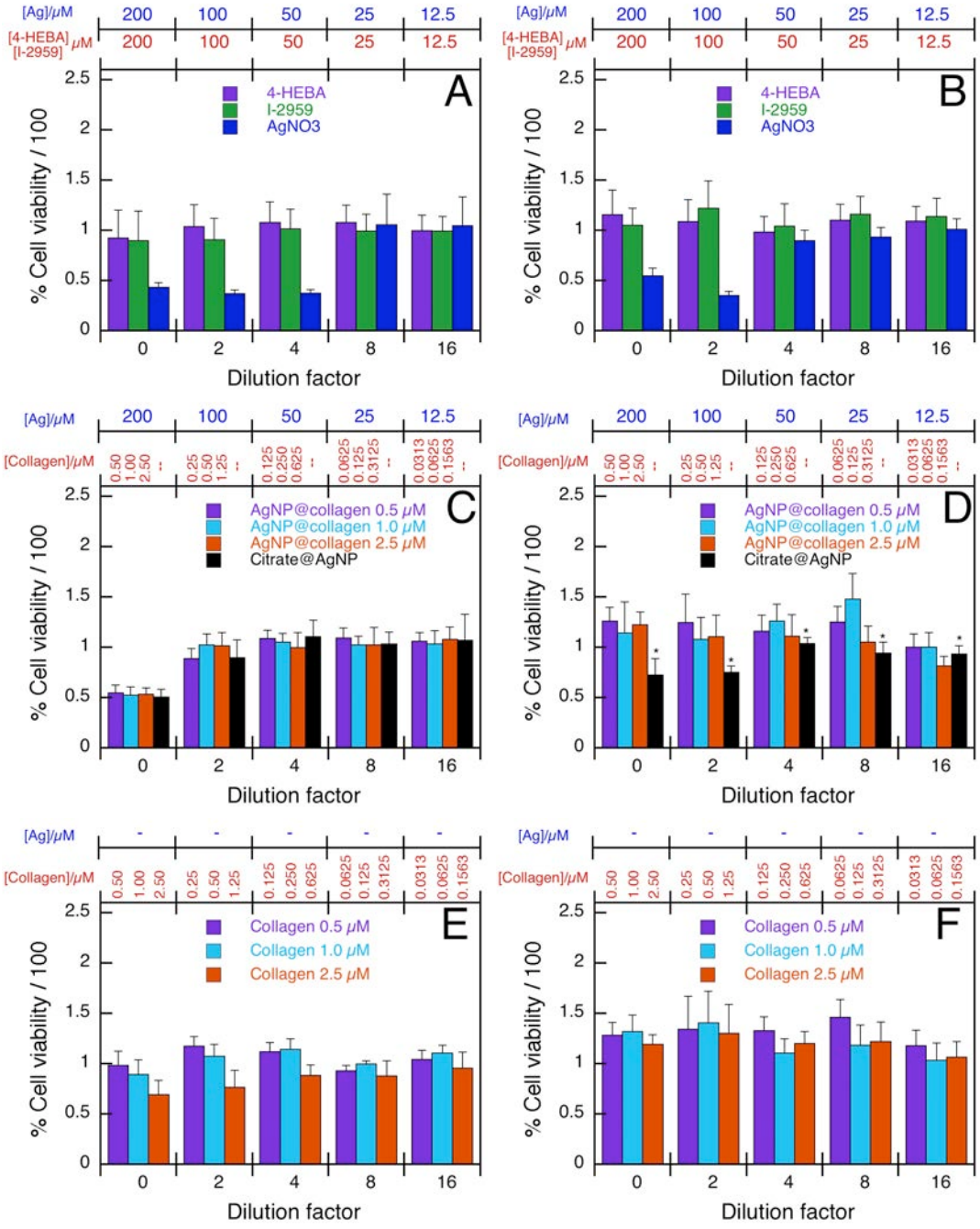

Figure 4.8: Cell viability measurements carried out by using MTS colorimetric assay (see experimental section) of human fibroblasts (left column) and human keratinocytes (right column) after 14 h incubation (A, B) in the presence of different concentrations of 4-HEBA, I-2959, and $AgNO_3$; (C, D) collagen AgNP prepared by using 0.5, 1.0, and 2.5 mM collagen or citrate/AgNP; and finally (F, E) type I collagen alone cytotoxicity at different concentrations (0.5, 1.0, and 2.5 mM).

Human keratinocytes were affected by these compounds as depicted in Figure 4.8, right column. In addition, mostly independently of the cell line employed here, low toxicity was detected at dilutions higher than 2.0 when collagen/AgNP (Figure 4.8 C and D) or type I collagen alone as shown in Figure 4.8 E and F. Citrate/AgNP seem to be more toxic for human keratinocytes (Figure 4.8D). No direct comparison between the toxicity observed in keratinocytes and fibroblasts by citrate/AgNP, can be concluded with any certainty by the data here since these particles spontaneously aggregate in keratinocytes culture medium (Figure 4.8 D). More interestingly, $AgNO_3$ toxicity only resembles toxicity of citrate/AgNP if they are aggregated as shown in Figure 4.8C and D. This may be an important discovery, as the toxicity of AgNP and their stability as well as the understanding of cell nanoparticle interaction comes into question here, specifically when comparing two different nanomaterials. Thus, in addition to the completely different nature of both cell lines (metabolism, cell membrane, and morphology) the aggregation state and stability of the biomaterial needs to be considered i.e. only for AgNP/collagen are the particles stable in all media tested.

4.1.4 Conclusions

Overall, both poly-L-lysine and collagen stabilized particles were synthesized as two new silver nanoparticle materials with potential biological applications. The stability of these particles in common cell culture media was assessed as well as the antibacterial properties and cytotoxicity of the nanoparticle composites. Only collagen stabilized AgNP showed all of the desired properties including broad stability in all media tested as well high antibacterial activity while displaying no observable cytotoxicity towards fibroblasts or karotinocytes. This is a very encouraging result for the possible implementation of AgNP stabilized by collagen for medical applications. These composites are currently being studied as an additive to artificial skin matrices in order to increase the success of artificial skin for patients with chronic skin lesions.

While my role in this project was limited to synthesizing stable particles for biocompatible media, it was rewarding to be involved in this project. The most important contribution from this work is that these particles are the first that we have seen that are better antibacterial agents with respect to total silver content (based on minimum inhibitory concentration), than silver salt ($AgNO_3$), while remaining non-toxic to cells.

REFERENCES

[1] DK Chatterljee, LS Fong, and Y Zhang. Nanoparticles in photodynamic therapy: an emerging paradigm. *Advanced Drug Delivery Reviews*, 60(15):1627–1637, 2008.

[2] SF Elswaifi, KS Hockey JR Palmieri Jr, and BA Rzigalinski. Antioxidant nanoparticles for control of infectious disease. *Infectious Disord Drug Targets*, 9(4):445–452, 2009.

[3] S Wadhwa, R Paliwal, SR Paliwal, and SP Vyas. Nanocarriers in ocular drug delivery: an update review. *Current Pharmaceutical Dessign*, 15(23):2724–2750, 2009.

[4] A Corma and H Garcia. Supported gold nanoparticles as catalysts for organic reactions. *Chemical Society Reviews*, 37(9):2096–2126, 2008.

[5] C Burda, X Chen, R Narayanan, and MA El-Sayed. Chemistry and properties of nanocrystals of different shapes. *Chemical Reviews*, 105(4):1025–1102, 2005.

[6] JW Alexander. History of the medical use of silver. *Surgical Infections*, 10(3):289–292, 2009.

[7] HJ Klasen. Historical review of the use of silver in the treatment of burns. i. early uses. *Burns*, 26(2):117–130, 2000.

[8] AM Schrand, MF Rahman, SM Hussain, JJ Schlager, DA Smith, and AF Syed. Metal-based nanoparticles and their toxicity assessment. *WIREs: Nanmed Nanobiotech*, 2(5):544–568, 2010.

[9] R Sun, R Chen, N Chung, C Ho, C Lin, and C Che. Silver nanoparticles fabricated in hepes buffer exhibit cytoprotective activities toward HIV-1 infected cells. *Chemical Communications*, 28(40):5059–5061, 2005.

[10] Jun Sung Kim, Eunye Kuk, Kyeong Nam Yu, Jong-Ho Kim, Sung Jin Park, Hu Jang Lee, So Hyun Kim, Young Kyung Park, Yong Ho Park, Cheol-Yong Hwang, Yong-Kwon Kim, Yoon-Sik Lee, Dae Hong Jeong, and Myung-Haing Cho. Antimicrobial effects of silver nanoparticles. *Nanomedicine: Nanotechnology, Biology and Medicine*, 3(1):95–101, 2007.

[11] T Aruvali. Nanodevices expectations in construction engineering. *Proceedings of Parnu 2012*, page 6, 2012.

[12] J Swift, CA Butts, J Cheung-Lau, V Yerubandi, and IJ Dmochowski. Efficient self-assembly of archaeoglobus fulgidus ferritin around metallic cores. *Langmuir*, 25(9):5219–5225, 2009.

[13] Y Nangia, N Wangoo, N Goyal, and CR Suri. A novel bacterial isolate stenotrophomonas maltophilia as living factory for synthesis of gold nanoparticles. *Microbial Cell Factories*, 8(1):39–46, 2009.

[14] RM Pattabi and M Pattabi. Synthesis, characterization, and intracellular uptake of carboxyl-terminated poly(amidoamine) dendrimer-stabilized iron oxide nanoparticles. *Spectrochimica Acta*, 74(1):195–199, 2009.

[15] T Sakai and P Alexandridis. Mechanism of gold metal ion reduction, nanoparticle growth and size control in aqueous amphiphilic block copolymer solutions at ambient conditions. *Journal of Physical Chemistry B*, 109(16):7766–7777, 2005.

[16] K Varner, A El-Badawy, D Feldhake, and R Venkatapathy. State-of-the-science review: Everything nanosilver and more. Technical report, 2010.

[17] P Murawala, SM Phadnis, RR Bhonde, and BLV Prasada. In situ synthesis of water dispersible bovine serum albumin capped gold and silver nanoparticles and their cytocompatibility studies. *Colloids and Surfaces B*, 73(2):224–228, 2009.

[18] Q Xiao, S Huang, ZD Qi, B Zhou, ZK He, and Y Liu. Conformation, thermodynamics and stoichiometry of HSA adsorbed to colloidal CdSe/ZnS quantum dots. *Biochimica y Biophysica Acta Proteins and Proteomics*, 7-8:1020–1027, 2008.

[19] D Eby, N Schaeublin, K Farrington, S Hussain, and G Johnson. Lysozyme catalyzes the formation of antimicrobial silver nanoparticles. *ACS Nano*, 3(4):984–994, 2009.

[20] A Ravindran, A Singh, AM Raichur, N Chandrasekaran, and A Mukherjee. Studies on interaction of colloidal Ag nanoparticles with bovine serum albumin (BSA). *Colloids and Surfaces B: Biointerfaces*, 76(1):32–37, 2010.

[21] J Mariam, PM Dongre, and DC Kothari. Study of interaction of silver nanoparticles with bovine serum albumin using fluorescence spectroscopy. *Journal of Fluorescence*, 21(6):2193–2199, 2011.

[22] R De-Llanos, S Sanchez-Cortes, C Domingo, JV Garcia-Ramos, and P Sevilla. Surface plasmon effects on the binding of antitumoral drug emodin to bovine serum albumin. *Journal of Physical Chemistry C*, 115(25):12419–12429, 2011.

[23] T Peters. *All about albumin proteins: Biochemistry, Genetics and Medical Applications*. Academic Press, 1996.

[24] B Honore and R Brodersen. Albumin binding of anti-inflammatory drugs. utility of a site oriented versus a stoichiometric analysis. *Molecular Pharmacology*, 25(1):137–150, 1984.

[25] TC Pinkerton and KA Koeplinger. Determination of warfarin-human serum albumin protein binding parameters by an improved hummel-dreyer high-performance liquid chromatographic method using internal surface reversed-phase columns. *Analytical Chemistry*, 62(19):2114–2122, 1990.

[26] U Kragh-Hansen. Structure and ligand binding properties of human serum albumin. *Danish Medical Bulletin*, 62(1):57–84, 1990.

[27] IE Borissevitch, TT Tominaga, H Imasato, and M Tabak. Fluorescence and optical absorption study of interaction of two water soluble porphyrins with bovine serum albumin. the role of albumin and porphyrin aggregation. *Journal of Luminescence*, 69(2):65–76, 1996.

[28] DE Epps, TJ Rub, V Canola, A Chari, and M Zamia. Determination of the affinity of drugs toward serum albumin by measurement of the quenching of the intrinsic tryptophan fluorescence of the protein. *Journal of Pharmacy and Pharmacology*, 51(1):41–48, 1998.

[29] E Alarcon, AM Edwards, AM Garcia, M Mu *n*oz, A Aspee, CD Borsarelli, and EA Lissi. Photophysics and photochemistry of zinc phthalocyanine/bovine serum albumin adducts. *Photochemistry and Photobiology*, 8(2):255–263, 2009.

[30] A Aspee, A Orrego, E Alarcon, CL Alarcon, H Poblete, and D Gonzalez-Nilo. Antioxidant reactivity towards nitroxide probes anchored into human serum albumin. a new model for studying antioxidant repairing capacity of protein radicals. *Bioorganic Medicinal Chemistry Letters*, 19(22):6382–6385, 2009.

[31] E Alarcon, EB Abuin, A Aspee, and EA Lissi. Evaluation of solute binding to proteins and intra-protein distances from steady state fluorescence measurements. *Journal of Photochemistry and Photobiology B*, 106(1):1–17, 2012.

[32] NC Nayac and K Shin. Human serum albumin mediated self-assembly of gold nanoparticles into hollow spheres. *Nanotechnology*, 46(19):265603, 2008.

[33] JC Bretschneider, M Reismann, G Von Plessen, and U Simon. Photothermal control of the activity of HRP- functionalized gold nanoparticles. *Small*, 5(22):2549–2553, 2009.

[34] HH Richardson, MT Carlson, PJ Tandler, P Hernandez, and AO Govorov. Experimental and theoretical studies of light-to-heat conversion and collective heating effects in metal nanoparticle solutions. *Nano Letters*, 9(3):1139–1146, 2009.

[35] C Fasciani, CJ Bueno Alejo, M Grenier, JC Netto-Ferreira, and JC Scaiano. High-temperature organic reactions at room temperature using plasmon excitation: Decomposition of dicumyl peroxide. *Organic Letters*, 13(2):204–207, 2011.

[36] JM Slocik, F Tam, NJ Halas, and RR Naik. Peptide-assembled optically responsive nanoparticle complexes. *Nano Letters*, 7(4):1054–1058, 2007.

[37] A Ben-Yakar, D Eversole, and O Ekici. Spherical and Anisotropic Gold Nanoparticles in Plasmonic Laser Phototherapy of Cancer. In: Kumar C (ed) Non-Magnetic Metallic Nanomaterials for Life Science, John Wiley and Sons, 2008.

[38] JC Scaiano, JC Netto-Ferreira, E Alarcon, P Billone, CJ Bueno Alejo, C-OL Crites, M Decan, C Fasciani, M Gonzalez-Bejar, G Hallett-Tapley, M Grenier, KL McGilvray, NL Pacioni, A Pardoe, L René-Boisneuf, R Schwartz-Narbonne, MJ Silvero, K Stamplecoskie, and W Tse-Luen. Tuning plasmon transitions and their applications in organic photochemistry. *Pure and Applied Chemistry*, 83(4):913–930, 2011.

[39] JT Holland, C Lau, S Brozik, P Atanassov, and S Banta. Engineering of glucose oxidase for direct electron transfer via site-specific gold nanoparticle conjugation. *Journal of the American Chemical Society*, 133(48):19262–19265, 2011.

[40] KG Stamplecoskie, JC Scaiano, VS Tiwari, and H Anis. Optimal size of silver nanoparticles for surface-enhanced Raman spectroscopy. *Journal of Physical Chemisty C*, 115(5):1403–1409, 2011.

[41] V Sharma, R Yngard, and Y Lin. Silver nanoparticles: Green synthesis and their antimicrobial activities. *Advances in Colloids and Interface Science*, 145(1-2):83–96, 2009.

[42] JS Suh and M Moskovits. Surface-enhanced Raman spectroscopy of amino acids and nucleotide bases adsorbed on silver. *Journal of the American Chemical Society*, 108(16):4711–4718, 1986.

[43] Q Wu, H Cao, Q Luan, J Zhang, Z Wang, J Warner, and A Watt. Biomolecule-assisted synthesis of water-soluble silver nanoparticles and their biomedical applications. *Inorganic Chemistry*, 47(13):5882–5888, 2008.

[44] S Cinta, E Vogel, D Maniu, M Aluas, T Iliescu, O Cozar, and W Kiefer. SERS mechanisms of the vitamin PP on different Au and Ag surfaces. *Journal of Molecular Structure*, 482-483(1-3):679–684, 1999.

[45] TM Herne, AM Ahern, and RL Carrel. Surface-enhanced Raman spectroscopy of peptides: Preferential n-terminal adsorption on colloidal silver. *Journal of the American Chemical Society*, 113(3):846–854, 1991.

[46] W Li, X Xie, Q Shi, H Zeng, Y Ou-Yang, and Y Chen. Antibacterial activity and mechanism of silver nanoparticles on escherichia coli. *Applied Microbiology and Biotechnology*, 85(4):1115–1122, 2010.

[47] V Edwards-Jones. The benefits of silver in hygiene, personal care and healthcare. *Letters in Applied Microbiology*, 49(2):147–152, 2009.

[48] W Liu, C Deng, CR McLaughlin, P Fagerholm, NS Lagali, and B Heyne. Collagen-phosphorylcholine interpenetrating network hydrogels as cornea substitues. *Biomaterials*, 30(8):1551–1559, 2009.

[49] P Fagerholm, K Merrett, W Jackson, R Munger, Y Liu, J Polarek, M Söderqvist, and M Griffith. A biosynthetic alternative to human donor tissue for inducing corneal regeneration: 24-month follow-up of a phase 1 clinical study. *Science Translational Medicine*, 2(46):46ra61, 2010.

[50] K Galiano, C Pleifer, K Engelhardt, G Brossner, P Lackner, C Huck, C Lass-Florl, and A Obwegeser. Silver segregation and bacterial growth of intraventricular catheters impregnated with silver nanoparticles in cerebrospinal fluid drainages. *Neurology Research*, 30(3):285–287, 2007.

[51] J Elechiguerra, J Burt, J Morones, A Camacho-Bragado, X Gao, H Lara, and M Yacaman. Interaction of silver nanoparticles with hiv-1. *Journal of Nanobiotechnology*, 29(3):6, 2005.

[52] V Alt, T Bechert, P Steinrücke, M Wagener, P Seidel, E Dingeldein, E Domann, and R Schnettler. An in vitro assessment of the antibacterial properties and cytotoxicity of nanoparticulate silver bone cement. *Biomaterials*, 25(18):4383–4391, 2004.

[53] H Jeon, S Yi, and S Oh. Preparation and antibacterial effects of Ag-SiO_2 thin films by sol–gel method. *Biomaterials*, 24(27):4921–4928, 2003.

[54] TF Tadros. *General Principles of Colloid Stability and the Role of Surface Forces*. Wiley, 2007.

[55] Malvern Instruments Ltd. *Zetasizer Nano Series*. Malvern Instruments Ltd, Users Manual, 2003-4.

[56] TL Doane, CH Chuang, RJ Hill, and C Burda. Nanoparticle ζ-potential. *Accounts of Chemical Research*, 45(3):317–326, 2012.

[57] T Cosgrove. *Colloid Science: Principles, Methods and Applications, 2nd Ed*. John Wiley and Sons Ltd, 2010.

[58] M Wikler and NCCLS document. *Performance standards for antimicrobial susceptibility testing : fifteenth informational supplement*, volume 25. 2005.

[59] B Levin and K Udekwu. Population dynamics of antibiotic treatment: a mathematical model and hypotheses for time-kill and continuous-culture experiments. *Antimicrobial Agents Chemistry*, 54(8):3414–3426, 2010.

[60] R Regoes, C Wiuff, R Zappala, K Garner, F Baquero, and B Levin. Pharmacodynamic functions: a multiparameter approach to the design of antibiotic treatment regimens. *Antimicrobial Agents Chemistry*, 48(10):3670–3676, 2004.

[61] K Udekwu, N Parrish, P Ankomah, F Baquero, and B Levin. Functional relationship between bacterial cell density and the efficacy of antibiotics. *Journal of Antimicrobial Chemistry*, 63(4):745–757, 2009.

[62] G Crumplin and J Smith. Nalidixic acid: an antibacterial paradox. *Antimicrobial Agents Chemistry*, 8(3):251–261, 1975.

[63] K Putsep, C Branden, H Boman, and S Normark. Antibacterial peptide from H. pylori. *Nature*, 398(6729):671–672, 1999.

Chapter 5

Lithography

5.1 Lithography: History and Emerging Challenges

The beginning of lithography can be traced back to 1790s when it was used for the mass production of advertisements for theatre, but more relevant here is the simultaneous invention of photography and photolithography in 1826. Since this time a knowledge of optics and physics has been used in photolithography in the development and progress of integrated chip fabrication that now have innumerable applications. Can anyone really imagine a world without computers, cell phones or calculators, to name a few things, for which semiconductor photolithography has been the enabling methodology for fabrication?[1] It is undeniable that photolithography has been one of the most important inventions of human history, but how does it work?

Put simply, photolithography uses light to cause a chemical reaction in the exposed area that results in a solubility switch in the material. For integrated chip design, this usually means that there is a polymer film, that is exposed through a mask such that desired portions of the film are irradiated while others are not. After the solubility switch, the film is "developed", which means that it is washed with an appropriate solvent for which only the exposed or unexposed portions of the film are selectively dissolved. A positive tone image is the term used to describe an image that was created in which the portions of the film exposed to light become more soluble and are washed away in the developing step, whereas negative tone images are created when the polymer becomes less soluble after exposure and is retained after washing, as illustrated in Figure 5.1.[2]

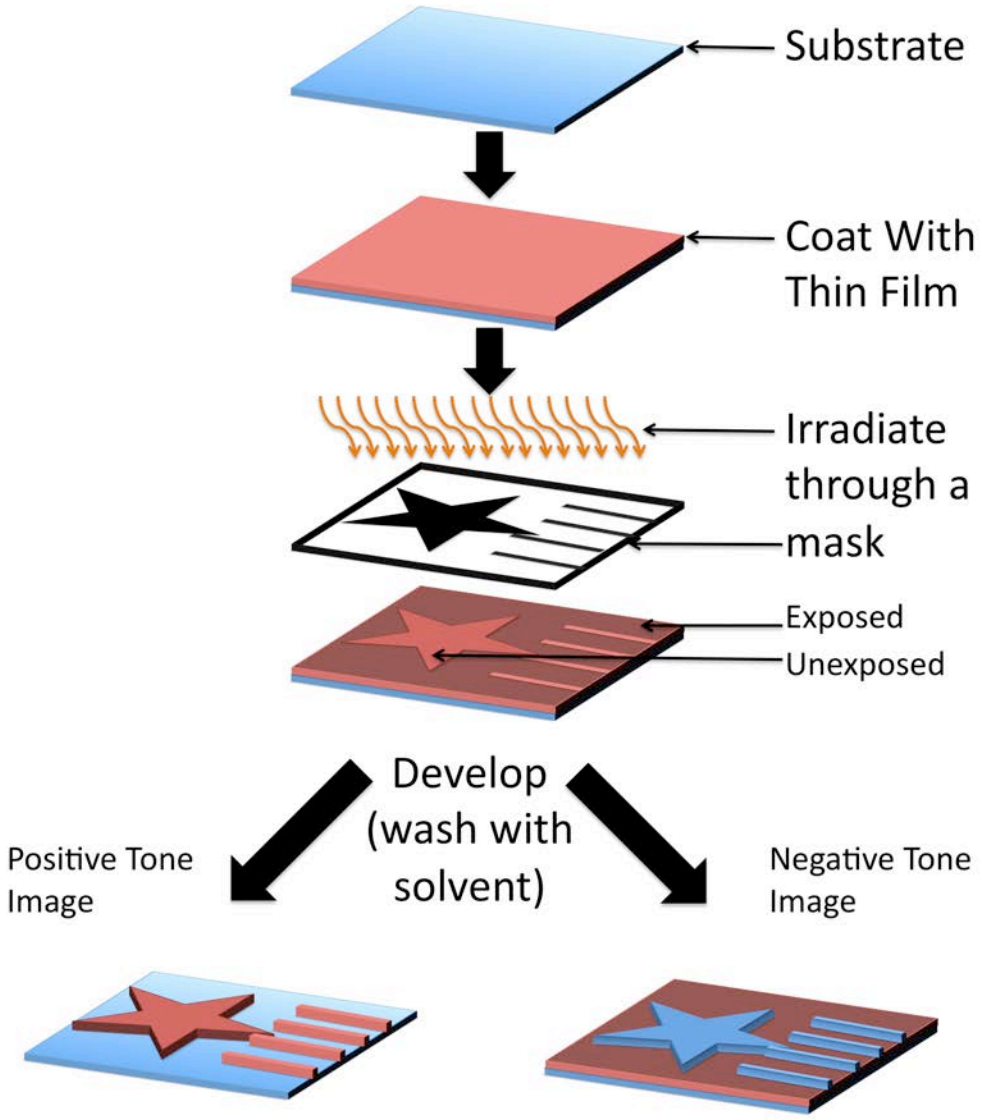

Figure 5.1: Positive and negative tone images illustrated in a typical photolithography scheme.

One of the most common methods to form a positive tone image has been to use a diazonaphtoquinones (DNQ) molecule as shown here:

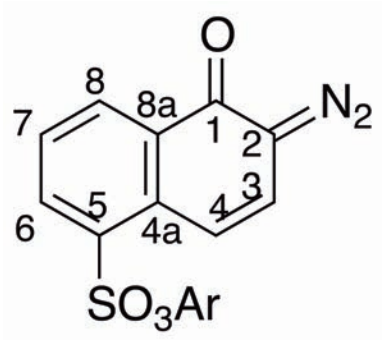

Figure 5.2: DNQ, a common molecule used as a UV absorbing photoresist.

The DNQ is often attached to polymer resins, usually in the 5 position via sulfonate ester linkages, and therefore does not diffuse throughout the polymer and provides a solubility switch for the resin when irradiated. The photochemistry of DNQ is shown in reaction Scheme 5.1, which is a well known Wolff rearrangement.[1] One of the reasons that DNQ has been used as frequently as it has is that it has a favourable absorption of UV lines in a Hg arc lamp excitation, traditionally a common source for exposure. Upon excitation, DNQ eventually results in formation of an indene carboxylic acid that is more soluble in base than the original DNQ. The carboxylic acid comes from reaction of water (can be atmospheric moisture) with the ketene formed from a Wolff rearrangement as shown.[1, 3, 4, 5] Basic developers are then used to wash the exposed regions and remove the resin in these areas.

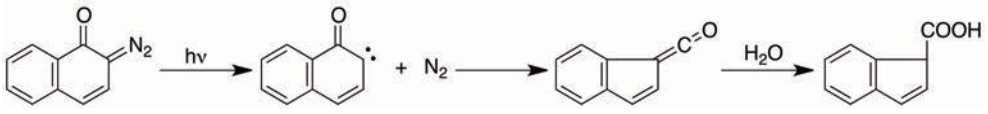

(5.1)

Current technology has also utilized photochemically generated acid from a photoacid generator (PAG) molecule, which increases the solubility of the exposed region through further chemical reactions. An example of a possible chemical scheme that uses a PAG to generate a positive tone image is shown in equations 5.2 - 5.3. Equation 5.2 shows the mechanism for which acid can be generated in several different pathways from a triphenylsulfonium salt, although this chemistry is not limited to this class of PAG

molecules.[6] Equation 5.3 provides an example of a reaction where a non-polar polymer can react with photochemically generated acid from Equation 5.2 rendering the exposed area soluble in polar solvents for development as a positive tone image.[2]

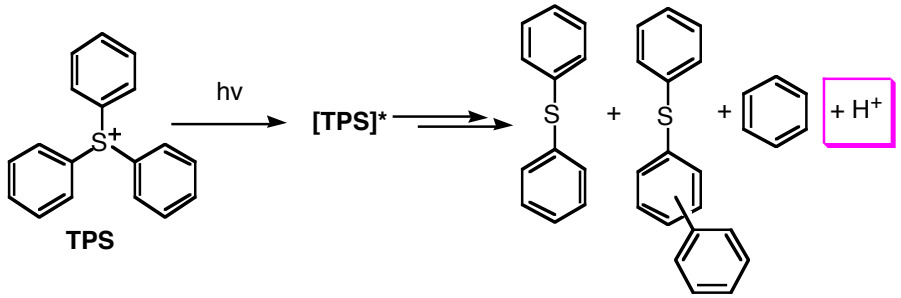

(5.2)

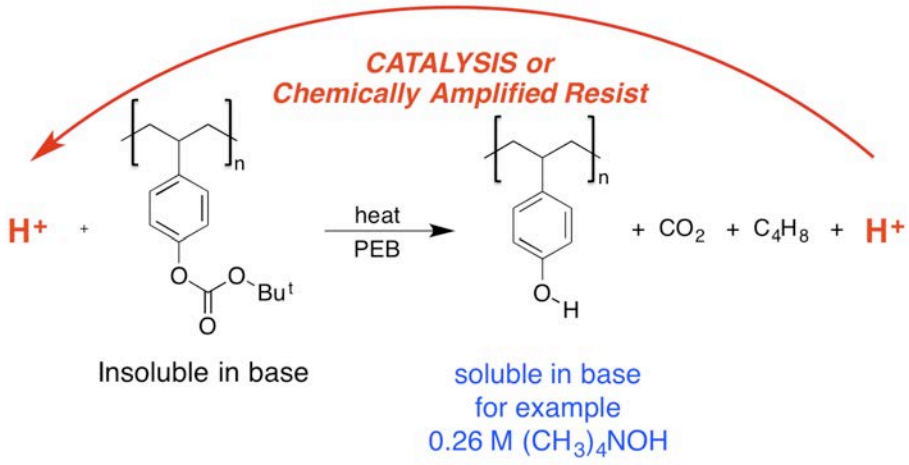

(5.3)

On the other hand, it is easy to imagine a polymer that cross-links by acid/base catalysed reactions, or by a radical reaction. This type of chemistry can be used such that the exposed area, with a radical initiator, then cross-links and is less soluble, generating a negative tone image. An example of this type of negative tone imaging is given in equations 5.4 - 5.5. In this example, azoisobutylnitrile is a photochemical radical initiator that forms radicals upon UV irradiation as shown in equation 5.4, followed by a radical chain reaction cross-linking the methacrylate monomers (trimethylpropanetriacrylate (TMPTA)) shown in 5.5 and rendering the film insoluble in the polymerized (exposed) regions.

(5.4)

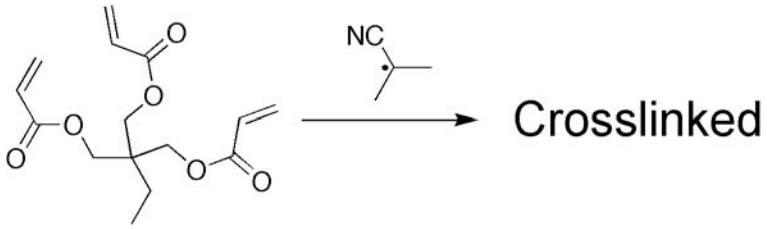

(5.5)

Photolithography has provided the motivation for a large volume of research and development of both positive and negative tone images. The size of features made on an integrated circuit determines the total number of features as well (smaller features means more can fit on a given chip), which ultimately means faster computing. For this reason there has been a demand for decreasing the size and increasing the number of features one can put on a chip. Development of both chemistry and optical physics has allowed for a steady progression of this technology. In 1965 Gordon Moore, one of the founders of Intel Corporation, made public a prediction that the number of components per integrated chip would double roughly every two years, and this prediction was plotted for one decade (until 1975).[7] While the prediction was made based on the historical advancements between approximately 1959-1965, it has since become a "law" that has driven the industry until present. Figure 5.3 shows the original data and prediction as well as curves for the continued trend in decreasing feature sizes with progress in the industry. It is noteworthy that the y-axis in Figure 5.3 is a logarithmic scale, and even so, both memory and microprocessor chips have followed closely with the prediction made by Moore more than 40 years ago.

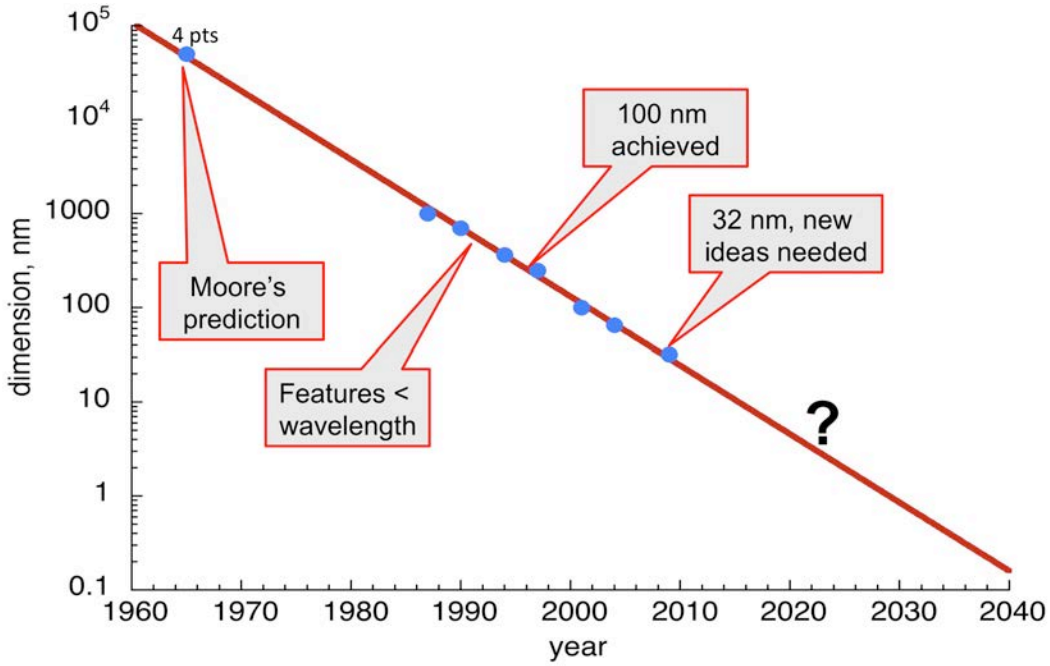

Figure 5.3: Feature size decrease with time that allows for more transistors on an integrated circuit by year; Moore's original data and prediction, and subsequent reduction of feature size manufactured for Intel chips that allowed the continuation of Moore's Law.

The diffraction limit of light is one of the main considerations when designing a technology for photolithography. The feature size is governed by how much one can focus light, which is inherently wavelength dependent. Shorter wavelengths of light can be focussed to smaller regions, which is why it is desirable to work with short wavelength excitation in order to attain smaller features. The current technology uses 193 nm lasers to attain minimal feature sizes. For the most part wavelengths shorter than this are too commonly absorbed by the entire film, resulting in many undesirable reactions. Even if these undesirable reactions were avoidable, extreme UV is also very costly to generate, which is another drawback for converting an entire industry standard for a technology that will inevitably become obsolete as well. So what kind of resolution, and therefore feature sizes, can be achieved with 193 nm light?

For those familiar with microscopes and optics, the resolution limit is generally considered to be wavelength divided by 2, which would be approximately 96 nm features. The diffraction limit is given as:

$$\text{Diffraction Limit} = \frac{\lambda}{2 \cdot NA} \tag{5.6}$$

where, NA is the numerical aperture and it is usually approximately 1, but can reach 1.4 with modern optics. However, this is one of the times when optical physics has been key so that if you adjust the numerical aperture of the lenses you can actually achieve wavelength divided by 3, which is 63 nm features. Furthermore, if one applies double exposure techniques, where a film is irradiated through a mask once, shifted a half a pitch and irradiated again, and the chemistry is designed such that only areas that receive both doses result in a solubility switch in that region, the feature size can be reduced by an addition factor of two, corresponding to 32 nm features. Lastly, using two photon technology, Intel has recently produced chips with 22 nm feature sizes. This relies on the fact that non-linear processes require a threshold energy which has a lower than normal diffraction limit. The overall breakdown of how one attains 22 nm features from 193 nm light is shown in Figure 5.4.

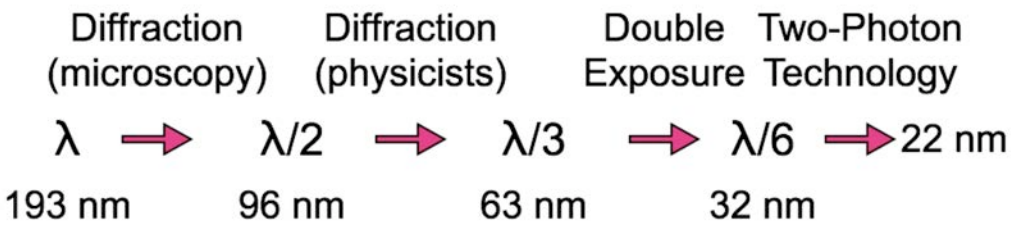

Figure 5.4: Schematic illustration of how 22 nm lines are realized by Intel Corp. with 193 nm exposure.

A somewhat disheartening conclusion can be reached from understanding the historical advancements in integrated chip technology, and that is that the technology is reaching a fundamental limit. Photolithography techniques and the smallest attainable features, are all still controlled by the diffraction limit of light. For this reason, fundamentally new approaches are required in the very near future.

5.2 Plasmon Approaches to Sub-diffraction Limit Resolution Lithography

The above discussion on Moore's Law and the rapid approach to the physical limits in photolithography is all based on the fact that light is passing through a mask, and so the diffraction limit of light passing through the mask determines the minimum feature size. What if a traditional mask is not required though? Nanoparticle plasmons are known to trap light in a very small region at the surface of the metal, previously described as the "enhancement region", where molecules experience higher polarizability and higher light intensities within approximately 5 nm from the nanoparticle surface.[8] Also, it is well understood that excitation of nanoparticle plasmon absorptions result in extreme local heating around the nanoparticle, which again provides a localized effect at the surface of particles that is not diffraction-limited.[9, 10] We show here two different methods of generating lithographic type features using this plasmon enhancement and the localized heating around nanoparticles, where in both cases sub-difraction limit features are attained.[11, 12] Conceptually, the lithographic mask has been removed from our work, but the nanoparticles behave as a mask in determining where these features are generated.

5.3 Plasmon-mediated photopolymerization maps plasmon fields for silver nanoparticles

When excited in the plasmon region, metal nanoparticles have intense localized electromagnetic fields in the direct vicinity of the particles.[13] The plasmon fields that characterize noble metal nanoparticles can influence the spectroscopic and thermal behavior of molecules in close proximity (<20 nm) to the metal surface. Such effects can result in enhanced fluorescence,[8] surface-enhanced Raman signals (SERS),[14, 15] and enhanced triplet formation,[16] as well as thermal processes characteristic of high-temperature behavior.[17, 10] In a recent example, plasmon-assisted processes were used to release fluorophores by triggering retro-Diels Alder chemistry.[18] Here, we explore the possibility of using plasmon-mediated chemistry to initiate polymerization processes that encapsulate particles in a way that effectively maps the plasmon field surrounding AgNP; we show that the enhanced field around AgNPs can be excited by nonpolarized light in a thin film containing AgNPs, an azo free radical initiator (azobisisobutyronitrile (AIBN)),

and a triacrylate. Plasmon excitation results in cross-linking of the triacrylate within the enhanced electromagnetic field around the AgNP. The cross-linked polymer is less soluble than its precursor and works as a negative image in which only the polymerized regions remain fixed to the film after washing with ethanol.[12]

The choice of AgNP (rather than, e.g., AuNP or CuNP) deserves comment. The absorption coefficient of metal nanoparticles has an inverse relationship with the imaginary part of the dielectric constant, so smaller imaginary dielectric constants give rise to large absorption coefficients. Silver has the lowest dielectric constant among Ag, Au, and Cu at the corresponding resonance frequency, making Ag a great candidate for high absorption of visible light. When the surface plasmon absorption is excited, there is a resultant electromagnetic field around the particles that enhances the electronic transition of molecules in the direct vicinity of the particles.[19, 20] The intensity of the electromagnetic field is related to conductivity, and Ag is known to have the highest resultant electromagnetic field among these elements. Overall, Ag has a high absorption coefficient and a high resultant electromagnetic field enhancement when excited at ∼400 nm (for spherical nanoparticles), and it is this field that leads to an enhancement of electronic transitions in neighboring molecules, in our case an azo photoinitiator. It is noteworthy that Au generally has higher stability against oxidation, and it may be possible to have the same effect with Au, as what is described for Ag here. As a metal, Ag is simply chosen for its superior photophysical properties for this application.

5.3.1 Experimental

AgNP Synthesis

Our experiments have been performed starting from small AgNP seeds (∼3.3 nm) prepared photochemically,[21, 22] followed by slow growth to achieve ∼40 nm particles using the same ascorbic acid reduction process as that used for the particles for SERS (see equations 2.6 and 3.1). The average diameter of the particles as prepared was determined to be 38.3 nm (sd = 6.0 nm) by drop-casting onto a quartz plate and imaging by SEM. AIBN was used as a free radical initiator and a triacrylate (TMPTA) as the monomer; these structures are shown equations 5.4 and 5.5. After several tests for compatibility of the various materials and the ability to produce good spin-coated films, acetonitrile was selected as casting solvent. The triacrylate used has the ability to cross-link extensively and thus produces rather insoluble polymeric structures, effectively acting as a solubility switch where polymerization occurs.[23, 24]

Plasmon Polymerization in Films

The films were produced by spin-coating (3500 rpm, 30 s) a solution containing 20 wt % TMPTA, 1 wt % AIBN, and >0.2% silver in the form of AgNP in ACN or DMF as solvents. Typical film thickness was ∼100 nm, as determined by interferometry using a Luzchem thin film analyzer (a calibration curve for spin speed vs film thickness was made for thicker films and extrapolated to the speed required for less than 100 nm thickness). Films were irradiated with a single 405 nm light-emitting diode (LED) with a light flux of ∼207 W/m^2. After irradiating with LED the films were washed with ethanol to remove any unreacted matrix components, whereas polymerized regions were retained due to insolubility in ethanol. UV-vis absorption spectra were recorded at various steps in the plasmon polymerization process to help characterize the films. Particularly whether silver nanoparticles had been formed, as indicted by a plasmon absorption, as well as if the particles had been retained on the film after subsequent washing. AFM and SEM measurement of particles with and without the polymerization process were recorded, and statistical analysis was used to ensure that the particle sizes measured by both methods were statistically confident. The null hypothesis was tested as a student t-test was used to show that the average values were valid to a 95 % statistical confidence. X-ray photoelectron spectroscopy was also used to characterize the films with respect to silver and carbon content.

5.3.2 Results and Discussion

The initiator, AIBN, is known to generate carbon-centered radicals either photochemically or thermally, in the latter case with an activation energy of 34.1 kcal/mol.[25] In our system we reasoned that plasmon-mediated excitation could promote AIBN decomposition in the vicinity of the AgNP and that this, in turn, would initiate localized polymerization. In principle, AIBN can also be decomposed by direct photolysis, but it is essentially transparent at 405 nm, the wavelength of the LED used for excitation. Figure 5.5 shows the corresponding absorption spectra recorded in solution.

The effect of LED AgNP excitation on the film spectroscopy and dissolution is illustrated in Figure 5.6, and shows clearly that while exposure does not change the optical properties of the film, it dramatically changes its dissolution behavior. Thus, ethanol washing of the unexposed film totally removes the AgNP, as evidenced by the absence of the 400 nm plasmon band following ethanol treatment; in contrast, in the exposed film, about 50% of the AgNP absorption remains after ethanol treatment. Note that the ab-

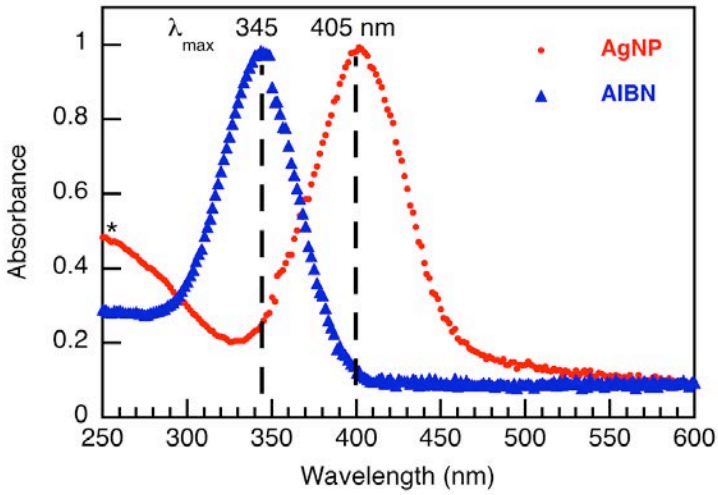

Figure 5.5: UV-vis absorption spectra of AIBN and AgNP. Normalized UV-vis absorption spectra of AIBN (blue) and AgNP (red) in acetonitrile, with dashed lines showing the position of the absorption maximum, especially highlighting the fact that AgNP can be excited at $\lambda > 400$ nm, where AIBN is transparent without plasmon enhancement. Note that the absorbance at 250 nm (marked *) for the AgNP solution is due to traces of products derived from the I-2959 photoinitiator used to reduce the Ag^{+} salt while making AgNP.

sorbance values are very low (0.025 max), which also results in a poor signal/noise ratio, which is anticipated since the films are only 100 nm thick. An equivalent concentration of AgNP in a 1 x 1 cm cuvette would correspond to a nominal absorbance of 2500.

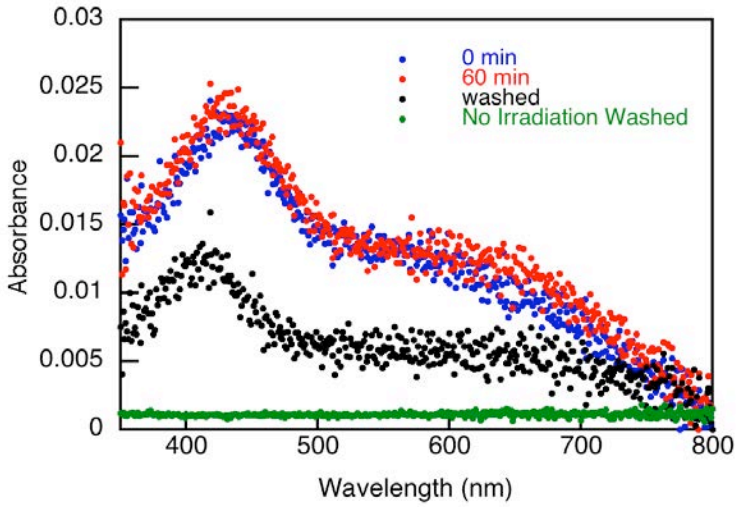

Figure 5.6: UV-vis absorption spectra of a film for plasmon-enhanced polymerization. UV-vis absorption spectra for a freshly prepared AgNP film (blue), a film irradiated with 405 nm light for 60 min (red), showing little change upon irradiation, the irradiated film after washing with ethanol (black), and a spectrum of a freshly prepared film that was washed without irradiation (green), showing that AgNPs do not persist on the films when washed with ethanol if they are not irradiated to induce plasmon enhanced polymerization. The black spectrum has a residual absorption for AgNPs that have been fixed to the film by 405 nm excitation.

In order to establish if the observation of Figure 5.6 was a true indication of plasmon-localized phenomena, a series of experiments were performed using SEM and AFM imaging techniques. SEM demonstrated that AgNP were retained on the surface; further, these particles were larger than those initially deposited, with an average size of 54 nm, compared with 38.3 nm initially, or a growth of approximately 16 nm, suggesting that a layer of $\sim$8 nm has been deposited on the AgNP Figure 5.7.

We noted in the SEM data some indication that particles in pairs or groups had a higher probability of being preserved in the films. Our AFM data confirm this observation. Figure 5.8 below contains typical SEM and AFM images of the AgNP films after polymerization that show that the particles that stay on the film tend to be pairs or

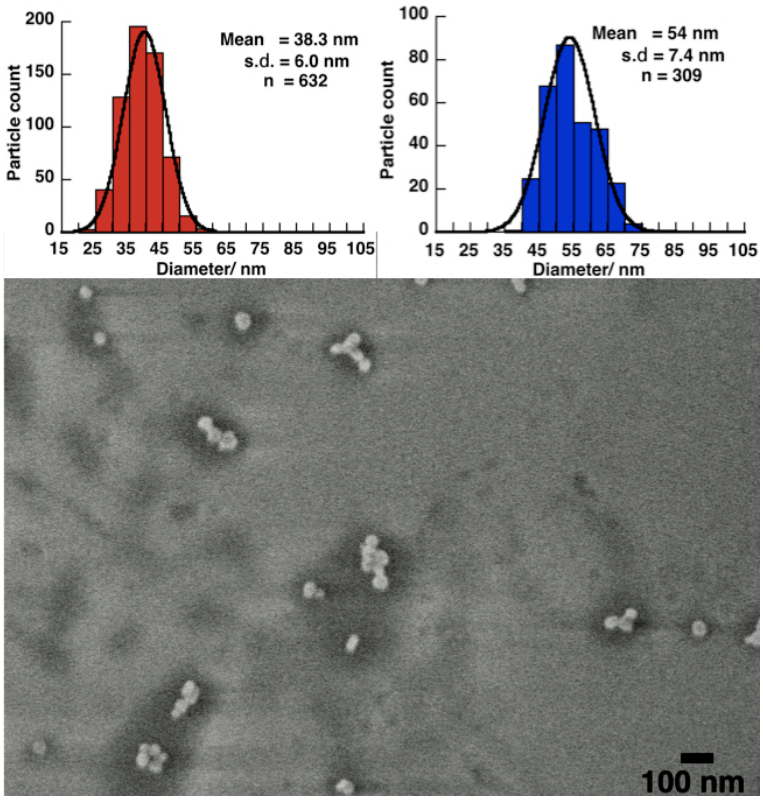

Figure 5.7: Histograms of AgNP size with and without polymerization and a representative SEM image of a polymerized AgNP film. Bottom: representative SEM image of AgNP after polymerization and washing with ethanol, showing the particles that remain on the film. Top: histograms of the AgNP sizes as measured from SEM images for particles drop-cast without monomer (red, left) and for particles after the polymerization and washing as in the SEM image (blue, right).

clusters of particles. The measured size of the particles by SEM was larger for the polymerized particles, as stated above, and to confirm this finding the height of AgNPs from the polymerized films was compared with the height of drop-cast AgNPs (as determined from cross sections such as those in Figure 5.9).

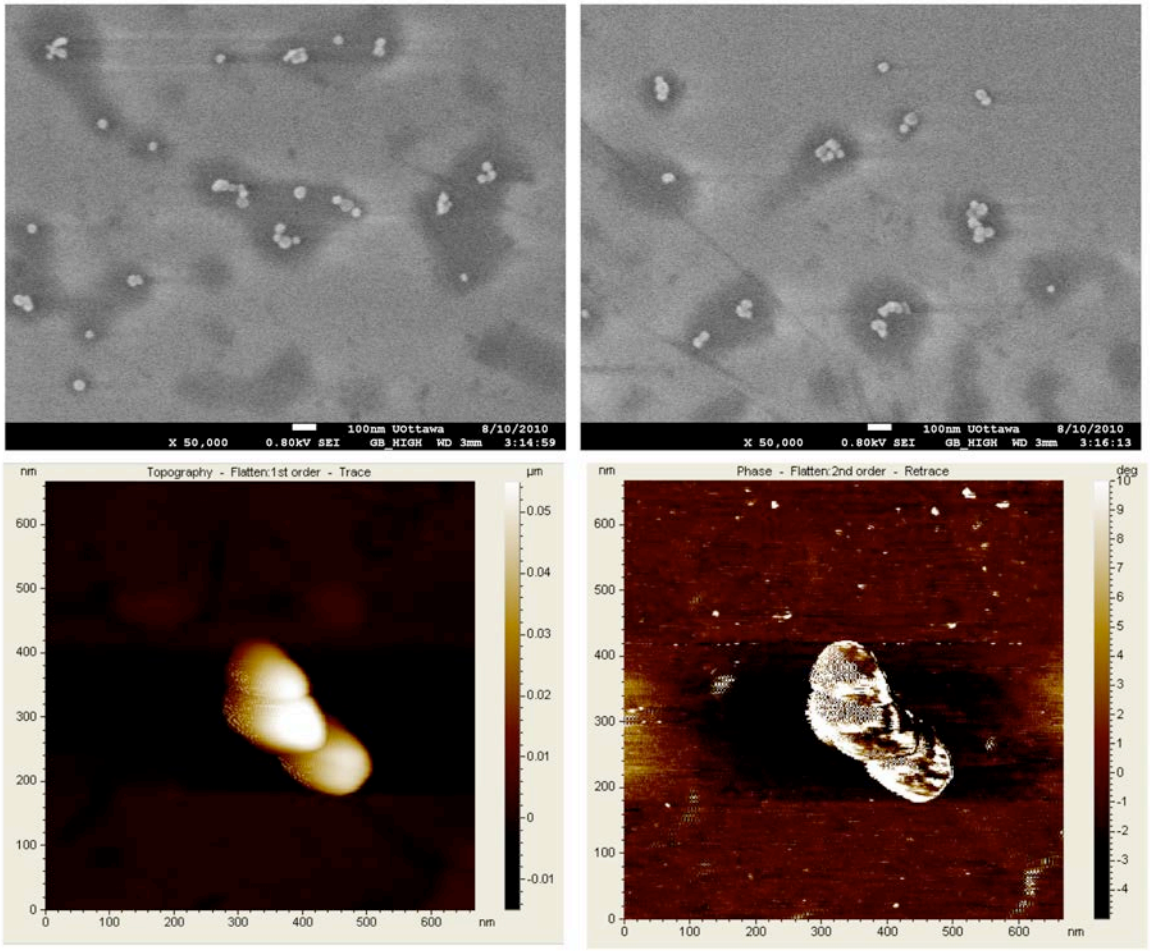

Figure 5.8: Top: SEM images of representative regions of a quartz disk after plasmon polymerization and washing. Bottom: AFM topography (left) and phase image (right) of a representative quartz disk after plasmon polymerization and washing.

We note that the height determination was performed on a random selection of particles (all particles imaged in AFM) with and without polymerization, and no preference was given to measuring dimers, trimers, or any aggregates of AgNPs. The line scans are a measure of the AFM topography in a line that is assigned over the particles, whereby

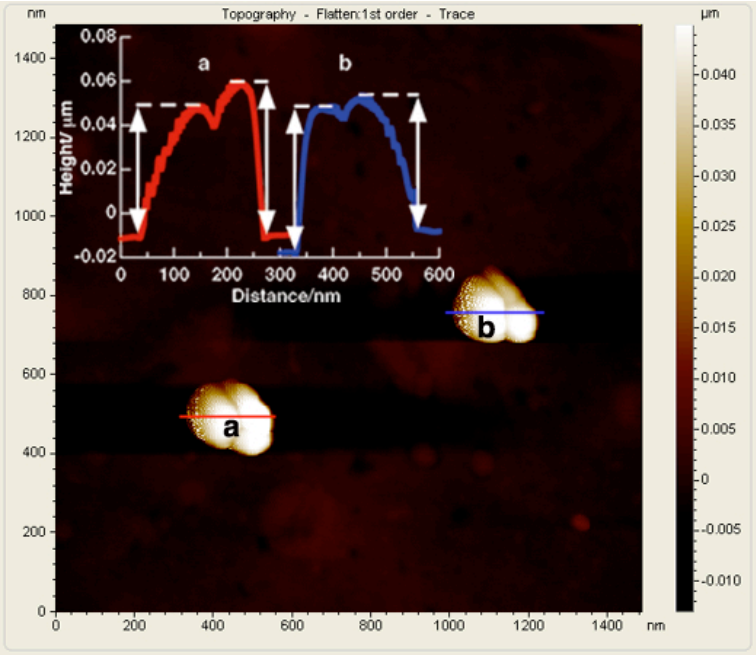

Figure 5.9: AFM image of a polymerized AgNP film. Main panel: representative topographic AFM image (scanning range 1.5 μm x 1.5 μm) of AgNPs after plasmon-enhanced polymerization and ethanol washing. Inset graphs: height profiles taken for two separate clusters of AgNP on the film. The height of AgNP by AFM was determined as the difference between the maximum/minimum of the cross section, as indicated by the arrows. Many particles measured in this way were analyzed to confirm a polymer shell on particles with statistical confidence.

the particle height is measured as the maximum minus the minimum in the line scan as indicated by the arrows in the line scans of Figure 5.9. Rigorous analytical analysis of statistically confident samples were reported for sizes of nanoparticles with and without polymer shells, and by both AFM and SEM imaging techniques. Once obtained, the statistical estimators that characterize both samples, it is necessary to prove whether or not these samples are significantly different by performing hypothesis testing (Equations 5.7 and 5.8).

$$H_0 : \bar{x}_{G1} = \bar{x}_{G2} \tag{5.7}$$

$$H_1 : \bar{x}_{G1} \neq \bar{x}_{G2} \tag{5.8}$$

where H_0 and H_1 represent the null and alternative hypothesis, respectively. In order to do this, an unequal variance t-test for two-sample means was performed (Equation 5.9) for the AFM and SEM data.[26, 27, 28]

$$t = \frac{[\bar{x}_{G1} - \bar{x}_{G2}]}{[\sqrt{\frac{s^2_{G1}}{n_{G1}} - \frac{s^2_{G2}}{n_{G2}}}]} \tag{5.9}$$

The data are summarized in the 5.1, showing that the average height of the polymerized AgNP was 53.6 nm, compared to 44.9 nm for the original particles, indicating a $\sim$10 nm size increase upon polymerization.

Table 5.1: Statistical estimators for SEM and AFM data for either polymerized or control (drop-cast) samples and t values calculated by an unequal variance test for two-sample means.

	AFM		SEM	
	Group 1	Group 2	Group 1	Group 2
n	28	37	309	632
$\bar{x}$	53.6	44.9	54	38.3
SD	7.7	11	7.4	6.0
s^2	59.7	125	54.4	35.8
ν	62		512	
t	3.67		35.526	
P	0.0005		<0.0001	

n is the sample size; $\bar{x}$ is the mean; SD is the standard deviation; s^2 is the variance; ν is the number of degrees of freedom; t is the calculated t (Eqation 5.1); P is the probability of rejecting H_0 when the means are equal.

AFM data: Comparing the experimental t-value in Table S3 with the corresponding $t_{0.05}$ value for 62 degrees of freedom, which is $t_{0.05,\nu=62} = 2.00$, we find that the calculated t value (3.67) is larger than the tabulated t-value. Overall, the null hypothesis (Equation 5.7) is rejected with 95% confidence, and therefore the means are significantly different. In summary of the statistical analysis of the AFM data, it is found that the particles that were irradiated to form a layer of polymer coating are in fact significantly larger than the particles that had been drop cast from solution and had no polymer coating at all. Also, the average size increase by polymerization was determined to be approximately 10 nm (diameter increase).

SEM data: Similar conclusions to those of the AFM data are extracted from the statistical analysis of SEM data. It should be noted that there is significantly more data obtained from SEM images simply due to the fact that the imaging technique provides a more rapid route to size measurements. Nevertheless, again we find that the null hypothesis is rejected, with a t-value of 32.526, where the tabulated t-value for 512 degrees of freedom with 95% confidence is 1.965, and again this indicates that the diameter of the particles in the PPE sample is statistically different from AgNP simply drop cast onto a quartz disk.

The AFM images reveal that polymer-coated particles have remained on the surface and that no polymer debris is observed in regions free from AgNP. Further, many particles are frequently in pairs or groups many more than observed in nonpolymerized drop-cast samples as already noted for the SEM data. Interestingly, the particles seem to grow (based on AFM height) about 10 nm, similar to the observation by SEM. We speculate that growth occurs on both sides of the particle in the x and y directions, while in the vertical or z direction growth occurs only above the particle, with little or no growth in the contact area between the substrate and the particle. XPS measurements (see Figure 5.10) show that there is a significant amount of carbon on the polymerized films even after washing with ethanol, as expected. Also, upon Ar-ion etching to remove the polymer, the carbon content decreases, and there is a small enhancement in the exposed Ag detected by XPS, which is consistent with the prediction that the polymer is coating the AgNP from the plasmon-directed polymerization process.

The results presented here demonstrate that it is possible to take advantage of localized plasmon fields to trigger spatially controlled chemical reactions in molecules that

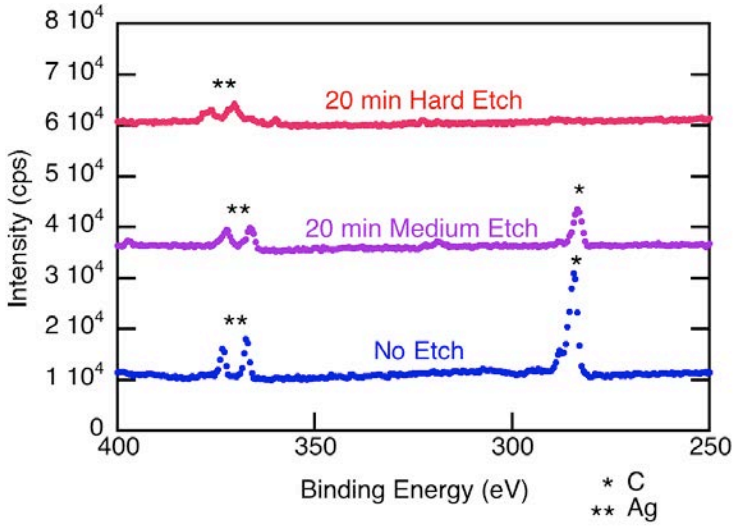

Figure 5.10: XPS spectra of a plasmon polymerized film of AgNP before and after Ar etching to remove the polymer film.

are not chemically bound to the surface; quite simply, the intense electromagnetic field in the immediate vicinity of the particle(s) selects the molecules for reaction. The LED 405 nm light was specifically chosen to excite the maximum absorption for spherical AgNP while avoiding excitation of AIBN that is not in the near vicinity of the particles. It is the plasmon-induced excitation of AIBN near AgNP that causes initiation of polymerization by photodegradation of AIBN and, therefore, selective cross-linking of the monomer only in the enhancement region. The formation of a highly insoluble cross-linked vinyl polymer acts as a solubility switch; further, these processes remain delicately confined to a well-defined region controlled by the plasmon field. Interestingly, it has been reported that the 2-cyano-2-propyl radical from AIBN shows transient binding to gold nanoparticles;[29] if a similar effect occurs with AgNP, this may assist to retain the geometric definition of the plasmon-intensified region as the polymerization occurs. The polymeric features observed are 8 to 10 nm in dimension, and are obtained with noncoherent 405 nm low-intensity excitation, and are over an order of magnitude smaller than those achievable by diffraction-limited processes. Further, SERS and nanoantenna studies suggest that plasmon fields are greatly intensified in the interparticle regions,[30, 31] a property that has been utilized to advantage in the design of antennas.[32] The apparent preference for particle aggregates of a few particles suggests that plasmon-mediated polymerization follows similar preferences. Of course, irradiation does not cause aggre-

gation of particles in the films, but rather that the particles on the films that randomly exist in close proximity have very intense EM field intensities between them that cause intense polymerization in these highly enhanced regions. Therefore, these particles have a higher probability of inducing significant cross-linking in the interparticle space, and thus a higher probability of being retained on the films. This suggests that the effect is electronic rather than thermal.[10, 18] The same has been observed in nanogaps designed with top-down strategies.[31] Further, from the statistical analysis of the AFM and SEM data, the standard deviation values, as an estimate of the variance of the population (s^2) in the heights and diameters, are different for drop-cast versus polymerized films.

While our work has taken advantage of random particle positioning resulting from the coating process, the results suggest that nanostructures in masks with well-defined geometric arrays could be used as plasmonic templates to generate custom lithographic features with a resolution of a few nanometers, potentially extending the lithographic limits well beyond those achievable with current top-down lithographic technologies. Thus, bottom-up self-assembly in the synthesis of nanostructures and in the polymerization stage could be combined with top-down mask design to achieve high resolution. Our work shows that plasmonic fields can be mapped and preserved by taking advantage of enhanced fields to initiate chemical processes capable of converting transient fields into permanent nanostructures.

5.4 Dual-stage lithography from a light-driven, plasmon-assisted process: A hierarchical approach to sub-wavelength features

In the previous sections we describe a method to enhance electronic excitation of a photoinitiator, AIBN, and in doing so, provide a method of exploiting plasmon excitation to generate sub-difraction limit polymer features. Enhanced excitation is not the only exploitable effect at the surface of particles when undergoing plasmon excitation. One interesting property of metal nanoparticles that, while recognized, has not been exploited extensively, is that the absorbed light in plasmon excitation is almost entirely released as heat during a very short period of time. The heat released causes brief but intense heating near the surface and has been used to denature proteins, cleave weak bonds, and release molecules bound to the surface of the particles.[18, 33, 10]

In the above reported work, enhancing AIBN photochemistry, dispersions of AgNP

in monomer films were used to selectively induce radical polymerization around metal nanoparticles leading to nanoparticles that were retained on the substrate; similar plasmon mapping approaches using photopolymers have been recently reported.[34] What we describe here, is how to use a radical-initiated process to generate well defined lines of AgNP using a lithographic mask. Since the particles are made in a radical-mediated process, the same type of chemistry could not be used selectively to induce polymerization and generate sub-diffraction limit features around the same particles. Therefore, a different polymerization strategy was employed, whereby the heat generated by plasmon excitation of AgNP was used to induce polymerization of caprolactam to nylon-6 in the near vicinity of metal particles. The detailed two-step process to: (1) generate films with colloidal AgNP in controlled regions using a radical initiated process, and (2) thermal polymerization to form an insoluble nylon-6 polymer selectively around AgNP, is discussed here. The latter process is not diffraction limited and can be used to generate <10 nm polymeric features.[11]

5.4.1 Experimental

Precursor solutions generally contained equal amounts of $AgCF_3COO$, I-2959, and cyclohexylamine at 1-2 wt%, 2wt% PMMA, 15 wt% caprolactam, and 75 wt% cyclohexanone as the solvent. PMMA is used only to help make better homogeneous films and is removed post synthesis in the washing step. Quartz disks were cleaned with concentrated nitric acid to remove silver nanoparticles and to oxidize organic components on the surface, followed by washing with copious amounts of water and finally acetone to dry before spin coating.

A volume of 50 μL of the above precursor solutions were spin coated at 2500 rpm onto one inch diameter quartz disks. Film thicknesses were measured to be 991 $\pm$ 31 nm for several spin coated films with a Luzechem thin film analyzer. A UV-Vis spectrum of the spin-coated films was acquired with a CARY 50 UV-Vis spectrophotometer, as well as spectra at each step of the polymerization and washing process.

Experiments were performed with a typical 365 nm LED irradiation for 30 s, followed by 405 nm LED irradiation for 30 s followed by washing with ethanol. As a comparison, an experiment was performed where the 405 nm irradiation was done first followed by 365 nm irradiation.

It is important to note that normal lithographic resolution is achievable in the first irradiation through a mask; the selection of large 3 μm lines reflects the preference

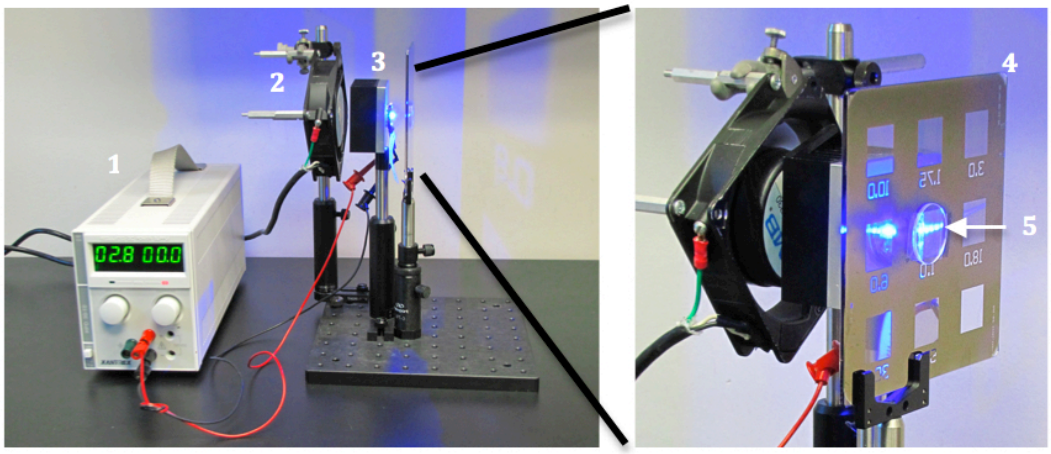

Figure 5.11: Experimental setup for the irradiation of spin-coated films. 1= power supply, 2 = cooling fan, 3 = LED mounted on an aluminum heat sink, 4 = lithographic mask, 5 = quartz disk with spin coated film.

for features where optical microscopy can be used as a tool. These particles are initially embedded in a caprolactam monomer film (see above), which makes transmission electron microscopy for imaging impossible. The LED powers were 500 mW and 460 mW for the 365 and 405 nm LED respectively, which was the maximum output of each LED.

The films were characterized at each step of the reaction using UV-Vis absorption spectroscopy as shown in Figure 5.12 for films containing 2% PMMA. After spin coating, the films show no absorption maxima in the visible region, but do have an intense absorption in the UV region due to I-2959 and caprolactam. Following 365 nm excitation there is a broad absorption from approximately 400 to 600 nm due to the plasmon absorption of AgNP.[21] Following 405 nm excitation the absorption shifts slightly, likely due to a change in refractive index of the medium surrounding the particles during the polymerization process; the increased absorption at 600-700 nm may also reflect minor polymer-induced aggregation. There is not a significant increase in integrated intensity of the plasmon absorption, indicating no further reduction of metal salt with 405 nm irradiation. Finally, after washing the films with water the unreacted caprolactam is removed, as evidenced by atomic force microscopy (AFM) imaging that shows the nylon-coated particles remaining only in the exposed areas (see Figure 5.15), typically showing 3-5 particles per μm.

For monitoring the heat generated by AgNP to form nylon-6, photo-DSC was used.

A Thermo Analysis DSC 2000 system was used, equipped with a metal halide arc lamp. A long pass filter was used to reduce the amount of UV light exposure. A typical solution for spin coating (CF_3COOAg, I-2959, and cyclohexylamine at 1-2 wt%, 15 wt% caprolactam, and 75 wt% cyclohexanone) was irradiated with a mercury arc lamp (both UV and visible light) to generate AgNP and subsequently heat the particles to form nylon-6. In a blank experiment the same precursor solution for spin coating as above was used, however CF_3COOAg was omitted such that, without the formation of AgNP, neither the first or second step in eventual formation of nylon-6 encapsulated AgNP was possible.

To show that the polymer is in fact encapsulating the particles and contributing to the solublility of our particle films, experiments were performed by adding <1% by weight of coumarin-6 into the solutions for spin coating.[35] After spin coating, the solutions containing the dye and all the nanoparticle/nylon precursors were irradiated with 365 nm and subsequently 405 nm LED light, through a lithographic mask with 6 μm feature sizes. The films were then washed with water just as in previous cases to remove any unreacted caprolactam; washing also removes free coumarin-6. The films were imaged by fluorescence lifetime imaging microscopy (FLIM) in order to observe/image the spacial location of the dye on the films.

5.4.2 Results and Discussion

The first step in the imaging process here uses chemistry that has been described before as the photochemical generation of fluorescent silver nanoparticles, and described elsewhere.[36, 37] The photoinitiator, I-2959 is irradiated for 30 minutes with 365 nm light from an LED to generate strongly reducing ketyl radicals; these radicals reduce the Ag^+ precursor to Ag^0 resulting in the spontaneous formation of AgNP. Earlier experiences in the Scaiano group with this system suggests this time should be sufficient to convert I-2959 quantitatively to products.[36, 37, 38] The CHA is helpful as a proton sink and increases the yield of Ag reduction in a process that is mediated by proton coupled electron transfer.[36] Irradiating the spin-coated films through a lithographic mask with 3 μm features generates lines of densely packed AgNP for which the experimental setup is shown in Figure 5.11.

In order to generate insoluble features selectively around the AgNP, a non-radical, heat-mediated polymerization process was then required. Caprolactam, with catalytic amounts of water and heat can generate nylon-6 polymers as shown in Scheme 5.10 (end

groups omitted). Polymerization of caprolactam requires temperatures above 100°C.[39, 40] Irradiation of AuNP has been demonstrated to produce ∼500°C as the surface temperature, since AgNP have a higher extinction coefficient, and we use shorter wavelengths to excite them (400 nm for AgNP vs. 530 nm for AuNP), higher surface temperatures are anticipated when irradiating AgNP.[10] The surface temperatures upon LED irradiation are more than sufficient to induce caprolactam polymerization. Here, the transient localized heat released at the surface of AgNP upon plasmon excitation with 405 nm light is used to selectively polymerize caprolactam to nylon-6 at the surface of the AgNP, where the highest temperatures are reached. Notably, high temperatures are reached locally even if the bulk temperature change is minor, as observed by photocalorimetric studies, in [11]. It is important to note that the 365 nm irradiated films display some absorption at 365 nm due to the AgNP plasmon transition (about 30% relative to the maximum at the end of exposure), and thus, upon prolongued irradiation it is possible for some polymerization to occur towards the end of the particle formation stage.

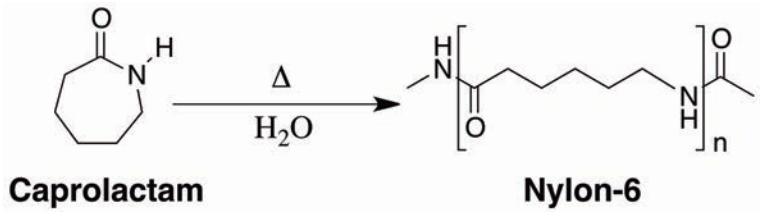

(5.10)

Experiments were performed with a typical 365 nm LED irradiation for 30 s, followed by 405 nm LED irradiation for 30 s, followed by washing with ethanol. As a control, an experiment was performed where the 405 nm irradiation was done first followed by 365 nm irradiation. UV-Vis absorption spectra of the films in both of these cases are shown in Figure 5.12.

Obtaining absorption spectra for the nanoparticles, with the quality of data shown in Figure 5.12, indicates that these thin films contain high concentrations of reduced metal in the form of AgNP, as evidenced by their plasmon absorption. By-products of I-2959 photolysis are radical recombination products, which partially regenerate the starting material. However, for total conversion of Ag^+ to Ag^0, an excess of I-2959 can be used to ensure complete conversion of the metal precursor. The data in Figure 5.12 may be better represented by a bar graph as shown in Figure 5.13. Examining the absorbance at 425 nm, one can see that only in the case where the first irradiation (365 nm) generates nanoparticles and the second irradiation polymerizes with plasmon excitation (405 nm) are the particles formed and retained on the substrate after washing. In other words,

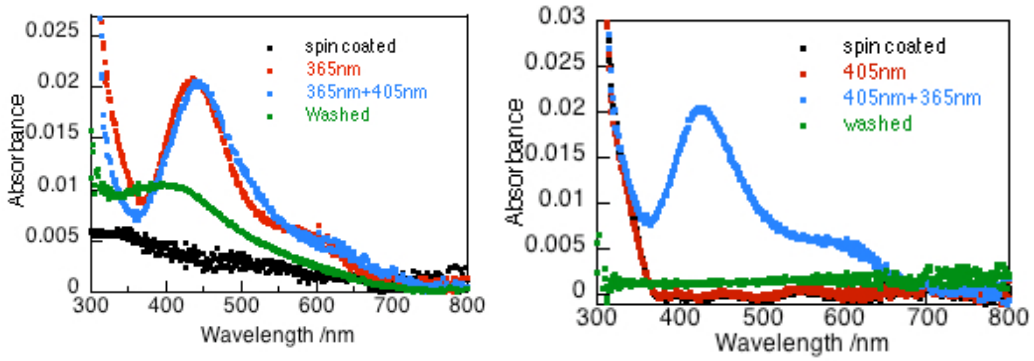

Figure 5.12: Left: UV-Vis absorption spectrum of films freshly spin coated film (black), irradiated with 365 nm LED to generate AgNP (red), irradiated with 405 nm LED to excite the plasmon absorption and polymerize caprolactam to nylon (blue), and after washing with water to selectively remove the soluble remaining unreacted caprolactam (green). Right: Same as left but with the 405 nm irradiation followed by 365 nm.

this pair of experiments is consistent with the proposed, two step reactions, first forming particles and secondly fixing them to the surface by forming a nylon shell. In the reverse (control) irradiation, particles are made in the second step, and are not subsequently heated, so they are formed, but are not retained in the washing step, as no nylon has been made through plasmon heating.

The broad absorption shown in all of the spectra for AgNP has been attributed to a combination of single spherical particle absorption (400 nm) and aggregate absorption, or absorption of several particles in close proximity that shift to longer wavelengths.[41, 42, 43] With the monomer matrix still present, it was not possible to image the film with higher resolution than optical microscopy. However, even with an optical microscope, the films before and after washing show alternating dark and light lines with 3 μm width as shown in Figure 5.14.

The polymer films were washed with water after the second irradiation step. Caprolactam is highly soluble in water, whereas nylon-6 is insoluble. Therefore, it was expected that only areas or spots with nylon-6 encapsulated particles would remain on the films. The AFM image shown in Figure 5.15 shows a hierarchy of features, where the 3 μm lines are used to control the position of AgNP formation and the subsequent 405 nm irradiation causes a solubility switch and the formation of nylon-6 to fix particles in the film while surrounding unreacted caprolactam is removed. Figure 5.15 also confirms the

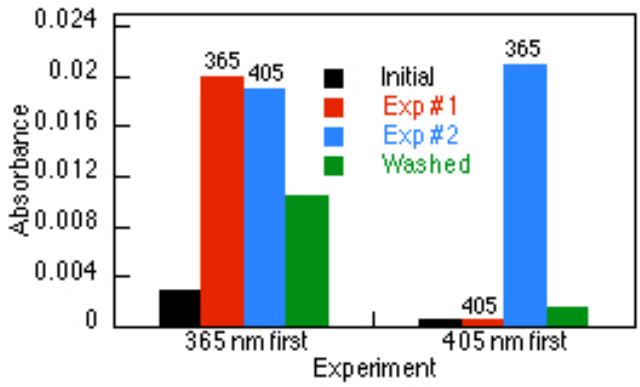

Figure 5.13: Absorbances at 425 nm for the experiment in Figure 5.12 but with the order of irradiation reversed (i.e., 405 nm then 365 nm).

presence of both single particles and small groups of particles as expected from UV-Vis absorption spectroscopy, and is consistent with the broad absorption spectra observed. A cross section is given in Figure 5.15b of the region indicated in Figure 5.15a with a line. The cross section reveals the height of the features scanned, showing varying heights likely due to single particles and variable sizes of multiple particle groups all with a nylon-6 coating. The smallest feature, likely only one particle plus nylon coating, have measured heights that are approximately 25 nm, which represents feature sizes significantly smaller than the diffraction limit for the visible light used to generate them. Measurement of 99 particles from various images led to an average height of 41 $\pm$ 13 nm. There is a significant polydispersity to the particle sizes observed, which is also expected to affect the amount of localized heating around a given nanoparticle or, and therefore the final feature size. While this is a proof of concept of using heat, which is normally considered detrimental to lithography due to expansion, to actually form polymer features in a controlled manner, an ideal experiment would require a higher degree of ordering of nanoparticles as in close packing or self-assembled monolayers.

In order to obtain electron microscope images of the particles with polymer shells we performed a separate experiment in which we used an identical solution as those employed for spin coating. The solution was directly excited with 365 nm LED irradiation for 5 min followed by 405 nm LED irradiation for an additional 5 min in order to perform the same chemistry to first form particles, then a nylon-6 shell, but in colloidal solution. SEM images of the resulting particles were reported as well and are consistent with AgNP

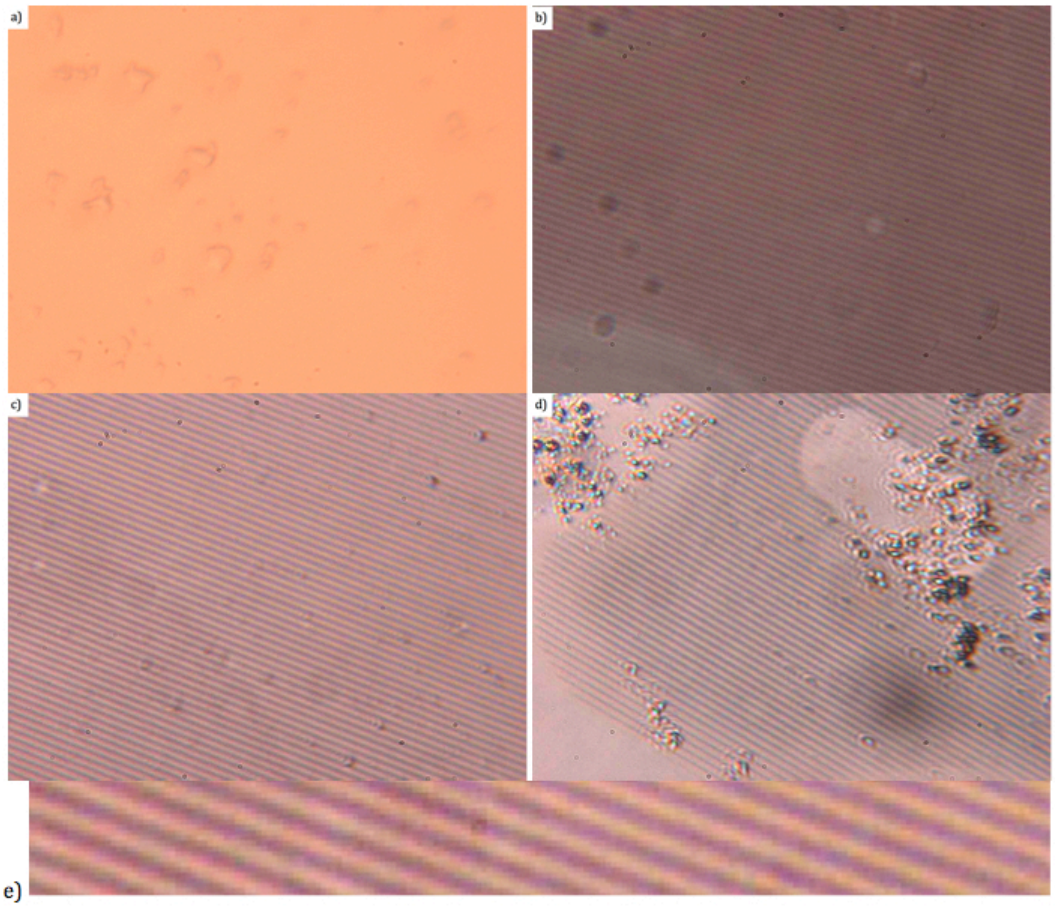

Figure 5.14: Optical microscope image of films (a) after spin-coating, (b) after 365 nm LED irradiation, (c) after 405 nm LED irradiation and (d) after washing with H_2O; (e) is an Expanded Section of Panel (c) emphasizing the quality of the pattern obtained.

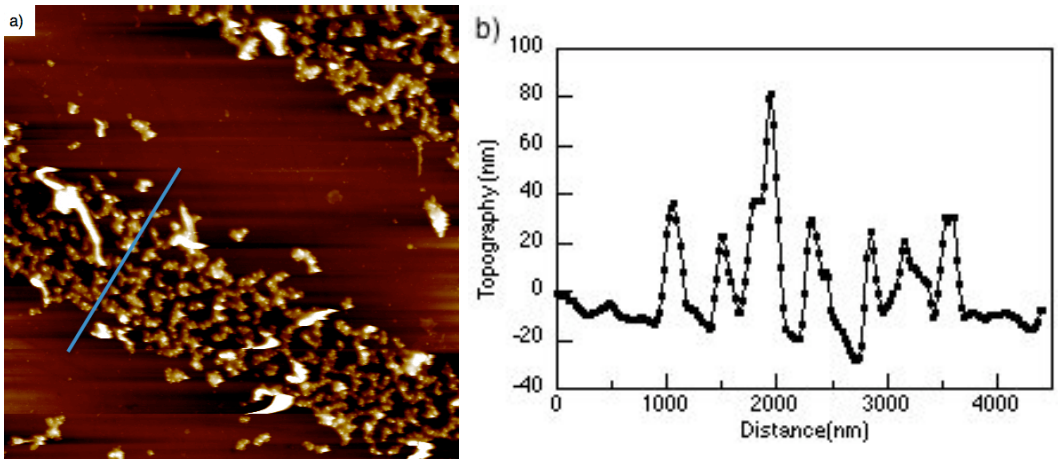

Figure 5.15: (a) Representative AFM image of films after spin-coating, two step irradiation process to generate AgNP and subsequently nylon-6 coating, followed by aqueous washing to selectively remove the caprolactam matrix. (b) A line scan depicting the height of the features in a line as indicated in (a).

cores with polymer grown on the surface.

During irradiation, the heat generated by plasmon excitation was monitored by DSC and the temperature with and without AgNP is shown in Figure 5.16. It is clear that the sample with Ag, and therefore, with a plasmon absorption, generates more heat than the sample without, even when the samples are irradiated with a broad spectrum of light as in the photo-DSC experiments.

To prove that the features were in fact polymer coated particles, coumarin-6 dye (shown below) was incorporated into the polymer film. Coumarin-6 was used because it is has a high quantum yield and well known lifetime of emission and is soluble in the films used. Coumarin-6 was convenient, but many dyes could have been used similarly.

A fluorescence lifetime imaging microscope (FLIM) was used to image the films; 6 μm was chosen here to have a sufficient number of lines to illustrate the process within a single scan window of the FLIM used as shown in Figure 5.17. Film irradiation through a 6 μm mask should enable the visualization of 6 μm wide lines comprised of spots corresponding to silver nanoparticles and a nylon-6 shell; however, the nylon now has trapped coumarin-6 in it, so that the spots appear bright, fluorescent, in the FLIM image. This is shown in Figure 5.17, with a scheme (top) to illustrate the process of trapping dye molecules. The bright lines in Figure 5.17 are in fact comprised of smaller bright

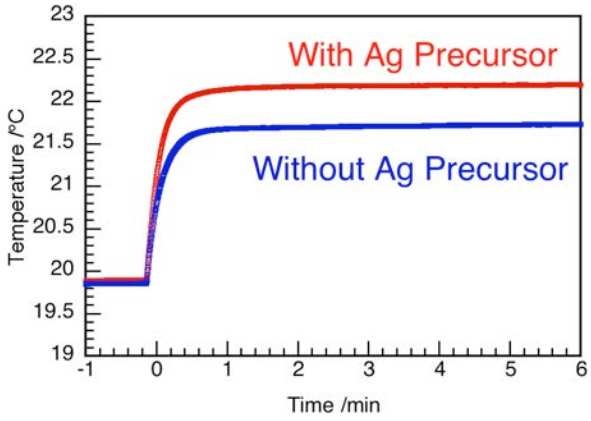

Figure 5.16: Representative DSC curves of Temperature over time when typical solutions for films were used with and without Ag content as indicated, illustrating the effect of plasmon heating on the bulk sample.

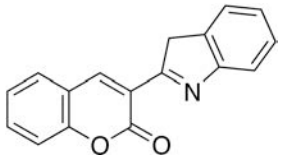

spots where the polymer shells have trapped coumarin-6 around the particles.

The excitation in the FLIM system was from a 375 nm diode laser, and the emission was monitored after a 405 nm long pass filter, that is, the monitoring systems captures emission signals at λ >405 nm. The average lifetime of the emission in Figure 5.17 can be fit to a two-component decay with 3.3 and 1.4 ns lifetimes, as illustrated on the right in Figure 5.18. These lifetimes are reasonable considering that coumarin-6 has a lifetime of 3.3 ns in acetonitrile[44] and that the lifetime (for molecules at the metal surface) should be a shorter lifetime due to quenching with silver nanoparticles. The multicomponent decay seen when nanoparticles are present is due to the interaction of dye with the nanoparticles to shorten the overall lifetime of the excited state.[8, 16] We note that nylon-6 has a much lower T_g temperature than PMMA, something that strongly influences lifetimes.[45]

A blank experiment with only coumarin 6 in the film and no nanoparticles was performed to illustrate the difference when nanoparticles are present. The image and lifetime trace are shown in the right of Figure 5.18. When particles are present the two compo-

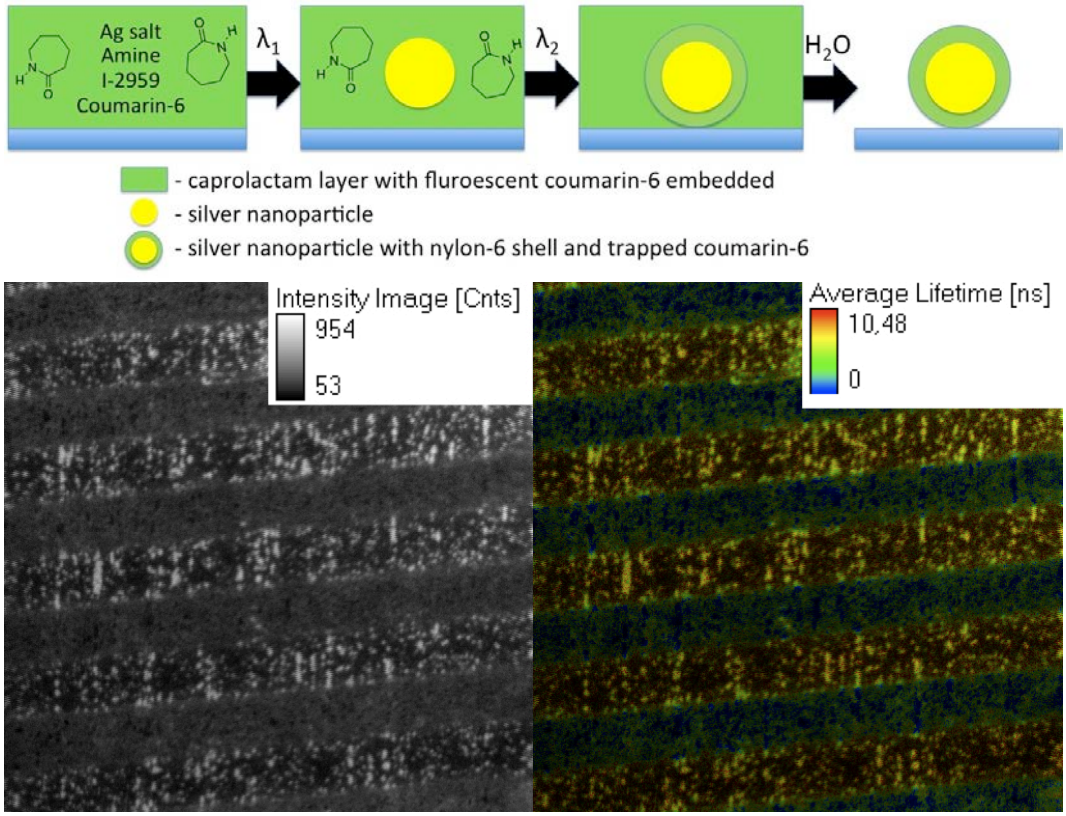

Figure 5.17: Scheme showing the formation of AgNP, followed by a nylon-6 shell due to plasmon heating, and finally a washed film with only the insoluble AgNP/nylon-6 retaining coumarin-6 embedded to give the fluorescence images (top). FLIM images of an 80 x 80 μm area of the films with coumarin-6; intensity image (bottom left), and lifetime image (bottom right) of films after irradiating through a 6 μm mask.

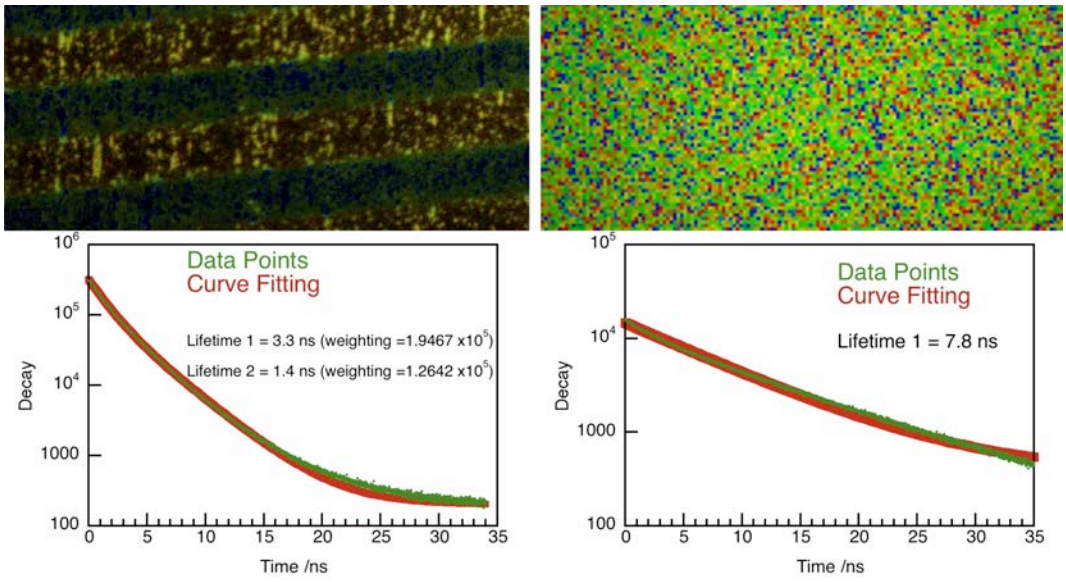

Figure 5.18: Lifetime trace of emission of coumarin-6 trapped in nylon-6 surrounding AgNP as shown in Figure 5.17 (left) and lifetime trace of emission of coumarin-6 in a spin coated PMMA film without nanoparticles (right), with corresponding FLIM images.

nent decay has lifetimes that are both shorter than the 7.8 ns measured for the dye alone in a PMMA film.

The choice of silver here, similar to the work with AIBN in the previous section, is not random and not simply employed because of our work with AgNP. Silver, like gold and copper nanoparticles absorb visible light, which is a convenient and inexpensive spectral region to both characterize and selectively irradiate. Further, of the three noble metals commonly used for their convenient visible absorptions, silver has the highest cross section for absorption, which, combined with its high energy (short wavelength) plasmon, results in the most efficient heat generation.[46] As noted the selection of 3 μm features allows visualization using both optical microscopy and AFM and serves as a proof of concept; 3 μm and 6 μm do not represent a resolution limit.

In summary, a two-step irradiation process is used to generate a dense concentration of AgNP with controlled spatial resolution by irradiating through a lithographic mask and initiating a radical mediated Ag^+ reduction, and, second to induce polymerization of caprolactam to nylon-6 in a thermal plasmon-activated process selectively on the surface of the AgNP. This two-step approach allows for microscopic control of positioning of the

features, and subsequently, generation of sub-diffraction limit nylon shells using plasmon excitation.

5.4.3 Conclusions

Whether polymer features are made by enhancing electronic transitions or by exploiting the extreme heating, one obvious criticism arises from these examples. The polymer features are made on the surface of randomly distributed particles. To implement this type of chemistry into a real working lithographic technology, there must be much better control of the positioning of particles with respect to each other, and with macroscopic ordering, in order to control the positioning of polymer features. If this type of control over particle positioning can be achieved, this will have dramatic effects on the plasmon absorption of the particle films, due to coupling of neighbouring plasmon fields.

The work here, however, is a proof of concept that photolithography can be done without a traditional mask, and therefore not reliant on the diffraction limit. Previously, the only sub-diffraction limit lithography shown was two-photon chemistry, that still had larger features than the features described in this chapter. The major contributions to the field discussed here are that plasmon excitation can be used to generate polymer features, even without two photon chemistry, in processes that are fundamentally NOT diffraction limited. The polymer features can be made by radical chemistry or by the extreme heat released upon plasmon excitation. The second process that uses plasmon heating also shows a higher level of control of positioning of the features, since the particles can be made lithographically, however the diffraction limit is in fact "limiting" then, in the formation of these features.

REFERENCES

[1] U Okoroanyanwu. *Chemistry and Lithography*. SPIE and John Wiley and Sons, 2010.

[2] GM Wallraff and WD Hinsberg. Lithographic imaging techniques for the formation of nanoscopic features. *Chemical Reviews*, 99(7):1801–1821, 1999.

[3] O Süss. über die natur der belichtungsprodukte von diazoverbindungen. übergänge von aromatischen 6-ringen in 5 ringe. *Justus Liebigs Annalen der Chemie*, 556(1):65–84, 1944.

[4] J Pacansky and D Johnson. Photochemical studies on a substituted naphthalene-2,1-diazooxide: The formation and identification of a ketene from a Wolff rearrangement. *Journal of the Electrochemical Society*, 124(6):862–865, 1977.

[5] J Pacansky and JR Lyerla. Photochemical decomposition mechanism for AZ-type photoresists. *IBM Journal of Research and Development*, 23(1):42–55, 1979.

[6] CN Sanrame, MSB Brandao, C Coenjarts, JC Scaiano, G Pohlers, Y Suzuki, and JF Cameron. Mechanism of photoacid generation for an arylcycloalkylsulfonium salt by ring opening and aryl cleavage. *Photochemical and Photobiological Science*, 3(11-12):1052–1057, 2004.

[7] GE Moore. Cramming more components onto integrated circuits. *Electronics*, 38(8):1–4, 1965.

[8] P Anger, P Bharadwaj, and L Novotny. Enhancement and quenching of single-molecule fluorescence. *Physics Review Letters*, 96(11):113002, 2006.

[9] Eduardo A Coronado, Ezequiel R Encina, and Fernando D Stefani. Optical properties of metallic nanoparticles: manipulating light, heat and forces at the nanoscale. *Nanoscale*, 3(10), 2011.

[10] Chiara Fasciani, Carlos J Bueno Alejo, Michel Grenier, Jose Carlos Netto-Ferreira, and J. C Scaiano. High-temperature organic reactions at room temperature using plasmon excitation: Decomposition of dicumyl peroxide. *Organic Letters*, 13(2):204–207, 2011.

[11] KG Stamplecoskie C Fasciani and JC Scaiano. Dual-stage lithography from a light-driven, plasmon-assisted process: A hierarchical approach to subwavelength features. *Langmuir*, 28(30):10957–10961, 2012.

[12] KG Stamplecoskie, NL Pacioni, D Larson, and JC Scaiano. Plasmon-mediated photopolymerization maps plasmon fields for silver nanoparticles. *Journal of the American Chemical Society*, 133(24):9160–3, 2011.

[13] A Moores and F Goettmann. The plasmon band in noble metal nanoparticles: an introduction to theory and applications. *New Journal of Chemistry*, 30(8):1121–1132, 2006.

[14] R Aroca. *Surface-Enhanced Vibrational Spectroscopy*. Wiley, 2006.

[15] KG Stamplecoskie, JC Scaiano, VS Tiwari, and H Anis. Optimal size of silver nanoparticles for surface-enhanced raman spectroscopy. *Journal of Physical Chemisty C*, 115(5):1403–1409, 2011.

[16] Natalia L Pacioni, María González-Béjar, Emilio Alarcón, Katherine L McGilvray, and J C Scaiano. Surface plasmons control the dynamics of excited triplet states in the presence of gold nanoparticles. *Journal of the American Chemical Society*, 132(18):6298–6299, 2010.

[17] JR Adleman, DA Boyd, DG Goodwin, and D Psaltis. Heterogenous catalysis mediated by plasmon heating. *Nano Letters*, 9(12):4417–4423, 2009.

[18] ABS Bakhtiari Bakhtiari, D Hsiao, G Jin, BD Gates, and NR Branda. An efficient method based on the photothermal effect for the release of molecules from metal nanoparticle surfaces. *Angewandte Chemistry International Edition*, 48(23):4166–4169, 2009.

[19] Hideki Nabika, Mai Takase, Fumika Nagasawa, and Kei Murakoshi. Toward plasmon-induced photoexcitation of molecules. *Journal of Physical Chemistry Letters*, 1(16):2470–2487, 2010.

[20] JA Schuller, ES Barnard, W Cai, YC Jun, JS White, and ML Brongersma. Plasmonics for extreme light concentration and manipulation. *Nature Materials*, 9(3):193–204, 2010.

[21] KG Stamplecoskie and JC Scaiano. Light emitting diode irradiation can control the morphology and optical properties of silver nanoparticles. *Journal of the American Chemical Society*, 132(6):1825–1827, 2010.

[22] KL McGilvray, MR Decan, D Wang, and JC Scaiano. Facile photochemical synthesis of unprotected aqueous gold nanoparticles. *Journal of the American Chemical Society*, 128(50):15980–15981, 2006.

[23] OB Uzum and E Karadag. Equilibrium swelling studies of chemically cross-linked highly swollen acrylamide-sodium acrylate hydrogels in various water-solvent mixtures. *Polymer-Plastics Technology and Engineering*, 49:9609–9616, 2010.

[24] HJ Hageman and LGJ Jansen. Photoinitiators for radical polymerization which counter oxygen-inhibition. *Makromolekulare Chemie*, 189(12):2781–2795, 1988.

[25] A Aspee, O Garcia, L Maretti, R Sastre, and JC Scaiano. Free radical reactions in poly(methyl methacrylate) films monitored using a prefluorescent quinoline-TEMPO sensor. *Macromolecules*, 36(10):3550–3556, 2003.

[26] BK Moser, GR Stevens, and CL Watts. The two-sample t test versus satterthwaite's approximate f test. *Communications in Statistics - Theory and Methods*, 18(11):3963–3975, 1989.

[27] BK Moser and GR Stevens. Homogeneity of variance in the two-sample means test. *American Statistics*, 46(1):19–21, 1992.

[28] GD Ruxton. The unequal variance t-test is an underused alternative to student's t-test and the Mann Whitney U test. *Behavioral Ecology*, 17(4):688–690, 2006.

[29] C Aprile, A Corma, ME Domine, H Garcia, and C Mitchell. A cascade aerobic epoxidation of alkenes over Au/CeO_2 and Ti-mesoporous material by in situ formed peroxides. *Journal of Catalysis*, 264(1):44–53, 2009.

[30] S Zou and GC Schatz. Silver nanoparticle array structures that produce giant enhancements in electromagnetic fields. *Chemical Physics Letters*, 403(1-3):62–67, 2005.

[31] K Ueno, S Takabatake, Y Nishijma, V Mizeikis, Y Yokota, and H Misawa. Nanogap-assisted surface plasmon nanolithography. *Journal of Physical Chemistry Letters*, 1(3):657–662, 2010.

[32] C Farcau and S Astilean. Silicon nanoparticles produced by femtosecond laser ablation in ethanol: Size control, structural characterization, and optical properties. *Journal of Physical Chemistry C*, 114(36):15266–15273, 2010.

[33] A Ben-Yakar, D Eversole, and O Ekici. *Spherical and Anisotropic Gold Nanoparticles in Plasmonic Laser Phototherapy of Cancer. In Non-Magnetic Metallic Nanomaterials for Life Science*, volume 10. John Wiley and Sons, 2008.

[34] C Deeb, C Ecoffet, R Bachelot, J Plain, A Bouhelier, and O Soppera. Plasmon-based free-radical photopolymerization: Effect of diffusion on nanolithography processes. *Journal of the American Chemical Society*, 133(27):10535–10542, 2011.

[35] JC Scaiano, M Laferriere, MG Ivan, and GN Taylor. A protocol for the verification of acid generation in 157 nm lithography. *Macromolecules*, 36(18):6692–6694, 2003.

[36] JC Scaiano and GL Hallett-Tapley KG Stamplecoskie. Photochemical Norish type I reaction as a tool for metal nanoparticle synthesis: Importance of proton coupled electron transfer. *Chemical Communications*, 48:4798–4808, 2012.

[37] L Maretti, PS Billone, Y Liu, and JC Scaiano. Facile photochemical synthesis and characterization of highly fluorescent silver nanoparticles. *Journal of the American Chemical Society*, 131(39):13972, 2009.

[38] S Jockusch, MS Landis, B Freiermuth, and NJ Turro. Photochemistry and photophysics of R-hydroxy ketones. *Macromolecules*, 34:1619–1626, 2001.

[39] RZ Greenly, JC Stauffer, and JE Kurz. The kinetic equation for the initiated, anionic polymerization of ϵ-caprolactam. *Macromolecules*, 2(6):561–567, 1969.

[40] HK Reimschuessel. Caprolactam polymerization. *Journal of Polymer Science*, 41(138):457–466, 1959.

[41] M Quinten. The color of finely dispersed nanoparticles. *Applied Physics B: Lasers and Optics*, 73(4):317–326, 2001.

[42] L Mulfinger, SD Solomon, M Bahadory, AV Jeyarajasingam, SA Rutkowsky, and C Boritz. Synthesis and study of silver nanoparticles. *Journal of Chemical Education*, 84(2):322, 2007.

[43] ER Encina and EA Coronado. Plasmon coupling in silver nanosphere pairs. *Journal of Physical Chemistry*, 114(9), 2010.

[44] G Jones, WR Jackson, CY Choi, and WR Bergmark. Sovent effects on emission yield and lifetime for coumarin laser dyes. requirements for a rotatory decay mechanism. *Journal of Physical Chemistry*, 89(2):294–300, 1985.

[45] JY Ye, T Hattori, H Nakatsuka, and Y Maruyama. Microscopic dynamics of the glass transition investigated by time-resolved fluorescence measurements of doped chromophores. *Physics Reviews B*, 56(9):5286–5296, 1997.

[46] K Tanabe. Field enhancement around metal nanoparticles and nanoshells: A systematic investigation. *Journal of Physical Chemistry C*, 112(40):15721–15728, 2008.

Chapter 6

Spasers

6.1 Plasmon Induced Polymerization As a Route to Self-Assembled Dipole Nanolasers

Much of the discussion in the chapters until now has described the controlled synthesis of AgNP, where the shape and size of the particles has been used to control the optical properties of the material. Here, it is shown how critical these factors are in the synthesis and function of some novel optically active materials, "spasers". Briefly, the spaser is a surface plasmon amplification by stimulated emission of radiation, and it requires composite materials made of a metal that supports a plasmon and a gain material, such as a dye, where the plasmon and dye overlap spatially and spectrally. Plasmons are an evanescent wave that decays with an exponential relationship from the surface of a nanoparticle, but if a dye molecule, which is within this plasmon field, and if that dye has an absorbance/emission that overlaps with the plasmon frequency the two can couple and transfer energy reversibly between each other. It is clear then that the spectral control described in earlier chapters that is obtained from shape control of AgNP is important in controlling the spectral overlap with chosen dyes; the situation is depicted in Figure 6.1.

A body of experimental evidence for the coupling of surface plasmon polaritons (SPP) with emitters for optical gain (mostly performed for the coupling of long-range SPP (LR-SPP)) with gain media provides the foundation for the development of dipole nanolasers. The first reported use of LRSPP for gain was by Plotz et al. in 1979, where they described amplified total reflection for a metal slab in contact with glass at varying angles.[1] Sudarkin and Demkovic later suggested lasing from SPP based on this work.[2] Siedel et

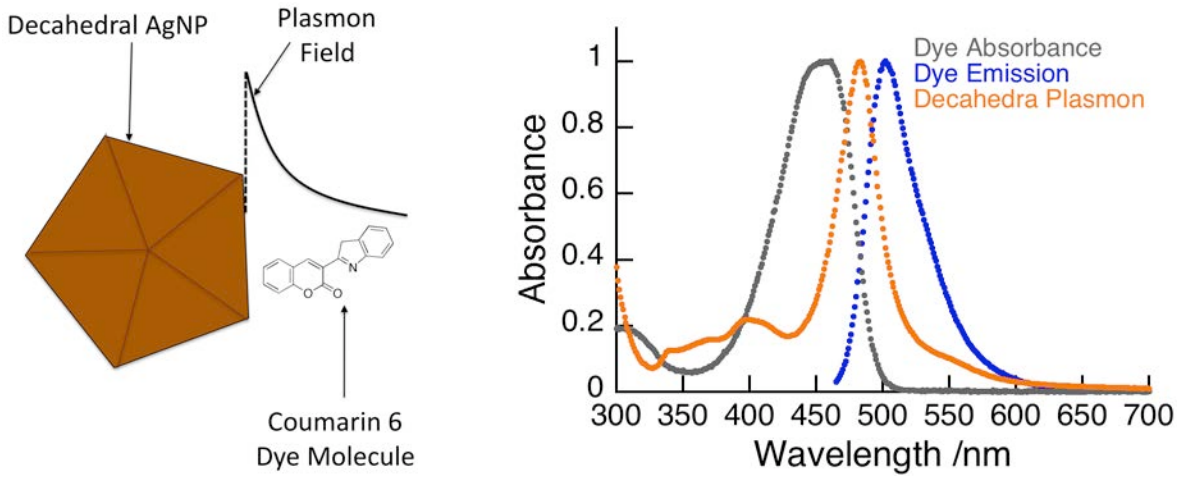

Figure 6.1: Example of spatial and spectral overlap of an decahedral AgNP with Coumarin 6, where the dye is within the field of the plasmon (left) so that the two can interact to transfer energy resonantly and reversibly.

al. first demonstrated spontaneous emission of SPP by flowing solutions of cresol violet and Rhodamine 101 over a silver film where non-zero changes in reflectance as a function of excitation angle were attributed to stimulated emission of the SPP through coupling with the dye as a gain medium.[3] The works discussed here are a small sampling of the research devoted to understanding the coupling of emitters/dipoles with SPP. Stockholm and others had theoretically predicted spontaneous emission of surface plasmons for similar plasmonic structures.[4, 5] In order to observe laser-like behaviour from plasmonic particles, the particles are required to be in close proximity to a gain medium, where the surface plasmon must overlap with the emitters both spectrally and spatially. Thus particles must be in close proximity to the emitters in the gain medium so that the plasmon field (that decays rapidly with distance from the surface, like all evanescent fields) overlaps with the emitters. The emission spectrum must have significant overlap with the plasmon resonance, such that the two can couple strongly; this is in fact not a difficult set of requirements. For example, in the work by Noginov et al., gold nanoparticles were chosen, with a broad plasmon resonance centred around 530 nm, and capped with a silica shell containing a high concentration of Oregon Green-488 dye (520 nm emission maximum) embedded in the SiO_2. This system fulfilled both requirements of spectral and spatial overlap between the plasmonic particles and the gain medium (dye molecules).[6]

A laser needs two fundamental components, a resonator (or feedback) and a gain medium, usually provided by a dye or semiconductor material. In the dipole nanolaser, metal nanoparticles can serve as the resonator, confining light of a given frequency, and the gain medium can consist of a large number of nearby dye molecules that couple to the nanoparticle. Increased excitation intensities result in stronger enhanced near-field effects, and therefore, drastically stronger excitation of the gain medium, that feeds energy through strong resonant coupling back into the surface plasmon. This is the feedback mechanism. Above a certain pumping threshold of excitation an instability arises in surface plasmon excitation (resulting from energy transfer from the gain medium) and emission of coherent surface plasmon, in other words lasing, is observed.[7] One of the characteristic features of this type of stimulated emission is the periodic fluctuation observed in emission vs. time traces.[4, 5, 8, 7]

It has been theoretically predicted that a single dipole interacting with a plasmon can produce the same effect, which was later disproven, as it was shown that many emitters in the gain medium are required to realize spontaneous emission of surface plasmons.[7, 9] It was also predicted that a quantum dot and metal nanoparticle bound together and with good overlap of the QD emission and metal particle plasmon could produce the dipole nanolaser effect, but this was also questioned due to the small separation of dipoles in such a system.[7, 9] Therefore, while experimentally involved, the spaser reported by Noginov et al. remains the only reported spaser to date. Thus, we have combined plasmonic nanoparticles with many dye molecules physically trapped in close proximity, but using a synthetically facile and versatile methodology, based on a self-assembly strategy.

Metal-oxide field effect transistors (MOSFET) are the active gain component that has been the enabling feature for conventional microelectronics, but they are reaching fundamental limits. It has been postulated that an active gain component for optoelectronics, such as the dipole nanolaser, could bring optoelectronics to the same level of performance.[7] Common lasers cannot be used as nanoamplifiers, because the resonator must be at least half of the wavelength of light, even though the smallest lasers are still much larger than this. The feedback in a SPP is much different, it is a periodic oscillation of electrons confined to the nanoparticle, and so the dimensions restricted by the size of the particle. However, the feedback is therefore an inherent property of the resonator, without external control, so that one might assume that nanoparticles cannot serve as nanoamplifiers, since the net amplification must be zero (an intrinsic property of CW lasers). As described by Stockman, however, the spaser can be operated in a time resolved mode. In this way, a short light pulse can cause a temporary instability

(population inversion) and result in net amplification. In other words, when pumping levels are low, and the spaser is not receiving the pulse of excitation, the spaser acts as a transistor in the "off state", analogous to a field effect transistor with no current flowing. However, when the pump pulse occurs, net amplification and a coherent plasmon is generated giving stimulated emission, which is analogous to the "on state" in a conventional transistor. This becomes clear when looking at the lifetime traces for emission of a spaser shown here and in Noginov's work, where below the pumping threshold for lasing, the dye shows a normal decay, whereas above this threshold, there is a delayed stimulated emission, which can serve as the signal when working as a nanoamplifier. Therefore, in time-gated operation, the spaser can in fact behave as a nanoamplifier.

The seminal work by Noginov et al. assembling the spaser using Au/silica/dye core-shell nanoparticles, requires significant synthetic time and skill. The goal of this chapter is to show our work towards a simple method for synthesizing dipole nanolasers with silver nanoparticles (AgNP) and a gain media. The technique uses visible light to induce self-assembly of polymer shells, which then spontaneously trap dye molecules around the particles as the gain medium. This technique uses optical synthesis of the particles/shells, which not only provides spatial and temporal resolution for synthesis, but is compatible with current photolithographic techniques, and could therefore be easily integrated for optoelectronic devices. We have recently reported on the use of silver nanoparticle (AgNP) plasmon excitation to enhance electronic transitions and result in selective polymerization on the surface of AgNP.[10] That work relied on radical chemistry to induce polymerization, and while it was a proof of principle it can be used with other radical initiators for similar results. Plasmon excitation is also known to relax predominantly by photothermal heat release.[9] The use of plasmon heating to polymerize caprolactam to nylon-6, forming a nylon shell on AgNP, was described earlier.[11] Here, this technique of localized optical heating for the generation of nylon-6 polymer shells is used again, but with carefully chosen dye molecules entrapped in the matrix, and particles with optimal shapes and optical properties to overlap with dye molecule absorbance. The AgNP shapes were also made by LED irradiation as described previously to obtain the desired decahedra (as well as plates when required).[12] Upon polymerization, the molecules in the matrix including dyes are fixed in the polymer layer around the particles, thus forming dipole nanolasers in self-assembled, light-induced processes.

The example shown here uses the heat generated by plasmon excitation for formation of nylon-6 shells around decahedral AgNP. More specifically we trap coumarin 6 as the dye molecule, in self-assembled nylon-6 features around the AgNP, as shown in Figure

6.2. Coumarin 6 is omitted from the scheme because it does not play a roll in the reaction, but it is embedded in the polymer to later act as the active gain component.

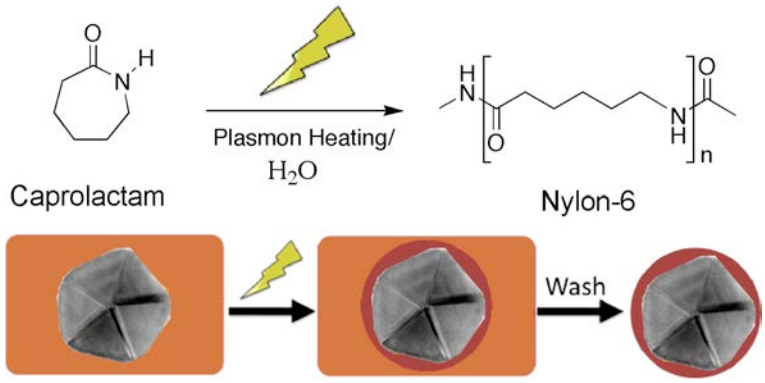

Figure 6.2: Scheme describing how plasmon excitation leads to extreme local heating that consequently polymerizes caprolactam to nylon-6 on the surface of the nanoparticles, trapping coumarin-6 in this insoluble polymer layer.

6.1.1 Experimental

Typical solutions containing less than 1% Ag decahedra, 2% coumarin 6, 50% caprolactam and acetonitrile as the solvent were spin-coated at 2500 rpm onto one inch quartz disks and irradiated with a 465 nm LED to form a polymer shell through plasmon heating (see 5.11 for experimental setup for LED irradiation). The reaction in the film was monitored by UV-Vis spectroscopy, showing that coumarin 6 (in the nylon-6 shell) is retained on the films after plasmon heating, even after the monomer has been removed. This methodology takes advantage of conventional lithographic type techniques, where a solubility switch is provided by light-induced polymerization and the monomer is removed in a washing step.[13] These particles were examined with Fluorescence Lifetime Imaging Microscopy (FLIM) and show bright spots where the dipole nanolasers are retained and dark areas around the spots where the non-polymerized film has been removed by washing (see Figures 6.2 and 6.3).

After spin-coating solutions onto quartz disks, the disks were irradiated with LED. For the formation of nylon-6 shells on decahedral particles, 505 nm LED excitation was used to selectively excite the particle plasmon. Selective excitation of the plasmon results in heating of the film only at the surface of the nanoparticle and therefore, polymerization

only around the particles. The chemistry for making nylon-6 features around decahedral particles can also be done directly with the solutions used for spin coating, with polymer shells grown on particles in solution by the same plasmon excitation. These particles with polymer shells could be centrifuged and re-suspended several times in acetonitrile to remove unreacted caprolactam and coumarin 6 not trapped in the shell around the particles. This made it possible to image the particles by SEM and TEM, as well as fluorescence microscopy.

To illustrate the versatility of this technique in making dipole nanolasers, acrylic polymer shells on Ag nanoplates were also assembled, in this case using plasmon enhanced electronic transitions for the self-assembly. In these experiments Ag nanoplates were used that have an absorption maximum at approximately 700 nm to better enhance transitions in the dye selected. Trimethylolpropane triacrylate was used as a monomer, and Eosin Y, with equimolar methyldiethanolamine were used as both radical initiator for the polymerization process and later as the dye for the gain medium. A solution containing ¡1% Ag nanoplates, 3% Eosin Y, 4% methyldiethanolamine, 40% trimethylpropane triacrylate, and acetonitrile as solvent, was then spin-coated at 2500 rpm onto a quartz disk and irradiated with a 590 nm LED. The films were washed with ethanol to remove any unpolymerized TMPTA and dye. The process was monitored by UV-Vis Spectroscopy. With washing in ethanol, unreacted acrylate, amine and Eosin Y (not near the surface of Ag nanoplates) is removed, leaving behind Ag nanoplates with acrylic shells containing high concentrations of EY.

6.1.2 Results and Discussion

Transmission (TEM), back scattering (SEM) and, energy loss back scattering COMPO SEM images of the particles are shown in Figure 6.3, illustrating the polymer shell on the decahedral particles. The back scattering SEM image in Figure 6.3 (top left) shows mostly the surface of the particle/shell, with only a slightly higher interaction of the electron beam with the metal centre. Transmission images, on the other hand (Figure 6.3, top middle) show clearly the decahedral particle core with a lighter polymer shell. COMPO images, like the one shown in Figure 6.3, top right, give bright spots for regions with energy loss for the electron beam that is due to heavy elements like Ag, thus showing the Ag core of the particles; note the clear pentagonal profile of the core. Figure 6.3 shows a single representative particle , but the particles were homogeneously coated with nylon shells, as seen in images of multiple particles with nylon-6 shells (Figure

6.4). Figure 6.3 also includes a UV-Vis absorption spectrum for the decahedral particles, absorption/emission spectra for coumarin 6, a FLIM image of bright dipole nanolaser spots, and a typical lifetime trace for the decahedra@nylon-6/coumarin 6 nanolasers.

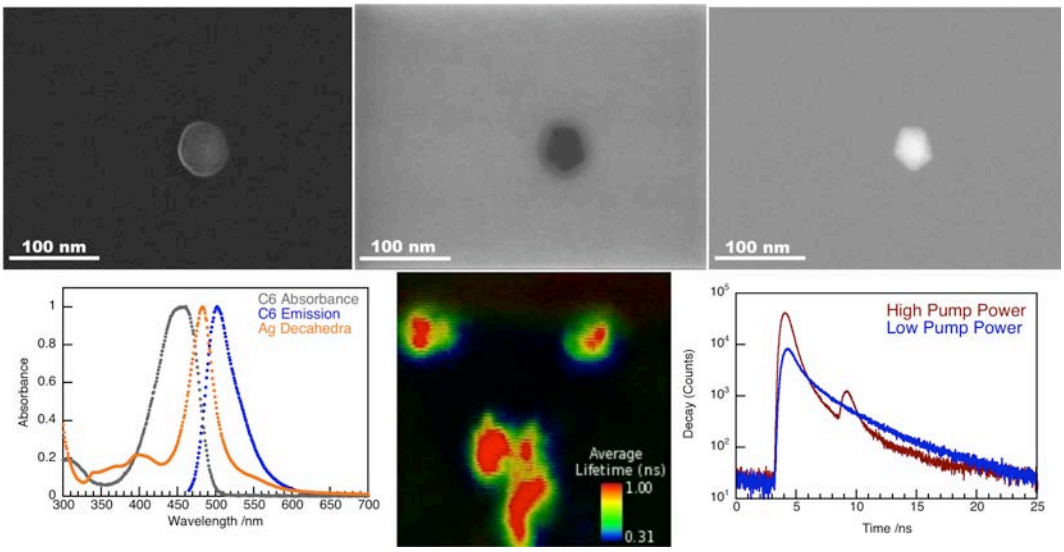

Figure 6.3: SEM back scattering image (top left), transmission (top middle) and COMPO (top right) images of the same single decahedral AgNP with a nylon-6 shell. Normalized UV-Vis absorption spectra of decahedral AgNP and coumarin 6, as well as emission spectrum of coumarin 6 (bottom left), FLIM images of the particles after the polymerization/washing procedure (bottom middle), and fluorescence lifetime traces of representative spots in the FLIM images above and below the lasing threshold (bottom right).

For FLIM measurements, above and below the pumping threshold for lasing, two arrangements were used for the instrumental setup. When obtaining the fluorescence lifetime traces above and below the pumping threshold, OD 3 filters were used. In the case where the pumping is below the threshold, the filter is placed in the excitation beam path, before the excitation beam hits the sample, as shown here (note the position of the OD3 filter):

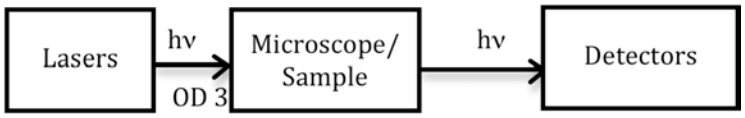

When pumping is required to be above the threshold for lasing, a neutral density OD 3 filter is placed in the beam path after the sample, but before the detector, as shown here (again note the position of the OD 3 filter):

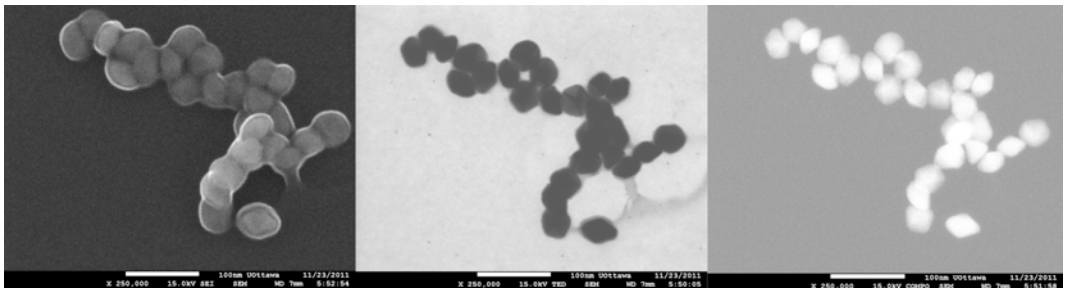

Figure 6.4: SEM images of the same group of decahedra, imaged by SEI, COMPO and TED that help to illustrate the polymer coating, not seen by COMPO, and seen clearly by SEI.

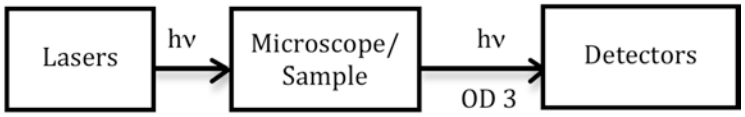

The overall beam intensity was held constant in both cases receiving the same total attenuation (OD3) before reaching the detector, but for pumping above the threshold the samples experienced 1000x the excitation. This was done by placing an neutral density OD3 filter either before the sample (for low excitation) or after the sample, in the fluorescence signal path (for excitation above the threshold for lasing). The integrated intensity of the lifetime trace is stronger when above the lasing threshold, as expected, since the whole system is based on gain of total emission. Also important to note is that neither of the decay profiles fit well to a single exponential decay, whereas coumarin 6 alone in a caprolactam film does fit monoexponential kinetics. This difference is another indication that the polymer films are in fact a shell-like coating that trap the dye molecule near the AgNP, since the energy transfer from the dye molecules to the AgNP results in a non-monoexponential decay of the dyes.[14]

The realization of a metal nanoparticle dipole nanolaser requires a gain medium (in this case dye molecules) which meets two criteria: (1) The metal nanoparticle are surrounded by many dye molecules close enough to the particle to couple with plasmon modes. (2) There is dye emission in a spectral region with significant overlap with the particle plasmon absorption. The decahedral particles with coumarin-6 trapped around them meet both of these requirements, with particular reference to the SEM images that show the polymer shells around decahedral particles, as well as the spectra in Figure 6.3 that show significant overlap between the plasmon absorption of the silver particles and

the emission spectrum of coumarin-6.

Radical polymerization can be used to generate dipole nanolasers as well, but these dyes were chosen as radical initiators which means they are reactive and not as robust as the nylon-6 system described here; further, since dyes with extended π conjugation are known to react with radicals, significant bleaching of dyes results.[15] EY/radical polymerization to form acrylate shells on Ag nanoplates, was done with 590 nm LED excitation was used in the same setup as the formation of coumarin-6/Ag decahedra nanolasers.

Unlike the coumarin 6/decahedra dipole nanolasers, with EY/AgNanoplates, the dye emission does not have a large overlap with the plasmon absorption of the Ag nanoplates. This combination was chosen to minimize dye and plasmon absorption during photochemical synthesis, such that the dye forms radicals selectively in the enhancement region around the particle surface forming an acrylate shell (Scheme 6.5).[10] This synthetic requirement, requires a large Stokes shift for dye emission to overlap strongly with the Ag plate plasmon absorption. Even with imperfect overlap of the Ag plate plasmon and the dye emission, there is enough coupling to result in lasing as evidenced by the multiple peaks in the emission lifetime trace at high pump powers.

The FLIM instrumentation allows for obtaining a spectrum of the emission as well. The emission spectra for both spaser assemblies are shown in Figure 6.6. For high energy density pumping of the spasers a narrow and intense emission spectrum is expected. The emission spectra for both dipole nanolaser assemblies do not show a narrow but intense emission spike for the spasing mode, in contrast with the work by Noginov et al.[6] The emission bandwidth is intimately related to the excitation pulse duration and energy (energy density), which give a lower peak pulse intensity in our work.[4] Also, Rosenthal et al. show that this avalanche of emission with a broad spectrum is in fact expected for dipole nanolasers, and only significantly above the lasing threshold, with multiple emitters in the gain medium, and with spatial separation between the emitter dipole and the plasmon, does the emission spectrum narrow as seen by Noginov.[5]

To ensure that bright spots were not obtained in films that did not have particles, and were not subjected to the polymerization process, blank experiments were conducted without putting Ag particles in the spin-coating solutions, and without washing (because nothing was retained on the films without Ag present). Representative images and lifetimes for these respective films are shown below. As expected, there are no bright spots, but rather a very homogeneous emission from the films. Also, the lifetime of each dye now has a monoexponential decay profile, as expected without particles. Since

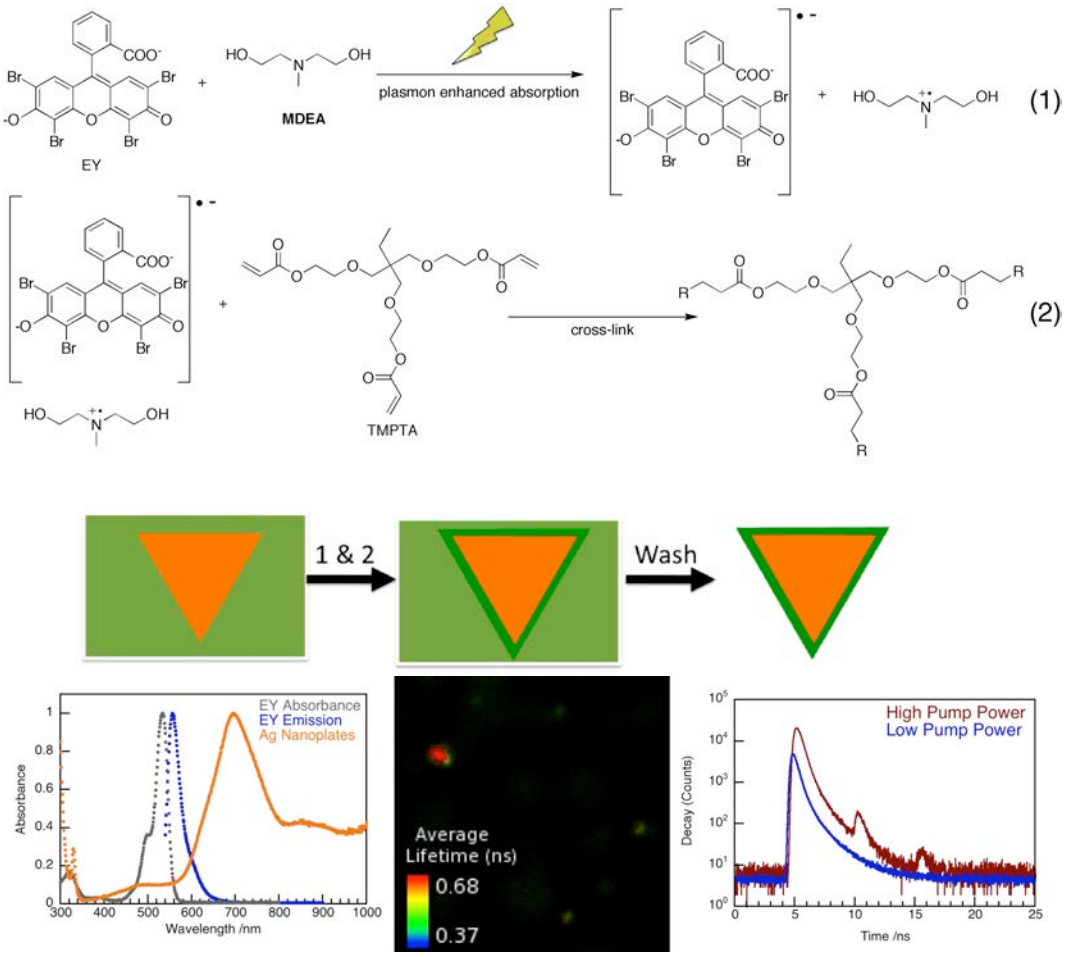

Figure 6.5: Scheme describing the synthetic steps for plasmon enhanced radical polymerization of acrylate features around Ag nanoplates, using and trapping eosin Y in the acrylate shell. UV-Vis absorption spectra for EY and Ag plates in solution, and emission spectrum for EY as indicated (bottom left), FLIM image of dipole nanolasers retained after synthesis/washing (bottom middle), and lifetime trace of bright spots in FLIM images above and below the threshold for lasing (bottom right).

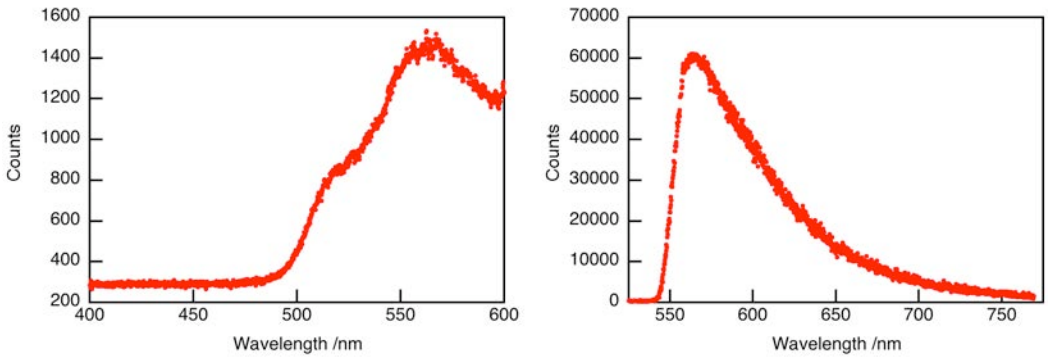

Figure 6.6: Emission spectra obtained using the FLIM, with a spectrograph coupled to the signal output to record spectral information on the emission from the nanolasers that are imaged. Left: Coumarin-6/AgDecahedra spasers emission spectrum and Right: Eosin Y/Ag nanoplates spaser emission spectrum.

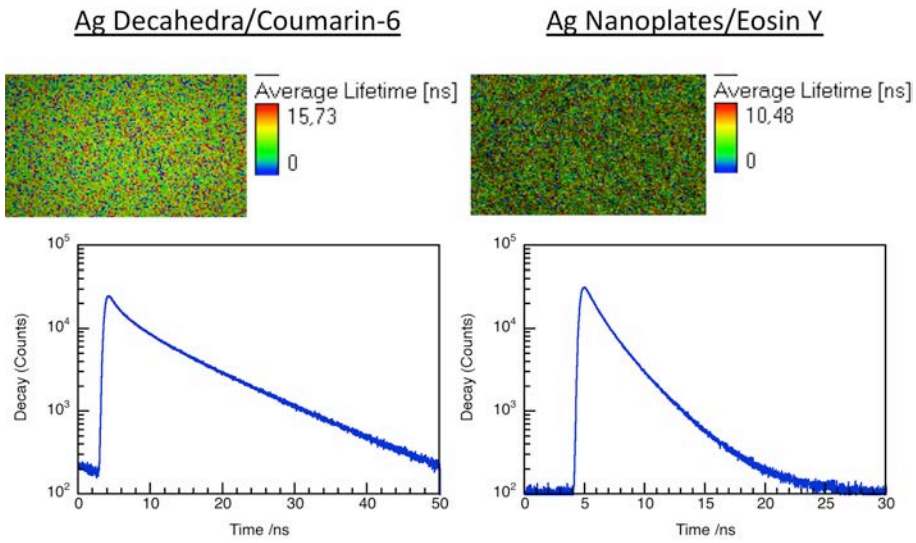

Figure 6.7: Images and lifetime traces for blank films containing respective dyes where the images show no intense emission, and the lifetime is a monoexponetial decay in both cases without the formation of nanolasers. Note the absence of discrete bright spots.

particles quench emission of the dye (one of the main processes required for energy transfer, and therefore lasing) even at low powers it is expected that the emission of dye molecules in the vicinity of AgNP will not have a monoexponential decay. The non-monoexponential decay in the spasers (Figures 6.3 and 6.5), is another indication that the dye molecules are in fact trapped in polymer that is surrounding AgNP.

6.1.3 Conclusions

Overall, a simple technique for fabrication of dipole nanolasers are presented. The self-assembly strategy uses fundamental properties of metal nanoparticles, the heat released upon plasmon excitation and the electromagnetic field enhancement in close proximity to excited metal particle surfaces. The method uses inexpensive LED irradiation of simple solutions to generate dipole nanolasers, that have immense potential in optoelectronics. Recent advances in AgNP research have lead to a number of techniques to control the morphology, and therefore optical properties of various shapes of AgNP with a diversity of surface functionalization. These particles can therefore be selected for desired optical properties and combined with numerous dyes for optimizing the active gain using the techniques illustrated here. One only needs to select the desired spectral properties. The technique is not only simple and versatile, it also has spatial and temporal control of the synthesis, and is fully compatible with current lithographic fabrication techniques.

This work represents the first report of a spasers made in a simple, light-induced self-assembly process, and as such provide a means to fabricating coherent plasmon fields for optoelectronics with the spatial and temporal control required advanced lithography. It is expected that this work will constitute a major contributions to optoelectronics research, especially since these active gain components are the limiting requirement for optoelectronics.

REFERENCES

[1] GA Plotz, HJ Simon, and JM Tucciarone. Enhanced total reflection with surface-plasmons. *Journal of the Optics Society of America*, 69:419–421, 1979.

[2] A N Sudarkin and P A Demkovich. Excitation of surface electromagnetic waves on the boundary of a metal with an amplifying medium. *Soviet Physics Technical Physics*, 34(7):764–766, 1989.

[3] J Seidel, S Grafström, and L Eng. Stimulated emission of surface plasmons at the interface between a silver film and an optically pumped dye solution. *Physics Review Letters*, 94(17):4, 2005.

[4] D J Bergman and M I Stockman. Surface plasmon amplification by stimulated emission of radiat ion: Quantum generation of coherent surface plasmons in nanosystems. *Physics Review Letters*, 90(2):027402, 2003.

[5] A Rosenthal and Talal Ghannam. Dipole nanolasers: A study of their quantum properties. *Physics Reviews A*, 79(4):7, 2009.

[6] M. A Noginov, G Zhu, A. M Belgrave, R Bakker, V. M Shalaev, E. E Narimanov, S Stout, E Herz, T Suteewong, and U Wiesner. Demonstration of a spaser-based nanolaser. *Nature*, 460(7259):1110–1112, 2009.

[7] Mark I Stockman. The spaser as a nanoscale quantum generator and ultrafast amplifier. *Journal of Optics*, 12:024004, 2010.

[8] M.A Noginov, I Fowlkes, G Zhu, and J Novak. Neodymium random lasers operating in different pumping regimes. *Journal of Modern Optics*, 51(16-18):2543–2553, 2004.

[9] Eduardo A Coronado, Ezequiel R Encina, and Fernando D Stefani. Optical properties of metallic nanoparticles: manipulating light, heat and forces at the nanoscale. *Nanoscale*, 3(10), 2011.

[10] KG Stamplecoskie, NL Pacioni, D Larson, and JC Scaiano. Plasmon-mediated photopolymerization maps plasmon fields for silver nanoparticles. *Journal of the American Chemical Society*, 133(24):9160–3, 2011.

[11] KG Stamplecoskie C Fasciani and JC Scaiano. Dual-stage lithography from a light-driven, plasmon-assisted process: A hierarchical approach to subwavelength features. *Langmuir*, 28(30):10957–10961, 2012.

[12] KG Stamplecoskie and JC Scaiano. Light emitting diode irradiation can control the morphology and optical properties of silver nanoparticles. *Journal of the American Chemical Society*, 132(6):1825–1827, 2010.

[13] GM Wallraff and WD Hinsberg. Lithographic imaging techniques for the formation of nanoscopic features. *Chemical Reviews*, 99(7):1801–1822, 1999.

[14] RX Bian, RC Dunn, XS Xie, and PT Leung. Single molecule emission characteristics in near-field microscopy. *Physics Review Letters*, 75(26):4772–4775, 1995.

[15] PB Punjabi, R Ameta, A Kumar, and M Jain. Visible light induced photocatalytic degradation of some xanthene dyes using immobilized anthracene. *Bulletin of the Chemical Society of Ethiopia*, 22(3):361–368, 2008.

Chapter 7

Summary

The inspiration for this work was to achieve control over the morphology and optical properties of AgNP through synthesis (bottom up type approaches). In all cases the controlled synthesis of these AgNP was performed with end-use as the paramount consideration. Nanoparticle research has been flooded with examples of synthesis of various types of particles, with vastly different surface functionalities and different morphologies. Often the question arises as to 'why?', or 'for what purpose?', and these works are criticized (possibly with good reason) on this basis. However, there are many nanomaterials researchers that are devoted to the understanding of new properties that arise from manipulations of these materials at the nanoscale. In the examples provided in this work, it is the structure-function relationship that is always considered most important, and has lead to some interesting new materials for real applications.[1]

In order to develop AgNP for particular applications, control over features such as size, shape, surface functionality (matrix compatibility) and optical properties is the key. Therefore, the first section of this work describes the synthesis of silver nanoparticles, most often stabilized by citrate. Some of the important photochemical aspects of the organic precursors and reactions are discussed as well as how to manipulate these parameters in order to trap small, fluorescent silver clusters. This work has lead to a better understanding of the nucleation processes in nanoparticle formation, as well as solvent effects on nanoparticle formation in non-protic solvents. For this reason this work was recently highlighted in JACS for its contribution to understand the kinetics of formation of clusters and characterization of their emission properties, as it relates to understanding the formation of nanoparticles.[2, 3]

Silver has been know for a long time to be optically active, even in comparison to other

noble metals, where excitation of the plasmon of AgNP often leads to morphological and optical changes.[4, 5, 6, 7, 8, 9] Therefore, the citrate stabilized particles are often used as a starting material for synthesis of other desired AgNP. In previous published works the shape control was often attributed solely to twinning defects in starting spherical AgNP, or to judicious choice of stabilizing agents, under either thermal or illumination conditions used in reshaping the particles. While these factors may play a role, and certainly do in thermal morphological changes, the choice of wavelength when exciting small spherical AgNP has been shown to be crucial to the final morphology and optical density of these colloids. Developed herein, is a simple method in which citrate stabilized spherical AgNP 'seeds' can be irradiated with inexpensive light emitting diodes to change their shape. The final shape and colour of the colloids is determined only by the choice of LED wavelength. A mechanism for the shape change is proposed and the particular redox properties, as well as strong optical properties of AgNP are attributed with the interesting photo activity of these colloids.[10]

The strong optical response (absorbance) of silver colloids has several interesting effects including an intense electromagnetic field around nanoparticles. The morphology control of the colloids determines the size and shape of this field, as well as the wavelength of excitation. Plasmon excited AgNP have been shown to strongly enhance the Raman spectrum of molecules near the surface, and all of the factors associated with shape control, like size, excitation wavelength and exposed facets, have potentially dramatic effects on this enhanced Raman spectroscopy. Therefore, different shapes and sizes of AgNP display different total enhancement factors. Herein the effect of size and shape of AgNP on the enhanced Raman spectrum of R6G was investigated. For spherical AgNP the optimal size was approximately 50 nm. This was due to the increasing magnitude of the EM field with larger particle size, offset by the decreasing surface area for R6G adsorption with increasing particle size. Of the different shapes, while small spheres had the larges surface area for adsorptions, decahedral particles gave the strongest enhancement. Decahedra are actually comprised of five prisms that spontaneously associate into a multi-twinned particle. It is well known that Raman enhancement is strongest at points between particles,[11] and so the anomolously high Raman signal with decahedral particles has been attributed to the strong fields at these twinning defect sites (where two particles come together). This is depicted schematically in Figure 7.1.[12]

Silver has been known for centuries to have antibacterial applications and has even been used in medical applications like surgical steel to prevent infections. The application of AgNP has been proposed for a number of medical applications as a direct antibacterial

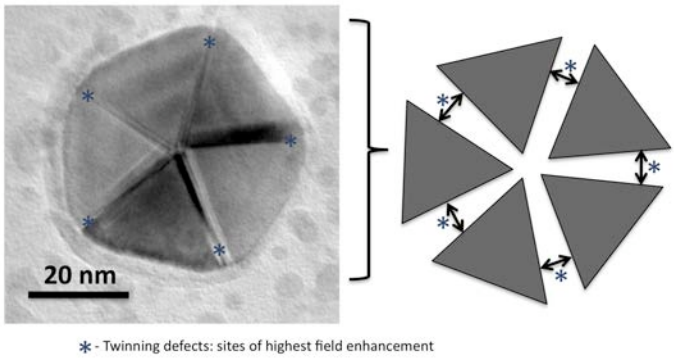

Figure 7.1: Decahedral particles made of 5 smaller prisms with twinning defects as indicated that serve as strong enhanced field points on the particles.

agent in materials such as prosthetics. A collaboration in the Scaiano group has lead to the promise of incorporating AgNP into artificial skin matrices and artificial cornea, both serving as prosthetics. The hope is that AgNP will inhibit bacterial growth and therefore, inhibit rejection of the prosthesis. In order to evaluate the use of these AgNP, the antibacterial ability as well as cell toxicity were assessed. It was found that AgNP inhibit bacteria growth very effectively, while cell toxicity studies show that the particles are not toxic to normal cells, even at concentrations much higher than those needed for antibacterial activity. This is a very encouraging set of results, especially for patients like diabetics who suffer from chronic lesions, requiring artificial skin.[13]

The same enhanced field around plasmon excited AgNP that is exploited in SERS, can effect electronic transitions in surface bound molecules as well (not just vibrational transitions). This has been used herein to selectively excite radical polymerization initiators on the surface of metal particles, and in doing so, cause polymerization on the surface of these particles. The matrix can be removed by solvents, leaving polymer features that are fundamentally not limited by diffraction. This is a potentially important work for lithography for microchip fabrication, where the feature size (and performance) are currently limited by diffraction. The same selective polymerization near the surface can be obtained by plasmon excitation for initiators that only require heating, due to the extreme heat produced at the surface of these particles. This has been demonstrated with the polymerization of caprolactam to nylon-6 on particles that are synthesized in-situ as well.[14, 15]

The 'self-assembly' of polymer features on plasmon excited AgNP used in generating

lithographic type features, has lead to a discovery that could be the most important contribution from this thesis. Similar polymerization processes have been induced around AgNP that are either decahedra or plate shaped, chosen for their respective plasmon absorption maxima. The polymerization process is used to trap selected dye molecules (chosen to have emission that overlap with the plasmon of the particles), coumarin 6 and Eosin Y. In both cases, the self-assembled, core-shell particles have dye molecules that couple with the plasmon of the AgNP, and above a threshold excitation level, they display delayed stimulated emission and optical gain. In other words, these are self-assembled, nano-sized lasers. There has to date been only one example of the fabrication of these so called 'spasers' with great potential in optoelectronics. However, this other example is synthetically challenging, especially when considering the localization required in chip fabrication. The self-assembly process used here can be used to overcome these limitation so that these spasers can be easily incorporated into functional optoelectronic chips.[16]

In keeping with the idea of relating structure with function, and in developing a complete picture of the properties of the nanomaterials synthesized and studied herein, several reviews have been written. These articles not only summarize selected portions of the work within this thesis, but also expand upon other works and aim to provide a more broad understanding of these materials and the chemistry used in synthesizing them.[17, 18, 19, 20] [21]

REFERENCES

[1] PR Sajanlal, TS Sreeprasad, AK Samal, and Thalappil Pradeep. Anisotropic nanomaterials: structure, growth, assembly, and functions. *Nano Reviews*, 2:5883, 2010.

[2] Garcia-Garibay. Advances at the frontiers of photochemical sciences. *Journal of the American Chemical Society*, 134(20):8289–8292, 2012.

[3] KG Stamplecoskie and JC Scaiano. Kinetics of the formation of silver dimers: Early stages in the formation of silver nanoparticles. *Journal of the American Chemical Society*, 133(11):3913–3920, 2011.

[4] AC Sant'Ana, TCR Rocha, PS Santos, D Zanchet, and MLA Temperini. Size-dependent sers enhancement of colloidal silver nanoplates: the case of 2-amino-5-nitropyridine. *Journal of Raman Spectroscopy*, 40(2):183–190, 2009.

[5] HH Huang, XP Ni, GL Loy, CH Chew, KL Tan, FC Loh, JF Deng, and GQ Xu. Photochemical formation of silver nanoparticles in poly(n-vinylpyrrolidone). *Langmuir*, 12(4):909–912, 1996.

[6] G V Krylova, A M Eremenko, N P Smirnova, and S Eustis. Photochemical preparation of nanoparticles of ag in aqueous alcoholic solutions and on the surface of mesoporous silica. *Theoretical and Experimental Chemistry*, 41(5):105–110, 2005.

[7] Masanori Sakamoto, Mamoru Fujistuka, and Tetsuro Majima. Light as a construction tool of metal nanoparticles: Synthesis and mechanism. *Journal of Photochemistry and Photobiology C: Photochemistry Reviews*, 10(1):33–56, 2009.

[8] B Pietrobon and V Kitaev. Photochemical synthesis of monodisperse size-controlled silver decahedral nanoparticles and their remarkable optical properties. *Chemistry of Materials*, 20:5186–5190, 2008.

[9] A Callegari, D Tonti, and M Chergui. Photochemically grown silver nanoparticles with wavelength-controlled size and shape. *Nano Letters*, 3(11):1565–1568, 2003.

[10] KG Stamplecoskie and JC Scaiano. Light emitting diode irradiation can control the morphology and optical properties of silver nanoparticles. *Journal of the American Chemical Society*, 132(6):1825–1827, 2010.

[11] G Chen, Y Wang, M Yang, J Xu, SJ Goh, M Pan, and H Chen. Measuring ensemble-averaged surface-enhanced Raman scattering in the hotspots of colloidal nanoparticle dimers and trimers. *Journal of the American Chemical Society*, 132(11):3644–5, 2010.

[12] KG Stamplecoskie, JC Scaiano, VS Tiwari, and H Anis. Optimal size of silver nanoparticles for surface-enhanced Raman spectroscopy. *Journal of Physical Chemisty C*, 115(5):1403–1409, 2011.

[13] EI Alarcon, CJ Bueno-Alejo, CW Noel, KG Stamplecoskie, NL Pacioni, H Poblete, and JC Scaiano. Human serum albumin as protecting agent of silver nanoparticles: role of the protein conformation and amine groups in the nanoparticle stabilization. *Journal of Nanoparticle Research*, 15:1–14, 2013.

[14] KG Stamplecoskie, NL Pacioni, D Larson, and JC Scaiano. Plasmon-mediated photopolymerization maps plasmon fields for silver nanoparticles. *Journal of the American Chemical Society*, 133(24):9160–3, 2011.

[15] KG Stamplecoskie C Fasciani and JC Scaiano. Dual-stage lithography from a light-driven, plasmon-assisted process: A hierarchical approach to subwavelength features. *Langmuir*, 28(30):10957–10961, 2012.

[16] KG Stamplecoskie and JC Scaiano. Self-assembled dipole nanolasers. *In Progress*.

[17] JC Scaiano and GL Hallett-Tapley KG Stamplecoskie. Photochemical Norish type I reaction as a tool for metal nanoparticle synthesis: Importance of proton coupled electron transfer. *Chemical Communications*, 48:4798–4808, 2012.

[18] JC Scaiano, JC Netto-Ferreira, E Alarcon, P Billone, CJ Bueno Alejo, COL Crites, M Decan, C Fasciani, M González-Béjar, G Hallett-Tapley, M Grenier, KL Mcgilvray, NL Pacioni, A Pardoe, L René-Boisneuf, R Schwartz-Narbonne, J Silvero, KG Stamplecoskie, and TL Wee. Tuning plasmon transitions and their applications in organic photochemistry. *Pure and Applied Chemistry*, 83(4):913–930, 2011.

[19] JC Scaiano, KG Stamplecoskie, KL McGilvray, and NL Pacioni. *A Paradigm for the Radical-Mediated Photochemical Synthesis of Metal Nanostructures*. John Wiley and Sons Ltd, 2012.

[20] KG Stamplecoskie and JC Scaiano. Silver as an example of the applications of photochemistry to the synthesis and uses of nanomaterials. *Photochemistry and Photobiology*, 88(4):762–8, 2012.

[21] KG Stamplecoskie and JC Scaiano. So we can make metal nanoparticle but can their surface plasmon fields provide a new way to photosensitize organic photoreactions? *In Progress*.

Chapter 8

Future Directions

The work presented herein has contributed to the understanding of the physical properties of AgNP, mostly pertaining to the optical properties and the effects of plasmon excitation. It has also helped the understanding of the synthesis and conditions under which these particles are stable. The applications discussed here are just the tip of the iceberg, where the general concepts can be exploited further in areas of biology for photodynamic therapy, in catalysis and particular photocatalysis to drive new reactions or increase rates in others, as well as light harvesting, to name a few examples.[1]

In the case of light harvesting, or photocatalysis (especially in light harvesting for applications like photocatalysis) there are still debatable issues that can be solved using nano-composite materials. One of the proposed mechanisms that describes enhanced photochemistry of TiO_2 is depicted in Figure 8.1, where visible light excitation of TiO_2/AuNP has been used for water splitting to form hydrogen.[2]

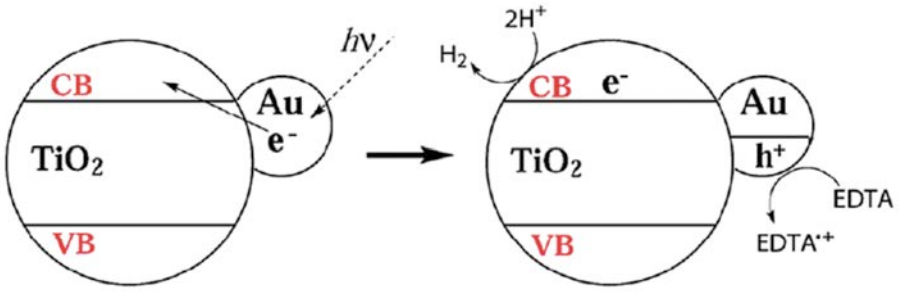

Figure 8.1: Scheme depicting how plasmon excitation can lead to increased charge carriers and therefore higher photocatalytic efficiency for TiO_2, taken from ref [2].

This mechanism has been called into question due to the fact that AuNP are known to be good electron acceptors for photoexcited TiO_2, and so the electron injection from AuNP to TiO_2 must be an energetically costly process. The plasmon enhancement of TiO_2 photo-activity has been otherwise described as a combination of 4 mechanisms; (1) increased visible light absorption by TiO_2 due to light trapping by surface plasmons, (2) improved exciton formation due to local EM field around excited NP, (3) improved electron transfer to adsorbed species, and (4) electron storage in the metal NP that can affect the Fermi level of TiO_2. In an attempt to quantify some of these effects, Kamat *et al.* have made solar cells with AuNP as photosensitizers and observed the effect of these nanoparticles on photocurrent with and without a SiO_2 (with and without the possibility of electron transfer).[3]

There are two common schools of thought on this issue, that may in fact both be true. One thought is that plasmon excitation can result in electron transfer from the NP to TiO_2, and the other thought is that this is energetically impossible and so the 4 mechanisms above are possible reasons for AuNP enhancement of TiO_2. It is possible that plasmon excitation, can cause an inter-band transition in AuNP due to similarity in energy of these two processes. This is seen in the long sloping baseline of UV-Vis absorption spectra of AuNP that show both plasmon and interband transitions. These interband transitions result in an electron/hole pair, similar to semiconductors, and can in fact result in electron injection into TiO_2. For AgNP however, the interband transitions are at much higher energies ($\leqslant$320 nm) than the plasmon transition (400 nm), so that the UV-Vis absoption spectrum for AgNP is more flat (no sloping baseline) since there are no observed interband transitions.[4] The absorbance spectra with the relevant transitions are shown in Figure 8.2.

The important point about AuNP here, is that both theories are correct in that plasmon excitation can result in inject electrons into TiO_2 (mediated by a transient exciton in the AuNP), and that it is not a plasmon excitation that directly injects electrons into TiO_2. The fact that plasmon excitation of AgNP can not result in interband excitation can be used to prove or disprove these ideas. For example, using AgNP and AuNP with and without SiO_2 shells should allow one to separate the near field and far field effects of both of these materials on the photocurrent and water splitting of both of these plasmonic materials. Furthermore, plasmon excitation of AgNP should not result in electron injection into TiO_2 (therefore, very minimal photocurrent with 400 nm light), whereas photocurrent would be observed with 530 nm excitation of AuNP on TiO_2 due to electron injection. This is just one example of how, the understanding of

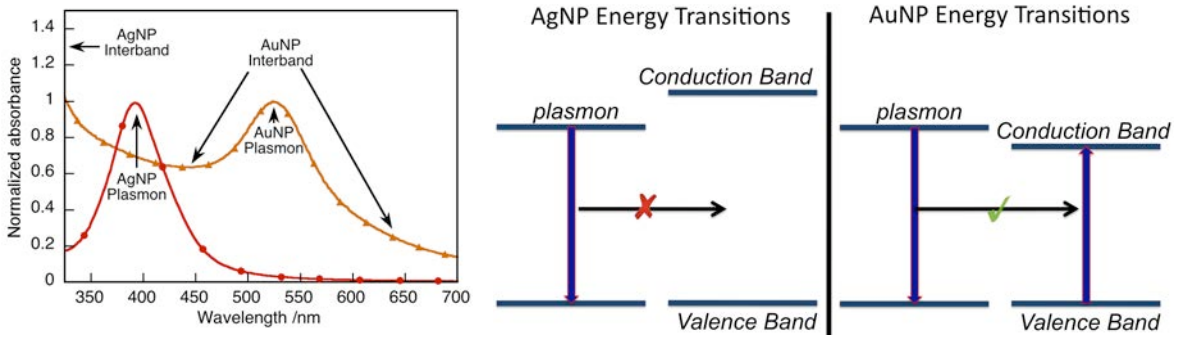

Figure 8.2: Left: UV-Vis absorption spectra for AgNP and AuNP, indicating the plasmon transitions as well as interband transitions for both. Right: Energy level diagram depicting the plasmon and interband transitions for AgNP and AuNP and how the AuNP transitions overlap in energy.

AgNP synthesized herein can be expanded to further understanding important process like light harvesting in NP sensitized TiO_2.

Light harvesting is an important field of chemistry, dominated by TiO_2, and the example above shows how AgNP can be used for in depth understanding of the mechanism of plasmon enhancement of some important photochemistry. There are many emerging examples of how plasmon excitation can be exploited for photothermal effects, electron transfers (redox chemistry) and by an antenna effect for enhanced photochemistry, discussed in our recent Perspective.[1] Within this Perspective, the effects of plasmon excitation are described in an attempt to provide synthetic chemists with the tools to develope novel synthetic strategies using plasmon excitation. The conceptual picture is a tool to exploit plasmon excitation in organic chemistry. An interesting example using methylene blue, where the excited state properties of methylene are directly affected by plasmon excitation of gold, is discussed. Here, 530 nm excitation has been used to excite both AuNP and methylene blue, and the excited state transients of methylene blue (and singlet oxygen production) are observed by LFP in order to understand the excited state dynamics as they are affected by plasmon excited nanoparticles. It is found that the probability of excitation can be increased by the nanoparticle, but the lifetime of the excited state is shortened, and therefore the formation of singlet oxygen is reduced due to quenching by the nanoparticle.[5]

Similarly, the plasmon polymerizations discussed herein for photolithography applications exploit the change in excitation of AIBN and Eosin Y, in order to induce polymer-

ization within the plasmon field. These effects are not limited to the examples discussed herein. For example, plasmon excitation can be used to enhance photochemistry involved in drug delivery. With the control of particle shape and optical density, it is possible to affect the absorption and photochemistry of many common photo-sensitive molecules for this purpose. The holy grail of photochemical drug release is to be able to sensitize the release of drugs with longer than normal wavelengths of light (750 - 800 nm), in order to get deep tissue penetration. Incorporating drugs with nanoparticles, particularly particles with strong long wavelength absorption like nanoplates, is a possible way of giving long wavelength absorptions for this drug release.

Only a couple of examples are discussed above for how silver nanoparticles, with shape/optical density control can be used. What is clear is that understanding of the properties and synthesis of these materials, the topic of this thesis, has contributed to a body of work that has possibly broad implications.

REFERENCES

[1] KG Stamplecoskie and JC Scaiano. So we can make metal nanoparticle but can their surface plasmon fields provide a new way to photosensitize organic photoreactions? *In Progress*.

[2] CG Silva, R Juarez, T Marino, R Molinari, and H Garcia. Influence of excitation wavelength (UV or visible light) on the photocatalytic activity of titania containing gold nanoparticles for the generation of hydrogen or oxygen from water. *Journal of the American Chemical Society*, 133(3):595–602, 2010.

[3] H Choi, WT Chen, and PV Kamat. Know thy nano neighbor. plasmonic versus electron charging effects of metal nanoparticles in dye-sensitized solar cells. *ACS Nano*, 6(5):4418–4427, 2012.

[4] A Henglein. Physicochemical properties of small metal particles in solution - microelectrode reactions, chemisorption, composite metal particles, and the atom-to-metal transition. *Journal of Physical Chemistry*, 97(21):5457–5471, 1993.

[5] Natalia L Pacioni, María González-Béjar, Emilio Alarcón, Katherine L McGilvray, and J C Scaiano. Surface plasmons control the dynamics of excited triplet states in the presence of gold nanoparticles. *Journal of the American Chemical Society*, 132(18):6298–6299, 2010.